Master of Science Thesis

Bridging Experimental Simulations with Computational Frameworks for Time-Resolved Characterization of Fluid-Structure Interactions

Bora Orcun CAKIR

30.09.2020

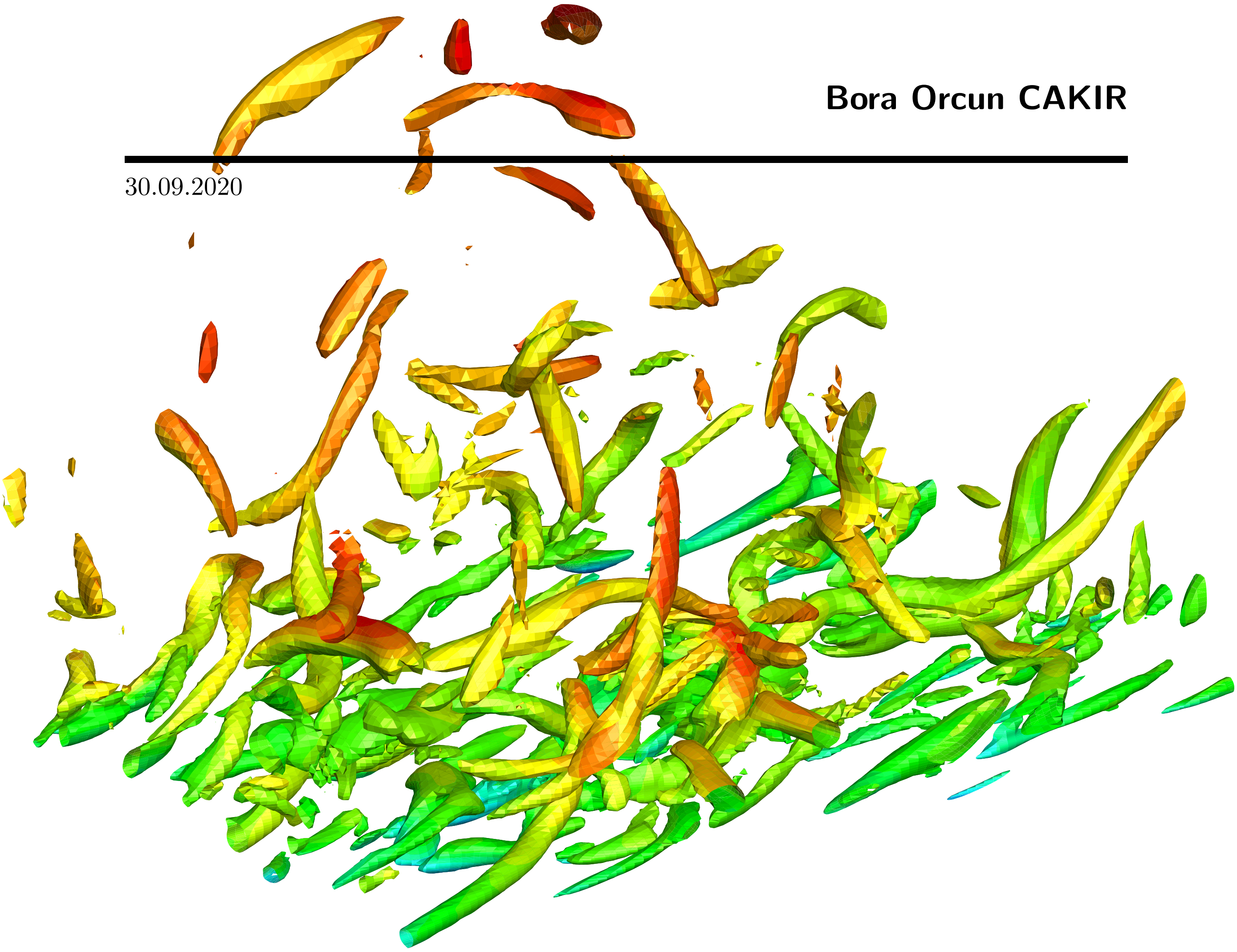

Faculty of Aerospace Engineering · Delft University of Technology

Challenge the future

Bridging Experimental Simulations with Computational Frameworks for Time-Resolved Characterization of Fluid-Structure Interactions

MASTER OF SCIENCE THESIS

For obtaining the degree of Master of Science in Aerospace
Engineering at Delft University of Technology

Bora Orcun CAKIR

30.09.2020

Faculty of Aerospace Engineering · Delft University of Technology

Delft
University of
Technology

DELFT UNIVERSITY OF TECHNOLOGY
DEPARTMENT OF
AERODYNAMICS

The undersigned hereby certify that they have read and recommend to the Faculty of Aerospace Engineering for acceptance a thesis entitled **“Bridging Experimental Simulations with Computational Frameworks for Time-Resolved Characterization of Fluid-Structure Interactions”** by **Bora Orcun CAKIR** in partial fulfillment of the requirements for the degree of **Master of Science**.

Dated: 30.09.2020

Prof. dr. ir. Bas van Oudheusden

Dr. Andrea Sciacchitano

Dr. ir. Alexander van Zuijlen

Dr. Daniele Ragni

Gabriel Gonzalez Saiz, MSc.

Acknowledgements

From the moment I have arrived at TU Delft for my master stuides, I was extremely fortunate to get acquainted with Dr. Bas van Oudheusden and receive his precious supervision. Our earliest discussions enabled myself to shape my complete study programme towards realizing my interest on the fusion of experimental and computational fluid dynamics frameworks over this thesis project. Therefore, I would like to express my utmost gratitude to my thesis supervisors Dr. Bas van Oudheusden and Dr. Andrea Sciacchitano for their relentless endurance on my ideas and supporting myself by all means. I would also like to thank to Gabriel Gonzalez Saiz for allowing me to take part in his experimental campaigns and sharing his knowledge without any boundaries for the content of his doctoral studies. Furthermore, I would like to express by kind appreciation to Dr. Richard Dwight and Dr. Alexander van Zuijlen for their discussions and directions in subjects of their respective expertise.

Last but not least, within the time period of this unexpected and incredibly challenging Covid-19 crisis, Prof. Stefan Hickel and Dr. Davide Modesti provided the numerical datasets for my validation studies, that composes a prominent part of this project. Thus, I would like to state my gratefulness to both of them for their kind efforts.

Delft, The Netherlands
30.09.2020

Bora Orcun CAKIR

Summary

Closure of Collar's triangle represents a complete framework of fluid-structure interactions (FSI) enabling the comprehensive understanding of different design elements compromising aeronautical applications. Experimental methods such as tomographic particle image velocimetry (Tomo-PIV) are proven to provide accurate acquisition opportunities of fluid properties in three dimensional domains. However, not only the closure problem requires simultaneous investigations of fluid and structure behaviors but also the maximum attainable measurement volumes for characterizing these behaviors are severely limited for conventional Tomo-PIV applications. Therefore, a large scale Tomo-PIV setup capable of measuring simultaneous flow motion via Helium Filled Soap Bubbles (HFSB) and structure motion by means of surface markers is employed for experimental investigations of turbulent boundary layer interactions with an unsteadily deforming elastic membrane.

Despite the aforementioned benefits of large scale tomographic PIV/PTV techniques, available spatial resolution characteristics for time-resolved flow field measurements are significantly restricted due to the tracer particle specifications of HFSB. This restriction requires additional post-processing algorithms to be applied over the raw experimentally acquired datasets in order to mitigate the effect of experimental trade-off between the temporal and spatial resolution specifications, and allow instantaneous flow field characterization. Although state-of-the-art data assimilation approaches provide the capability of reconstructing high resolution flow features by interpolating the available scattered particle tracking information for global time-resolved flow field reconstruction, drawbacks due to the inability of resolving the viscous effects for near wall flow behavior, incapability of handling physical intrusions to the flow field and propagation of measurement errors, compromise accurate characterization of flow structures in close proximity of the FSI interface.

First of all, these algorithms are developed for reconstructing flow features involved with engineering applications where the flow conditions are dominated by turbulent characteristics. However, the fluid behavior in close proximity of walls are dictated by non-negligible viscous forces. Hence, achieving dense interpolation of flow properties of near wall features requires proper characterization of viscous effects for which the thesis proposes the employment of wall function applications for appropriate boundary condition determination. Secondly, even though the available data assimilation methods are able to handle flow behavior around objects, characterization of regions in direct interaction with the object boundaries is not possible. Therefore, in order to handle non-uniform solid boundaries, computational FSI frameworks of the Arbitrary Lagrangian-Eulerian (ALE) and the immersed boundary treatment methods are utilized. Furthermore, as the local closure of Collar's triangle demands fluid loading over the structural surfaces to be determined, surface pressure information is required to characterize the aeroelastic interactions. Hence, an alternative approach of non-intrusive surface pressure reconstruction from PIV data over unsteadily deforming non-uniform boundaries is introduced via interpreting the ALE method with boundary fitted coordinate systems. Finally, measurement and processing errors contained within the experimental procedures propagate through the data assimilation algorithms. Therefore, to enable the the mitigation of experimental measurement and processing errors, an alternative approach of governing equation based dense flow field interpolation is developed using solenoidal and irrotational radial basis functions (RBF).

Capabilities of the proposed methods within the thesis project are demonstrated with various theoretical, numerical and experimental test cases. The wall function application enabled accurate characterization of average streamwise velocity profiles as well as providing slight improvements on the fluctuating velocity components compared to the no-slip boundary condition implementation. Both approaches introduced for handling of physical intrusions resulted in increased coherence levels of flow behaviors within the respective test cases, where the local variations of velocity components revealed promising improvements against the state-of-the-art assimilation algorithms favoring the developed methods in terms of providing greater agreements to the reference flow fields. The introduced surface pressure reconstruction scheme with boundary fitted coordinates yielded relative error levels confined below 4% compared to analytical flow field properties where the resultant errors are computed to be related to the numerical truncation errors rather than the discretizations of mesh deformations or vectorial transformations. The developed alternative approach of dense flow field interpolation with solenoidal and irrotational RBFs allowed inherent mass conservation for the velocity field reconstructions that significantly increased the agreement of the interpolated velocity and vorticity fields with the reference flow field information while irrotationality imposition on the material accelerations provided elevated accuracy levels for pressure field computations.

Consequently, the proposed methods of wall function implementation, ALE-VIC+ and ImVIC+ are utilized for experimental characterization of surface pressure variations over the unsteadily deforming elastic membrane exposed to turbulent boundary layer conditions. The instantaneously available low density particle tracking information is assimilated towards dense interpolation of material accelerations to capture temporal evolution of static pressure values at the central membrane location. The superior accuracy specifications of both ALE-VIC+ and ImVIC+ against linear interpolation owing to the kinematic characterization of the influence of membrane motion on the flow field properties provided greater agreements of the non-intrusive time-resolved pressure field computations with the pressure tab measurements.

Contents

Chapter 1

Introduction

The trend of engineering development is towards utilizing the lightest and highest performing design elements to allow the most cost efficient solution to be obtained. Using state-of-the-art material production techniques and enhancing the load bearing capacities of available forms, enables designers to further push the limits of performance and cost-efficiency. In case of aeronautical applications, this is done in a sense that leads the utilization of lower weight materials with improved resistance against loads only in the necessary areas. In previous eras, determination of these regions are performed by various departments composing different elements of aeronautical design. Although these departments were to work in collaboration, the internal work of analysis performed separately, where the mainframe work of the design process relied on a comprehensive feedback mechanism around "the Collar's Triangle" defining the main aspects of aeroelasticity (Collar, 1978). The Collar's triangle refers to the set of factors defining an aerodynamic body composed of elastic forces, inertial forces and aerodynamic forces, Fig.1.1.

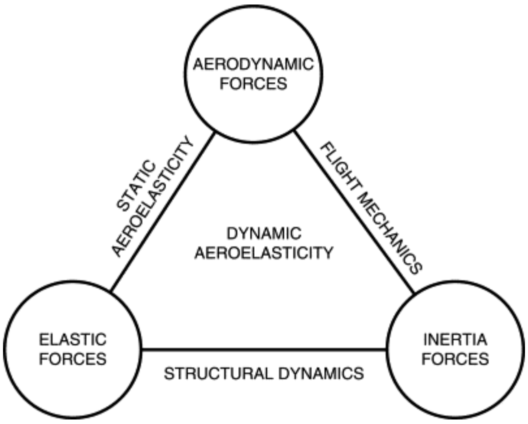

Figure 1.1: Collar's triangle of aeroelasticity (Cecrdle, 2015).

However, the line of progression on structural and aerodynamic requirements demands a single framework capable of analyzing structural and aerodynamic components simultaneously to increase the fidelity of design elements and closing the Collar's Triangle. This requirement initiated the field of Fluid-Solid Interactions (FSI) where a complete investigation scheme is to be created to analyze both aerodynamic performance and structural integrity.

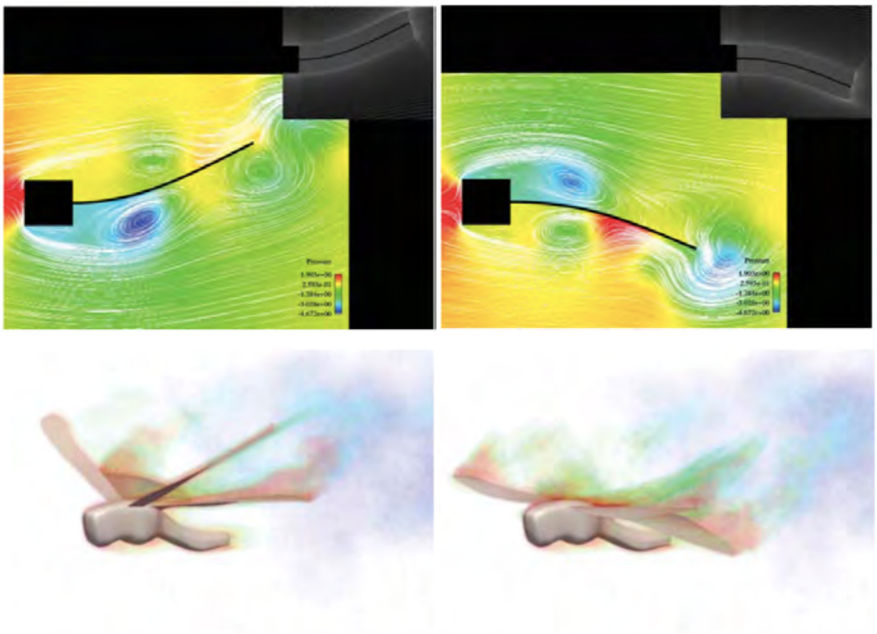

Figure 1.2: Numerical simualtions of 2D flow over an elastic beam mounted downstream of a square cross-sectioned rigid block (Bazilevs et al., 2008)(top) and instantaneous vorticity distributions around a 3D flapping wings (Takizawa et al., 2011)(bottom).

FSI, being a superior tool able to tackle a complete engineering problem, suffered from various incompatibility issues especially over the surface of fluid-solid interaction, due to the fact that fluid and solid computational domains, and their corresponding numerical discretizations require different descriptions (Zienkiewicz et al., 2014). The relation of fluid and structural domains over the interaction interface can be briefly explained as the surface pressure generated by the fluid determines the structural stresses and the corresponding deformations, which in turn dictates the flow behaviour. Hence providing a reliable and accurate method of information transfer over the interface of fluid and solid domains has became the main stream of scientific concentration in the field of FSI where various mathematical algorithms are proposed over a wide range of scientific and engineering applications. Moreover, the region of FSI interface also possesses the greatest vulnerabilities against the capabilities of numerical methods to resolve the most challenging problems of computational fluid dynamics (CFD), boundary layer and wall interactions of flow features. Although many advance methods in CFD exists to provide sufficient fidelity characteristics to achieve accurate representations of physical flow behaviour in these regions, it is certain that not only their immense computational expense but also the lack of reliability of their nature urges a strong need for calibration and validation.

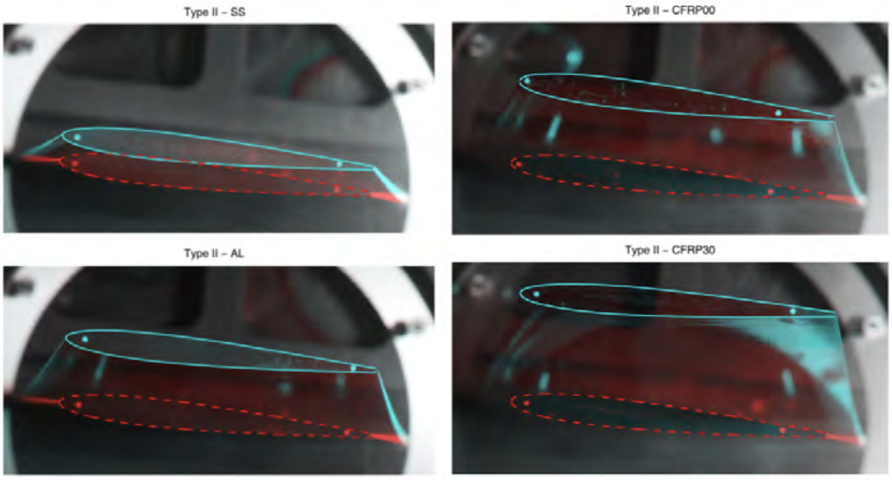

Figure 1.3: Experimental steady tip displacements of flexible hydrofoils exposed to turbulent flow at $Re = 10^6$ (Zarruk et al., 2014).

Therefore the necessity of exploiting experimental techniques for enabling simultaneous acquisition and reconstruction of fluid and structure behaviors emerges. This urge is further promoted by the capabilities of experimental methods to provide non-intrusive global measurement possibilities such as volumetric techniques of particle image velocimetry (PIV) and particle tracking velocimetry (PTV). Nevertheless, as the validation of FSI simulations strongly depend on the information transfer through the fluid-structure interface, being able to obtain the fluid information at the surface of interaction is still a critical point. Since the interaction between fluid and solid domains refers to an iterative procedure, it requires a capability of transient reconstruction of the pressure fields over the structure surface. This necessity of time resolution might challenge the limits of available spatial resolution specifications depending on the measurement technique in use, reducing the reliability and accuracy of volumetric and surface information reconstruction. Thus, it is of utmost importance to utilize the available information most effectively and increase the resolution of spatial information by means of data assimilation methods for the purpose of elevating the accuracy of time-resolved surface pressure determination.

Accordingly, various data assimilation techniques are developed for utilizing statistical analysis and flow governing equations for enhancing the characterization capabilities of experimental measurement campaigns by increases the instantaneous spatial resolution specifications. Nevertheless, there exists three main drawbacks of these approaches which are significant for accurate characterization of FSI problems. Firs of all, these algorithms are developed for reconstructing physical flow behavior of engineering applications where the flow conditions are dominated by turbulent characteristics while the fluid behavior in close proximity of walls are dictated by non-negligible viscous interactions between the fluid and solid domains. Hence, achieving dense interpolation of coherent flow properties for near wall features requires proper characterization of viscous effects. Thus, the first objective of the thesis project emerges as;

To account the effect of viscous interactions in close proximity of wall surfaces for determination of boundary conditions of available

> ***data assimilation algorithms utilizing a wall function implementation.***

Secondly, the available data augmentation methods are based on characterizing the flow properties within regions of sole fluid presence. Hence, even though they are able to handle the flow behavior around objects, characterization of regions in direct interaction with the object boundaries is not possible. Therefore, the second objective of the thesis is designated as;

> ***To enable the handling of non-uniform solid boundary intrusions of unsteadily deforming surfaces for available data assimilation algorithms by employing computational FSI frameworks of the Arbitrary Lagrangian-Eulerian and immersed boundary treatment methods, providing the capability of determining the flow behavior in close proximity of the FSI interface.***

Furthermore, as the local closure of Collar's triangle demands fluid loading over the structural surfaces to be determined, surface pressure information obtained from the experimentally acquired datasets plays an important role for proper characterization of FSI problems. Although various approaches have been proposed for determining the pressure distribution over non-uniform surfaces, these methods require individual handling of the close surface elements for each time instant which inherently increases the computational cost of the numerical procedures. Hence the third objective of the thesis project is determined;

> ***To achieve non-intrusive surface pressure reconstruction from PTV data over unsteadily deforming non-uniform boundaries via interpreting the Arbitrary Lagrangian-Eulerian method with boundary fitted coordinate systems generated by means of radial basis function based mesh deformations.***

Moreover, measurement and processing errors contained within the experimental procedures of PIV and PTV yield deviations of velocity fields from the physical laws of fluid motion. As the available data from the experimental campaigns is employed in the assimilation algorithms, the measurement errors propagate towards the dense interpolations over the prescribed computational domains compromising the accuracy of resultant flow field information. Therefore, the final objective of the thesis concentrates on developing an alternative approach for the data assimilation frameworks of increasing time-resolved spatial resolution characteristics of large scale Tomo-PIV experiments, while filtering the errors contained within the measurements as;

> ***To mitigate experimental measurement and processing errors for time-resolved flow field characterization using governing equation based dense flow field interpolation methods with solenoidal and irrotational matrix valued radial basis functions.***

Consequently, the thesis report is composed of 5 main chapters. Initially, Chapter 2 briefly overviews the available flow measurement methods in the field of PIV while referring to the developments enabled large scale measurement campaigns. It also documents the state-of-the-art computational methods introduced for pressure reconstruction from PIV and experimental data assimilation for PTV. Chapter 3 introduces the literature background for advanced techniques employed in CFD for discretizing near wall properties of boundary condition definitions, handling non-uniform solid intrusions within the flow field and their unsteady deformations present in FSI problems, and experimental data assimilation methods proposed for solenoidal filtering applications in order to mitigate the effect of measurement errors. Implementations of the proposed methods and their implementations within the thesis project to achieve the aforementioned objectives of data assimilation and surface pressure reconstruction are provided in Chapter 4 where their validation studies performed over various cases of theoretical, numerical and experimental datasets are presented in Chapter 5. Finally, Chapter 6 documents the experimental investigations of turbulent boundary layer interactions with an unsteadily deforming elastic membrane while employing the developed approaches for time resolved characterization of fluidic behavior as well as surface loading, towards enabling the local closure Collar's triangle.

Chapter 2

Combining Computational Fluid Dynamics and PIV

The work involved within the thesis project is of a multi-disiplinary nature for combining experimental simulations with computational framework. Hence, the literature review presented in this chapter starts with a brief background on the state-of-the-art optical measurement methods of tomographic PIV/PTV and measurement approaches utilized for experimental characterization of FSI problems. Then, it concentrates on the identification of the advantages and disadvantages of previously proposed experimental data augmentation techniques for time resolved flow field characterization based on statistical and physical fundamentals, and the pressure reconstruction schemes using PIV data in order to draw concluding remarks that enabled the development introduced approaches throughout the thesis.

2.1 Particle Image Velocimetry

Particle image velocimetry (PIV) refers to a non-intrusive optical measurement technique for extraction of dynamic flow information by seeding the fluid domain with tracer particles that are illuminated with various light sources. Images of measurement domain are recorded and the flow information is reconstructed by correlating the displacements of tracers particles in a prescribed space (Raffel et al., 1998). It is considered to be a great improvement on the flow measurement techniques where availability non-intrusive data acquisition in a global manner on significantly larger domains highlights the main factors of its superiority.

Following the fast development trend of digital data processing tools, illuminating systems and cameras; PIV setups that are capable of resolving greater scales of turbulence and capturing detailed flow characteristics at higher flow speeds became available (Saarenrinne et al., 2001). These advanced level of experimental capabilities provided by PIV allowed many researchers to diagnose detailed flow features in considerably challenging cases.

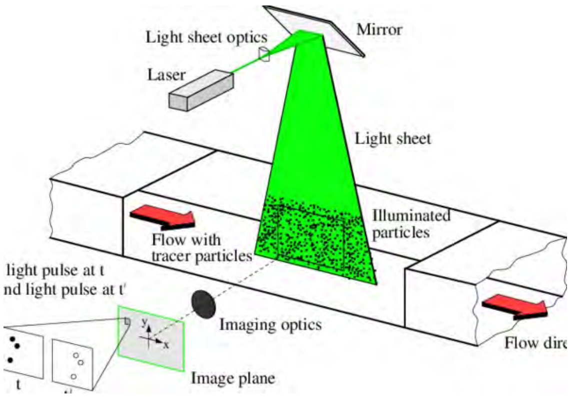

Figure 2.1: Illustration of an experimental setup of particle image velocimetry (Kompenhans et al., 1999).

2.1.1 Tomographic PIV

On the other hand, actual engineering applications are far from the simplified cases of two dimensions. Most of the applications are well in the regime of turbulent flow conditions where the definition requires a necessity of three dimensional considerations (Nieuwstadt et al., 2016). Although, investigating flow behaviour in a reduced domain of two dimensions establishes an ideal case which enables a basic understanding of flow features, it is certain that simulation of real life scenarios in scaled models also requires not only experiments designed to simulate the appearance 3D flow structures but also measurement techniques able to provide three dimensional flow field information. In order to perform this task in a non-intrusive manner, stereoscopic PIV is developed to acquire out-of-plane velocity components in combination with planar velocity information. However, since it is based on a planar projection of the measurement domain to a 3D flow field captured by two cameras, an exact setting of the laser sheet at the origin of out-of-plane coordinate axis is required (Wieneke, 2005). Therefore, tomographic PIV (Tomo-PIV) is introduced by Elsinga et al. (2006) stood out with its performance of acquiring three dimensional flow information over a three dimensional measurement domain.

Scarano and Ghaemi (2012) documented the detailed description of Tomo-PIV working principles where the step by step approach of its application is as follows,

- Thickness of the light sheet of illumination (a laser sheet for the initial applications of Tomo-PIV (Elsinga et al., 2008)) is expanded to generate a 3D measurement volume. Since the expansion procedure of the light sheet is performed from a single source using optical tools, Fig.2.3, a greater light intensity is required.

- The tomographic image recording system composing of multiple cameras capturing the illumination volume from various angles, where also single-camera based 3D PTV applications are proposed by Peterson et al. (2012) and Aguirre-Pablo et al. (2019), acquires the scattered light of the tracer particles.

- Three dimensional particle field is represented by processing the captured particle images via the tomographic reconstruction algorithm which utilizes multiplicative

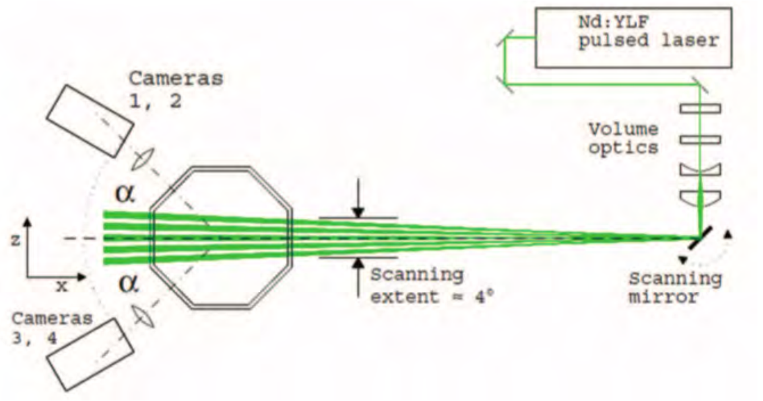

Figure 2.2: Sketch of the Tomo-PIV setup demonstrating the illumination volume (Casey et al., 2013).

algebraic reconstruction techniques (MART)(Atkinson and Soria, 2007), resulting in a three dimensional distribution of scattered light intensity of the tracer particles within the measurement volume.

- Then via three-dimensional cross-correlation of volumetric intensity distributions, particle motion within the measurement volume is obtained.

It should be noted that the relation of particle locations in recorded images to the physical space is established by means of calibration procedures. Hence, a precise calibration of the experimental setup appears as a fundamental step for accurate measurement campaigns.

Nevertheless, the application of Tomo-PIV is accompanied with certain drawbacks originated by its lack of capability to measure large volumes due to dispersed intensity of light illumination, light scattering performance of tracer particles and resolution characteristics of recorded images. Furthermore, since the optical aperture of the cameras are adjusted to be small in order to capture the complete depth of measurement volume, the recorded intensity of scattered light of tracer particles is mitigated especially compared to planar PIV applications (Tokarev et al., 2013). Consequently, there exists an inverse relationship between the scattered and captured light intensity magnitudes and the depth of the measurement volume which puts strict limitations on the maximum allowable measurement volume for Tomo-PIV applications. Elsinga et al. (2006) performed the introductory Tomo-PIV experiments with a measurement volume of 13 cm^3. Further applications by Schröder A (2009), Violato et al. (2011) and Ghaemi and Scarano (2011) were only be able to reach 20 cm^3 while the maximum measurement volume size attained is documented to be $6 \times 22 \times 8$ cm^3 while limiting the acceptable signal-to-noise ratio distribution to a depth of 5 cm (Fukuchi, 2012).

2.1.2 Large Scale Tomo-PIV/PTV with HFSB

Use of larger diameter tracer particles with superior light scattering characteristics is a possible solution for performing PIV measurements over larger volumes. Nevertheless, the size of tracer particles limits its flow tracing capabilities, thus reducing the coherence

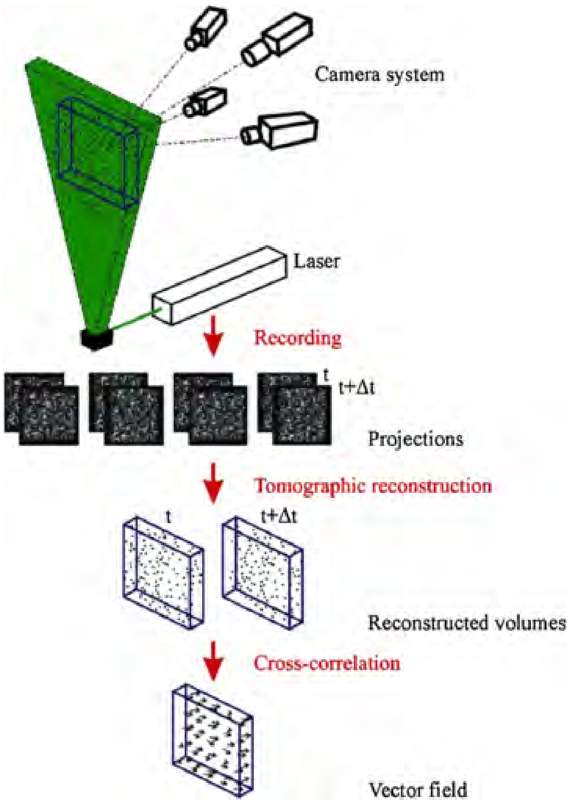

Figure 2.3: Schematic illustration of tomographic PIV reconstruction framework (Scarano and Ghaemi, 2012).

of its motion with the flow of interest. Since the fundamental working principle of PIV relies on the capability of tracer particles to represent the actual flow behavior throughout the complete measurement domain, the density deficit between the tracer particles and the working fluid originates a primary source of error due to the influence of gravitational forces on the tracer particles (Adrian, 2005). In analogy to Stoke's drag law, the slip velocity, which is the velocity lag between tracer particles and the working fluid in a continuously accelerating flow, refers to the essential parameter of representing the scale of error owing to the density difference between the tracer particles and the working fluid.

The slip velocity is defined as follows,

$$U_{slip} = U_p - U = d_p^2 \frac{\rho_p - \rho}{18\mu} a \tag{2.1}$$

where ρ_p is density of tracer particles, ρ is density and a is the acceleration of fluid medium the tracer particles are seeded in. Therefore, as the difference of density between the tracer particles and the working fluid decreases, the quality of tracer particles can be maintained even for large tracer particle sizes (Melling, 1997). In that regards, the use of neutrally buoyant Helium Filled Soap Bubbles (HFSB) as tracers of flow visualization methods and also for PIV experiments in aerodynamics is proposed (Caridi, 2018).

2.2 Experimental Investigations Fluid-Structure Interactions

Development of scientific facilities for the sole purpose of conducting aeroelastic experiments requires new measurement techniques both for structural and fluidic responses. Although there were available methods for acquiring data from both domains, performing the acquisition procedures simultaneously in a non-intrusive manner was necessitated for accurate characterization of aeroelastics phenomena. Hence, previously empoyled strain gages for measurements of structural loads and deformations, and pressure tabs for obtaining pressure information revealed unpreferable characteristics as they tend to modify the structural response of the solid bodies, while surface orifices or pitot tubes caused the fluid to deviate from the desired model behaviour. In order to minimize the influence of measurement devices on the experimental simulations, small pressure transducers for surface pressure fluctuation measurements (Patterson and for Aeronautics, 1952), electronically scanning pressure sensors for obtaining both steady and unsteady pressure information (Malon, 1977) and thin surface-films to determine boundary layer characteristics were developed (Stack et al., 1987). For non-intrusively determination of the global flow behaviour in aeroelastic circumstances, Schlieren flow visualization methods are utilized for capturing the shock movements due to aileron buzz (Settles, 1986) and laser velocimetry techniques are applied to resolve vortical structures occurring over wing bodies at high angle of attack operation (William Sellers and Kjelgaard, 1997).

2.2.1 Benchmark Case Studies

The introduction of high fidelity numerical solvers that are to characterize simultaneous fluid and structure kinematics was associated with the necessity of validation to prove the capabilities of the developed computational packages. Most of the experiments conducted for this purpose are documented in combination with a numerical solution scheme since their sole objective was to validate the computational simulations in which the aforementioned intrusive techniques and their advanced versions are employed. Strain gauges are used by many researches for deformation measurements of structural components. They are employed by Tang and Dowell (2001) over an elastic high-aspect ratio wing with a slender body for measuring the flutter response and characterizing the limit-cycle oscillations to evaluate the accuracy limitations of theoretical models proposed by Patil et al. (2001) and Tang and Dowell (2004), and Augier et al. (2015) for obtaining twisting deformation information of complaint hydrofoils integrated on a Mirage derive system mounted on an instrumented kayak. The presented data acquisition techniques of surface mounted devices, accompanied with the pressure probes to determine flow velocity distributions, not only affected the measurement in terms of intrusiveness, but also required corrections to represent the accurate structural characteristics of the solid bodies under fluid forces. Moreover, the quantitative measurement methods were only be able to provide localized information within the measurement domains and the global flow visualization techniques utilized in these experiments were limited in terms of providing quantitative results.

Following the development of digital image recording and processing techniques, optical measurement methods are utilized in PIV setups for global acquisition of flow field information which also enabled the measurements surface displacements without altering the structural characteristics of elastic bodies. Many benchmark studies introduced novel measurement techniques for simultaneous acquisition of non-intrusive flow and structural motion data. Espinosa et al. (2006) used pin-type velocity sensor and dynamic membrane pressure transducers to record fluid velocity and pressure history while determining the panel deformations utilizing image correlations of shadow moire for evaluation unsteady structural deformations of solid panels loaded by underwater blasts. Gomes and Lienhart (2006) employed planar and 3D PIV images for the determination of flow field characteristics and structural deformations on an experimental setup of flow over a circular cylinder with an elastic plate mounted facing rearward direction in which an adaptive time-phase resolution detection algorithm is introduced for compatibility of temporal resolution specifications with the periodicity of structural motion. Furthermore, Zarruk et al. (2014) employed cross-correlation of spanwise oriented images to derive steady tip displacements and deformation modes of flexible hydrofoils exposed to turbulent flow conditions.

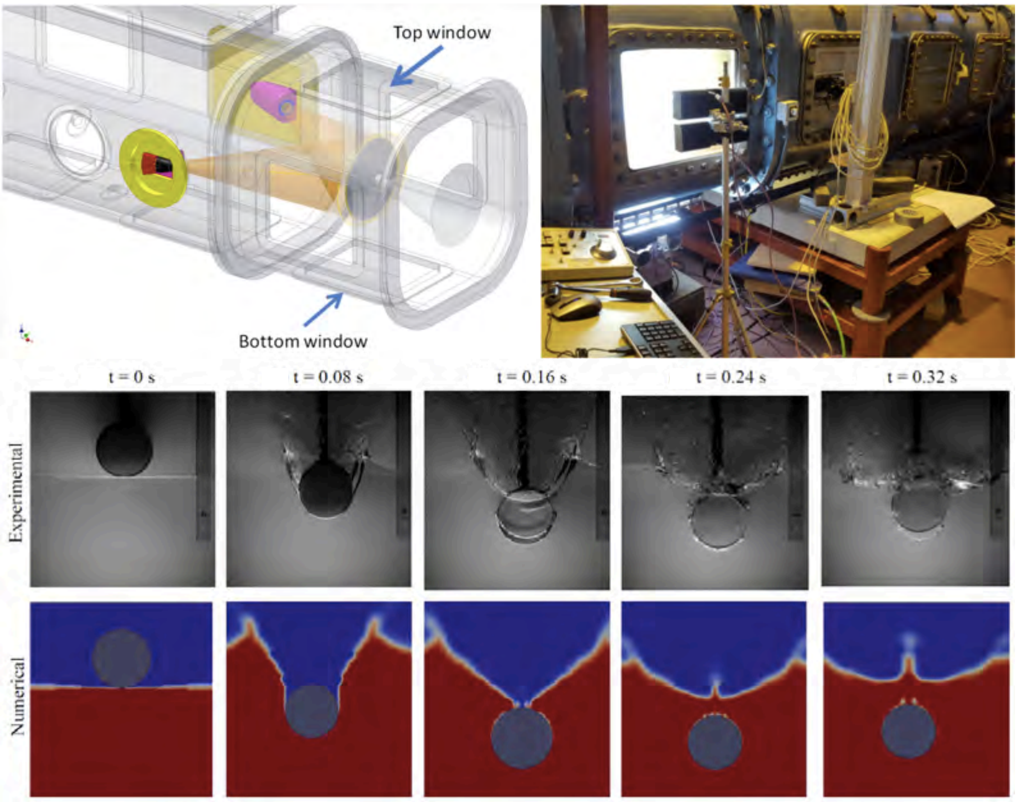

Figure 2.4: Schematic illustration and pictures of the cavitation tunnel test setup for flexible composite propellers (Maljaars et al., 2018)(left) and free surface evolutions captured with experimental and computational investigations of buoyant bodies (Facci et al., 2019)(right).

More recently, Maljaars et al. (2018) used digital image correlation (DIC) over the images obtained using stereo-photography to reconstruct the deformed shapes of flexible composite propellers in a water cavitation tunnel for validation of the developed Blade Element Method (BEM)-Finite Element Method (FEM) and Reynolds Averaged Navier Stokes (RANS)-FEM coupled analytical and numerical solvers. Also, Mella et al. (2019) used DIC in comparison with Lucas-Kanade (LK) optical flow method (Patel and Upadhyay, 2013) to reconstruct the prescribed oscillatory motion of shakers where the accuracy limits of the methods are analyzed for various image acquisition frequencies and special resolutions. Proceeding the accuracy superiority of LK obtained with lower tracking error over the benchmark case, both methods are applied on an experimental setup of an elastic cylindrical stick clamped from one edge exposed to a range of turbulent water flows to measure spatio-temporal variation of cylinder's location. Furthermore, Facci et al. (2019) used Spectrasymbol thinpot linear potentiometers, accompanied with an accelerometer mounted inside the cylinder, for determining the motion of a buoyant cylinder for water entry and exit conditions. Even though in all of these studies PIV based experimental techniques are employed for quantification of flow velocity fields, the absence of a non-intrusive pressure determination method obligated the use of surface mounted devices such as pressure transducer or piezoelectric pressure sensor in case the surface pressure information is desired.

2.3 Pressure from PIV

The pressure information of a flow field possesses an important role of determining the scales FSI both for fluid and solid domains. Surface pressure dictates the loading distribution over objects which in case of non-rigid bodies, determines the deformations and hence the associated shape. The shape variation of aerodynamic surfaces in turn influences the flow characteristics which stabilizes when a certain degree of equilibrium in this iterative procedure is achieved. Capturing pressure information over the flow field and over the surface interacting with the flow is performed by means of various methods including orifices over the experimental models acting as pressure tabs, pitot tubes measuring pressure over prescribed locations within the measurement volume or pressure transducers and microphones determining the acoustic variations caused by the variations in pressure fields. However, their capabilities to resolve instantaneous pressure variations in the flow field or over surfaces is limited not only due to the intrusiveness of their nature and the corresponding deviation of fluid characteristics (Yu et al., 2005), but also owing to their inability to provide global information over the measurement volume and their restricted dynamic response capabilities (Morris and Langari, 2016).

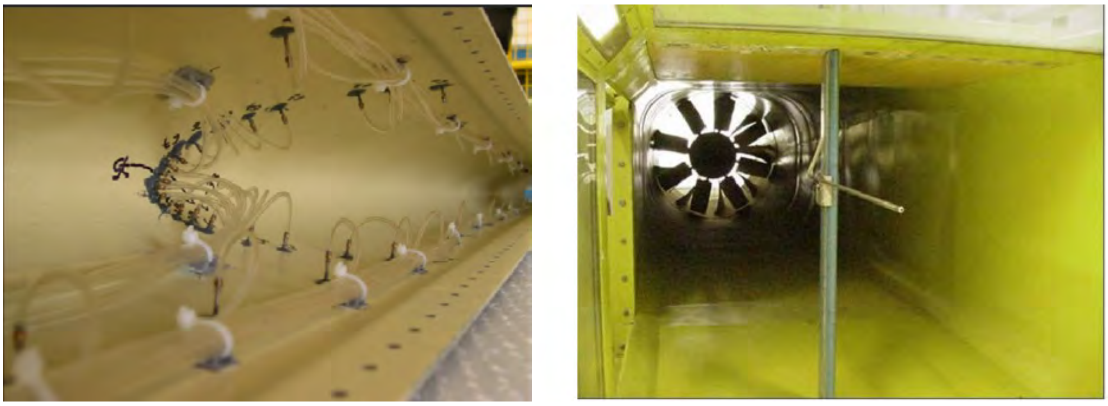

Figure 2.5: Interior of leading edge structure equipped with pressure taps (Rufolo et al., 2007)(left) and pitot-static tube located within the wind tunnel (Assato et al., 2005)(right).

Considering the superiority of PIV in terms of global non-intrusive velocity field determination and its broad spectrum of applicability, a pressure reconstruction approach relying on the acquired velocity data and the flow governing equations proposes a great opportunity of obtaining simultaneous time-resolved velocity and pressure information on a global scale. In that regards, many velocity-based pressure and surface loading computation procedures are proposed over the years. Prior to the modern era of digitized PIV, the simplest method of pressure calculations related to velocity information is represented by the Bernoulli equation which is valid for steady, incompressible and inviscid flow regimes while irrotaionality is also necessitated for its global application within the flow field rather than on specific streamlines. However, since the underlying assumptions that provide the validity of Bernoulli equation are far from ideal for engineering applications, a more generalized approach utilizing the set of equations defining the flow behaviour is required. In that regards, Imaichi and Ohmi (1983) obtained distribution of pressure information by numerically integrating two dimensional Navier-Stokes equations on a velocity data of flow past cylinder. Although the overall accuracy of the results revealed a significant degree of correlation with the expected flow physics of von Karman vortex-streets downstream of the sphere, neglecting the unsteady terms in the original NS equations appeared as a major source of error analyzing the instantaneous flow field information.

Upon the availability of digital image and data processing capabilities for flow measurement setups, detailed acquisition and processing experimental velocity information facilitated the computation of pressure fields. In early applications of pressure field determination from velocity information, Jakobsen et al. (1997) computed pressure fields of wave experiments by calculating acceleration of fluid particles, which is directly related to the pressure gradients through NS equations, using both the Lagrangian and Eulerian approaches. Additionally, Gurka et al. (1999) employed a two step algorithm for calculating pressure fields from Poisson equation relating pressure to velocity after computing the pressure gradients from NS equations in order to set the Neumann boundary conditions, that are stated to be the correct representation of boundary layer characteristics (Gresho and Sani, 1987).

2.3.1 Theoretical Framework

The relation of velocity and pressure can be represented by one of the most fundamental theorems of fluid dynamics. Bernoulli's principle relating velocity and pressure in a steady, inviscid and incompressible flow domain yields a considerably simplified methodology for computation of pressure information from velocity data (Anderson, 2010).

$$p + \frac{1}{2}\rho V^2 = p_\infty + \frac{1}{2}\rho V_\infty^2 \tag{2.2}$$

However under realistic circumstances involving turbulent flow features, satisfying the conditions that validate Bernoulli principle would be exceptional. Therefore, the relation between velocity and pressure should be established over more generalized mass and momentum conservation laws. Considering Navier-Stokes equations under incompressible flow assumption, which is sufficiently valid for flow speeds under $M < 0.3$ (Marchioro and

Pulvirenti, 1994), instantaneous velocity and acceleration fields yield the spatial variation of static pressure.

$$\nabla p = -\rho \frac{D\mathbf{u}}{Dt} + \mu \nabla^2 \mathbf{u} \tag{2.3}$$

From the Navier-Stokes equations where the velocity pressure relation is set, the pressure field is computed either by constructing a Poisson equation over the static pressure or directly integrating the pressure gradients along the locations of interest. Applying the divergence operator to both sides of Eq.2.5, the Laplacian of pressure becomes related to the variations in the velocity field as follows,

$$\nabla^2 p = \nabla \cdot (\nabla p) = \nabla \cdot \left(-\rho \frac{D\mathbf{u}}{Dt} + \mu \nabla^2 \mathbf{u} \right) \tag{2.4}$$

As referred in Eq.2.4, the pressure gradient is composed of two main components, the divergence of particle acceleration on a Lagrangian frame of reference and the divergence of viscous diffusion of momentum. The influence of the viscous terms on the pressure gradient computation is notably referred to be negligible especially in cases of high-Reynolds number, turbulent flow conditions where the superiority of inertial forces over viscous effects is apparent (Murai et al., 2007). An order of magnitude comparison between the acceleration and viscous contribution also highlights the validity of the assumption of neglecting the viscous influence where especially in case of investigation performed with airflow, the viscosity order of $O(10^{-5})$ drives the viscous effects to be insignificant.

Consequently, the computation of pressure distribution over the measurement domain is performed by spatially integrating the pressure gradients by means of solving the Poisson equation accompanied with the proper boundary conditions. Even though various numerical methods are present for the integration of pressure gradients over the computational domain, Poisson equation is shown to yield the most accurate results especially for external flows which refers to the field of aerodynamics (Charonko et al., 2010). Moreover, since the effect of viscous contribution is proven to be insignificant for the overall pressure reconstruction procedure, calculation of accurate pressure gradients is dominated by the combination of spatial and temporal variations in particle's velocity represented by $D\mathbf{u}/Dt$. The term $D\mathbf{u}/Dt$ is the material derivative of velocity vectors which refers to the Lagrangian acceleration of a fluid particle corresponding to a frame of reference attached to the particle (Voth et al., 1998).

2.3.2 Determination of Material Accelerations

According to the physical definition of the acceleration terms and their mathematical interpretations, there exists two main approaches dictating the evaluation of tracer particle motions in terms of the track they follow and how their properties vary along those paths. Even though in terms of the mathematical expressions, both Lagrangian and Eulerian approaches correspond to the same physical terms, their implementation are based on different physical interpretations of particle motion. This difference yields various orders of error propagation throughout the pressure computation procedure depending on the velocity variation definitions in temporal and spatial domains.

Eulerian Approach

Eulerian perspective refers to a stationary frame of reference in space where the motion of particles are observed from. The definition of a non-moving frame for capturing flow information facilitates the representation of a flow field on a specific region of interest which is or can be considered stationary with respect to the motion of the fluid particles passing through. Since the observation frame is stationary, the flow features are attributed to a steady grid structure defined in compliance with the structural surfaces.

The computation of material acceleration terms using an Eulerian approach requires decomposing the to its local and convective components,

$$\frac{D\mathbf{u}}{Dt} = \frac{\partial \mathbf{u}}{\partial t} + (\mathbf{u} \cdot \nabla)\mathbf{u} \tag{2.5}$$

where the temporal variation of velocity at each location is computed over at least two time instants and the spatial variation of the velocity vector components are calculated over the structured grid locations using various numerical algorithms.

Relying on the dominance of two dimensional flow features represented by in-plane velocity information, Jensen et al. (2001) computed acceleration fields of waves using an extended two camera planar PIV system (Chang and Liu, 1998). Additionally, Christensen and Adrian (2002) introduced particle image accelerometry for time resolved measurement of acceleration fields utilizing the Eulerian approach by numerically differentiating unsteady velocity data on a structured grid. Employing the Eulerian approach for determination of material acceleration terms, Fujisawa et al. (2005) evaluated the instantaneous pressure fields and the related forces acting on a circular cylinder of stationary and oscillating conditions exposed to uniform flow by the solution of Poisson equation using the velocity information obtained via planar PIV images to construct the system of equations and the suitable boundary conditions. Also, Murray et al. (2007) utilized the solution of Poisson equation to estimate surface pressure loads over 2D PIV data obtained over a rectangular cavity, revealing the dependence of pressure on various sources of velocity fluctuations. Moreover, Panciroli and Porfiri (2013) assessed the Poisson equation based non-intrusive pressure field determination using velocity information by comparing the pressure fields of a water entering rigid body with the analytical potential flow solution (Wagner, 1932).

3D Flow Effects

The simplified flow fields of two dimensions only appear to represent scientific benchmark cases created to set the foundation of the methodology and the development of its theoretical background. On the other hand, practical engineering applications contain three dimensional elements not necessarily dictating the primary flow direction but affecting the flow characteristics severely. Therefore, although 2D simplified flows recorded by planar PIV are dominated by two dimensional velocity components, especially in cases of turbulence indicating out-of-plane motion, neglecting its presence may lead to significant deviations from the actual flow features (Baur and Kongeter, 1999; Lorenzoni et al., 2009). In case the plane of 2D data set is not aligned with the main flow direction where

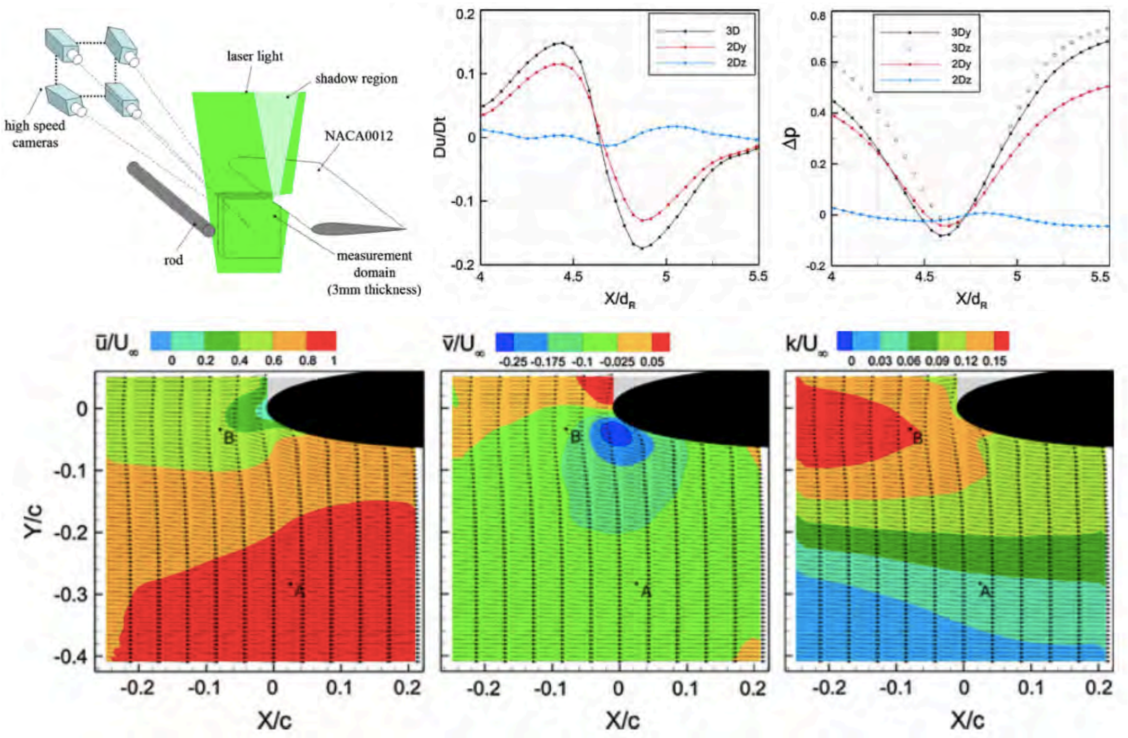

Figure 2.6: Airfoil-rod experimental setup (top-left), material acceleration (top-middle), fluctuation of static pressure (top-right) at y/c=-0.125 computed from 2D and 3D velocity measurements. Mean velocity components in x-direction (bottom-left) and in y-direction (bottom-middle), and normalized turbulent kinetic energy (bottom-right) over the midplane of measurement volume (Violato et al., 2011).

the order of magnitudes of out-of-plane velocity vectors compared in-plane velocity magnitudes increased considerably, up to 100% relative errors with respect to the pressure fields of 3D reconstruction procedure are obtained (Violato et al., 2011).

With the development of Tomo-PIV (Elsinga et al., 2006), the complete 3D velocity field reconstruction has become possible which in turn enabled the determination of 3D pressure gradients for the construction of Poisson equation (van de Meerendonk et al., 2018). Since Tomo-PIV is a volumetric technique rather than a planar one that requires its application on multiple planes for the determination of out-of-plane pressure gradients, the pressure gradients composing the complete three dimensional measurement domain can be extracted directly from the acceleration computation (Pröbsting et al., 2013). Hence, the availability of three dimensional volumetric setup of Poisson equation led the reconstruction of 3D volumetric pressure fields from PIV data sets (de Kat and van Oudheusden, 2012). Ghaemi et al. (2012) evaluated the pressure distribution of a fully developed turbulent boundary layer using instantaneous velocity fields attained with Tomo-PIV and compared it with the pressure fields computed using a two camera PIV setup. Both pressure fields are validated with pressure measurements performed using microphones where the superiority of Tomo-PIV based pressure reconstruction is concluded over 2C-PIV.

Particle Tracking Velocimetry

In addition to the fact that accurate pressure computation from velocity information is strongly affected by the presence of out-of-plane velocity components Jakobsen et al. (1997) noted the accuracy difference between the two approaches of Eulerian and Lagrangian perspectives for material acceleration determination which also dictates the pressure gradients within the flow field. The aforementioned applications of 2D and 3D pressure computation schemes employed Eulerian approach for the determination of material acceleration term, due to fact that they were based on velocity fields obtained with various PIV techniques. However, many studies referring to the difference between the application of these two approaches result in notable accuracy differences favoring Lagrangian approach over an Eulerian one, specifically when the time scales of the flow is smaller than the temporal resolution of the experimental measurements (Pan et al., 2016; Huhn et al., 2016; Van Gent, 2018).

There exists two main approaches that could be utilized for obtaining acceleration information of a flow field from a Lagrangian perspective. The natural way would be considered as tracking and reconstructing the trajectory of the particle's motion and differentiating the temporal variation of its velocity over that trajectory. This is obtained via the particle velocimetry methods (Agui and Jimenez, 1987) where their application in three dimensional flows is introduced by Maas et al. (1993) and Malik et al. (1993). Further on, Lagrangian approach is used to reconstruct particle accelerations from Tomo-PTV which reduced the precision errors on the material derivatives up to a factor of 2.5 compared to PIV-based Eulerian approaches (Novara and Scarano, 2012). Moreover, since tomographic techniques are independent of image correlation and particle identification opposed to 3D-PTV methods, they provide a higher level of robustness especially against high density seeding of tracers (Novara and Scarano, 2013). Nonetheless, in the 3D-PTV techniques and iterative particle reconstruction methods (Wieneke, 2012), the post processing of particle distributions is performed individually for every single snapshot of a time series and require a large number of iterations to reach convergence. Therefore in order to take advantage of available processed data from previous time instants for the processing of the current time step in case of sufficient temporal resolution, a Lagrangian particle tracking algorithm of Shake-The-Box is introduced by Schanz et al. (2016). In spite of the fact that it increases accuracy of particle position, velocity and acceleration determination, the time requirement for processing a complete time set is lowered with a factor of 5 to 8 compared to Tomo-PIV processing algorithms.

Due to the limited tracer particle densities available for large scale 3D tomographic measurements, utilization of particle tracking approaches provided an opportunity of elevated particle track identification which increased the accuracy of material acceleration determination. As an illustration of the accuracy difference between time-averaged and instantaneous pressure field reconstruction with direct interpolation of PTV data on a cartesian grid, Schneiders et al. (2016b) reconstructed volumetric and surface pressure fields of flow past a circular cylinder. The scattered particle tracking data is interpolated on a uniform cartesian grid using Adaptive Gaussian Windowing (AGW)(Agui and Jimenez, 1987) where the standard deviation of the Gaussian was set to be equal to the spatial resolution of the interpolated grid. The computed surface pressure information is compared with the pressure transducers mounted on the surface downstream of the ver-

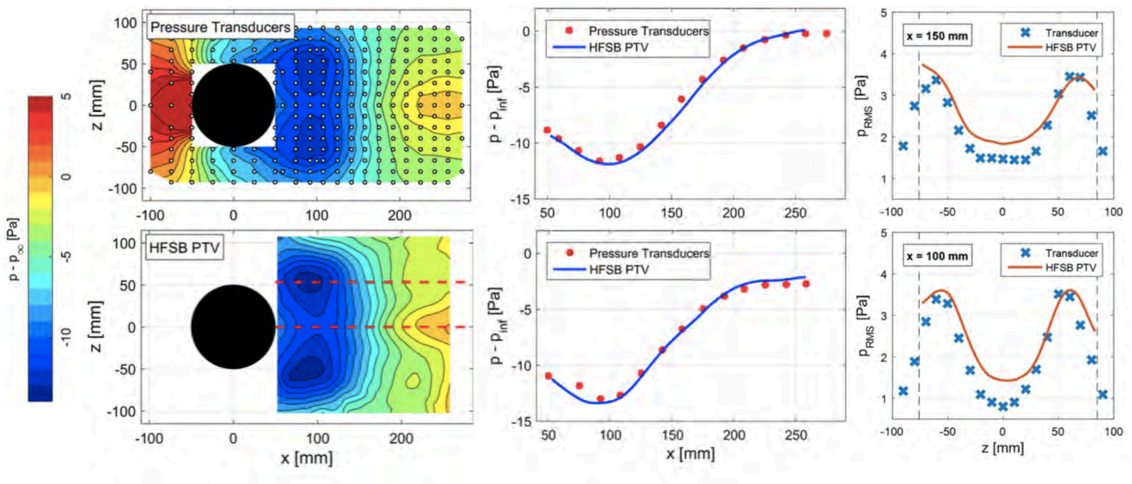

Figure 2.7: Time averaged surface pressure measurements with pressure transducers (top-left) and pressure reconstruction from PTV (bottom-left), at z=0 mm (top-middle) and at z=53.3 mm (bottom-middle), RMS of surface pressure fluctuations at x=150 mm (top-left) and at x=100 mm (bottom-left)(Schneiders et al., 2016b).

tical cylinder. The use of HFSB enabled expansion of the measurement domain up to a factor of 2 compared to conventional Tomo-PIV applications and employment of particle tracking rather than particle imaging yield reasonably accurate reconstruction of mean and instantaneous pressure fields in comparison with surface pressure transducers even in a field with low seeding densities of tracer particles.

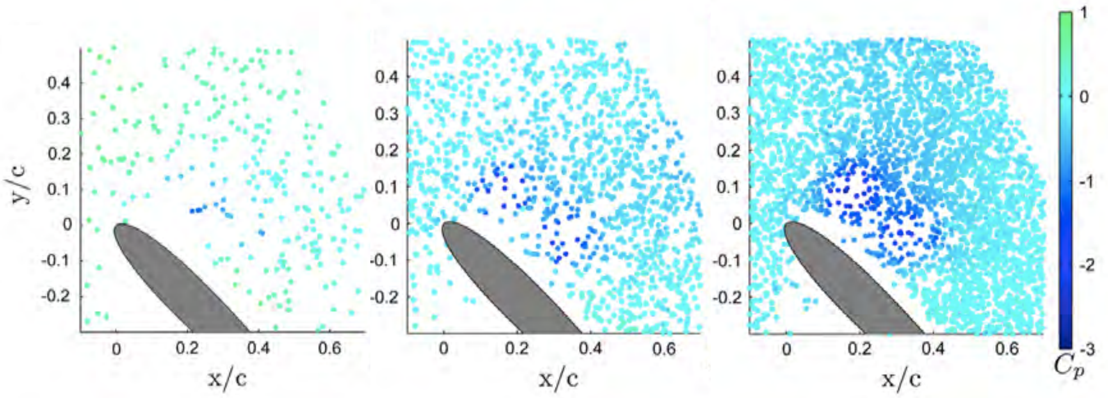

Figure 2.8: Reconstructed experimental pressure fields around an impulsively accelerating NACA0012 airfoil at three different particle densities (Neeteson and Rival, 2015).

Moreover, Neeteson and Rival (2015) proposed a novel solution approach of utilizing Poisson equation for pintegration of pressure gradients on scattered Lagrangian domains by constructing the numerical computational domain using Voronoi tessellation (VOR) (Hirata, 2005) and Delaunay triangulation (Blazek, 2005). The Delaunay triangulation generates tetrahedral volumetric cells when applied to a field data of node locations in a three-dimensional space. Then VOR is employed to gather a set of tetrahedral cells that would correspond to a set of associated node locations to create polyhedrons with faces belonging to the neighboring tetrahedral volumes of the data locaitons associated with each Voronoi cell (Aurenhammer, 1991). Hence, with the proper definition of unstructured grid formation based on the scattered particle locations, the Poisson equation is iteratively integrated over internal domains with the Laplacian of pressure defined using numerical discretizations derived by Sukumar and Bolander (2003). The algorithm both tested on an analytical case of Hill's spherical vortex which represents a simplified solution the NavierStokes equations (Hill, 1894), and on an experimental test case of an impulsively accelerating NACA0012 airfoil. While the pressure field reconstruction of analytical vortex revealed the insensitivity of quantitative pressure variation throughout the reconstruction domain to spatial density of particle information, the experimental results are compromised in cases of low spatial resolution due to the presence of turbulent flow structures.

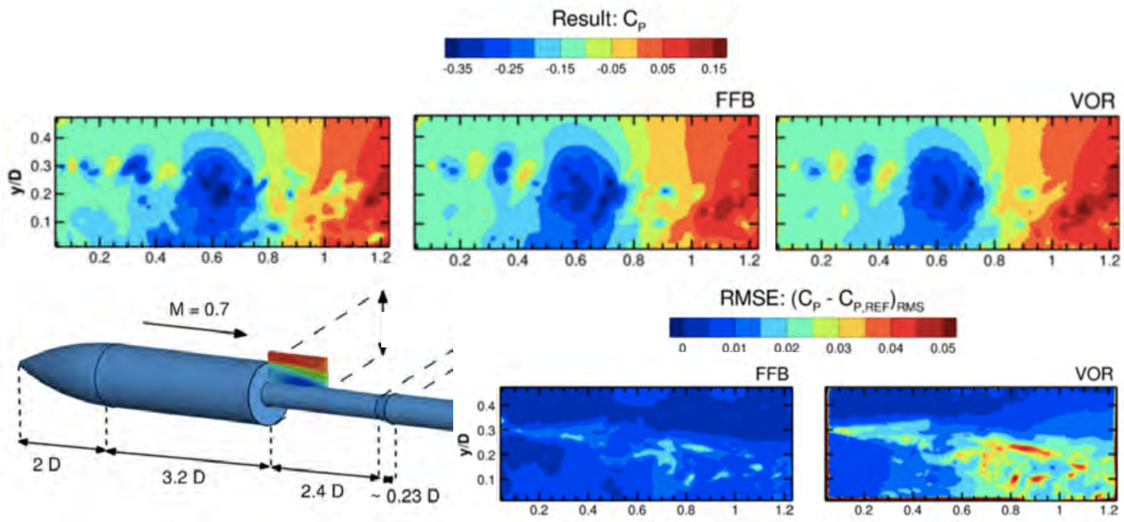

Figure 2.9: Transonic base flow pressure distributions with ZLES (top-left), 3D B-spline particle track reconstruction (top-middle) and Voronoi based unstructured iterative Poisson integration (top-right). Sketch of base flow geometry (bottom-left). RMS of pressure error distributions obtained with 3D B-spline (bottom-middle) and VOR (bottom-right) compared against the reference flow field (van Gent et al., 2017).

However, in a comparative assessment of various pressure reconstruction techniques, van Gent et al. (2017) demonstrated the superior accuracy levels associated with the solution of Poisson equation on gridded data by comparing the reconstructed pressure fields obtained from a zonal detached eddy simulation (Deck, 2012) of an axisymmetric base flow at Mach 0.7. The 3D B-spline particle track detection Gesemann et al. (2016) for pressure determination caused rms errors reaching approximately 7% of the maximum pressure variations on the reference pressure field and VOR exceeding rms error levels of 13% while with pressure field computed over uniformly gridded data the relative rms error levels were bounded with a maximum percentage of approximately 3%.

2.3.3 Surface Pressure Reconstruction

In FSI frameworks, it is desirable to approximate the surface loading directly due to the fluidic influences. There are two main approaches introduced to accomplish this task. One considers a control volume approach for utilizing the momentum balance for which only the far field pressure information is required that can be obtained from the Bernoulli principle provided that the far field flow conditions do not violate certain assumptions (Oudheusden et al., 2007; Ragni et al., 2009; Mcclure and Yarusevych, 2019). The second approach is the calculation of pressure information along the boundaries of the interaction interface by means of various pressure gradient integration methods (Murai et al., 2007; Violato et al., 2011; de Kat and van Oudheusden, 2012). The letter method reveals a more broad spectrum of applicability as not only the overall loading yielded by the fluid is computed but also its local distribution information is attained. However, due to the numerical discretization orders and non-uniformity of geometric planforms, computing pressure distributions over the surfaces is prone to severe accuracy issues.

The pressure computations in regions surrounded by non-uniform surfaces where the existing reconstruction approaches of pressure from PIV data are utilized generally performed in computational domains defined certain distances away from the surfaces at the nearest neighboring grid locations (de Kat and van Oudheusden, 2012; Liu et al., 2016; Jeon et al., 2018). The reasons for this procedure are documented either referring to the structured uniform velocity data obtain from the measurement techniques which causes loss of data points especially in cases of moving boundaries or due to the scarcity of spacial resolution for near surface regions specifically for instantaneous calculations (Fujisawa et al., 2005; Kunze and Brücker, 2011; Auteri et al., 2015). However this approach introduces significant error to the pressure estimation procedure owing to the significant dependency of the reconstruction process to the boundary conditions (Pan et al., 2016).

Following the immersed boundary treatment methods that define the fluid properties on Cartesian grid systems following a Eulerian approach of flow characterization (Mittal and Iaccarino, 2005), Shams et al. (2015) proposed a ghost cell approach that assign fluid properties to the grid nodes fall inside the physical intrusions that would satisfy the proper boundary conditions. Although the approach diminished the possible requirement of a boundary fitted coordinate system that would yield increased computational cost levels, the reconstructed pressure fields yield significant deviations from the analytical pressure distributions. Furthermore, it is also stated that the presence of ghost cells would arise problems of numerical stability in case finite difference method discretizations.

Avoiding the reduced particle density specifications associated with employment of HFSB based measurements by means of time averaging the particle traking data within he stationary domains, Jux (2018) evaluated applicability of three different interpolation methods of the linear extrapolation, the quadratic interpolation with the von Neumann boundary condition, and the stagnation model approach for calculating the surface pressure values from the Cartesian pressure distribution obtained via the solution of Poisson relation with the velocity data of PTV obtained performing coaxial volumetric velocimetry (Schneiders et al., 2018) measurements around a sphere. However, the comparison of pressure interpolations over the spherical surface with the surface pressure tabs revealed the incapability of these algorithms to meet the actual pressure distributions.

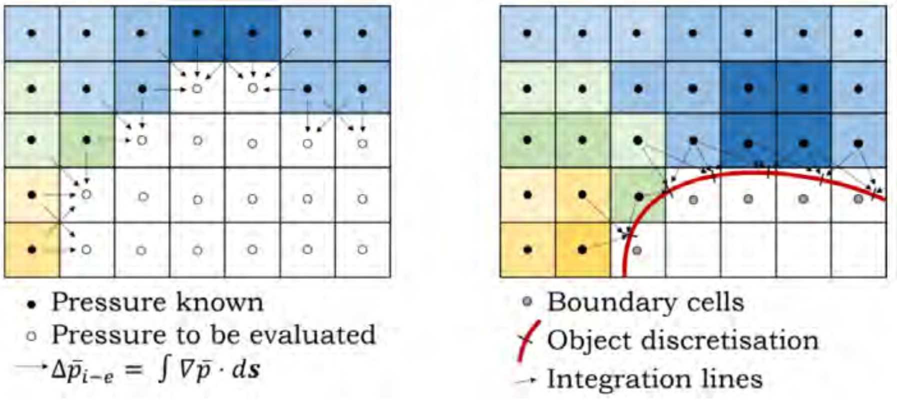

Figure 2.10: 2D demonstration of surface pressure reconstruction in the rotational fluid domain (Jux, 2019).

Therefore, Jux (2019) proposed a partitioned domain approach separating the fluid domain to its rotational and irrotational regions where the pressure information over the irrotational domain is obtained via applying the Bernoulli equation and the Poisson equation is solved for the integration of pressure gradients within the rotational domain. Then the surface pressure is computed considering smaller kernels of neighboring grid locations close to the surface of interest. Specific lines of integration are defined to relate the pressure gradient information between the already computed Cartesian grid locations and the surface boundary. As the method is applied to reconstruct surface pressure information over a sphere as well as a 3D cyclist model, its capability of handling complex geometric contours intruding the flow field is demonstrated (Jux et al., 2020).

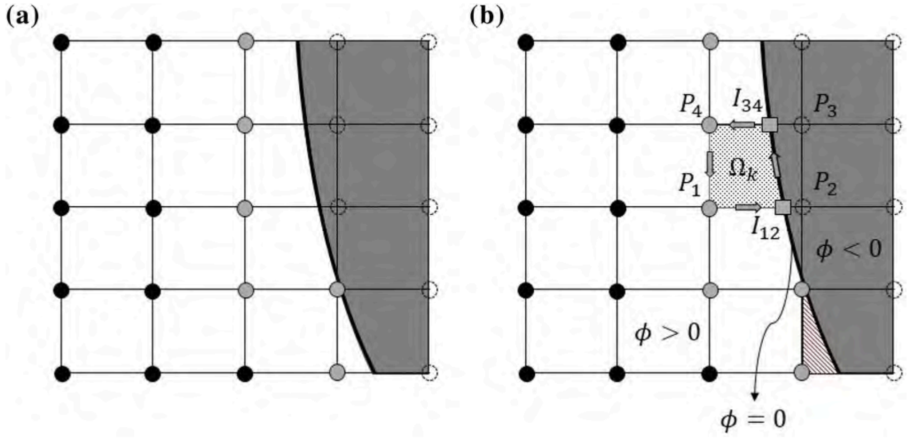

Figure 2.11: Schematic illustration of nearest-neighbor (left) and cut-cell (right) approaches where the full grid nodes are demonstrated by the block dots, the nearest neighbor nodes are via the grey dots and the hollow dots with dashed lines represent the interior nodes of the solid structure (Pirnia et al., 2020).

Furthermore, Pirnia et al. (2020) employed a finite element approach for computation of two-dimensional pressure information via integrating the pressure gradients using the Poisson equation. They proposed the cut-cell approach for handling the immersed boundaries with appropriate boundary condition definitions. The integral form of Poisson equation allowed proper definition of boundary conditions over the exact interface surfaces.

2.3.4 Dirichlet Boundary Condition Determination

Furthermore, since Poisson equation is solved for the pressure distribution using fully homogeneous Neumann boundary conditions, the result of such a solution is not unique due to the absence of a Dirichlet boundary condition implementation,. Hence, the pressure field information is obtained with respect to an indeterminate constant defined to be the average value of static pressure calculated over the solution domain. Therefore, with the known pressure value at a certain location of the computational domain, a relative shift is applied for the unique solution of the pressure field information. In that regards, various approaches are proposed in the literature for defining an exact pressure value. The most common approach is referred to equip the experimental setup with an additional pressure measurement tool to determine a reference static pressure value (Jaw et al., 2009). However, this is not always applicable due to the intrusive nature of the pressure measurement devices. Employing pressure probes for this purpose introduces a set of challenges such as the presence of the tool modifying the flow behavior in close proximity of the measurement device (Robey, 2001) and elevating the level of difficulty for the optical methods to capture accurate flow behavior around the probe location which is aimed to be mitigated by means of employing miniature static pressure probes (Kawata and Obi, 2014). Therefore, the use of pressure transducers for measurements in near wall regions provided a more reliable approach. As a set of wall pressure transducers are placed over the surface of interest, static pressure readings of a single transducer is utilized to unify the pressure field distribution in terms of exact values and the rest of the set is used to validate the PIV based pressure reconstruction over the wall surface (Scarano and Ghaemi, 2012).

Nevertheless, depending on the experimental setup specifications, employing an additional pressure measurement tool to determine the exact static pressure value at a reference pressure location might not be possible. This condition might originate due to the inability of reconstructing pressure from the PIV data over the exact surface locations where the readings of surface pressure tabs become uncorrelated with computational grid locations (Terra et al., 2017). Additionally implementation of any surface pressure measurement devices might alter the structural characteristics of the interface elements which cause deviations from the actual physical behavior determining the FSI problem (Jeon and Sung, 2011). Therefore, various researchers employed the Bernoulli equation to determine a reference pressure value based on the velocity measurements captured within the flow regions that validate the usage of Bernoulli theorem for incompressible flows (de Kat and van Oudheusden, 2012; Dabiri et al., 2014; Jux et al., 2020; Gunaydinoglu and Kurtulus, 2020).

2.4 Particle Tracking Data Assimilation

Despite the fact that particle tracking approach reveals a greater level of accuracy in terms of determining particle location, velocity and acceleration information especially with low seeding densities of tracer particles, the data obtained from PTV is scattered over the measurement domain. Since interpolating the scattered data on a grid system would involve certain numerical errors that propagate through the steps of pressure reconstruction procedure, alternative approaches for dense flow field interpolations over structured grid formation are proposed.

2.4.1 Statistical Data Augmentation Approaches

Initially, the AGW was proposed by Agui and Jimenez (1987) where scattered information in a measurement volume is captured on a predefined grid using a Gaussian weight averaging over the windows of Euclidean distances defined with respect to the grid location of interest. Furthermore, the computed Gaussian average is scaled with a standard deviation commonly chosen to be the spatial separation of grid locations.

$$\mathbf{u}(\mathbf{x}) = \frac{\sum_i \alpha_i \mathbf{u}_i}{\sum_i \alpha_i} \tag{2.6}$$

where α_i is defined by the exponential function containing the Euclidean distance of particle locations with respect to the grid nodes and the standard deviation, σ.

$$\alpha_i = exp\left(\frac{-|\mathbf{x} - \mathbf{x}_i|^2}{\sigma^2}\right) \tag{2.7}$$

Furthermore, a more advanced algorithm based on Gaussian windowing is developed by Casa and Krueger (2013), where a Gaussian radial basis function (RBF) derived by Weiler et al. (2005) is utilized with an iterative optimization procedure to obtain the best fit of data interpolation on a grid structure with respect to the original scattered data.

$$\mathbf{u}_j(\mathbf{x}) = \sum_{i=1}^{N} b_{j,i} exp\left[\frac{-\|\mathbf{x} - \mathbf{x}_i\|^2}{2\sigma_{j,i}^2}\right] \tag{2.8}$$

The method contained two optimization procedures performed separately on the Gaussian weights $b_{j,i}$ and standard deviations $\sigma_{j,i}$. First the Gaussian weights are optimized by minimizing the difference between the velocity distributions obtained using the RBF interpolation and the velocity information of particle tracking data using a least-squares approach to ensure manageable computational cost levels while standard deviations are implemented as an initial guess based on half the spatial resolution of the grid formation. Then, the second optimization is performed over the standard deviations using the optimized Gaussian weights. The method is compared with Taylor expansion (TE) interpolation (Malik and Dracos, 1995) and AGW schemes for boundary layer reconstruction on a uniform grid from scatter particle information against the theoretical velocity profiles of a steady-state solution for a flow near an infinite rotating disk (White, 2006). The Gaussian RBF based interpolation method yielded superior agreement with the theoretical results, especially compared to TE.

Although these methods are able to accurately represent the flow information on user defined grid systems, reliable interpolation procedures require sufficient particle densities

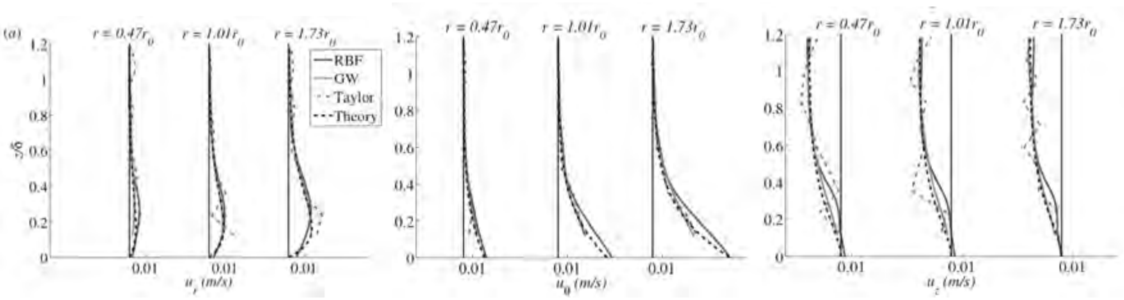

Figure 2.12: Velocity boundary layer profiles over an infinite rotating disk obtained with RBF, AGW, TE and analytic solution of simplified Navier-Stokes equations (Casa and Krueger, 2013).

where large scale Tomo-PIV applications with HFSB results in lower spatial resolution specifications than the computational grid description. Therefore, various interpolation methods are introduced utilizing the incompressibility condition of divergence free flow fields as an additional constraint. Vedula and Adrian (2005) presented an 'optimal' interpolator determination in which the cost function is constructed similar to the RBF approach of Casa and Krueger (2013), using the RMS of the difference between the interpolated values and the scattered velocity information. The interpolation of scattered data is performed such a way that would ensure a divergence free velocity distribution over the grid.

2.4.2 Fluid Dynamics Based Data Augmentation Approaches

In that regards, Gesemann et al. (2016) introduced the use of 3D cubic B-splines for increasing signal-to-noise ratio of particle information reconstruction over particle velocity and accelerations. The method includes two main steps referred as *TrackFit* and *FlowFit*. *TrackFit* initiates the reconstruction algorithm with a noise reduction of the particle intensity signals similar to Wiener/Kalman filter (Cohen Tenoudji, 2016) by calculating

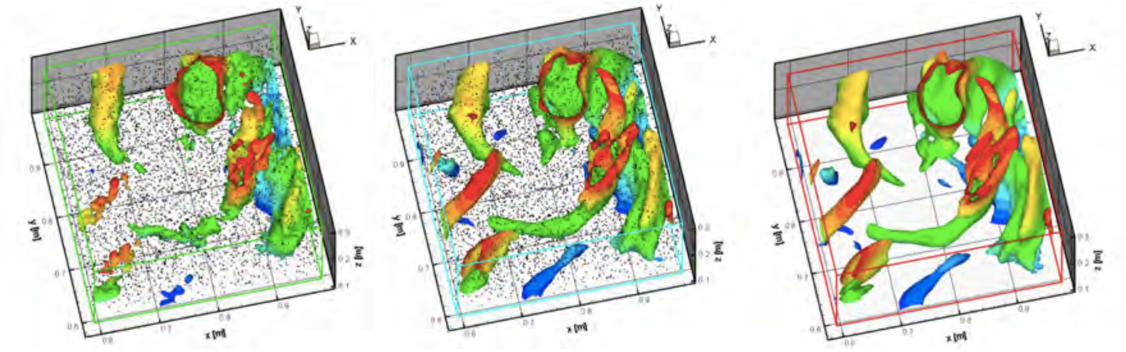

Figure 2.13: Vorticity reconstruction over 6554 particles with linear interpolation (letft), 3D B-spline (middle) and DNS results (right)(Gesemann et al., 2016).

B-splines over particles tracks which also provides the first and second order gradients of particle velocities since the least order of the spline is considered to be 2 using three particles of different time instants. Then, 3D B-splines are calculated for velocity and acceleration (or pressure) information by *FlowFit* where an iterative minimization of a cost function is performed to reach a certain degree of convergence between the particle locations, velocities and accelerations while enforcing divergence free field constraints for incompressible flows. Furthermore performance of the method is evaluated in comparison with DNS results of "Forced Isotropic Turbulence" of John Hopkins Turbulence Database (Li et al., 2008) where the significance of considering temporal information by means of particle accelerations is highlighted both in terms of the proximity of the reconstructed flow field to the DNS simulations and the improved signal to noise ratio.

2.4.3 Vortex-in-Cell Simulations for Dense Velocity and Acceleration Interpolation

The ability of using the temporal domain to enhance the statistical characteristics of spatial information provided the opportunity of elevating both the accuracy specifiations of flow field reconstruction and the resolution levels. In that regards, Schneiders et al. (2015) developed the VIC+ method, based on Vortex-in-Cell (VIC) model presented by Christiansen (1973). The VIC+ method provides an alternative algorithm to the previously introduced flow physics based data assimilation approaches in order to reconstruct the low density scattered distribution of instantaneously acquired particle tracking information on a regular mesh formation with elevated level of spatial resolution. Hence, when the raw PTV data that cannot be directly utilized to represent the time-resolved flow behavior within limits of the required fidelity specifications, it can be assimilated by means of the VIC+ approach to meet the necessary resolution characteristics while enabling the representation of the fluid behavior on a global sense over the prescribed computational domain.

The VIC method is proposed as a solution of Navier-Stokes equations by defining the vorticity transport equation.

$$\frac{D\omega}{Dt} = (\omega \cdot \nabla)\mathbf{u} - \omega(\nabla \cdot \mathbf{u}) + \frac{1}{\rho}\nabla \times \nabla p + \nabla \times \frac{\nabla \cdot \tau}{\rho} + \nabla \times \frac{\mathbf{B}}{\rho} \tag{2.9}$$

for which the initial condition for the vorticity field is discretized by computing the *curl* of the velocity field obtained from PIV data,

$$\omega = \nabla \times \mathbf{u} \tag{2.10}$$

where the velocity field is in turn related to the vorticity vectors by Possion equation (Koumoutsakos, 2005). Applying the *curl* operator to both sides of Eqn.4.7 and expanding the vector identity on *curl of a curl* one obtains,

$$\nabla \times \omega = \nabla \times (\nabla \times \mathbf{u}) = \nabla(\nabla \cdot \mathbf{u}) - \nabla^2 \mathbf{u} \tag{2.11}$$

considering the incompressible flow conditions, which yields $\nabla \cdot \mathbf{u} = 0$, 2.11 reduces to,

$$\nabla^2 \mathbf{u} = -\nabla \times \omega \tag{2.12}$$

Accordingly the vorticity transport equation allows the computation of local time derivative component for the Lagrangian acceleration term only by means of velocity and vorticity fields via eliminating the contribution of pressure gradients through the mathematical identity of $\nabla \times (\nabla \phi) = 0$, in which ϕ refers to any scalar field i.e. pressure. Hence, neglecting the contribution of viscosity, considering conservative body forces and applying incompressibility condition, the local time rate of change of vorticity can be expressed as

$$\frac{\partial \omega}{\partial t} + (\mathbf{u} \cdot \nabla)\omega = (\omega \cdot \nabla)\mathbf{u} \tag{2.13}$$

Hence, VIC+ also provides an opportunity to increase the resolution of material derivative information as its optimization procedure is based on maximizing the proximity of not only the velocity vectors to the measured values but also accelerations. Thus, the VIC+ algorithm refers to the contribution of material acceleration terms over Vortex-in-Cell framework where the velocity-vorticity formulation of the momentum transport equation enables the calculation of temporal velocity derivatives in absence of pressure information (Schneiders and Scarano, 2016).

$$\frac{D\mathbf{u}}{Dt} = \frac{\partial \mathbf{u}}{\partial t} + (\mathbf{u} \cdot \nabla)\mathbf{u} \tag{2.14}$$

while the spatial gradients of velocity field are computed from the gridded data, the unsteady term is computed using the Poisson relation of velocity field with vorticity vectors.

$$\nabla^2 \frac{\partial \mathbf{u}}{\partial t} = -\nabla \times \frac{\partial \omega}{\partial t} \tag{2.15}$$

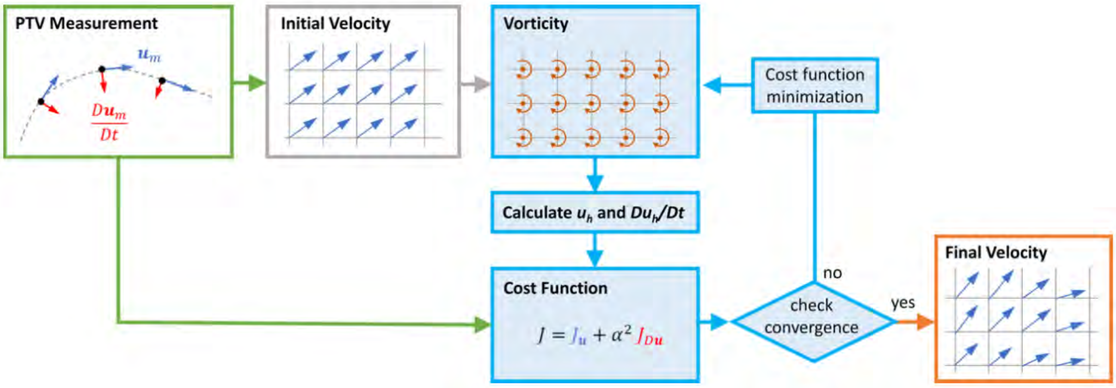

Figure 2.14: Reconstruction framework of VIC+ scheme where the input from the PTV measurements are provided (green box) from which an initial estimation for the velocity field is calculated (gray box). The initial estimate is used to start the VIC+ optimization procedure (blue boxes). The velocity and material derivative fields are optimized towards minimizing the cost function generated by comparing the flow field information to the PTV measurements (orange box)(Schneiders and Scarano, 2016).

Numerical Implementation

The VIC+ algorithm provides a pseudo hybrid particle-mesh treatment for the flow field information by means of defining pointwise vortex blobs (Draghicescu and Draghicescu, 1995) and projecting their contribution on a grid-base system using Gaussian RBFs. Accordingly the computational grid for the VIC+ procedure is equipped with weights of RBFs which are employed to represent a vorticity field that corresponds to the dense reconstruction of measured particle information. The RBFs are defined as,

$$\phi(r) = e^{-\frac{r^2}{2\sigma^2}} \tag{2.16}$$

where the support radius σ is defined with a slight relaxation of 1.1 of the grid spacing h, $\sigma = 1.1h$. Hence, the vorticity field is defined as,

$$\omega_h = \frac{1}{h^3} \sum \Gamma_i \phi(||\mathbf{x} - \mathbf{x}_i) \tag{2.17}$$

in which Γ_i refers to the RBF weights, or in other words the circulation strengths of the vortex blobs. The corresponding velocity and acceleration fields are computed following the aforementioned procedure and two main cost functions are defined over the velocity and Lagrangian acceleration terms with respect to the actual particle information obtained directly from the measurements, and combined to a single cost function to be minimized via a weighted sum. The optimization problem of minimizing the resultant cost function is solved by employing the limited-memory Broyden Fletcher Goldfarb Shanno method (L-BFGS, (Liu and Nocedal, 1989)).

The optimization problem requires a gradient for the computed cost function to be determined, $\partial J/\partial \xi$. Although there exists various numerical methods for the gradient to be calculated, the VIC+ procedure embarks an adjoint gradient method due to lower computational resource requirements (Plessix, 2006). The adjoint gradient procedure enables the calculation of the exact optimization gradients while performing this task with an equal computational cost to the determination of the cost function at each iteration. The reader is referred to Schneiders and Scarano (2016) for a full description of the VIC+ procedure, whilst formulations of only the relevant components of the complete algorithm are extensively provided in the following sections.

The compliance of increased spatial resolution by means of VIC+ is tested using turbulent boundary layers PIV measurements against DNS simulations of Bernardini and Pirozzoli (2011) and sub-sampled Tomo-PIV measurements of jet in water against measured velocity and acceleration information. The VIC+ method is comparatively assessed against other interpolation techniques in both cases. For the turbulent boundary layer, VIC+ was able to provide significantly increased details in chaotic flow structures with 40% reduced rms error levels at y/δ_{99}, while proving its superiority over linear interpolation and solenoidal filtering on reconstructions of dense particle tracks of jet flow.

The performance characteristics of VIC+ method is further demonstrated using the experiments performed by Jodai and Elsinga (2016) on creation of hairpin vortices in turbulent boundary layers (Schneiders et al., 2017). The DNS compared results revealed

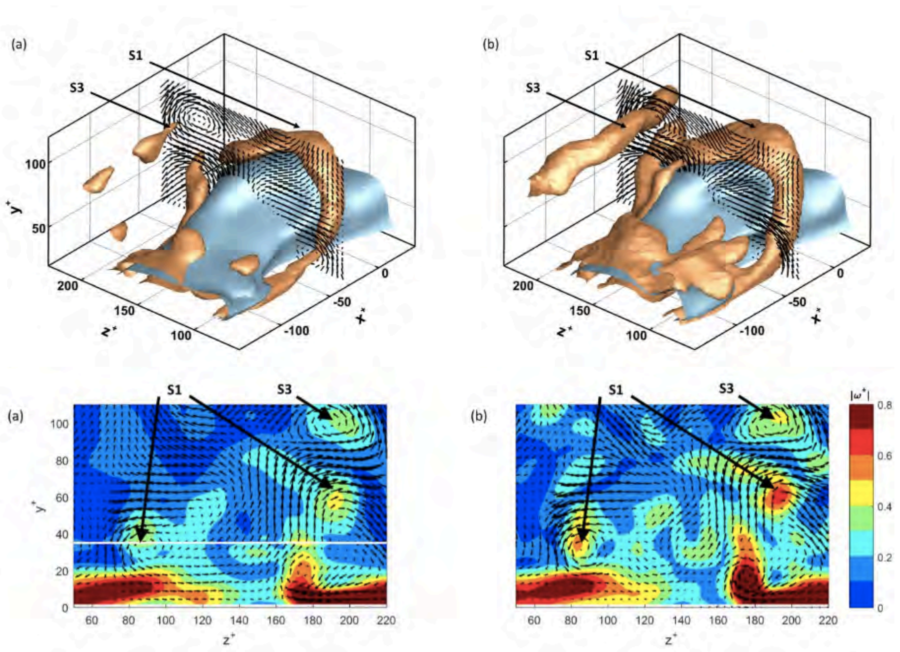

Figure 2.15: Isosurfaces of vorticity distribution (top) accompanied with instantaneous in-plane velocity vectors at x^+=-35 (bottom) obtained from Tomo-PIV measurements (a) and VIC+ (b)(Schneiders and Scarano, 2016).

an increase of agreement up to a tolerance of 5% for $y^+ > 25$ compared to the 50% of tomographic PIV measurements. Furthermore, VIC+ and VIC without the implementation material derivatives are compared in terms of velocity and vorticity field reconstructions over Tomo-PIV measurements of turbulent boundary layers provided by Pröbsting et al. (2013) with the DNS simulations performed by Bernardini and Pirozzoli (2011). The RMS of velocity fluctuations in the normal direction to the wall and velocity components in the spanwise direction are captured with 5% relative errors to the DNS reference using VIC+, while pure PIV data yielding around 20% and VIC method without $D\mathbf{u}/Dt$ reaching even slightly higher values.

Further Advancements of Data Assimilation Schemes with VIC Framework

Furthermore, although the application of VIC+ is proven to be successfully increasing the spatial resolution of flow field information using scattered measurement data, the data utilized for the optimization procedure is based on a single time instant. Nevertheless, in case of its application over the data sets processed with Shake-the-Box algorithm, the material acceleration information is computed over various time instants which provides the opportunity of considering the temporal evolution of particle motions while the velocity field utilized represents a single time instant. Therefore, in order to take advantage of recorded temporal history of particle tracks, the optimization procedure of VIC+ based on the velocity and vorticity distributions is expanded over Lagrangian particle trajectories reconstructed over multiple time instants (Schneiders et al., 2016a). The method introduced is referred as VIC++ where the main objective is set to utilize the full potential of the temporal range of two dimensional measured data to increase the density of velocity information over the specified measurement domain in consistence with the temporal evolution of particle tracks. Accuracy characteristics of VIC++ is strongly dominated by the number of time instants considered for the optimization procedure as increased track lengths over time provided a better correlation between the densified flow field information and the measured data by elevating the number of particles received from the measurements which are also used to compute a more precise cost junction.

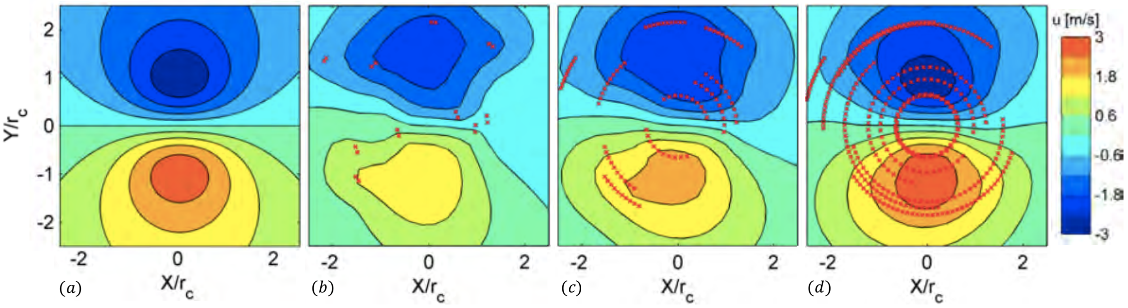

Figure 2.16: x-component of velocity vectors for 2D Gaussian vortex reference (a) and, VIC+ with $N_t = 2$ (b), $N_t = 10$ (c) and $N_t = 40$ (d)(Schneiders et al., 2016a).

Further on, an extended version of VIC++ is introduced as Time-Segment Assimilation (TSA) where the optimization problem of reconstructing a dense field of velocity information is performed on three dimensional measurement domains (Schneiders and Scarano, 2018; Gonzalez Saiz et al., 2019). Based on a minimum of 4 time consecutive velocity distributions, TSA performs an iterative optimization procedure using the velocity information of a particle along with its propagation over a chosen time segment. The instantaneous vorticity distributions and the corresponding velocity fields are again computed using the vortex-in-cell framework (Christiansen, 1973) by solving the Poisson equation for velocity with the source terms being $-\nabla \times \omega$. Finally, the cost function is constructed by interpolating the velocity distributions at each iteration on the measured data locations over the complete set of time instants.

2.5 Concluding Remarks

Despite the fact the VIC+ is proven to yield accurate dense reconstruction of flow field information even in the near wall region which also contains a viscous sublayer, actual validity of the algorithm is only consistent above the buffer layer due to the fact that viscosity is neglected throughout the employed physical formulations of acceleration terms. Nevertheless, as the optimization parameters of velocity and acceleration errors in comparison to the measured particle data are scaled in accordance to the relative variance of PTV velocity and acceleration measurements, the contribution of acceleration information on the cost function determination is deteriorated compared to the contribution of velocity errors. The non-dimensional form of the cost function J^* is expressed as follows,

$$J^* = \frac{1}{\sigma_u^2} J_u + \frac{1}{\sigma_{Du}^2} J_{Du} \tag{2.18}$$

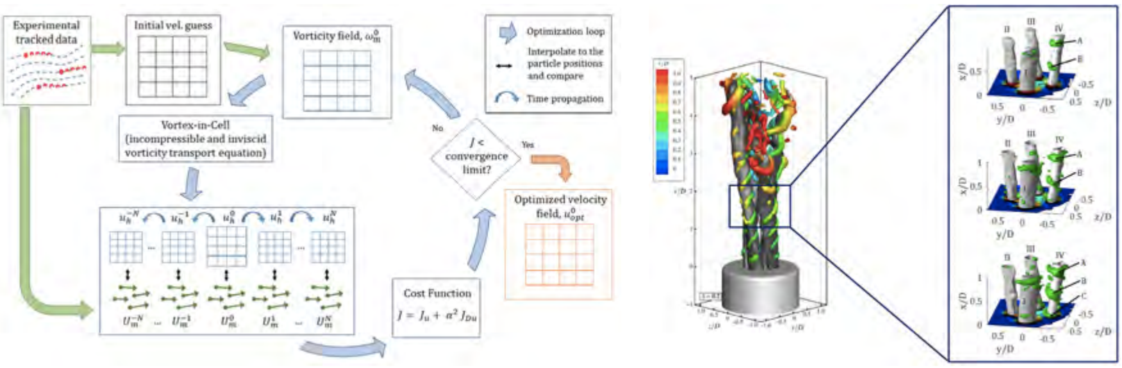

Figure 2.17: Schematic of Time-Segment Assimilation (TSA) reconstruction framework (left). Isosurfaces of time resolved $Q \cdot D^2/U_e^2 = 7$ (green) and velocity magnitude $U/U_e = 0.8$ (grey) with trilinear interpolation (top-left), TSA over 3 samples (middle-left) and TSA over 13 samples (bottom-left) for the experimental investigation of a multichannel swirling jet flow (Gonzalez Saiz et al., 2019).

while the J_u and J_{Du} corresponds to the individual cost function values of velocity and acceleration terms respectively, σ_u and σ_{Du} are defined by means of the standard deviation of PTV data.

$$\sigma_u = \sqrt{\frac{1}{n_{PTV}} \sum_{p=1}^{n_{PTV}} ||\mathbf{u}_p - \overline{\mathbf{u}_p}||^2} \quad \sigma_{Du} = \sqrt{\frac{1}{n_{PTV}} \sum_{p=1}^{n_{PTV}} ||\frac{D\mathbf{u}_p}{Dt} - \frac{\overline{D\mathbf{u}_p}}{Dt}||^2} \tag{2.19}$$

Therefore, in case the application of VIC+ is performed with the availability of particles within the viscous sublayer, accurate reconstruction of velocity information is also possible although the computed acceleration terms are compromised because of the neglected effect of viscosity which is more influential in the viscous sublayer (Cebeci, 2013).

Considering the application of VIC+ for instantaneous dense volumetric reconstruction of velocity and acceleration information from large scale Tomo-PTV measurements, the low density of tracer particles yields considerably lower spatial resolution specifications within the near wall region. Hence, not only the invalidity of VIC+ framework but also the absence of measured particle tracking information to drive the optimization procedure prohibits accurate reconstruction of viscous sublayer properties. This condition causes the implementation of a no-slip boundary condition over exact wall surface to yield inaccurate reconstruction of flow field information not only at the wall neighboring cells but also the adjacent 3∼4 grid layers in the wall normal direction. Therefore, the boundary condition definitions for velocity values at the near wall regions require a specific treatment other than the exact no-slip condition naturally existing on the wall surfaces due to the influence of viscosity (Rapp, 2017).

Furthermore, the nature of FSI problems contains non-uniform domains which originate another set of challenges in terms of not only the reliability of numerical computation procedure but also exact conformation of the surface of interest. Without proper definition of solid boundaries, accurate determination of fluid properties along the structural surfaces becomes significantly problematic as boundary conditions for and the information transfer between fluid and solid domains are strongly dependent on the interface description. Since aeroelastic problems generally include unsteadily changing structure forms, their motions and deformations in time should be captured and implemented on the computational domain for accurate correlation of FSI. The current pressure reconstruction and data augmentation algorithms are introduced on uniformly structured computational grids where the accuracy orders of the numerical schemes kept uncompromised. Thus, computation of fluid information in cases of non-uniform surfaces introduces significant drawbacks in terms of numerical accuracy and appropriate surface definition for implementation of adequate boundary conditions. More recently proposed methods for managing non-uniform solid intrusions, separate the computational domain in to multiple regions where close surface locations are handled by varying the integration direction for pressure reconstruction algorithms. Although these methods provide accurate results in comparison with the extrapolation techniques, the improvements are associated with increased levels of complexity and computational cost.

Moreover, as the measured flow field information is used for numerical simulation aided assimilation algorithms, the errors related to the measurement data propagates throughout the numerical processes as well as significantly affecting the accuracy of the assimilation procedures. Especially, considering the application of VIC+ where the experimentally acquired information is to be the exact representative of physical flow field features within the prescribed computational domains and the optimization procedure is set to define the objective function over the measurement information, the optimization is driven towards the erroneous flow field information. Even though the VIC+ bases the dense field interpolation algorithm over the Navier-Stokes equations, the velocity computation procedure do not impose any restriction on the mass conservation which corresponds to the divergence freedom of velocity vectors for incompressible flows. Hence, not only the divergence errors present in the measurement data are propagated throughout the VIC+ procedure but also an additional component of continuity errors are imposed due to the mathematical foundation of the algorithm. Although FlowFit method proposed by Gesemann et al. (2016) contains cost function terms penalizing the non-divergence components within the velocity field, constructing an objective towards minimizing the divergence of velocity vectors may lead to optimization points that deviate from the actual flow behavior since the problem definition of divergence free velocity vectors reveals a singular system with infinitely many solutions (Dong and Egbert, 2018).

Consequently, the state-of-the-art data augmentation algorithms do not contain any viscous considerations which requires the viscous terms to be included within the formulations of governing equations. Nevertheless, CFD frameworks contain approximate techniques of viscous influence characterizations for appropriate boundary condition determination which provides a cost-efficient solution in order to account for the effect of viscous forces. Furthermore,the available data assimilation and pressure reconstruction methods utilizing flow field information obtained by non-intrusive measurement techniques should be modified to enable the handling of non-uniform solid boundaries. This can be achieved by interpreting advanced computational frameworks introduced for the numerical investigations of FSI problems. Moreover, the presence and propagation of measurement errors yield a significant challenge for the data assimilation methods to reconstruct the dense flow field interpolations in coherence with the physical flow features. The noise canceling methods introduced to filter out errounous flow field information acquired throughout the experimental campaigns, provide an outstanding opportunity for modifying the available data assimilation frameworks and developing alternative approaches.

Chapter 3

Advanced Computational Techniques for Numerical and Experimental Data Processing Frameworks

In accordance to the conclusions drawn from the literature overview provided in Chapter 2, modifications and alternative approaches of the available experimental data assimilation algorithms and surface pressure reconstruction schemes involve fundamentals established over the techniques developed for computational fluid dynamics (CFD) frameworks. Accordingly, characterization of near wall fluid properties for boundary condition definitions beyond the laminar regime of turbulent boundary layers is commonly performed in CFD simulations via the use of wall function applications. Treatment of unsteadily deforming non-uniform boundaries encountered in fluid-structure interaction (FSI) problems are performed by means of various methods where two main approaches can be discretized with respect to the mesh formation procedure they adapt. Boundary fitted coordinate systems and their deformations in relation to the structural response of the elastic surfaces are employed for the Arbitrary Lagrangian-Eulerian method whereas the immersed boundary treatment methods are proposed to satisfy the appropriate boundary conditions while preserving uniform mesh formation. Last but not least, there exists multiple approaches introduced over the coarse of experimental data augmentation literature in order to elevate the physical coherence of measurement data to the actual flow behavior via filtering errors introduced throughout the experimental data acquisition and processing procedures. Hence, this chapter provides an extensive background on the computational frameworks introduced for numerical simulations and experimental data assimilation applications which create the basis for the developed methods in this thesis work.

3.1 Wall Function Applications

Implementation of wall functions for determination of velocity values at the wall neighboring finite volume cells is a popular approach among numerical simulation frameworks for viscous flow solutions. Resolution of exact flow behavior within the close wall region requires extremely high spatial resolution specifications with significantly fine grid spacing definitions, i.e. DNS and LES. Employing wall functions for near wall velocity approximations offers a cost-efficient opportunity in cases where the major emphasis is on accurate characterization of large scale flow features, i.e. RANS (Craft et al., 2002).

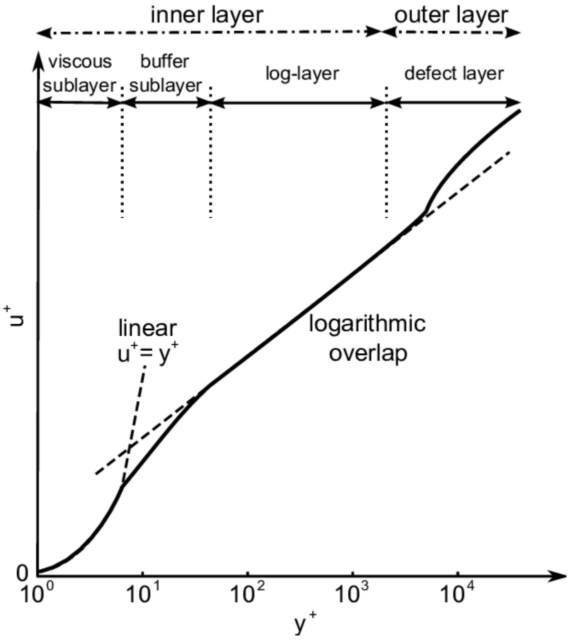

Figure 3.1: Near wall normalized velocity profile with respect to the wall normal units of a turbulent boundary layer (Marinus, 2011).

3.1.1 Law of the Wall

The *Law of the wall*, first introduced by von Kármán (1930), refers to a logarithmic relation between the wall normal distance units and the average normalized velocity profile over the overlap region of inner and outer layers of a turbulent boundary layer. The applicability of the logarithmic law is only valid within the close proximity of the wall surface as well as its application is entitled to severe constraints of flow conditions (Afzal, 2001). The formulation for the velocity profile in compliance with the *Law of the wall* is expressed as follows in terms of non-dimensional velocity and wall distance units,

$$u^+ = \frac{1}{\kappa} ln(y^+) + C \quad u^+ = \frac{u}{u_\tau} \quad y^+ = \frac{y u_\tau}{\nu} \tag{3.1}$$

where u_τ and ν refer to the shear velocity and kinematic viscosity respectively. The κ, the von Karman Constant, and C are documented to be κ 0.41 and $C = 5$ for smooth walls according to the empirical studies of von Karman himself. Even though these constants and the logarithmic law are valid strictly for well-developed equilibrium boundary layers

(Mellor and Gibson, 1966), its implementation as an approximation for the velocity values is proven to be reliable for a wide range of applications within certain ranges of accuracy tolerances (Mandal and Mazumdar, 2015).

As represented in Eq.(2.13), the determination of the velocity information by means of the *Law of the wall* is dictated via the value of shear velocity, u_τ. Although in specific cases of measurements, i.e. turbulent flow over flat plate, this value can be computed theoretically and known a priori, treating this term as a constant inherently diminishes any possible variations of the velocity components that are present throughout the spanwise plane (Weyburne, 2011). Hence, even though the logarithmic law is a representative of the averaged velocity profiles for the turbulent boundary layers, in order to capture the distributions of local velocity profiles as well as time varying components of streamwise velocity, the approximation procedure of velocity values using the *Law of the wall* can be performed over the instantaneously available local velocity profiles.

3.1.2 Clauser Chart Method

The friction velocity u_τ is an important parameter for characterization of turbulent boundary layers since many scaling laws as well as skin friction contribution is related to u_τ. However, its direct measurement in the experimental environment is not always possible unless specific equipment dedicated for shear stress measurement over surface is used (Haritonidis, 1989). Hence, its deduction generally requires an indirect method to be applied over experimentally acquired information.

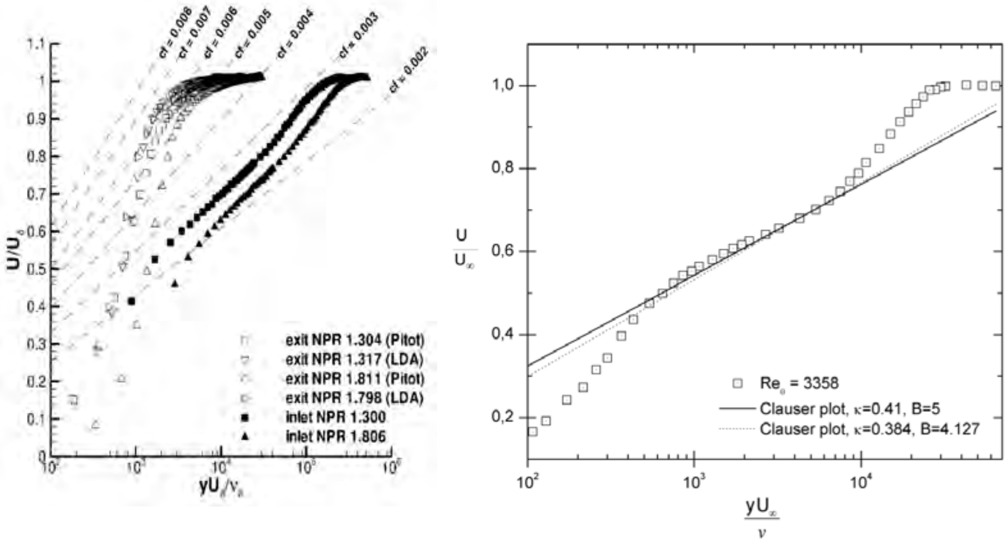

Figure 3.2: Velocity profile approximations for experimentally acquired boundary layer data with various skin coefficient values (Trumper et al., 2018)(left). Superposed Clauser plot for an experimental velocity profile reconstructed via LDA measurements (Zanoun et al., 2014)(right).

In that regards, a common method of choice is the Clauser chart method among experimental researchers (Fernholz and Finleyt, 1996). Proposed by Clauser (1956), the Clauser chart method utilizes the measured mean velocity profiles in the wall normal direction to fit an extrapolation function over the log-layer region, Fig.3.1. The method assumes the universal logarithmic law, namely the *Law of the wall*, within the overlap region of inner and outer layers of the turbulent boundary layer profile and performs a fitting on the measured velocity values using Eq.(2.13). Although the values of κ 0.41 and $C = 5$ are considered to be independent of the Reynolds number, there exist common applications of the Clauser chart method in literature with variations of these constant within the ranges of $0.38 < \kappa < 0.45$ and $3.5 < B < 6.1$ (Zanoun et al., 2003). It is referred that, in many situations these variations are to obscure the experimental data uncertainties (Wei, 2005).

3.2 The Arbitrary Lagrangian-Eulerian Method

The computational modelling of FSI problems contains unsteady deformations of boundary contours for which a great set challenges emerge for accurate description of boundary conditions and information transfer between the solid and fluid domains. Hence, treating these problems numerically requires appropriate description of kinematics for both regions. In fact, this description fundamentally determines the the nature of FSI simulations where it reflects the accuracy and reliability characteristics of the introduced numerical schemes for task of preserving high level of robustness throughout large scales of boundary distortions.

The conventional approaches of continuum mechanics reveal two main frameworks for discretizing the physical behavior of fluid and solid mechanics, referred as Eulerian and Lagrangian descriptions. While Eulerian perspective defines the continuum motion over a fixed computational grid formation, Lagrangian description refers to individual tracking of particle motions with a non-stationary mesh structure. Regarding the respective advantages and drawbacks of these approaches, Eulerian description, widely employed for fluid dynamics problems, provides a computationally efficient approach for characterizing fluid behavior with large distortions of contiuum motion. Numerically handling these circumstances requires significantly high spatial resolution specifications and accurate description of boundary conditions. On the other hand, Lagrangian approach provides a physical description of tracking particle motions which significantly increases the accuracy of the characterization procedures for highly time dependent problems. Nonetheless, consistent preservation of the elevated accuracy levels demands persistent adaptability of non-stationary mesh structures.

In order to avoid the individual shortcomings of pure applications of Eulerian and Lagrangian perspectives while benefiting from their respective advantages, a technique referred as the Arbitrary Lagrangian-Eulerian (ALE) method is introduced by Noh (1963) for numerical solution of hydrodynamic problems containing of fluid motion enclosed with unsteadily moving bundaries. The initially referred name of Coupled Eulerian-Lagrangian description provided a two-dimensional description of the appropriate boundary conditions within the finite difference framework. Further on its application is demonstrated to be employed for numerical simulations of a wide range of fluid speeds by Hirt et al. (1974) where the name of the approach is updated as Arbitrary Lagrangian-Eulerian.

The ALE method enabled the extension to three dimensions for unsteady simulations of blast loading of structures interacting with shock waves (Stein et al., 1977). Moreover, the ALE method is implemented with a finite element framework by Belytschko and Kennedy (1978) where the first application of a non-linear simulation for the FSI framework is presented. As within the ALE formulation the structural domain is analyzed with a Lagrangian method while the flow is characterized with an Eulerian description, the separate implementation of finite volume or difference methods for the fluid side and the finite element method for the structural domain allowed the numerical models to preserve their individual favorable properties for different kinematic behaviors of each domains (Hughes et al., 1981).

3.2.1 Boundary Fitted Coordinate Systems

Generation of boundary fitted coordinate systems for exact surface shape conformation is a common approach in CFD where its implementation is used in a large variety of numerical algorithms as it allows the generation of a mesh structure which coincides with the boundary of the interacting domains (Pardo et al., 2012; Romeiro et al., 2018). Thus, the relative numerical approximations of integral and differentiation terms can be represented on these grid locations (Thompson et al., 1985; Anderson et al., 2016).

The straightforward idea lying behind a boundary fitted coordinate system is keeping a coordinate value constant following the curvature of a boundary during which the other coordinate values belonging to the curvilinear coordinate system will follow a monotonic variation.The overall structure of the curvilinear coordinate system is constructed with a unique correspondence with the cartesian coordinate system to allow one-to-one mapping between the coordinate systems. The generated boundary fitted coordinate system must comply with the condition of avoiding crossing coordinate lines of the same coordinate axis, so that a unique mathematical transformation can be established between the physical and computational spaces (Johnson and Thompson, 1978).

Simply and Multiply-Connected Regions

Generation of boundary fitted computational grids with the property of one-to-one mapping of the physical coordinate systems requires the computational domain to be consisting of simply connected regions. A simply-connected region is defined if any contour within the domain surrounded by closed boundaries can be reduced to a theoretical zero volume in absence of any hanging nodes (Jenkins, 2002). Hence, simply-connected domains do not contain re-entrant boundaries when mapped on a coordinate system. In case of most general simply-connected regions, the generation of a boundary fitted coordinate system is fairly natural as the boundary surfaces or edges are described by segmentation for which the smoothness of the boundary definition depends on the grid resolution, Fig.3.3. The generation of a mapping function for these grid formations is relatively straightforward as they correspond a smooth deformation of Cartesian coordinate systems.

On the other hand multiply connected regions contain re-entrant boundaries and internal gaps that prevent the exact collapse of the computational domain to a theoretical zero volume. Although, the definition of multiply-connected regions allows treatment of

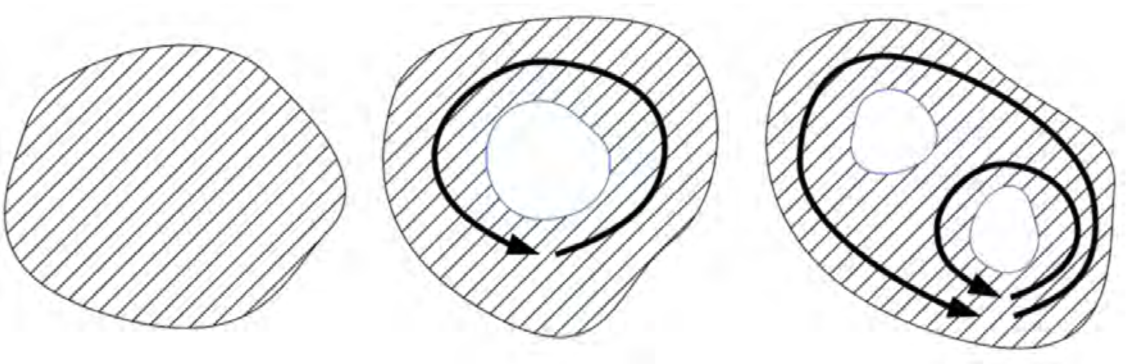

Figure 3.3: Simply-connected (left) and multiply-connected (middle& right) regions (Ahmad, 2007).

geometries with further increased complexity levels, the mapping procedure that constructs the link between the computational and physical coordinate systems is rather complicated as well. Thompson et al. (1985) refers to an extensive survey on handling such geometries especially on three dimensional computational domains. Nevertheless, the boundary fitted coordinate systems introduced for the work content of this thesis only considers simply-connected regions that provides a volumetric mapping on a uniformly structured computational grid.

3.2.2 Grid Generation Systems

Generation of a boundary fitted coordinate is performed via constructing a mapping function describing the computational coordinates by means of the physical coordinates. Hence, each computational coordinate location, (η, ψ, ϕ), is defined using a combination of Cartesian coordinates, (x, y, z). This task can be accomplished by employing an elliptic partial differential equation and solving the constructed equation for the coordinate variables of (η, ψ, ϕ).

Introduced by Thompson et al. (1974), utilizing a system of elliptic PDEs for the generation of a boundary fitted coordinate system inherently prevents any overlapping or collapsing grid cells provided that the extremums of the generated curvilinear grid structure appear over the boundaries of the computational domain. Furthermore, as the elliptic PDEs provide an inherent diffusion due to the order second derivatives terms, the resultant computational grid structure is off any discontinuities that may appear over the domain boundaries and propagate towards the inner regions (Sonnemans, 1992). Accordingly, the employed Laplace equation for the mesh generation procedure is in the following form,

$$\nabla^2 \psi^i = 0 \quad i = 1, 2, 3 \tag{3.2}$$

The Laplace equation is solved for each dimensions individually in which the control of grid smoothness is establish by means of the Euler equations defined for a functional minimization. However, the absence of any control parameters imposed on the mesh generation algortim yielded severly lowered mesh quality characteristics throughout the tranformed grid domains. Hence, Thompson et al. (1976) proposed the use of a Poisson equation in order to define the transformation layout within the grid structure where the source terms are utilized as control parameters of mesh quality.

$$\nabla^2 \psi^i = P^i \tag{3.3}$$

in which the source terms P^i are employed to control the mesh specifications such as orientations and density of the grid lines by enforcing spatial resolution parameters. In that regards, various source term formulations are suggested depending on the desirable quality specifications (Thompson et al., 1975; Ghia et al., 1976).

Moreover, further control parameters can be added in form of additional source terms to the generation procedure of the grid system as orthogonality of the coordinate lines can be induced. Alternatively grid orthogonality can be achieved by elevating the order of the partial differential equation to 4, thus constructing a system of biharmonic equations which indeed requires additional boundary conditions to be provided (Haussling, 1979).

3.2.3 Mesh Deformation

In most cases of unsteady motion of solid boundaries, a natural approach can be introduced as completely regenerating the grid structure to meet the surface definition requirements at each time step. However, this process generally requires considerable scales of user interaction for ensuring the mesh quality is not compromised and stay within the limits of the initially created form. Moreover, since the mesh must be updated in each time step on an unsteady or iterative manner, an efficient and reliable deformation method is necessary in terms of performance and computational efficiency. Therefore an accurate grid deformation algorithm without altering the initial mesh properties drastically, provides a valuable solution for unsteady simulations for which many methods are proposed and can be ordered in two main categories as physical analogy based and interpolation based schemes (Luke et al., 2012).

Physical Analogy Based Mesh Deformation Algorithms

One of the first physical analogies established with mesh deformation is the torsional spring introduced by Farhat et al. (1998). It is proposed as an advancement over the linear spring theory applied on mesh cells to deform the mesh structures based on their connectivity information with respect to each other. Hence, it introduces additional torsional springs at the node locations to prevent colliding of mesh vertices and collapsing cells. However, with the addition of torsional springs to the system of equations to be solved for a new equilibrium state, the computational expense of the method (Degand and Farhat, 2002) is increased. Additionaly, in case of large deformations hanging nodes may appear which require either implementation of extra spring elements or direct removal of those imperfections from the system of equations (Niu et al., 2017). Moreover, Löhner and Yang (1996) used solid body elasticity as constraints on mesh deformations by assuming the mesh forms to be represented as elastic solid bodies and the deformations as the strains. The introduced model solved the strain energy equation for the equilibrium positions of updated mesh locations that results in the minimum attainable strain energy levels. Although the it yields more accurate deformations of the mesh structure, this is achieved at the expense of increased computational time (Wick, 2001). Furthermore, Helenbrook (2003) proposed the use of a biharmonic operator, ∇^4, to diffuse the mesh deformation information captured at the boundaries of the computational domain to the interior regions. By employing a Galerkin finite element procedure for the numerical implementation, it enabled direct size manipulation of mesh cells over the boundary. However, even thought it provided a comparatively similar level of accuracy of mesh deformations with spring analogy, the computational cost levels of are elevated with a factor of $\sim$2.

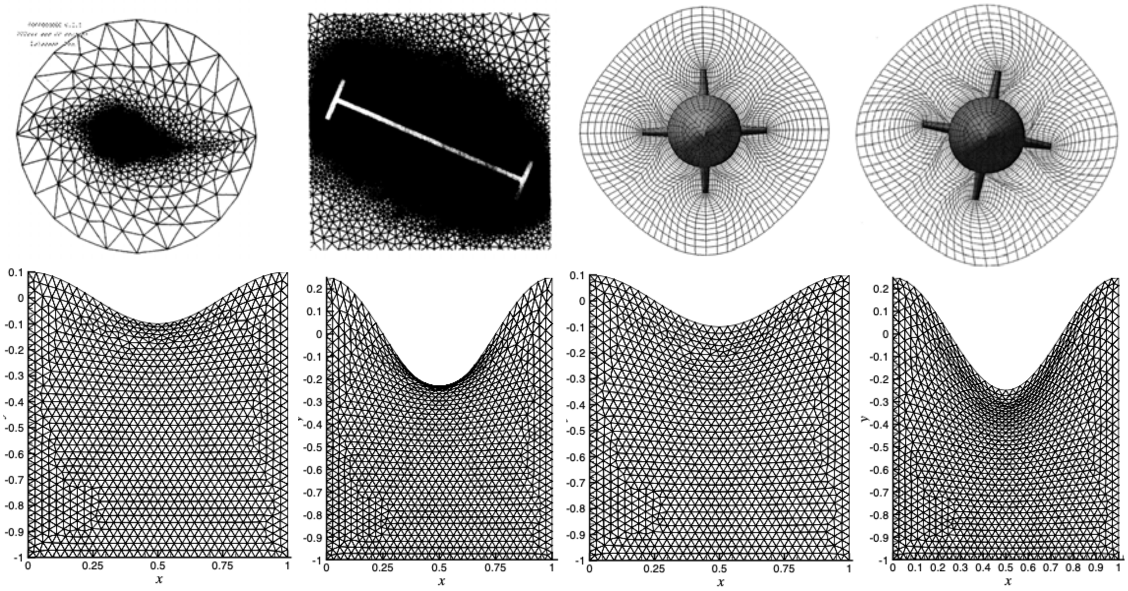

Figure 3.4: Mesh formation of the flow domain around a suspension bridge (top-left)(Farhat et al., 1998), original and deformed grid structures for a generic store with body and fin (top-right)(Tsai et al., 2001). Free-surface mesh deformations at amplitudes of A=0.1 & A=0.25 with Laplacian (bottom-left) and biharmonic operators (bottom-right)(Helenbrook, 2003).

Interpolation Based Mesh Deformation Algorithms

Interpolation based schemes consider the computational domain as a numerical problem where the boundary conditions are provided in terms of the motion or deformation of structural surfaces. Hence, the corresponding numerical problem is solved for the interpolation of the deformation of boundary nodes into the interior domains. Since these methods are independent of any connectivity requirements between the mesh cells, they can easily be applied on arbitrary mesh structures without any specific consideration of hanging nodes. Accordinly, an unsteady grid motion method is introduced by Wang and Przekwas (2012), in which at each time step the computational grid of the fluid is remapped using the pre-defined deformation functions based on a transfinite procedure (Chawner, 1990). Initially, the transformation of the grid locations are implemented on the moving boundary nodes depending on the fluid physics computed at previous time steps. Then the motion information is interpolated to the interior grid locations to influence the complete computational domain.

Also for multidisciplinary design optimization combining fluidic and structural computational domains and their iterative solution, structured mesh formation algorithms based on trans finite interpolation (TFI) methods are proposed by Jones and Samareh-Abolhassani (2012). However, a significant defect of TFI based mesh regeneration algorithms appears as the computational domains are constructed around curved boundaries that causes the method to fail by resulting in intersecting and/or overlapping mesh cells in case of large deformations. Also a Delanuay triangulation based interpolation approach is proposed by Liu and Katz (2006) in which a simple barycentric interpolation algorithm is used. Although the interpolation of boundary deformations into the interior domain revealed considerably accurate and high quality cell forms, the near boundary mesh structures suffered from inconsideration of orthogonality preservation (Wang et al., 2014).

3.2.4 Radial Basis Function Based Mesh Deformations

The employment of radial basis functions (RBF) is well established on FSI applications as they are already utilized for schemes of information transfer over the fluid-structure interface where the matching of mesh locations is an exceptional case (Smith et al., 2000; Beckert and Wendland, 2001). Their utilization for mesh deformation algorithms is first introduced by de Boer et al. (2006, 2007) for which the mesh motion calculated on the boundary nodes by a point-by-point algorithm is interpolated on the internal domain using RBFs. Already with its first application, RBF based mesh adaptation method shown to be able to generate high quality mesh formations even in case of large deformations. A high variety of RBF's are tested within this method, where CP C^2 RBF with a compact support is proven to be of best performance with the choice of support radius appearing as an important factor of resultant mesh quality (Rendall and Allen, 2010).

Comparative Applications of RBF

Since the RBF based deformation methods rely on the solution of a linear system of equations constructed over the known displacement locations, computational efficiency of the methods is strongly dominated by the linear system size which is determined by the selection of known displacement locations. In order to make this decision wisely to reduce the computational costs without compromising accuracy of the method, Rendall and Allen (2009) employed the greedy method to restrict the constraint points to a reduced number of surface locations which are selected by a procedure of error minimization over the interpolated locations of the interaction surface. Despite its increased cost-efficiency in terms of computational expense, the problem of not being able to capture the surface deformations exactly except the selected constraint locations arose accuracy issues which required corrections to be applied to the mesh structure after the deformations are performed. Even though various correction algorithms are introduced for this purpose, alternative approaches for ensuring appropriate selected of the reduced number of surface locations are introduced such as re-determining the constraint locations at every time level (Sheng and Allen, 2013) or employing an adaptive selection algorithm (Gillebaart et al., 2016).

Accordingly, a multiscale RBF interpolation method is presented by Kedward et al. (2017) that uses multiple interpolations performed over different scales of restricted surface locations to guarantee the exact surface representation while preserving the computational efficiency. The method is used to enable adaptations of 2D and 3D structured mesh forms under large deformations with a capability of preserving the initial mesh orthogonality within 1%. Moreover, the assessment of a multi-scale RBF based deformation algorithm is extended to three dimensional complex unstructured mesh and deformation configurations by Wang et al. (2018), where a double-edge greedy algorithm is combined with the mesh deformation algorithm to accelerate point selection procedure at each scale.

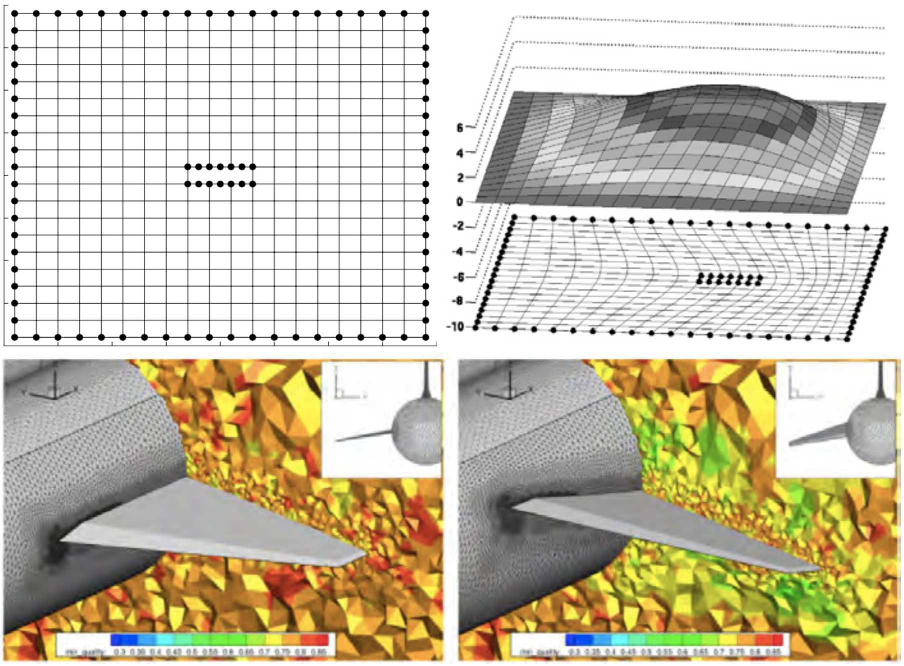

Figure 3.5: Original (top-left) and deformed (top-right) structured mesh formations employing RBF based mesh deformation algorithms (de Boer et al., 2007). Mesh quality for an undeformed portion of the tetrahedral volume mesh (bottom-left) and the deformed grid structure for horizontal tail deflection of 12^o (bottom-right) as well as surface meshes on fuselage panels (Michler, 2011).

Many applications of RBF based mesh deformation schemes revealed their superiority in terms of reducing the computational cost of deforming a complete computational domain while preserving mesh quality characteristics. Michler (2011) employed RBF based mesh deformations for simulating the unsteady control surface deflcetions of a fighter aircraft in which the computational cost of the mesh deformation procedure is reduced by restricting the deformation volume to close proximity of the control surfaces. Bos et al. (2013) used both Laplacian, solid body rotation stress (Sakr et al., 1995) and RBF based models for mesh adaptation where for the Laplace equation is solved similar to the biharmonic operator with a variable diffusion coefficient as a mesh quality control. The cell orthogonality and skewness metrics are utilized to assess the resultant mesh quality properties for which the computational domains updated by means of RBF based mesh deformations resulted in significantly superior quality levels over the other two algorithms.

Radial Basis Functions

There exist a vast spectrum of RBFs in literature, well document for interpolation of multivariate information. The overall categorization of the RBFs can be made by separating them into two main groups. The first one is the RBFs with ca ompact supports which yield a piecewise function formulation for the interpolation operation as follows,

$$\phi(x) = \begin{cases} f(x) & 0 \geq x \leq 1 \\ 0 & 1 < x \end{cases} \tag{3.4}$$

where $\phi(x)$ corresponds to the interpolation function that is commonly represented in a normalized form, $\phi(x/r)$, with a support radius r (Fornefett et al., 2001). In case of a RBF with compact support, the computed value at a certain location is only influence by a number of surrounding nodes whose count is determined by a prescribed support radius. Hence, as the support radius is increased, more information is captured for the interpolation which generally yields more accurate results, although there are some exceptions (Porcu, 2013). Nevertheless, with the increasing number of data considered for the interpolation, there exists a cost penalty in terms of the computational effort caused by dense and large linear systems. A variety of RBFs with compact support are provided in Tab.3.1.

Table 3.1: Radial basis functions with compact support.

No.	Name	f(ξ)
1	CP C^0	$(1-\xi)^2$
2	CP C^2	$(1-\xi)^4(4\xi+1)$
3	CP C^4	$(1-\xi)^6(\frac{35}{3}\xi^2+6\xi+1)$
4	CP C^6	$(1-\xi)^8(32\xi^3+25\xi^2+8\xi+1)$
5	CTPS C^0	$(1-\xi)^5$
6	CTPS C^1	$1+\frac{80}{3}\xi^2-40\xi^3+15\xi^4-\frac{8}{3}\xi^5+20\xi^2 log(\xi)$
7	CTPS C^2_a	$1-30\xi^2-10\xi^3+45\xi^4-6\xi^5-60\xi^2 log(\xi)$
8	CTPS C^2_b	$1-20\xi^2+80\xi^3-45\xi^4-16\xi^5+60\xi^2 log(\xi)$

The second kind of RBFs are defined with a global support where the interpolation function obtains information from the complete set of available data points. Even though, globally supported RBFs benefit from continuous function definition and utilization of all available data for the construction of the interpolation function, the previously referred computational cost deficiencies are even more amplified due to the requirement of handling large systems without any sparsity of data entries. A set of popularly employed globally supported RBFs are provided in Tab.3.2, while more detailed descriptions of their individual performance characteristics can be found in Wendland (1998, 1999); Buhmann (2003).

Table 3.2: Radial basis functions with global support.

No.	Name	Abbreviation	f(x)
9	Thin plate spline	TPS	$x^2 log(x)$
10	Multiquadric biharmonics	MQB	$\sqrt{a^2+x^2}$
11	Inverse multiquadric biharmonics	IMQB	$\sqrt{\frac{1}{a^2+x^2}}$
12	Quadric biharmonics	QB	$1+x^2$
13	Inverse quadric biharmnics	IQB	$\frac{1}{1+x^2}$
14	Gaussian	Gauss	e^{-x^2}

3.2.5 Arbitrary Lagrangian-Eulerian Method for Vortex Simulations

As its application is commonly referred for flow simulations based on velocity-pressure formulations using finite volume or finite elements methods, conformal mapping is also employed in case of vortex simulations to accurately handle solid boundaries within the computational domains. Thames et al. (1977) used boundary fitted coordinate systems for numerical simulations of viscous and potential flows around two dimensional arbitrary bodies where the flow governing equations of incompressible vorticity transport and streamfunction-vorticity relations are described in curvilinear grid formations, conforming various body shapes of airfoils and arbitrary objects. Furthermore, Bernard (1999) referred to the use of boundary fitted coordinate systems for simulations of complex external flows for which the conformal mapping allowed the introduction of a thin layer of computational grid in order to advance the surface vortex sheets created at each time step.

Regarding their employment for Vortex-in-Cell (VIC) simulations, Cottet and Poncet (2004) utilized a conformal mapping approach for three dimensional direct numerical simulations of wall bounded flows in which the particle-mesh hybrid approach involved a grid structure fitted to the surface shape of a sphere in close proximity of the solid object. Hence, the advantage of an Eulerian treatment for lowering the high computational cost enabled efficient discretization of an immense number of vortices located closer to the wall surfaces without losing accuracy. Also, Kudela and Kozlowski (2009) employed a boundary fitted coordinate system for flow simulations around arbitrary shaped objects using the VIC framework where fourth order interpolation kernels used by Cottet and Koumoutsakos (2000); Sagredo and Tercero (2003) are modified for the near wall regions as one sided interpolation functions for particle-mesh switching of vorticity distributions.

3.3 Immersed Boundary Treatment in CFD

Vortex methods have a proven value of predicting complex unsteady flow features via removing the necessity of grid generation methods commonly employed for conventional Eulerian approaches as their formulation is based on discretizing a vorticity field corresponding the Lagrangian description of Navier-Stokes equations (Sarpkaya and Ihrig, 1986; Sethian and Ghoniem, 1988; Slaouti and Stansby, 1992; Ould-Salihi et al., 2001). However, as the number of particles included for the determination of a flow field increases which also relates to higher fidelity and resolution capabilities, a significant deficiency of computational resource utilization arises. In that regards, an alternative hybrid mesh-particle approach such as the VIC framework introduced by Christiansen (1973) allows the fast FFT based Poisson solvers to be employed over a predefined computational grid (Wu and JaJa, 2013).

Accordingly, as the fast Poisson solvers are utilized to characterize the rotational component of the flow behavior on a regular structured mesh, physical intrusions within the flow field are required to be handled employing additional velocity or forcing terms. The additional boundary treatment is introduced to modulate the dynamic behavior of the flow for the boundary condition enforcement of immersed surfaces enabling the complete numerical simulation to be performed on a fixed Cartesian grid. Therefore, the need for boundary fitted coordinate systems and introducing transformation operations between computational and physical coordinate systems is obliterated, as well as the mesh adaptation requirements for moving boundaries of FSI problems.

3.3.1 Immersed Boundary Methods for Velocity-Pressure Formulations

Velocity-pressure based immersed boundary treatment approaches base the mathematical formulation of additional dynamics terms for kinematic boundary condition satisfaction on the Navier-Stokes equation where the velocity distribution over the spatial and temporal domain is determined by pressure distributions and viscous effects. Hence, within the velocity-pressure framework of momentum conservation equation, variation of fluid properties is enforced by additional source terms to alter the flow behavior according to the prescribed solid boundary formations.

Continuous Forcing Approach

The immersed interface methods, first proposed by Peskin (1972) for viscous flow simulations around human heart valves, compute an additional kinematic or dynamic term in order to allow the satisfaction of appropriate boundary conditions over the immersed interface locations. Peskin (1972) introduced additional forcing terms to be added to the Navier-Stokes equations in the form of body forces calculated in accordance to the elastic response of flexible leaflets where the spatial discretization of the additional forcing distributions is determined via a force density function (Peskin, 2002).

The application of countinous forcing terms as immersed surface treatment is successfully emloyed among a large variety of numerical flow simulations including laminar, turbulent, multiphase and compressible flow conditions (Tu et al., 2013). Proceeding the applications of Peskin (1982) for investigating the fluid behavior interacting with heart valves, Beyer (1992); Beyer and LeVeque (1992) employed the immersed boundary method for development of a computational simulation model for aeroacoustic characterization of cochlear dynamics. Further on, as Unverdi and Tryggvason (1992) developed a front tracking method for analyzing bubble dynamics in two-dimensional multi-fluid flows, Zhu and Peskin (2003) numerically simulated various modes of flexible filament motion in a flowing soap film experimentally characterized by Zhang (2000).

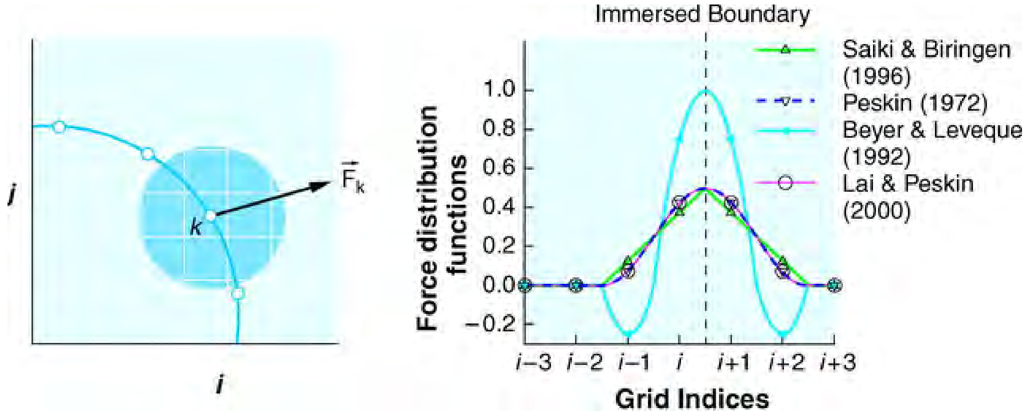

Figure 3.6: Forcing introduced by a Lagrangian boundary discretization point (left) and forcing intensity distributions over the surrounding grid location by means of different distribution functions (right)(Mittal and Iaccarino, 2005).

Discrete Forcing Approach

Another approach for treating immsersed boundary on a fully Cartesian grid formation is proposed as cut-cell method where the conformation of non-uniform boundary contours is performed via irregularly shaped grid cells introduced in the vicinity of the immersed boundaries (Leveque and Calhoun, 2001). Application of the cut-cell method is commonly employed among the numerical flow simulation throughout a wide range of problem definitions and Reynolds numbers (Tu et al., 2013).

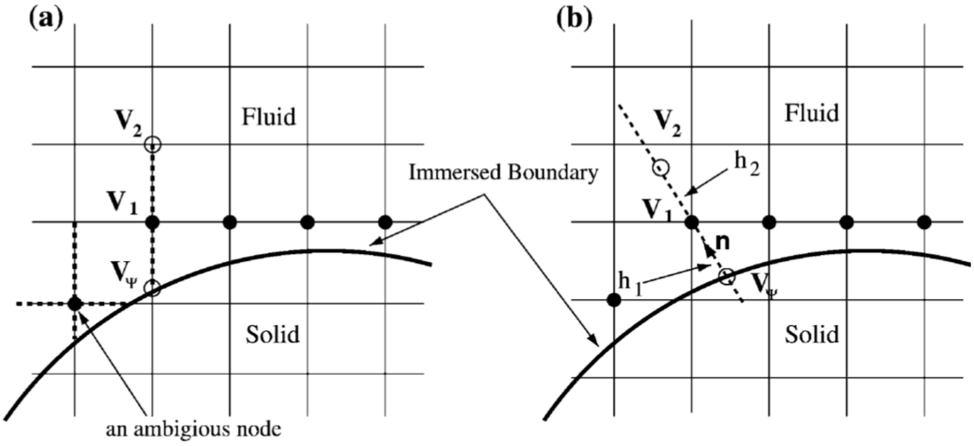

Figure 3.7: Treatment of immersed boundary locations and the cells in close proximity of the immersed interface in which the filled circles represent the grid locations with forcing application based on the methods proposed by Fadlun et al. (2000)(left) and Balaras (2004)(right).

Accordingly, Ghias et al. (2004) used the immersed boundary method to provide numerical simulation solutions around complex geometries for flow conditions of subsonic compressible flow speeds. The boundary conditions over the interface surface are satisfied employing a ghost cell approach in combination with a bilinear interpolation scheme.

In order to satisfy the exact boundary conditions at the immersed boundary surface, the flow variables are calculated over the ghost cells located inside the immersed object. Furthermore, Mittal et al. (2002) used a sharp-interface based numerical solver employing a cut-cell approach for investigation of single and dual paired wing flapping modes which allowed the simulation of moving boundaries of the flapping wings without modifying the global grid structure. The same approach is utilized for numerical characterization of diaphragm-driven synthetic jets (Utturkar et al., 2002) as well as flutter and tumble characteristics of free falling objects (Rajat Mittal and Udaykumar, 2004).

3.3.2 Immersed Interface Methods for Vortex Simulations

Implementation of immersed boundary methods for vortex simulations is also a popular approach for utilizing vortex dynamics in the purpose of numerically characterizing fluid behavior especially in cases of complex FSI problems.

Since models such as VIC framework allow the significant improvement sover the trade-off of fidelity and computational efficiency, immersed boundary methods allow the Eulerian grid structure of the VIC framework to be preserved while presence of non-uniform physical objects within the computational fields are handled with appropriate boundary condition definitions.

Boundary Conditions for Particle Vortex Methods

Using the Lagrangian based vortex particle methods, Ploumhans and Winckelmans (2000) employed the formulations of integral boundary equations in order to impose appropriate boundary conditions over the interaction surfaces for high fidelity simulations of viscous flows around generic bluff bodies. The no-through and no-slip boundary conditions arising due to the aforementioned flow conditions are handled by means of surface singularities assigned over the immersed boundary surfaces. In case of the no-through boundary condition, a distribution of vortex sheets over the interface surface allows the cancellation of penetrating velocity components through the boundary surface. However, the resulting integral boundary equation corresponds a Fredholm integral equation of first kind that yields a ill-posed numerical problem when discretized for the surface normal velocity vectors. Hence, instead the vortex sheet strengths over the immersed interface surface are determined via expressing the no-through boundary condition in terms of the tangential velocity components yielding a Fredholm integral equation of second kind (Beale and Greengard, 1994). Nonetheless, in order to obtain a well-conditioned system with a unique solution for multiply connected regions, Kelvins theorem of circulation conservation or Kutta condition is required to be introduced as an additional constraint to achieve an overdetermined linear system of equations (Cottet and Koumoutsakos, 2000).

Panel Methods

The numerical implementation of boundary integral equations for adequate description of boundary conditions over the interface surfaces is performed using the panel method introduced by Hess and Smith (1967). The panel method allows discretization of boundary surfaces by means of quadrilateral or triangular shaped panels (for three dimensional applications) over which a distribution of singularity elements is placed. Hence the boundary integral components over the boundaries are computed either analytically or numerically by constructing a linear system to determine the singularity strengths in relation to the boundary conditions.

Accordingly, Ploumhans et al. (2002) extended the implementation of boundary integral equations in use of immersed boundary treatments to three dimensions. The numerical tool developed for direct numerical simulations of bluff body flows using particle vortex methods is utilized for simulation of flow around a sphere at various Reynolds numbers. The slip velocity appearing on the surface of the immersed boundary of the sphere is canceled using a vector valued vortex sheet distribution whose orientation required only two components paralel to the quadrilateral surface as canceling the tangential velocity components inherently satisfies the no-slip boundary condition due to the linked boundary conditions (Prabhakara, 2004).

Immersed Boundary Treatment for VIC

The approach of immersed boundary treatment for taking advantage of the fast Poisson solvers is implemented to the VIC method by Walther and Morgenthal (2002) where a two dimensional implementation for flow simulations around complex geometries in combination with a local particle-particle correction algorithm for resolving subgrid scales is proposed. The immersed boundary surface is discretized with vortex sheets of linearly varying strength to yield a second order accurate method for boundary condition enforcement at the central locations of the panels, namely the collocation point, and the additional equation for the linear system to be unique is derived from the Kelvin's theorem of circulation. The proposed approach is tested by simulating the impulsively started flow behavior around a circular cylinder and a 12 leaf cactus (Morgenthal and Walther, 2007).

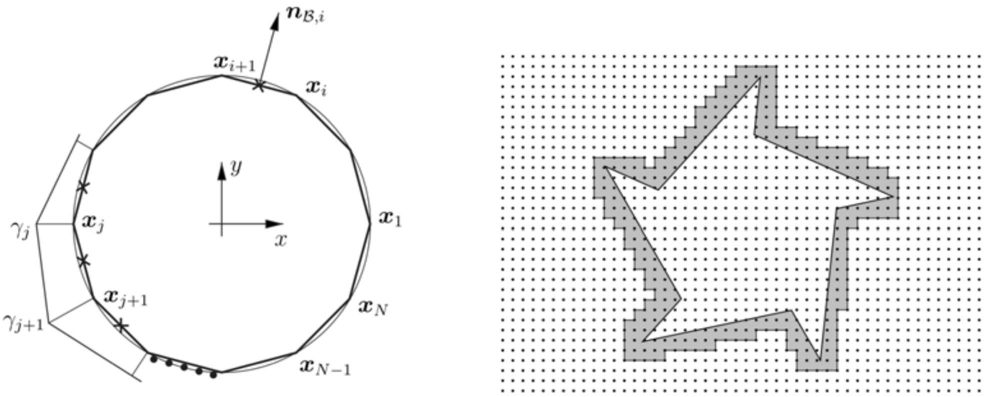

Figure 3.8: Schematic illustration for the boundary element designation of immersed boundary treatment with surface singularity elements assigned as vortex sheets for a two-dimensional application (left) and hybrid meshing strategy where the outer region is discretized with regular mesh formations while the close proximity region is not meshed due to the already available large density pointwise vortices (right)(Morgenthal and Walther, 2007).

The extension of immersed boundary treatments in vortex simualtions to three dimensional fluid simulations is performed by Cottet and Poncet (2004) where the panel discretization of the immersed surfaces is performed by reconstructing the object shape by assigning the boundary conditions for the zero normal velocity characterization at the closest computational grid cells. The no-through boundary condition at these locations is satisfied by solving an additional Possion equation for a scalar potential function of ϕ whose Laplacian yields a function g that vanishes outside the immersed object. For achieving greater surface conformation and increasing accuracy of flow characterization in close proximity of the interface surfaces, Kim et al. (2012) redesigned the immersed interface method with a scalar potential function, ϕ^*, assigned to the exact surface locations that yields a Laplace equation $\nabla^2\phi^* = 0$ within the fluid domain. Furthermore, unlike their previous efforts of combining vortex simulations with panel methods for flow simulations around axisymmetric bodies where the geometric definitions of the object are divided into rectangular panels (Kim et al., 2005), they utilized triangular panels assigned with linear distribution of singularity strengths in order to increase the fidelity for surface representations of complex geometries.

Flows with Moving Boundaries

Investigating fluid behavior interacting with moving boundaries, the previously described Eulerian-Lagrangian approach is also employed for the framework of immersed interface methods. As the flow features are discretized via the Eulerian form of flow governing equations, the motion of the boundaries are traced following a Lagrangian approach (Udaykumar et al., 1999). Since the immersed boundary methods allow a stationary Cartesian grid to be used for the calculation of fluid properties, the need for computationally expensive mesh deformation algorithms are diminished. Hence, not only the grid motion requirements are deteriorated but also the numerical accuracy deficiencies due to the mitigated mesh qualities of the computational grids, vectorial transformations and the need for kinematic contributions of the grid-related quantities are removed (Tezduyar, 2001).

3.3.3 The Helmholtz Decomposition

The Helmholtz decomposition corresponds to a decomposed velocity field to a irrotational and a solenoidal component which is unique up to a constant (Joseph, 2006).

$$\mathbf{u} = \mathbf{u}_\omega + \mathbf{u}_\phi + \mathbf{u}_\infty \tag{3.5}$$

where $\mathbf{u}_\omega$ represents the rotational solenoidal field such that

$$\omega = \nabla \times \mathbf{u} = \nabla \times \mathbf{u}_\omega \tag{3.6}$$

when the *Curl* operator is applied to both sides of Eq.(3.6) and the incompressibility constraint is considered to drive the velocity field divergence free, $\nabla \cdot \mathbf{u}_\omega$, we obtain the velocity-vorticity relation also employed by the Vortex-in-Cell framework.

$$\Delta \mathbf{u}_\omega = -\nabla \times \omega \tag{3.7}$$

On the other hand, the irrotational component of velocity is defined by means of a scalar potential function ϕ which yields a curl-free velocity field by mathematical identity,

$$\nabla \times \mathbf{u}_\phi = \nabla \times (\nabla \cdot \phi) = 0 \tag{3.8}$$

Again introducing the incompressibility constraint on the irrotational velocity component, one obtains the Laplace's equation for the scalar potential ϕ

$$\Delta \phi = 0 \tag{3.9}$$

It is observable that the velocity field defined by the Helmholtz decomposition in Eq.(3.5) is not unique as any scalar potential field can be added to the vector field. Thus, the uniqueness of the irrotational velocity field is induced by means of appropriate kinematic boundary conditions for the flow field to represent accurate physical fluid behavior in contact with a physical object. A velocity field interacting with an impermeable solid boundary needs to satisfy the no through boundary condition regardless of its viscosity specifications.

$$\mathbf{u} \cdot \mathbf{n} = (\mathbf{u}_\omega + \mathbf{u}_\phi + \mathbf{u}_\infty) \cdot \mathbf{n} = \mathbf{u}_b \cdot \mathbf{n} \tag{3.10}$$

where $\mathbf{u}_b$ represents the motion of the solid boundaries.

Solution of the Laplace equation for the scalar potential ϕ is proposed following two different approaches. The first one is referred as the grid-based method where the Laplacian is discretized over the complete computational domain by means of finite-difference or finite-element methods and the resulting linear system of equations is solved for the unknown distribution of the scalar potential function ϕ. Although for simple geometries this approach would provide fast solutions using simple inversion techniques, the computational cost significantly increases with increasing complexity of geometric contours.

The second approach is to define the Laplace equation for the scalar potential in terms of Green's function formulation which yields a set of boundary integral equations when the kinematic boundary conditions are enforced (Mengaldo et al., 2017). The boundary integral equations represent an unknown distribution of singularities over the interface surfaces discretized numerically by means of panel methods which result in a set of algebric equations to be solved for the unknown strength distributions of surface singularities to satisfy the required boundary conditions.

3.4 Solenoidal Filtering Applications for Assimilation of Experimental Data

Volumetric quantitative flow visualization techniques such as 3D particle tracking velocimetry (PTV)(Maas et al., 1993; Malik et al., 1993) and tomographic particle image velocimetry (Tomo-PIV)(Elsinga et al., 2006) yield three components of the velocity vectors which not only allow more accurate characterization of coherent structures within the fluid domains, but also provide a greater level of accuracy in terms of reconstructed pressure field by removal of errors due to the out-of-plane velocity or acceleration information (Ponchaut et al., 2005). Nevertheless, there exists various sources of errors over the procedures of image acquisiton and flow field reconstructions. As these errors are characterized by means of spurious nonzero divergence of measured velocity vectors, mass conservation is violated for incompressible flows (de Silva et al., 2013). Various algorithms are proposed to filter out the divergence errors for volumetric velocity measurement techniques where approaches are generalized in three main groups depending on the base principle them embrace.

3.4.1 Helmholtz Representation

Named after Hermann von Helmholtz, the Helmholtz representation refers to a vectorial decomposition in which a vector field, finite and yielding continuous 1^{st} & 2^{nd} order derivatives, composes of a solenoidal (divergence free) and an irrotational elements as represented in Eq.(3.5) (Joseph et al., 2007). Then, applying the divergence operator to both sides of Eq.(3.5) and considering the solenoidal property of $\nabla \cdot \mathbf{u}_{sol} = 0$ yields the Poisson relation in the form of,

$$\nabla^2 \phi = \nabla \cdot \mathbf{u} \tag{3.11}$$

Hence, the the solution of Eq.(3.11) provides the scalar potential ϕ from which the solenoidal velocity field can be computed utilizing the Eq.(3.5). However, properly defining a well-conditioned problem for the solution of the Poisson equation is relatively difficult especially since in absence of wall bounded flow domains the boundary conditions are defined in terms of velocity rather than a scalar potential. Even though there are possible formulations that allow defining the boundary conditions by specifying various constraints on the velocity gradients, since the measured velocity data is prone to mass conservation errors at the first place, not only these methods yield ill-conditioned numerical problems but also the divergence errors contained within the measurements propagate throughout the solenoidal reconstruction algorithms (Kudela and Regucki, 2002).

Accordingly, Song (1993) introduced a projection method of volumetric velocity measurements onto divergence free fields to eliminate spurious divergence errors which is treated as noise. The algorithm, referred as PSDF, suppresses the measurement noise levels to improve the accuracy of the quality of phase-contrast MR angiograms. Yang et al. (1993) used the method of projection onto convex sets (POCS) to reconstruct volumetric velocity field information from gappy & noisy data sets acquired via Magnetic Resonance (MR) flow visualization. The POCS, similar to PSDF, finds a divergence free velocity field as a combination of multiple solenoidal velocity fields that representing the measured velocity distribution with the greatest agreement (Gubin et al., 1967; Sezan and Stark, 1982). Furthermore, Suzuki (2009) developed a hybrid approach for vortex shedding simulation of a fully separated flow over an airfoil with a linear combination of PTV measurements and DNS velocity fields updated by a time marching procedure. The hybrid algorithm not only acted as a noise filter, suppressing the spurious spanwise velocity components but also improved the fidelity of unsteady flow fields.

3.4.2 Least-Squares Variational Filters

Another approach employed by Liburdy and Young (1992) and Sadati et al. (2011) is introducing a unconstrained minimization problem composed of three different objective functions;

(i) The root mean square of the difference between the filtered solenoidal velocity field and the measured one.

(ii) Velocity gradient smoothness which can be expressed by a strain-rate tensor (Chicone, 2017).

(iii) The divergence of the velocity field($\nabla \cdot \mathbf{u}$).

where the last two cost parameters are to be weighted according to the user-defined inputs for which a generalized cross-validation algorthim is employed in order to obtain the optimum-weight distribution among these three parameters (Sadati et al., 2011). Moreover, de Silva et al. (2013) re-defined the optimization on a constraint basis which inherently dismissed the requirement of providing weights over the optimization parameters and named their approach as divergence correction scheme (DCS).

3.4.3 Reconstruction with a Solenoidal Basis

The third approach is the employment of a solenoidal basis for the reconstruction of the velocity fields which inherently satisfies the divergence free condition. Various choices are proposed in literature in terms of defining a solenoidal basis. Battle and Federbush (1993) introduced divergence free wavelets for construction of vector fields with vanishing divergence components for direct imposition of divergence-free condition representing the mass conservation for incompressible flows. Schiavazzi et al. (2014) utilized the concept of solenoidal wavelets to introduce solenoidal waveform reconstruction (SWR) for suppression of continuity errors within the three dimensional velocity field measurements. The measurement volume of velocity vectors is equipped with vortices around the grid edges which reconstructed a solenoidal velocity distribution via converting the measured velocity values to face fluxes ensuring mass conservation at a finite volume level.

Furthermore, Narcowich and Ward (1994) derived matrix valued RBFs formulating the scalar valued RBFs on a vector space and applying the curl operator in order to diminish the divergence of the resultant vector field inherently due to the mathematical identity of $\nabla \cdot (\nabla \times \mathbf{u}) = 0$ where $\mathbf{u}$ is an arbitrary vector field. Moreover, the approximation of any sufficient smooth divergence-free vector fields by means of superimposing solenoidal RBFs is proven by the density theorem of (Lowitzsch, 2005). Additionally, Azijli and Dwight (2015) introduced solenoidal Gaussian progress regression (SGPR) to filter out non-zero divergence components by reconstructing the velocity field information over solenoidal RBFs. The proposed filter application is formulated within the Bayesian framework in order to include the measurement uncertainty information naturally. The numerically and experimentally validated applications of SGPR demonstrated the improved accuracy characteristics of the divergence free reconstructions over DCS and SWR methods.

3.4.4 Solenoidal Radial Basis Functions

The exploration of divergence-free radial kernels for data interpolation starts with the vector spline approximation method proposed by Amodei and Benbourhim (1991) where a spline minimization problem is defined over the vectorial coupling achieved by divergence and curl operators. Then Handscomb (1991, 1993) performed local interpolation and differentiation of divergence-free vector fields by employing surface and thin-plate splines. Furthermore, Dodu and Rabut (2002, 2004) extended the use of radial interpolation formulations to obtain both divergence free and irrotational free vector fields individually to complete the Helmholtz-Hodge decomposition (Ribeiro et al., 2016).

In terms of constructing the interpolation framework via RBFs, Narcowich and Ward (1994) introduced the matrix-valued RBFs to provide generalized approximations to interpolation problems on scattered information. As stated previously, the proposed divergence free formulation applied a discrete curl operator on any scalar RBF chosen by the user in the following form,

$$\Phi(\mathbf{x}) = [\nabla\nabla^T - \nabla^2\mathbf{I}]\phi(\mathbf{x}) \tag{3.12}$$

where $\mathbf{I}$ and ϕ corresponds to the 3×3 identity matrix for the three dimensional formulation and the scalar radial basis function respectively. As the mathematical identity dictates divergence of a curl is zero, the resultant interpolated field also corresponds to a solenoidal vector field.

Solenoidal radial basis functions are employed in various occasions throughout the computational fluid dynamics literature for solution of incompressible flows. Schräder and Wendland (2011) developed a mesh-free discretization algorithm for approximating solutions to Darcy's problem (Fanchi, 2002). The algorithm based on the collocation of solenoidal positive definite interpolation kernels, allows the production of analytical incompressible flows while its application is independent of problem order, dimensions and geometric forms. Moreover, Wendland (2009) proposed an algorithm composed of linear combination of analytical solenoidal approximation spaces for the solution of Stokes equations. The matrix-valued kernels are used to construct the divergence free interpolation functions which provided arbitrarily smooth high order approximations irrespective of the space dimensions.

Among the applications of these methods for reconstruction of velocity fields that satisfy mass conservation, Busch et al. (2013) introduced the use of normalized convolution and solenoidal RBFs in synergistic combination, for divergence-reduction of 3D phase-contrast flow data. Using reference computational simulations, a reduction of 87% of measurement imperfections in terms of the velocity divergence is obtained for erroneous image reconstructions. Also, Vennell and Beatson (2009) employed a two-dimensional divergence-free interpolator constructed by means of solenoidal RBFs where a greedy fit (Marchi, 2009) approach is proposed to increase computational efficiency of the algorithm whilst preserving numerical accuracy of the described interpolation surface. The proposed interpolation function provided direct enforcement of physical coherence of velocity vectors via satisfying continuity.

Chapter 4

Numerical Implementations

The computational frameworks developed within the thesis project concentrates on research objectives provided in Section 1.

Firstly, the numerical discretizations of governing equations employed for the data assimilation algorithms are formulated to represent flow features dominated by turbulent structures with negligible influence of viscosity. However, in close proximity of wall boundaries, FSI interfaces, turbulent boundary layer profiles contain sublayers of influential viscous force presence. Hence, the present data assimilation algorithms fail to cohere with the appropriate flow physics not only due to the physical formulations they are based on but also because of the scarcity of particle tracking information for large scale Tomo-PTV measurements in near wall regions. Therefore, in order to provide appropriate boundary condition definitions for computational domains in contact with the interface surfaces a wall function approach is implemented for the VIC+ algorithm in Section 4.1.

Moreover, referring to the discussions on the treatment of unsteadily deforming non-uniform boundaries encountered in FSI problems, both ALE, Section 4.2, and immersed boundary treatment, Section 4.3, methods are implemented individually for VIC+ in accordance to their respective advantages and disadvantages. Additionally, the ALE approach is also utilized for a surface pressure reconstruction scheme with boundary fitted coordinate systems, Section 4.4.

Furthermore, the propagation of measurement errors as well as the additional error sources originating due to the theoretical framework structure and numerical procedures of the data assimilation algorithms, amplifies the deviation of the resultant flow field information from the actual flow behavior. In order to solve this problem, two different methods employing solenoidal, Section 4.5, and irrotational, Section 4.6, radial basis functions for reconstructing the velocity and acceleration fields are proposed for increasing the accuracy of dense flow field interpolations for time-resolved flow characterization of 3D-PTV.

4.1 Wall Function Approach for VIC+

There exists many turbulent wall function approaches which are of a complex mathematical nature composed of modelling parameters and formulations accounting for the effects of smaller scale turbulent structures on the overall flow behavior. Nonetheless, simplified approaches of approximating turbulent boundary layer profiles can provide a sufficiently reliable opportunity for VIC+ as the algorithm optimizes the overall flow field towards the actual measurement information. Therefore, for the present wall function approach the general logarithmic law of equilibrium turbulent boundary layers developed over flat wall surfaces is employed.

The steps of the wall function implementation for determining the boundary condition values for the stream velocity component is as follows,

Step 1: Computational domain generation

Since the grid spacing for the computational domain of VIC+ approximately corresponds to spatial resolution specifications 4 times greater than input of PTV extracted directly from the experimental campaigns instantaneously, reconstruction of the physical flow behavior within the sublayers of a turbulent boundary layer is quite unlikely. Hence, the computational domain is created with a small displacement from the physical wall surface, to exclude the inner layers of the TBL structure from the problem definition and describe the domain boundary closest to the wall starting from the logarithmic region directly.

Step 2: Initial velocity field reconstruction

The scattered particle tracking information over the computation domain are gridded by binning the particle data of velocity and accelerations using spherical bins of radius $2h$, thus capturing particle information within a volume of $6\pi h^3$. The binning procedure is performed using the AGW method in accordance to the Eq.(2.8)

Step 3: Local wall function reconstruction

For each individual streak of grid locations in the wall normal direction, the Clauser chart method is employed to perform a non-linear data fitting via defining an optimization problem of matching measurement data profiles. The optimization variable is either set to determine the skin friction coefficient or the shear velocity that represents the linear profile of logarithmic variation of velocity values with respect to the wall units, Eq.(3.1).

Step 4: Velocity boundary condition computation

The velocity values at the displaced computational grid locations of the near wall region whose measured particle information cannot be captured due to the absence of particle tracks are approximated using the logarithmic law for which the shear velocity is computed following the above steps.

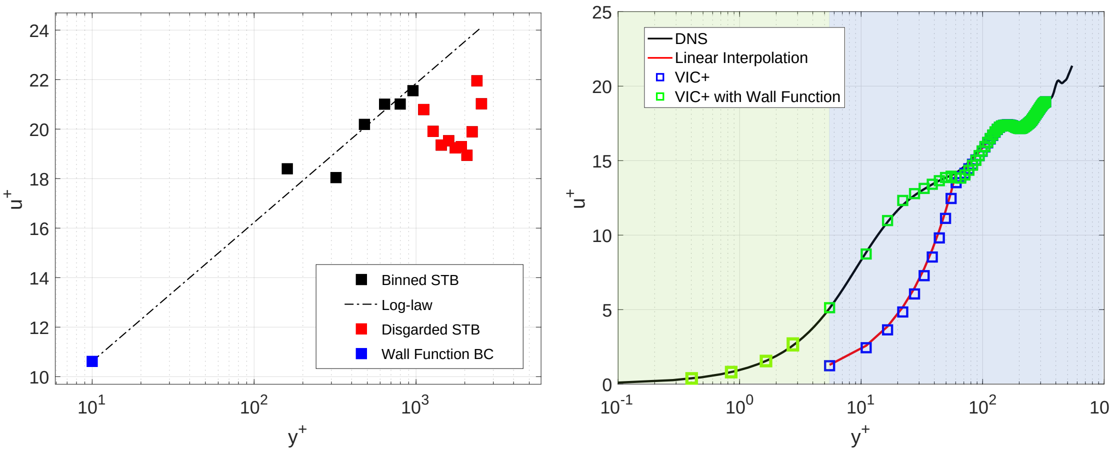

Figure 4.1: Determination of velocity boundary condition with the wall function implementation over the raw STB data (left). The representative velocity boundary layer profiles with and without the wall function implementation on VIC+ in comparison to the reference DNS data (right).

Step 5: Complete boundary layer velocity field interpolation

After the VIC+ is applied with the computed boundary conditions for velocity at the displaced locations of the computational domain in the near wall regions, the gap remaining between the computational domain and the exact wall surface is filled with locally approximated velocity profiles based on the dense reconstructed fields obtained from VIC+ by means two different interpolation formulations over the viscous sublayer and buffer layer.

- **Viscous Sublayer:** The linear relationship of non-dimensional wall normal distance and normalized velocity is used to approximate the velocity profile within the viscous sublayer. The Clauser chart method is applied again over the reconstructed velocity fields of VIC+ locally for each location over the horizontal plane to determine the corresponding shear velocity values. Then the relation of $u^+ = y^+$ is applied within the range of $0 < y^+ < 7$.
- **Buffer Layer:** Due to the fact that, an analytical expression for a theoretical buffer layer is absent and the general form is derived through various interpolation methods between the viscous sublayer and the turbulent logarithmic layer, a third order polynomial is fitted using the last two approximated velocity values of viscous sublayer for $0 < y^+ < 7$ and the first two available velocity values of logarithmic layer for $y+ > 20$. Hence, the uniquely defined polynomial of order third by means of 4 data points (Li et al., 2020) is used to calculate an approximate velocity profile for the buffer layer region.

It is worth mentioning that as the presence of non-zero pressure gradient disturbing the equilibrium condition of the turbulent boundary layer do cause the Clauser-chart method to yield deviations of velocity profiles from the physical flow behavior. In that regards the, it is shown by means various empirical studies that the relation of streamwise velocity component and the wall-normal distance is a result of overlapping inner and outer layers of a TBL structure which are defined by different scaling parameters (Millikan, 1938). Furthermore, Dixit and Ramesh (2008) demonstrated that the matching of overlapping inner and outer layers can be expressed by extending the relation order to higher degrees of approximations which provides a pressure-gradient scaling of log law parameters used to reconstruct the streamwise velocity profile in the wall-normal direction.

Therefore, a non-universal pressure-gradient depending scaling for the log law can be expressed in terms of varying constants as,

$$\frac{1}{\kappa} = \frac{1}{\kappa(\nabla_p)} \qquad C = C(\nabla_p) \tag{4.1}$$

In that regards, Dixit (2009) proposed a modified Clauser-chart method which utilizes pressure gradient based polynomial formulations of κ and C in order to perform a optimization over the aforementioned constants to generalize the use of universal logarithmic laws under various conditions of pressure gradients for equilibrium and near-equilibrium turbulent boundary layers. Nevertheless, the application of such a modified method for extraction of local shear velocity values is outside the scope of this thesis and the application of a general Clauser-chart method is considered to be appropriate as both numerical validation cases and experimental measurement campaign consisted of either zero or relatively small pressure gradients that wouldn't compromise the accuracy of boundary velocity approximations beyond to required tolerances.

4.2 Arbitrary Eulerian-Lagrangian Method for VIC+

The implementation of ALE method for the Vortex-in-Cell simulations composes of two main steps in which a computational grid is generated according to the surface information and the flow governing equations within the VIC framework are solved over the generated boundary fitted coordinates. Accordingly, the modified version of VIC+ algorithm with the ALE implementation is referred as "ALE-VIC+".

Step 1: Boundary fitted coordinate system generation.

Depending on the availability of the surface information, two different approaches can be followed to reconstruct the corresponding boundary shapes. If the immersed boundary shape is known a priori, it is directly provided as an input to the grid generation schemes along with the appropriate volume dimensions for the boundary fitted coordinate system to be created. In case where the unsteady motion of the solid boundary is captured by means of optical measurement methods, the captured structural motion is instantaneously provided to the grid generation algorithms. Hence, after an initial boundary fitted grid structure is generated according to the structural boundary profile, the generated mesh is deformed by means of the RBF deformation schemes with regards to its instantaneous motion so that the exact interaction between the fluidic and solid domains can be expressed in a time-resolved manner.

The formulation of RBF based mesh deformation interpolation method is described by de Boer et al. (2007). The interpolation function, s, defining the interpolation of surface displacements to the internal fluid domain, is approximated by a sum of basis functions ϕ,

$$s(\mathbf{x}) = \sum_{j=1}^{n_b} \alpha_j \phi(\|\mathbf{x} - \mathbf{x}_{b_j}\|) + p(\mathbf{x}) \tag{4.2}$$

where $x_{b_j} = \left[x_{b_j}, y_{b_j}, z_{b_j}\right]$ represents the boundary nodes of the interaction surface for which the displacements values are known. n_b refers to the number of nodes defining the interaction surface while the basis functions ϕ are constructed based on the Euclidean distance of internal mesh locations to the boundary nodes. Then, the following interpolation conditions determine the basis function and polynomial coefficients α_j and p.

$$s(\mathbf{x}_{b_j}) = \mathbf{d}_{b_j} \tag{4.3}$$

in which $\mathbf{d}_b$ refers to the known displacement values of the boundary nodes. Moreover, an additional requirement for the closure of the mesh deformation interpolation is defined for the polynomial q to an order not exceeding the one of polynomial p.

$$\sum_{j=1}^{n_b} \alpha_j q(\mathbf{x}_{b_j}) = 0 \tag{4.4}$$

While the choice of basis function formulations, ϕ, dictates the degree of p, in case the ϕ is selected to be conditionally positive definite, a unique interpolant is associated to the polynomial q. In fact, provided that the ϕ are conditionally positive definite with a polynomial order of smaller or equal to 2, q can be assigned as a linear function (Beckert and Wendland, 2001). Hence, utilizing this condition enables the exact recovery of the solid boundary deformations over the interaction surface. Accordingly, a linear system of equations over the known displacement values of the solid boundaries is constructed to obtain the coefficients of the basis functions, α_j and the linear polynomial.

$$\begin{bmatrix} \mathbf{d}_b \\ 0 \end{bmatrix} = \begin{bmatrix} M_{b,b} & P_b \\ P_b^T & 0 \end{bmatrix} \begin{bmatrix} \alpha \\ \beta \end{bmatrix} \tag{4.5}$$

where α and β include the basis function and polynomial coefficients respectively. The matrix $M_{b,b}$ represents the basis functions computed over the surface boundary locations with respect to each others and P_b, an $n_b x4$ matrix with row j given by $\left[1, x_{b_j}, y_{b_j}, z_{b_j}\right]$, corresponds to the coordinates of each node. The linear system is solved for the coefficients of the basis function and the polynomial separately for each dimension employing a Gauss elimination rule (Attenborough, 2003). Finally, internal deformations of the computational domain are computed using the basis functions and polynomials whose coefficients are calculated through the aforementioned steps.

$$\mathbf{d}_{in_j} = s(\mathbf{x}_{in,j}) \tag{4.6}$$

There are many choices of radial basis functions to be employed for the mesh deformation algorithm. Nevertheless, with the superior accuracy of mesh deformations in terms of the mesh quality metrics provide by de Boer et al. (2007), CP C^2 RBF is utilized to update the computational grid as the immersed surface deforms or moves within the measurement domain.

$$f(\xi) = (1-\xi)^4(4\xi+1) \tag{4.7}$$

Step 2: Computation of transformations variables for vector operations on curvilinear coordinates.

According to the updated boundary fitted coordinate system, a one-to-one mapping between the physical and a computational coordinate systems for the solution of flow governing equations is performed. This mapping provides the transformation variables to be used for accurate description of mathematical operators constructing the link between the two computational grids.

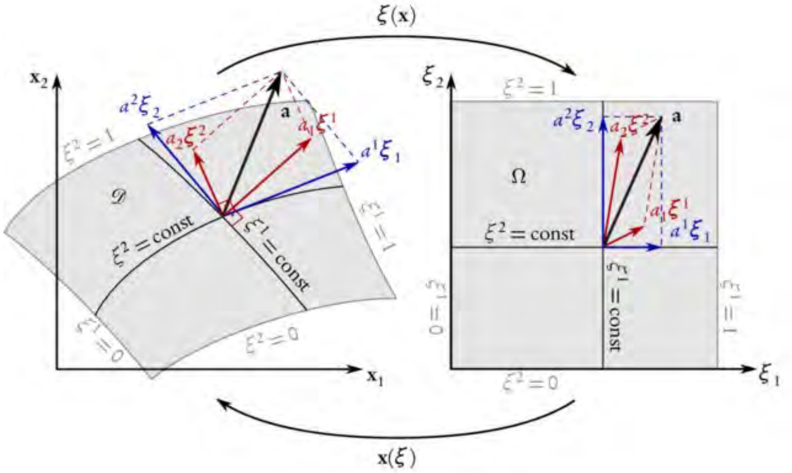

Figure 4.2: Two dimensional representation of the physical curvilinear coordinates (left) and the corresponding computational coordinates (right)(Fosas de Pando, 2012).

The location of a point as well as a vector in a three-dimensional space is described means of an appropriate coordinate system. In terms of the physical interpretation of particles motions, the general convention is to employ the Cartesian coordinates in which the flow field properties are provided by PIV/PTV measurements. Nevertheless, with regards to the solid boundary contours interacting with the flow field, the conformation of the interaction surfaces may yield curvilinear formations. Therefore, to be able to perform mathematical calculations of fluid properties on curvilinear grid systems, a transformation between the computational grid structure and physical coordinates is required.

The computational grid locations of a curvilinear system can be expressed as function of position vectors defined in Cartesian coordinates,

$$x_2 = x_2(x_1, y_1, z_1) \quad y_2 = y_2(x_1, y_1, z_1) \quad z_2 = z_2(x_1, y_1, z_1) \tag{4.8}$$

where subscript 1 and 2, refer to the Cartesian and curvilinear coordinates respectively. In Cartesian coordinates, the coordinate differentials dx, dy, dz correspond to infinitesimal distances measured in each directions of the coordinate system. Accordingly, the transformation variables defining the link between the two coordinate systems can be expresses by means of a Jacobian matrix,

$$\frac{\partial(x_2, y_2, z_2)}{\partial(x_1, y_1, z_1)} = \begin{bmatrix} \frac{\partial x_2}{\partial x_1} & \frac{\partial x_2}{\partial y_1} & \frac{\partial x_2}{\partial z_1} \\ \frac{\partial y_2}{\partial x_1} & \frac{\partial y_2}{\partial y_1} & \frac{\partial y_2}{\partial z_1} \\ \frac{\partial z_2}{\partial x_1} & \frac{\partial z_2}{\partial y_1} & \frac{\partial z_2}{\partial z_1} \end{bmatrix} \tag{4.9}$$

Futhermore, description of a Laplacian operator in boundary fitted coordinate systems by means of applying the chain rule for derivative terms results in a lengthy expression with multiple appearances of cross derivatives. Nevertheless, since the Laplacian is performed over a scalar value, or a single component of a vector, it can be expressed in terms of the local coordinates of the conformal grid structures with relative ease. In order to formulate the Laplacian operator in boundary fitted coordinates, local properties of the conformal grid shall be determined to describe the linkage between the physical and computational meshes. In that regards, the metrical coefficients of the local curvilinear coordinate system are calculated considering the coordinate differentials of boundary fitted grid structure. Let the distance between two neighboring points of the curvilinear grid referred as dl_x which corresponds to the Eucledian distance between points (x_2, y_2, z_2) and $(x_2 + dx_2, y_2, z_2)$. Then the metrical coefficients are defined as follows,

$$h_x = \left| \frac{dx_2}{dl_x} \right| \quad h_y = \left| \frac{dy_2}{dl_y} \right| \quad h_z = \left| \frac{dz_2}{dl_z} \right| \tag{4.10}$$

Hence, these properties are defined for each grid location of the curvilinear mesh and expressed as a function of the boundary fitted grid coordinates,

$$h_k = h_k(x_2, y_2, z_2) \quad k = x, y, z \tag{4.11}$$

Utilizing the metrical coefficients for the derivative descriptions of the Laplacian operator,

$$\nabla^2 = h_x h_y h_z \left[\frac{\partial}{\partial x_2} \left(\frac{h_x}{h_y h_z} \frac{\partial}{\partial x_2} \right) + \frac{\partial}{\partial y2} \left(\frac{h_y}{h_x h_z} \frac{\partial}{\partial y_2} \right) + \frac{\partial}{\partial z_2} \left(\frac{h_z}{h_y h_x} \frac{\partial}{\partial z_2} \right) \right] \tag{4.12}$$

Step 3: Vortex-in-cell+ on boundary fitted coordinates.

The calculated transformation variables are utilized for performing gradient and Laplacian operators for the flow field properties on the physical computational grid of boundary fitted coordinates while preserving the orientation of the velocity and acceleration vector on the Cartesian descriptions, which deteriorates the requirement performing vectorial transformations for multiple instants in each step of the optimization procedure.

Step 4: Cost-function computation.

As the orientation of velocity and acceleration vectors are preserved on the Cartesian descriptions, the resultant variables over the ALE-VIC+ framework are linearly interpolated at the original particle locations for calculating the error between the dense flow field interpolation and the measurement data, Eq.(2.18).

Step 5: Adjoint gradient computation and optimization.

Following the exact procedure of adjoint gradient computation introduced for VIC+ with, additional modifications are implemented to take into account the link between the physical and computational grid structures. Hence, the adjoint gradient for the proceeding steps of the optimization procedure is calculated and the optimization procedure is performed until a specified convergence criteria is achieved.

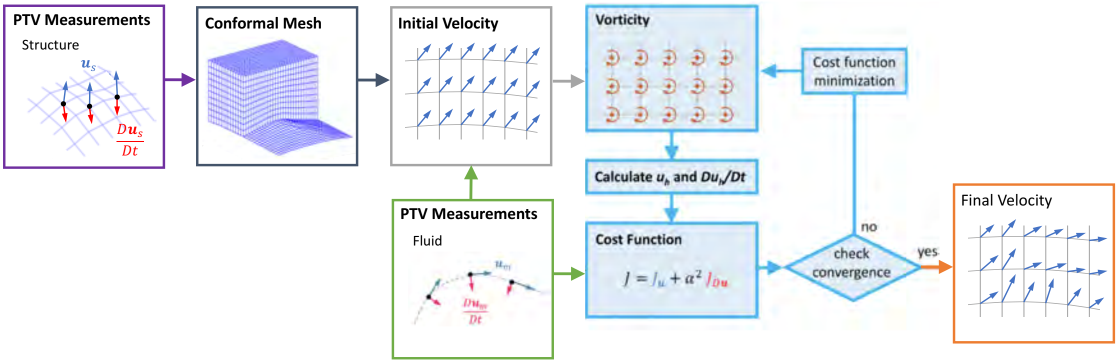

Figure 4.3: ALE-VIC+ reconstruction framework. The PTV measurements for the structural component is provided (purple box). The rectangular structured computational grid is deformed for boundary fitted coordinate generation (black box). The PTV measurements for the flow is provided (green box). An initial velocity estimate is made (gray box), which is input into the VIC+ iterative procedure (blue boxes) to find the optimization variables that yield a velocity and material derivative distributions of minimum discrepancy with the PTV measurements (orange box).

4.3 Surface Pressure Reconstruction with Boundary Fitted Coordinates

Deforming surfaces within the measurement volume yield non-uniformly shaped solid bodies that interact with fluid particles and dictate their motion. Treating these surfaces with uniformly structured grids and defining a computational domain accordingly, not only compromises the numerical definition of pressure reconstruction process but also but also leads to the loss of proper surface description (Pan et al., 2016). Hence, in order to handle the unsteady deformations, the complete computational domain defining the pressure reconstruction region is to be deformed over an initially uniform structured grid by implementing suitable mesh deformation algorithms.

4.3.1 Interpretation of the Arbitrary Lagrangian-Eulerian Method

The ALE framework for FSI problems refers to the characterization of fluid properties over a predefined grid system complying with the Eulerian perpective while the motion ofthe interaction interface is identified following a Lagrangian approach (Noh, 1963). In case of planar or tomographic particle image velocimetry providing gridded velocity fields directly after the image processing procedures, the acceleration can be computed following an Eulerian approach or pseudo-particle tracking methods. Whereas, the tomographic particle tracking techniques or recently developed Shake-the-Box (STB) algorithm provide scattered particle information of particle locations, velocities and material accelerations which is required to be gridded on the prescribed computational grid to represent flow field properties.

Furthermore, motion of the structural surfaces is generally captured in terms of a Lagrangian approach where the surface motion traced using various methods of surface tracers (Hwang et al., 2007). Hence the acquired particle tracking information, describing the motion of immersed boundaries, is preserved on the Lagrangian perspective in order to impose the corresponding deformations to the computational grid. Moreover, the accelerations of surface boundary tracers are incorporated with the fluid behavior to represent the exact pressure gradients over the interaction interface, which are to be integrated for reconstructing the pressure distributions over the immersed surfaces.

Step 1: Generation of the computational grid.

There exists a various number of well established approaches for boundary conforming grid generation. Although these algorithms are commonly employed in many computational studies, the specific purpose of the boundary fitted surface pressure reconstruction approach proposed in this thesis is to handle unsteady deformations of the immersed boundaries for characterization of FSI problems. Among the many methods that have been introduced for efficiently updating the grid structure in between time steps of boundary deformations/motions, the present algorithm of pressure reconstruction employs a radial basis function based mesh deformation scheme. Similar to the ALE-VIC+ approach, the choice of radial basis function type for the mesh deformation scheme is made in favor of CP C^2 RBF, Eq.(4.7).

Step 2: Determination of pressure gradients.

Considering the form of Navier-Stokes equations for incompressible flows, the pressure gradients over a measurement volume can be expressed in terms of the material acceleration terms, body forces and viscous stresses. Among these various contributing factors, the practical applications of engineering products are mainly dominated by turbulent flow behavior where the inertial forces reveal a significant superiority over the viscous influence. Therefore, referring to the aforementioned discussion on the negligible contribution of viscosity in Subsection 2.3.1, the viscous effects can be omitted without any significant impact observed within the uncertainty limits of pressure reconstruction schemes from PIV data. Furthermore, under the assumption of conservative body forces, its contribution to the pressure gradients is also removed from the momentum transport equation.

According to the various comparative review studies, the superiority of Lagrangian methods for determination of material acceleration in terms of accuracy and reliability is comprehensively documented. Therefore, the current method also utilizes the Lagrangian acceleration information either captured by particle tracking approaches such as STB or reconstructed by means of various data augmentation methods. Therefore, the material derivatives of velocity vectors are provided to the divergence of Navier-Stokes equation, Eq.(2.4), in order to determine the pressure gradients.

Step 3: Transformation of the coordinate system.

The conformal mapping provided by means of the previously mentioned grid generation schemes enables the direct or assimilated experimental flow information to be represented over the exact boundary contour. However, constructing a Poisson equation for the integration of pressure gradients over a curvilinear grid structure not only requires an extensive derivation of transformation variables in order to preserve the physical orientation of flow properties, but also prevents the use of Fast FFT solvers for increased computational efficiency.

The pressure gradients assigned to each computational grid location possesses a physical orientation which is in compliance with the Cartesian coordinate system. However, in order to express the pressure gradients over the computational grid, the local transformation variables between the physical and computational grid formations are determined according to the vector transformation Jacobian. Hence, employing the chain rule to represent the pressure gradients over the computational grid with indicial components of x_2, y_2, z_2,

$$\begin{aligned}
\frac{\partial p}{\partial x_2} &= \frac{\partial p}{\partial x_1}\frac{\partial x_1}{\partial x_2} + \frac{\partial p}{\partial y_1}\frac{\partial y_1}{\partial x_2} + \frac{\partial p}{\partial z_1}\frac{\partial z_1}{\partial x_2} \\
\frac{\partial p}{\partial y_2} &= \frac{\partial p}{\partial x_1}\frac{\partial x_1}{\partial y_2} + \frac{\partial p}{\partial y_1}\frac{\partial y_1}{\partial y_2} + \frac{\partial p}{\partial z_1}\frac{\partial z_1}{\partial y_2} \\
\frac{\partial p}{\partial z_2} &= \frac{\partial p}{\partial x_1}\frac{\partial x_1}{\partial z_2} + \frac{\partial p}{\partial y_1}\frac{\partial y_1}{\partial z_2} + \frac{\partial p}{\partial z_1}\frac{\partial z_1}{\partial z_2}
\end{aligned} \tag{4.13}$$

Accordingly, a FFT based Poisson solver can be employed in consideration of a fully rectangular structured grid formation. Finally, as the pressure gradients are integrated over the computational grid, the resultant scalar variables of static pressure distribution do not necessitate any additional transformations between the computational and physical grid structures, thus the pressure information possesses an exact one-to-one mapping between the two grids.

Step 4: Integration of pressure gradients.

The integration of pressure gradients within the measurement domain is performed using the Poisson equation constructed in Eq.(2.4) is solved for the pressure distribution using homogeneous Neumann boundary conditions at each face of the computational domain.

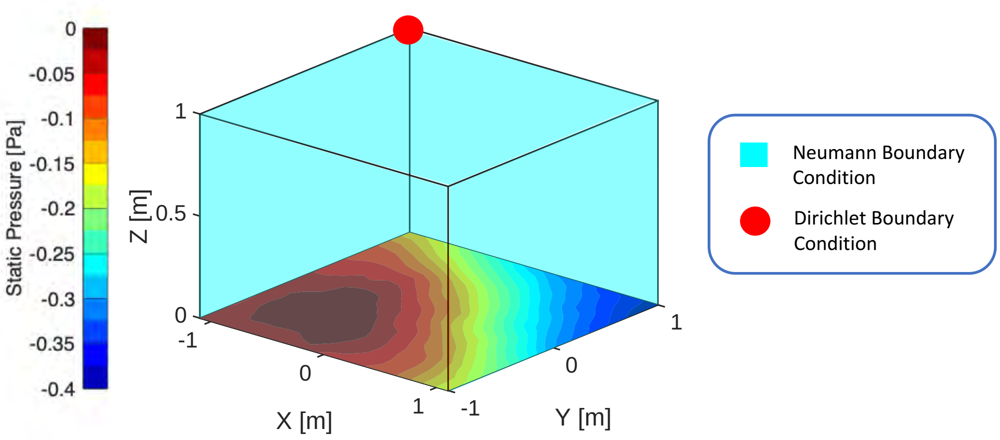

Figure 4.4: Schematic of boundary condition implementation for the pressure reconstruction procedure with the light blue surfaces representing the Neumann boundaries while the red dot corresponds to the reference pressure location for uniqueness of exact static pressure values.

Step 5: Dirichlet boundary condition determination.

For the validation studies the exact pressure information at a specified location is provided from the reference cases while the determination procedure of a reference pressure value for the experimental measurement campaign is performed over the velocity values captured at a reference pressure location. The corresponding velocity magnitude is utilized to calculate the exact static pressure value via the Bernoulli principle.

4.4 Immersed Boundary Treatment for VIC+

Implementation of the immersed boundary treatment for VIC+ method is based on the theory of vector decomposition provided via the Helmholtz theorem. As the VIC method allows rotational component of the flow behavior to be characterized by means of distributed vortices and their respective velocity induction over a prescribed domain, the potential flow component of the velocity field due to the presence of a non-uniform surface intrusion is characterized by superimposing an additional velocity field to satisfy the appropriate boundary conditions. The proposed modification is named "ImVIC+".

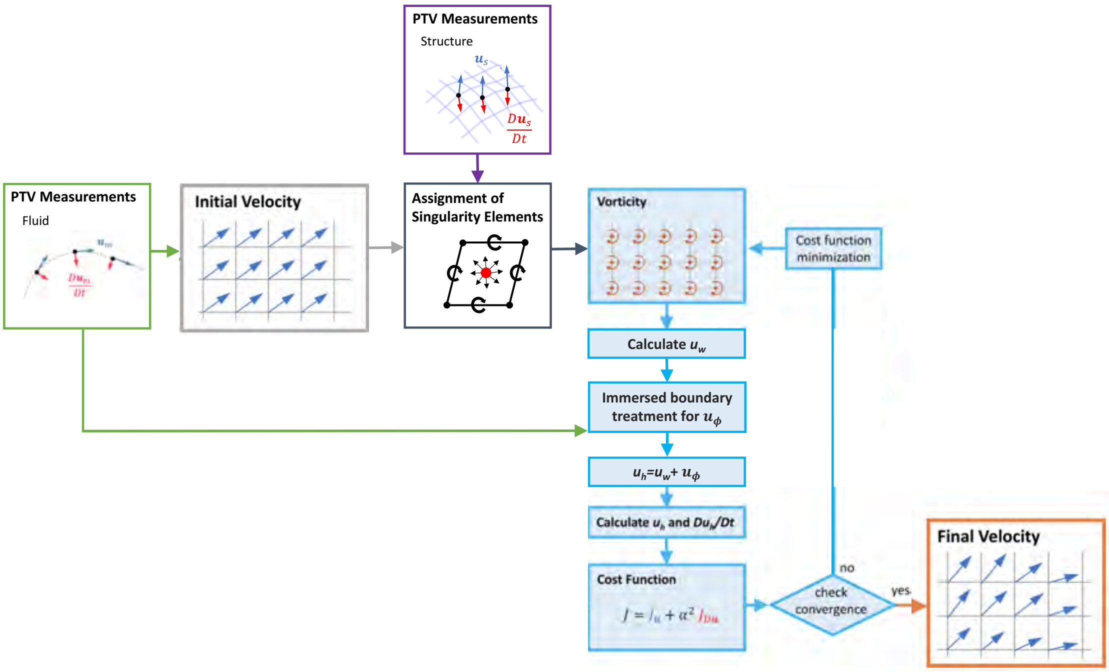

Figure 4.5: ImVIC+ reconstruction framework. The PTV measurements for the flow is provided (green box). An initial velocity estimate is made (gray box). The PTV measurements for the structural component is provided (purple box). Surface elements are assigned with singularities (black box). The resultant velocity fields is used as an input into the VIC+ iterative procedure while velocity fields are corrected with immersed boundary treatment (blue boxes) to find the optimization variables that yield velocity and material derivative distributions of minimum discrepancy with the PTV measurements (orange box).

Step 1: Solid boundary characterization.

In case of experimental campaigns composed of a FSI problem where a physical solid boundary is intruding the fluid domain, there exist two options for the determination of locations and surface contours of the solid object. For a vast majority of experimental campaigns, the solid object location and shape are known apriori since the experiment is planned accordingly including the object location, its aerodynamic form and various possible orientations with respect to the flow direction. Another approach recently being test over the course of this thesis project as well, is to provide simultaneous measurements of the solid boundary tracers in order to determine the location and shape of the structure interacting with the fluid. Considering the structural information is obtained by means of either one of the aforementioned approaches, the solid boundary surface is characterized by means of quadrilateral panels each equipped with singularity elements of sources and doublets to introduce a scalar potential influence of the physical intrusion.

Step 2: Surface singularity attachment and potential influence determination.

With the singularity elements attached to the solid boundary surface by means of quadrilateral panels, the scalar potentials induced by each source and doublet element are com-

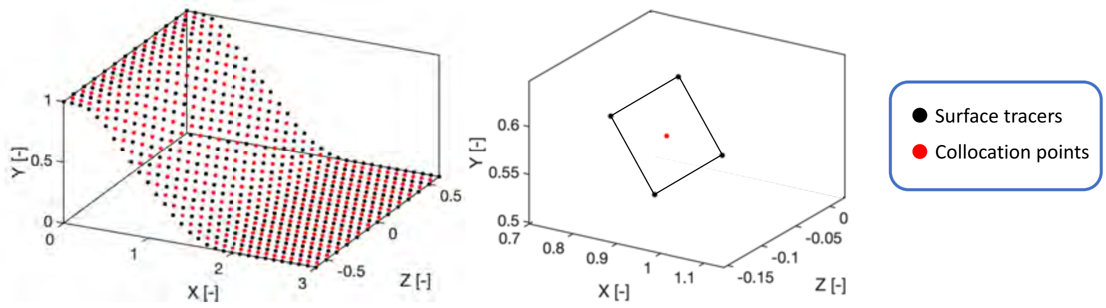

Figure 4.6: Surface description for the periodic hill structure with surface tracers indicated with black dots and collocation points with red dots for the corresponding quadrilateral panels.

puted both over the surface elements and the complete computational domain. Elaborating on the potential induced by a single surface element composed of a quadrilateral source and a quadrilateral doublet, the respective influences of both singularity components are computed via following the formulations of (Katz and Plotkin, 2001).

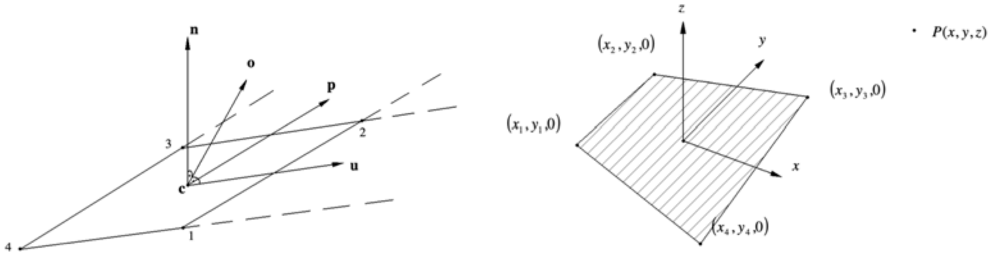

Figure 4.7: Coordinate system representation for the quadrilateral panel.

First of all, collocation point for the panel of interest is calculated at the central location of four points composing a quadrilateral surface,

$$c_x = \frac{x_1 + x_2 + x_3 + x_4}{4} \quad c_y = \frac{y_1 + y_2 + y_3 + y_4}{4} \quad c_z = \frac{z_1 + z_2 + z_3 + z_4}{4} \tag{4.14}$$

and the corresponding unit vectors for the panel surface are computed to generate a local coordinate system.

$$\begin{aligned} u_x &= \frac{x_1 + x_2 - (x_3 + x_4)}{2} \quad u_y = \frac{y_1 + y_2 - (y_3 + y_4)}{2} \quad u_z = \frac{x_1 + z_2 - (z_3 + z_4)}{2} \\ p_x &= \frac{x_3 + x_2 - (x_1 + x_4)}{2} \quad u_y = \frac{y_3 + y_2 - (y_1 + y_4)}{2} \quad p_z = \frac{x_3 + z_2 - (z_1 + z_4)}{2} \end{aligned} \tag{4.15}$$

then the final unit vector **o** is determined by the cross product of **n** and **u**. Proceeding the generation of a local coordinate system for the quadrilateral panel, the scalar potential induced by a constant source panel

$$\begin{aligned}\Phi = \frac{-\sigma}{4\pi}\Bigg[\Bigg(&\frac{(x-x_1)(y_2-y_1)-(y-y_1)(x_2-x_1)}{d_{12}} ln\frac{r_1+r_2+d_{12}}{r_1+r_2-d_{12}}+\\ &\frac{(x-x_2)(y_3-y_2)-(y-y_2)(x_3-x_2)}{d_23} ln\frac{r_2+r_3+d_{23}}{r_2+r_3-d_{23}}+\\ &\frac{(x-x_3)(y_4-y_3)-(y-y_3)(x_4-x_3)}{d_34} ln\frac{r_3+r_4+d_{34}}{r_2+r_3-d_{34}}+\\ &\frac{(x-x_4)(y_1-y_4)-(y-y_4)(x_1-x_4)}{d_41} ln\frac{r_4+r_1+d_{41}}{r_4+r_1-d_{41}}\Bigg)\\ &-\|z\|\Bigg(tan^{-1}\left(\frac{m_{12}e_1-h_1}{zr_1}\right)-tan^{-1}\left(\frac{m_{12}e_2-h_2}{zr_2}\right)+\\ &tan^{-1}\left(\frac{m_{23}e_2-h_2}{zr_2}\right)-tan^{-1}\left(\frac{m_{23}e_3-h_3}{zr_3}\right)+\\ &tan^{-1}\left(\frac{m_{34}e_3-h_3}{zr_3}\right)-tan^{-1}\left(\frac{m_{34}e_4-h_4}{zr_4}\right)+\\ &tan^{-1}\left(\frac{m_{41}e_4-h_4}{zr_4}\right)-tan^{-1}\left(\frac{m_{41}e_1-h_1}{zr_1}\right)\Bigg)\Bigg]\end{aligned} \tag{4.16}$$

and a quadrilateral dipole, whose equivalent is a vortex ring,

$$\begin{aligned}\Phi = \frac{\mu}{4\pi}\Bigg[&tan^{-1}\left(\frac{m_{12}e_1-h_1}{zr_1}\right)-tan^{-1}\left(\frac{m_{12}e_2-h_2}{zr_2}\right)+\\ &tan^{-1}\left(\frac{m_{23}e_2-h_2}{zr_2}\right)-tan^{-1}\left(\frac{m_{23}e_3-h_3}{zr_3}\right)+\\ &tan^{-1}\left(\frac{m_{34}e_3-h_3}{zr_3}\right)-tan^{-1}\left(\frac{m_{34}e_4-h_4}{zr_4}\right)+\\ &tan^{-1}\left(\frac{m_{41}e_4-h_4}{zr_4}\right)-tan^{-1}\left(\frac{m_{41}e_1-h_1}{zr_1}\right)\Bigg]\end{aligned} \tag{4.17}$$

at a point P of coordinates (x,y,z,) are computed following aforementioned equations where,

$$
\begin{aligned}
m_{12} = \frac{y_2 - y_1}{x_2 - x_1} \quad m_{23} = \frac{y_3 - y_2}{x_3 - x_2} \quad m_{34} = \frac{y_4 - y_3}{x_4 - x_3} \quad m_{41} = \frac{y_1 - y_4}{x_1 - x_4} \\
r_k = \sqrt{(x - x_k)^2 + (y - y_k)^2 + z^2} \quad k = 1, 2, 3, 4 \\
e_k = (x - x_k)^2 + z^2 \quad k = 1, 2, 3, 4 \\
h_k = (x - x_k)(y - y_k) \quad k = 1, 2, 3, 4
\end{aligned}
\tag{4.18}
$$

in which the parameters σ and μ refer to the strengths of sources and dipoles respectively whose values are to be determined according to the appropriate boundary conditions imposed over the solid boundary surface.

Step 3: Vortex-in-Cell method application for rotational component calculation.

The initial estimation for the velocity field information is provided in terms of a freestream velocity value which is composed of an irrotational component of vorticity absence. Hence, the computational grid locations are equipped with pointwise vortices of zero strength and the vorticity distribution over computational domain is utilized to compute the velocity distribution in accordance to the boundary conditions containing the freestream conditions for the velocity vector magnitudes using the Vortex-in-Cell method.

Step 4: Determination of potential flow component.

The calculated velocity field based on the initial estimation yields a flow field that penetrates through the physical intrusion surfaces for which a no-through boundary condition applies physically. Therefore, the normal velocity components for each panel are calculated via a dot product of the local velocity vectors with the surface normals and equated to the relative source strengths of the corresponding panels.

$$\sigma_i = \mathbf{n}_i \cdot \mathbf{V}_i \tag{4.19}$$

where i indicates the corresponding panel of interest. The reason for equating the source strengths to the normal velocity magnitudes is referred to the fact that for non-lifting flows especially, the wall penetration of the flow in counteracted directly by means of source elements and it allows to reduce the strengths of the dipoles for numerical uniqueness (Tarafder et al., 2010).

Furthermore, since the self induced scalar potential should vanish at collocation points over a surface of singularities (Lewis, 1991), the dipole strengths are calculated by constructing a linear system of equations that total sum of potential induction at the central locations of the quadrilateral panels equals to zero.

$$\sum_{i=1}^{N} a_i \mu_i + \sum_{i=1}^{N} b_i \sigma_i = 0 \tag{4.20}$$

where N represents to the total number of panels, a_i and b_i correspond to the influence coefficients of constant dipoles and sources at the panel i respectively. Even though, equating source strengths directly to the normal velocity magnitudes at each panel surface provides an elevated numerical uniqueness for the linear system, depending on the surface shape and flow state, there exists a possibility of singularity for the coefficient matrix. Hence, in order to guarantee solubility of the linear system of equations, two different physical conditions of Kutta condition (Houghton et al., 2017) and Kelvin's theorem of total circulation conservation (Panton, 2020) can be defined to confine the doublet strengths. In order to establish a higher level of genericity including both lifting and non-lifting flows, conservation of total circulation is utilized to drive the system to be overdetermined and imposes the corresponding vortex rings (dipoles) to comply with the conversation of circulation while their strengths are being determined. The corresponding overdetermined linear system is solved employing a least squares method (Soifer, 2013).

Step 5: Potential velocity component computation.

The determined strengths of the surface singularity elements are employed to compute the scalar potential field over the complete computational domain utilizing the influence coefficients computed at Step 2. The calculated scalar potential field is differentiated in all three dimensions to determine the corresponding velocity vector components.

$$u_\phi = \frac{\partial \phi}{\partial x} \quad v_\phi = \frac{\partial \phi}{\partial y} \quad w_\phi = \frac{\partial \phi}{\partial z} \tag{4.21}$$

Step 6: Resultant velocity and acceleration field determination.

The velocity fields of rotational and irrotational components are superimposed to calculate the resultant velocity field distributions.

$$\mathbf{u} = \mathbf{u}_\omega + \mathbf{u}_\phi \tag{4.22}$$

The corresponding velocity vorticity fields are utilized to calculate the material derivative distributions over the computational domain in accordance to the inviscid Navier-Stokes formulation.

Step 7: Cost function determination and optimization procedure.

The cost function for the optimization procedure is determined over the error accumulation of velocity and material acceleration values at the original particle track locations in comparison to the measured data. For the optimization procedure, it is assumed, due to the dependence of the potential flow component to the rotational elements, that the errors directly relate to the Vortex-in-Cell base which is dictated by the vorticity distributions. Hence, for each step of the optimization procedure, the gradient is calculated in terms of the vorticity strengths and the corresponding potential flow component is calculated to correct the velocity field distributions in order to satisfy the physical boundary condition of no penetration through the solid surfaces.

4.5 Solenoidal Basis Reconstruction of Dense Velocity Fields with Material Accelerations

Unlike the the Vortex-in-Cell model where the vorticity distribution is determined over a distribution of circulation strengths and the velocity field in computed using the Poisson equation, the velocity field is reconstructed by means of a divergence free matrix-valued radial basis function formulation. Hence, the optimization variables are assigned to be the RBF weights for the velocity distribution. The solenoidal basis reconstruction algorithm is christened as "Sol+" where the sign "+" refers to the fact that the material accelerations are also included over the momentum conservation equation to the optimization problem.

The framework of the dense flow field interpolation with solenoidal basis functions is constructed in the following manner.

Step 1: Matrix valued RBF computation for solenoidal basis.

The matrix-valued radial basis functions are computed using a scalar RBF of Gaussian type over the computational domain for the interpolation procedure.

$$\Phi(r) = [\nabla\nabla^T - \nabla^2\mathbf{I}]e^{-\frac{r^2}{2\sigma^2}} \tag{4.23}$$

where $r^2 = \|\mathbf{x}\|$ and σ refers to the global support for the Gaussian scalar radial basis function.

Step 2: Initial weight computation for solenoidal RBF interpolation.

The initial weights of the matrix-valued radial basis functions are determined from the initial condition for the velocity distribution either provided via a linear interpolation of the scattered measurement data or a predefined initial condition of freestream velocity value.

$$\mathbf{u} = \Phi\Gamma \tag{4.24}$$

Step 3: Velocity field reconstruction by solenoidal RBF interpolation.

The velocity distribution is computed using the solenoidal RBF interpolation over the computational domain. Hence complying with the density theorem of Lowitzsch (2005), the linear combination of arbitrary number of matrix-valued radial basis function which individually satisfy the divergence free condition, yields a solenoidal velocity field that provides consistent imposition of mass conservation throughout the optimization procedure.

$$\begin{pmatrix} u_1(\mathbf{x}) \\ u_2(\mathbf{x}) \\ u_3(\mathbf{x}) \end{pmatrix} = \sum_{i=1}^{m} \begin{bmatrix} \phi_{yy} + \phi_{zz} & -\phi_{xy} & -\phi_{xz} \\ -\phi_{xy} & \phi_{xx} + \phi_{zz} & -\phi_{yz} \\ -\phi_{xz} & -\phi_{yz} & \phi_{xx} + \phi_{yy} \end{bmatrix}_i \Gamma_i \tag{4.25}$$

where the velocity vector $\mathbf{u}$ is defined at an arbitrary point $\mathbf{x}$ and Γ_i corresponds to the radial basis function weights. ϕ refers to the scalar valued Gaussian radial basis function,

$$\phi = e^{-\frac{r^2}{2\sigma^2}} \tag{4.26}$$

Then the vorticity distribution is computed by applying the discrete curl operator to the velocity field using second order finite difference approximations for the velocity gradients.

Step 4: Material acceleration field reconstruction.

The local time derivative of vorticity is computed using the vorticity transport equation where the previously calculated velocity and vorticity fields are employed to compute its components, Eq.(2.13). Then, the local time derivative of velocity is computed similar to VIC+ procedure via applying the temporal derivation on both sides of the Poisson equation relating vorticity to velocity for which the resultant equation is solved with the Dirichlet boundary conditions at all faces. Then, the complete Lagrangian acceleration terms are obtained by combining the local time derivative component of velocity data with the convective terms of the velocity field, Eq.(2.14).

Step 5: Adjoint gradient computation for the optimization procedure.

For the optimization procedure to drive towards the experimental data of velocity and acceleration information, a gradient of the cost function J is required. As the optimization procedure is performed over a large number optimization variables, namely the particle strengths of the solenoidal velocity distribution, an efficient gradient computation procedure is required in order to maintain the computational resource requirements at acceptable levels. Therefore, the adjoint gradient procedure discretized within the VIC+ algorithm of Schneiders and Scarano (2016) is employed.

In terms of computing the adjoint gradient contribution of the solenoidal matrix valued radial basis functions, the self-adjoint definition of Hermitian matrices is used where a complex square matrix, in this case of a real square matrix since there is no imaginary part for the interpolator, that is equal to its conjugate transpose is referred as a Hermitian matrix, thus is self-adjoint (Frankel, 2004). Therefore, throughout the adjoint gradient comptutation, the direct gradient term for the particle strength vector is computed by applying the matrix operation of the solenoidal interpolation function to the penultimate gradient vector.

4.6 Solenoidal Basis Reconstruction of Dense Velocity Fields with Irrotational Material Accelerations

With regards to the formulation of inviscid Navier-Stokes equations, the Lagrangian acceleration terms are equal to the pressure gradients. Since the static pressure is a scalar variable, the vector identity of gradient of a scalar component refers to an irrotational

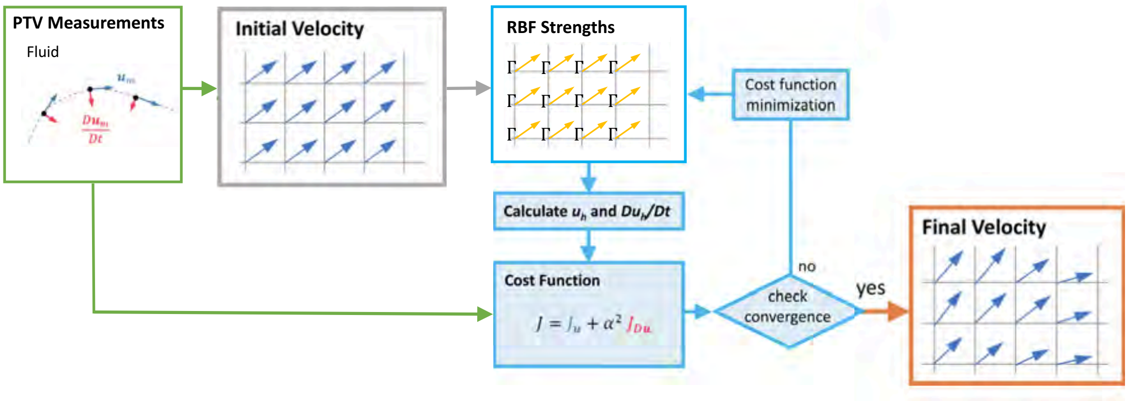

Figure 4.8: Sol+ reconstruction framework. The PTV measurements for the flow is provided (green box). An initial velocity estimate is made (gray box). The initial strengths for the vector valued divergence free radial basis functions are calculated where the resultant velocity fields is used as an input into the VIC+ iterative procedure (blue boxes) to find the optimization variables of vectorial velocity strengths that yield velocity and material derivative distributions of minimum discrepancy with the PTV measurements (orange box).

vector field. Therefore, the consistent formulation of NS equations demand the material acceleration vector field to be curl free. Therefore, acceleration fields computed with the elements of velocity and vorticity constructed by means of the steps introduced for Sol+, are regressed with an irrotational Gaussian basis to increase the mathematical coherence of the material acceleration terms with the flow governing equations. The addition of the irrotational Gaussian process regression over the Sol+ algorithm yielded the modified name of ”ISol+”.

4.6.1 Irrotational Gaussian Process Regression

Employing the Gaussian process regression approach introduced by Azijli and Dwight (2015) using solenoidal radial basis functions for cancellation of divergence errors accumulated within experimental data acquisition and processing techniques, the matrix valued radial basis function formulation is modified to yield a curl free structure. The resultant method is referred as the Irrotational Gaussian process regression (IGPR). IGPR is used to filter non-zero curl vector components on the material acceleration fields considering the contribution of the viscous terms are negligible in most practical applications where the fluid behavior is associated with turbulent flow features at relative high Reynolds number values.

$$\Phi(\mathbf{x}) = -\nabla\nabla^T \phi(\mathbf{x}) \tag{4.27}$$

Accordingly, the matrix-valued RBFs can be formulated in relation to the objective vector field. As demonstrated for the solenoidal reconstruction basis, the relevant treatment of scalar valued interpolation function can yield irrotational vector fields. Introduced by Fuselier and Wright (2015), the curl-free RBF interpolation is formulated by applying the divergence operator to the scalar valued RBF which results in a scalar interpolation field, then the gradient operator is applied to obtain the matrix-valued RBF with three dimensional vectorial components that construct an irrotational vector field. Hence, Eq.(4.27) determines an analytically irrotational vector field via the function weights in accordance to the density theorem of Lowitzsch (2005) which proves the reconstruction of a curl-free vector field by means of multiple curl-free vector fields.

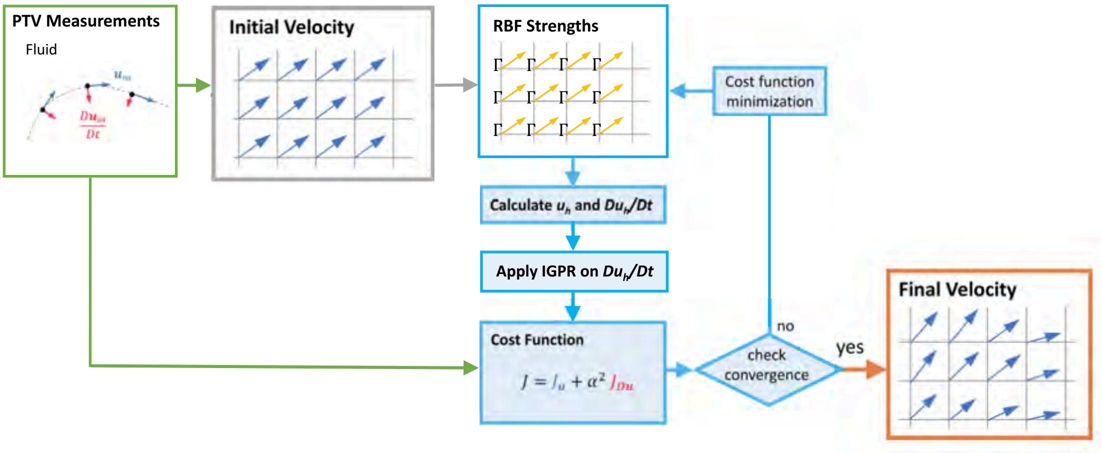

Figure 4.9: ISol+ reconstruction framework. The PTV measurements for the flow is provided (green box). An initial velocity estimate is made (gray box). The initial strengths for the vector valued divergence free radial basis functions are calculated where the resultant velocity fields is used as an input into the VIC+ iterative procedure (blue boxes) to find the optimization variables of vectorial velocity strengths that yield velocity and material derivative distributions of minimum discrepancy with the PTV measurements (orange box).

The numerical implementation procedure follows a similar approach to Sol+ where the only modification is made posterior to the material acceleration field computation. Hence, the corresponding adjoint gradient calculation procedure is modified accordingly.

Computation of Velocity and Material Acceleration Distribution

- Following the exact steps of Sol+ algorithm throughout the velocity calculation procedure from the solenoidal matrix valued radial basis functions, the resultant velocity field prior to the acceleration computation is ensured to be mass conservative.

- The correct vorticity field corresponding to the solenoidal velocity distribution is computed via applying the curl operator.

- The resultant velocity and vorticity fields are utilized over the vorticity transport equation to obtain local time derivative for vorticity evolution in time, which is used to construct the Poisson relation to be solved for local time derivative of velocity.

- As the convective and temporal terms for the material accelerations are computed using the available velocity and vorticity information, IGPR is applied on the resultant Lagrangian acceleration distribution to ensure of its irrotationality.

Computation of Adjoint Gradient

The adjoint gradient computation procedure is modified to include the IGPR method for the material acceleration field computation. The modified algorithm proceeds with the steps introduced for Sol+ exactly while only implementing the IGPR over the gradients computed for the material acceleration for their contribution to the optimization variables.

Chapter 5

Validation Studies

The performance specifications of the proposed algorithms of combining computational frameworks with experimental post processing procedures in Chapter 4 are characterized by means of various theoretical, numerical and experimental cases. First of all, DNS simulations of a well-developed turbulent channel flow is employed for the verification of the wall function implementation where a preliminary characterization of the base VIC+ algorithm is also performed without any modifications to the reference dataset towards stimulation of realistic large scale experimental conditions, Section 5.1. Then, DNS simulations of a flow over periodic hill case is utilized for the verification of both ALE-VIC+ and ImVIC+ methods in Section 5.2 and Section 5.3 respectively. Moreover, for the characterization of accuracy specifications of surface pressure reconstruction approach with boundary fitted coordinate systems, the exact fully 3D solutions for the unsteady incompressible Navier-Stokes equations defined by Ethier and Steinman (1994) are used where the uncertainty quantification is performed with Monte Carlo simulations (Metropolis and Ulam, 1949), Section 5.4. Finally, the comparative assessments of Sol+ and ISol+ algorithms with the present VIC+ method are established over a theoretical flow field of wave lattice forms and the experimental investigation of a transitional circular jet performed by Violato and Scarano (2011), Section 5.5.

5.1 Wall Function Approach for VIC+

The wall function approach for approximating the streamwise velocity component for the application of VIC+ procedure for the purpose of reconstructing time-resolved dense velocity and acceleration fields from scattered particle tracking data is validated over direct numerical simulations of a well-developed channel flow.

The DNS simulations for the well-developed channel flow is generated over a domain of $3 \times 2 \times 3\ h^3$ where h corresponds to the channel height. The inflow conditions are stated to compose of a non-dimensional velocity of $2/3$ at a Reynolds number of 2×10^5. The time step size is given as $\Delta t = 0.085$ in non-dimensional time units. The flow field information is extracted after the well-developed conditions for the turbulent boundary layers are established for which pressure gradients within the boundary layer where zero.

Table 5.1: Simulation and boundary layer parameters for the DNS simulation of well-developed channel flow.

Bulk flow velocity	u_{bulk}	2/3
Bulk Reynolds number	Re_{bulk}	20,000
Friction Reynolds number	Re_{τ}	550
Friction velocity	u_{τ}	0.0367

In order to provide an accurate representation of scattered particle track information the DNS results are randomly sampled with various concentrations (500 par/h^3, 1000 par/h^3 and 2000 par/h^3) of particles throughout the computational domain with respect to various concentration specifications employed for the initial validation studies of VIC+ (Schneiders and Scarano, 2016). Simulation of particle tracking velocimetry data structure of particle tracks providing Lagrangian flow information with velocity and material acceleration properties is achieved via a pseudo-particle tracking approach applied over the instantaneously extracted flow field data. The procedure is initiated with random downsampling of high density flow information of the DNS data field in accordance to the prescribed particle concentrations for a selected time instant. Then a Runge-Kutta 4 (Zheng and Zhang, 2017) time integration procedure is followed to compute the particle propagation in time for an interval of 2 time units where the first consecutive time instant is utilized as a intermediate step to increase the accuracy of the numerical integration processes. In order to minimize the truncation error propagation due to the numerical approximations, the integration procedure is applied in both forward and backward directions in time. In accordance to the preferred track lengths documented to yield accurate fluid properties for Shake-the-box algorithm, the tracks selected to be composed of 7 particles whose motion is reconstructed over 13 time instants centering the time instant of interest. Then the particle track locations are equiped with 0.2 voxels of Gaussian noise in all three dimensions to stimulate measurement and reconstruction errors. Finally, the corresponding particle tracks are normalized with polynomials of order 2 to compute velocity and material acceleration properties. Moreover, in order to account the fact that presence of particles in the near wall region is a rare situation, particles within the close proximity of the wall are removed from the analyzed data sets wit $y^+ \sim$50 considered to be the threshold for track removal, Fig.5.1.

Each individual case of particle densities are reconstructed with VIC+ using various grid spacing specifications according to the relative track concentrations available in the computational domain. Three main interpolation approaches are evaluated in comparison to each other. The AGW and trilinear interpolation methods are initially performed both to provide a baseline of reconstruction improvements as well as for boundary condition determination. Secondly, VIC+ is applied considering the full computational domain starting from the exact wall surface, hence the velocity values comply with the no-slip boundary condition at the wall locations. Finally, the available particle track information is binned in order to capture flow physics independent of any possible errors linear interpolation introduces which is used as the input of wall function approach. Thus, the computational domain is displaced in the wall-normal direction with $y^+ \sim$20 and the

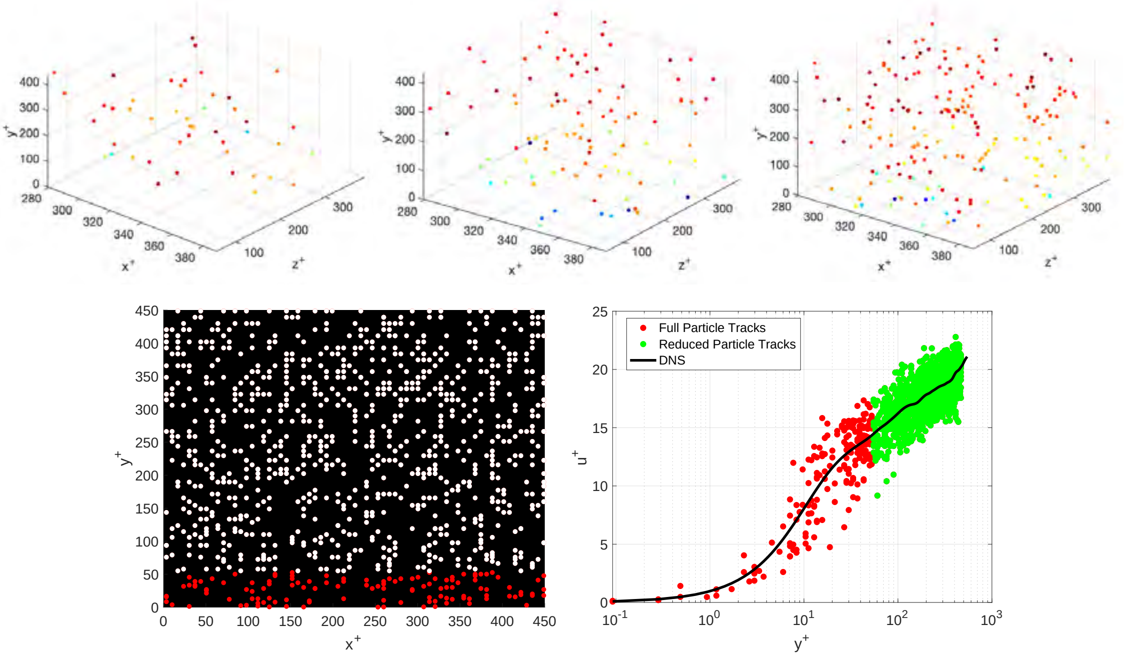

Figure 5.1: Downsampled particle tracks with concentrations of 500 par/h^3 (top-left), 1000 par/h^3 (top-middle) and 2000 par/h^3 (top-right) colored with the non-dimensional streamwise velocity, u^+. Particle distribution of available tracks (white) and removed tracks (red) at C= 2000 par/h^3 (bottom-left). Particle distributions of full and reduced particle tracks along the wall-normal direction, plotted with averaged DNS streamwise velocity profile (bottom-right).

boundary condition for the streamwise velocity component is obtained from the reconstructed local log law profile following the aforementioned procedure. Finally, proceeding the application of the VIC+ algorithm, the resultant velocity field information is utilized to reconstruct the streamwise velocity profiles throughout the viscous and buffer layers of the TBL structure.

The results of these different approaches are compared in terms of instantaneous streamwise vorticity fields as well as the spatial statistics of velocity profiles in comparison to the reference DNS data. As an initial demonstration of VIC+'s capability for dense reconstruction of flow field information, it is applied directly to the downsampled scattered DNS data at different particle concentrations without performing any of the aforementioned manipulations for realistic measurement stimulation.

According to the well-developed turbulent boundary conditions established within the channel walls the vortical structures observed for the reference DNS solution reveal a forest of hairpin vortices that form arch-like structures in the outer layer as the large vortical structures shed by unstable streaks disturb the containment of quasi-streamwise vortices in the near-wall region. The resultant flow behavior is characterized by the reorganization of near-wall streaks with the pattern of well-known wall turbulent of vortex streak appearances with a spacing of $y^+ \sim 100$ non-dimensional wall units, (Eitel-Amor et al., 2014). The computational domain for the VIC+ application is selected to be constructed around a near-wall vortex streak located at Z/h=0.35 (illustrated with $\omega_x =$

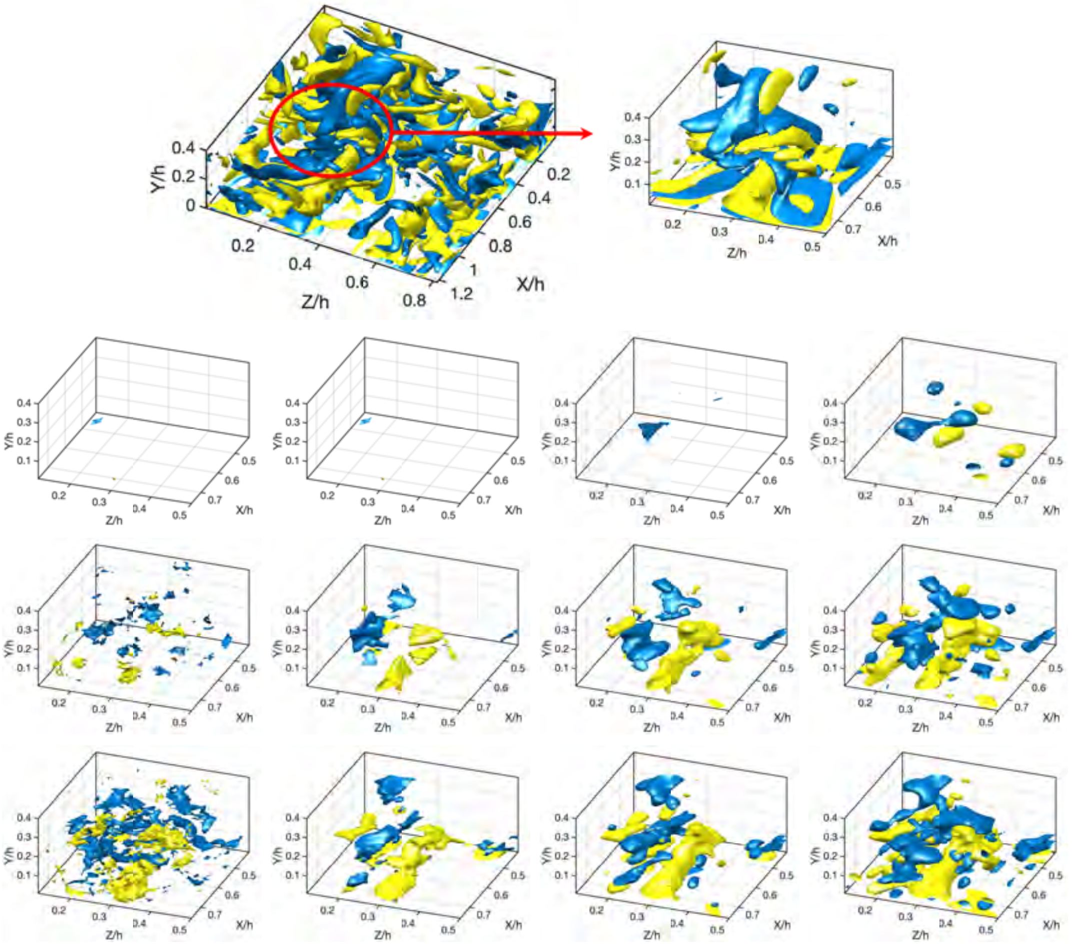

Figure 5.2: Instantaneous non-dimensional streamwise vorticity profiles of ω_x = -2.5 (blue) and ω_x = 2.5 (yellow) with reference DNS results (top), AGW (1^{st} column), trilinear interpolation (2^{nd} column), VIC (3^{rd} column) and VIC+ (4^{th} column) with C= 500par/h^3 (1^{st} row), C= 1000 par/h^3 (2^{nd} row) and C= 2000 par/h^3 (3^{rd} row).

2.5, yellow) where the roll up hairpin vortices are illustrated with both vorticity isosurface levels of $\omega_x = 2.5$ (yellow) and $\omega_x = -2.5$ (blue).

As demonstrated by the vorticity distributions over the computational domain (Fig.5.2) and the velocity profiles for mean and fluctuating velocity components (Fig.5.3), the application of VIC+ elevates the accuracy of the dense reconstruction of velocity fields using flow governing equations to approach to the objective of measured data information establishing a greater level of correlation with the physical features of the flow while increasing the spatial resolution characteristics of the instantaneous flow field. For the low concentration case of C= 500 par/h^3, the AGW, linear interpolation and VIC completely fails to capture any of the vorticity features represented for the reference solution of the DNS simulations while application of VIC+ enables the reconstruction of local vorticity presence even though their resemblance to the physical flow behavior is barely acknowledged. Nevertheless, as the particle concentration is increased, the agreement of both the linearly interpolated and VIC+ applied initial low resolution data with the reference field is increased since it provided more particles to approach to the reference case in terms of shorter distances for linear interpolation and in terms of greater number of optimization objectives driving the VIC+ procedure closer to the resultant flow fields.

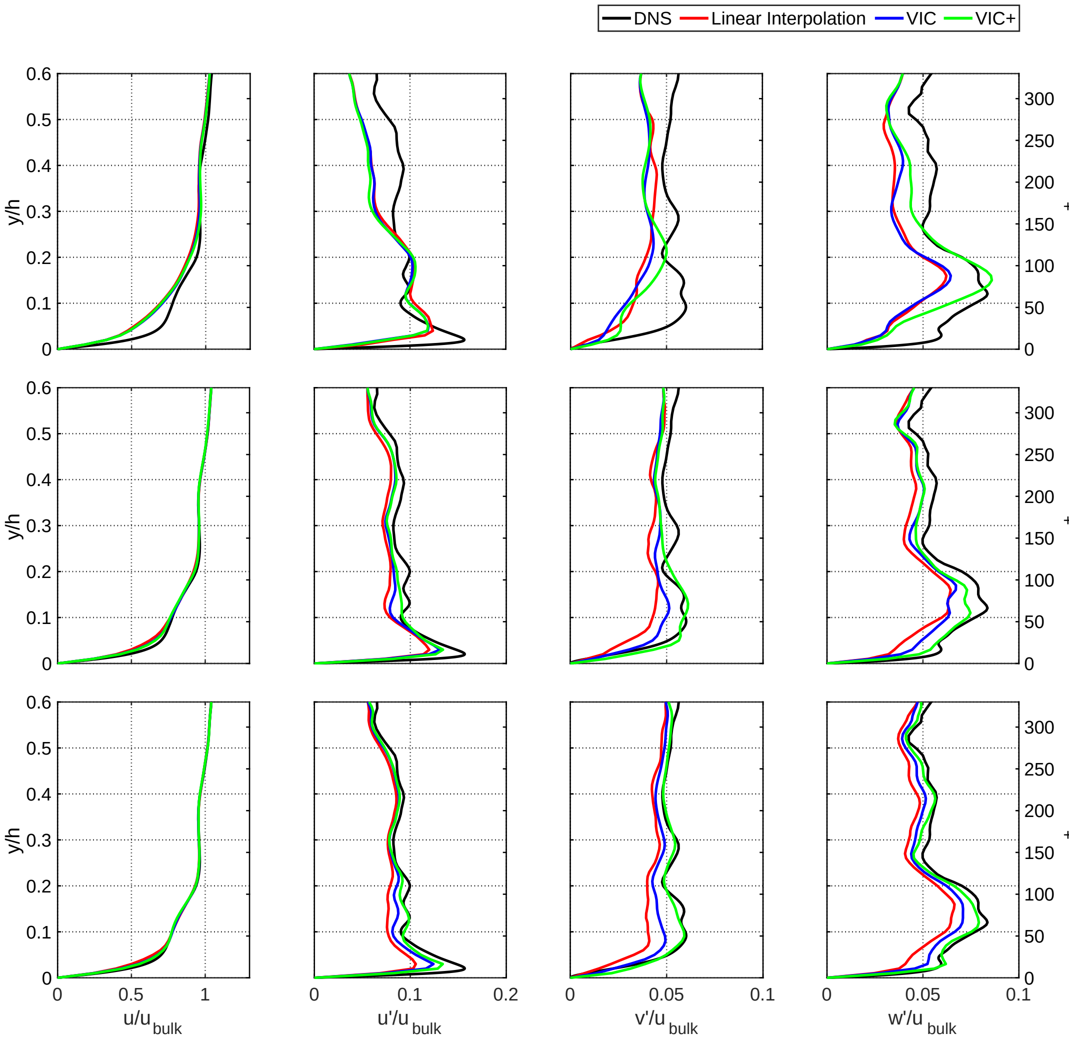

Figure 5.3: Profiles of mean streamwise and fluctuating velocity components reconstructed with reference DNS, linear interpolation, VIC and VIC+ over particle concentrations of with C= 500 par/h^3 (1st row), C= 1000 par/h^3 (2nd row) and C= 2000 par/h^3 (3rd row).

Similarly, the boundary layer velocity profiles relate to the comparative accuracy characteristics of VIC+ against the aforementioned set of interpolation methods. While the lowest particle track density over the prescribed computational domain yielded similar profiles fluctuating velocity components for all reconstruction approaches with inadequate levels of agreements with the reference profiles, increasing particle concentrations revealed the superiority of VIC+ for enabling the resolution of instantaneous flow features especially for the secondary flow structures in comparison to VIC. Finally, in terms of the spanwise average of streamwise velocity profiles, small improvements obtained with the application of VIC+ whereas VIC and linear interpolation yielded similar accuracy specifications, Fig.5.3.

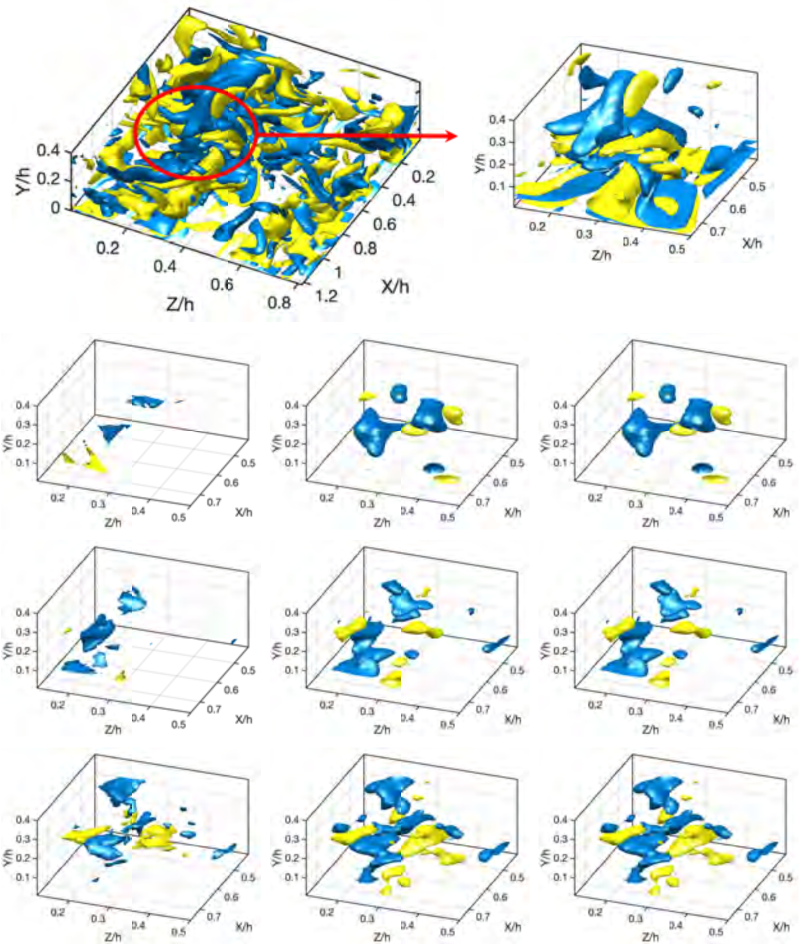

Figure 5.4: Instantaneous non-dimensional streamwise vorticity profiles of ω_x = -2.5 (blue) and ω_x = 2.5 (yellow) with reference DNS results (top), trilinear interpolation (1^{st} column), VIC+ no-slip BC (2^{nd} column) and VIC+ with wall function application (3^{rd} column) with C= 500 par/h^3 (1^{st} row), C= 1000 par/h^3 (2^{nd} row) and C= 2000 par/h^3 (3^{rd} row).

For the cases that necessitate the employment of wall function approach for velocity boundary condition approximation due to the absence of particles close to wall, there exists a clear underestimation of the velocity magnitudes below the threshold of y^+ ~50 where the particles from the downsampled reference data set are removed, Fig.5.20. This is due to two main reasons. First of all, the velocity profiles within the viscous sublayer represent a linear relationship between u^+ and y^+. As the normal distance to the wall is increased the relation transitions towards a logarithmic one over the buffer layer. Therefore, when the linear interpolation of scattered particle information is performed on the structured computational domain providing the information of a non-slip boundary at the wall surface, the linear interpolation in the region of absence of particles causes the velocity profiles fall short of the actual flow velocities. Moreover, the absence of any particles within that regions leaves the optimization procedure absent of any objective measurement information for which the VIC+ algorithm cannot define a suitable gradient to modify the vorticity distribution accordingly, Fig.5.4. Even though, the Gaussian distribution of radial basis function weights for pointwise circulation strength definition encapsulate more than one neighboring points for its modification throughout the optimization cycle, the scaling of its relative influence with the distance to a error definition location is considerable small to perform necessary modifications on the radial basis function weights to capture the physical flow behavior. Hence, the initially provided velocity profiles remain mostly unchanged which reveals the deteriorated velocity profiles reconstructed by the linear interpolations to persist even when the VIC+ is applied.

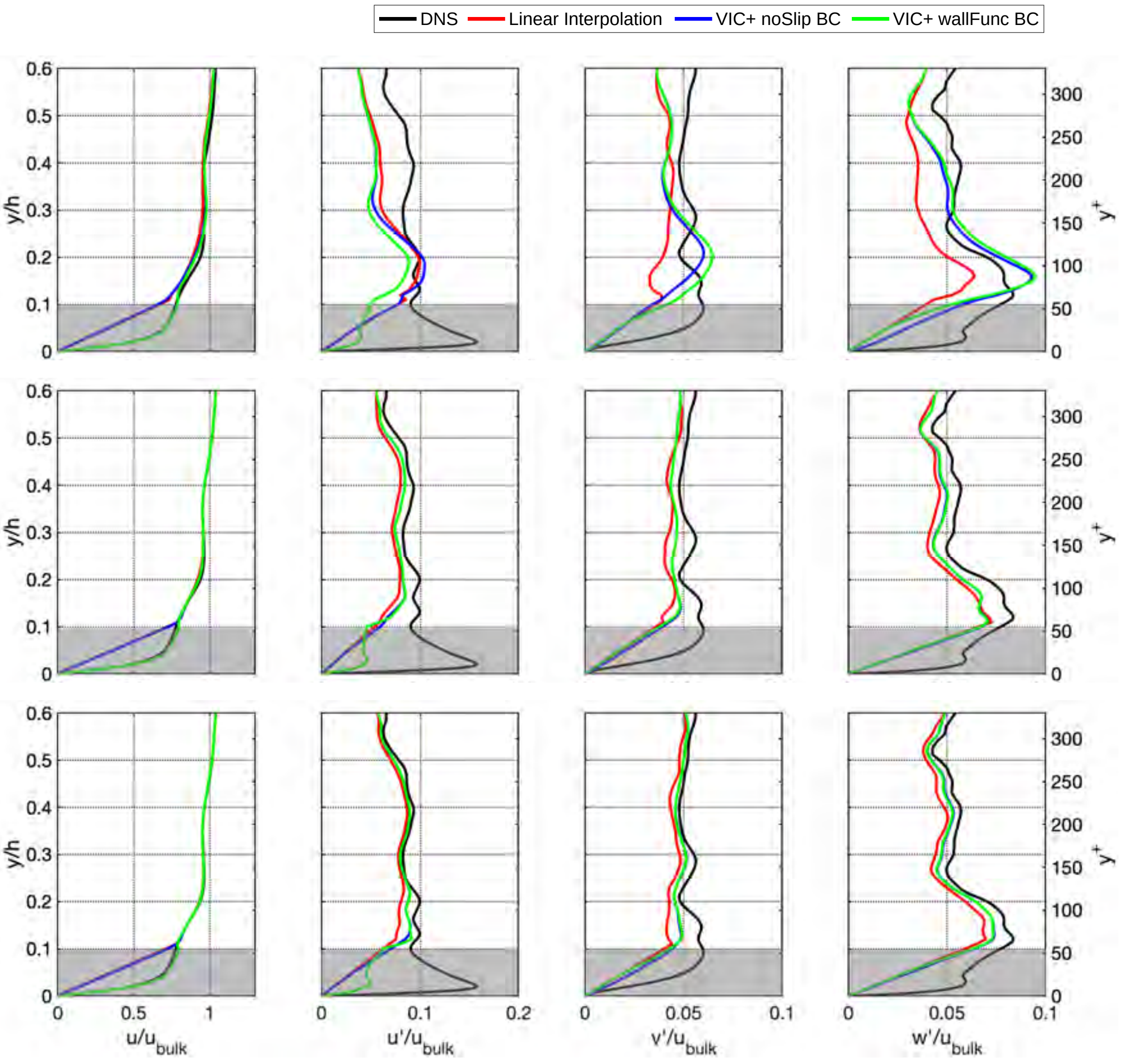

Figure 5.5: Profiles of mean streamwise and fluctuating velocity components reconstructed with reference DNS, linear interpolation, VIC+ no-slip BC and VIC+ wall function application over particle concentrations of with C= 500 par/h^3 (1^{st} row), C= 1000 par/h^3 (2^{nd} row) and C= 2000 par/h^3 (3^{rd} row).

Utilizing the wall function approach implementation for VIC+ enabled proper characterization of the unresolved regions of viscous and buffer layers, due to the aforementioned reasons of invalidity of adapted flow governing equations and absence of particle tracks.

As the local velocity profiles for the turbulent boundary layer specification captured via binning the available particle information are used to compute the skin friction coefficients for the logarithmic law equations, the spanwise average of streamwise velocity profiles are reconstructed with a great agreement to the reference velocity profiles in comparison to the standard VIC+ method. However, owing to the fact that the *Law of the wall* provides an universal representation for the turbulent boundary layer profiles of average streamwise velocity specifications, fluctuating components revealed significantly low magnitudes to meet the reference profiles although the logarithmic profiles are computed locally in the wall normal direction. Nevertheless, a slightly improved fluctuation profiles are attained over the sublayers with the wall function implementation in terms of the streamwise velocity, as the interpolations for sublayer velocity profile reconstruction utilized available particle information above $y^+ \sim 50$ whereas for the standard algorithm of VIC+ with the application of no-slip boundary condition at the exact wall location a retarded velocity variation from the surface to the first particle available region is caused by the smooth gradients of velocity variation in absence of any objective variables.

Furthermore, due to the fact that the wall function application only handles the streamwise velocity components as boundary conditions while the spanwise and normal velocity components are computed based on the same linear interpolation used for the no-slip boundary condition implementation, the spatially averaged fluctuation levels yield similar profiles to the with the VIC+ results of no-slip boundary condition. The major difference is observed below 0.4 with which the computational domain of the wall function applied VIC+ is displaced. Hence, whilst the VIC+ with no-slip boundary condition included that region within the computational grid of the VIC+ which slightly modifies the velocity values of the secondary components according to the viscosity transport equation, for the case of the VIC+ with wall function application that region is filled proceeding the VIC+ application using linear interpolations in terms of the secondary velocity components between the initial layer of the computational grid and the no-slip boundary of the wall surface. Thus, this linear interpolation introduces a slight underestimation of those velocity components compared to the full computational grid including the exact wall surface for the VIC+ with no-slip boundary condition.

5.2 Arbitrary Lagrangian-Eulerian Method for VIC+

Validation studies of the proposed ALE-VIC+ method are performed with a direct numerical simulation (DNS) of flow over periodic hills. The simulations are conducted with a computational domain composed of two consecutive hill forms connected over a region of 144 h^3, where h represents the non-dimensional heights of the hills. Hence, the length dimensions of the domain in Cartesian coordinates are provided over normalized values with h. The numerical simulations are performed with periodic boundary conditions connecting the inflow and outflow boundary conditions while the non-uniform surface contours of the hills are treated by means of an immersed boundary method to account for their influence over the fluidic domain (Chen et al., 2014). The inflow conditions are adjusted with a non-dimensional initial velocity distribution of $u = 1$ which corresponds to a hill height based Reynolds number of $Re_h = 10,595$ as the non-dimensional kinematic viscosity is prescribed to be $\nu = 9,45 \times 10^{-5}$.

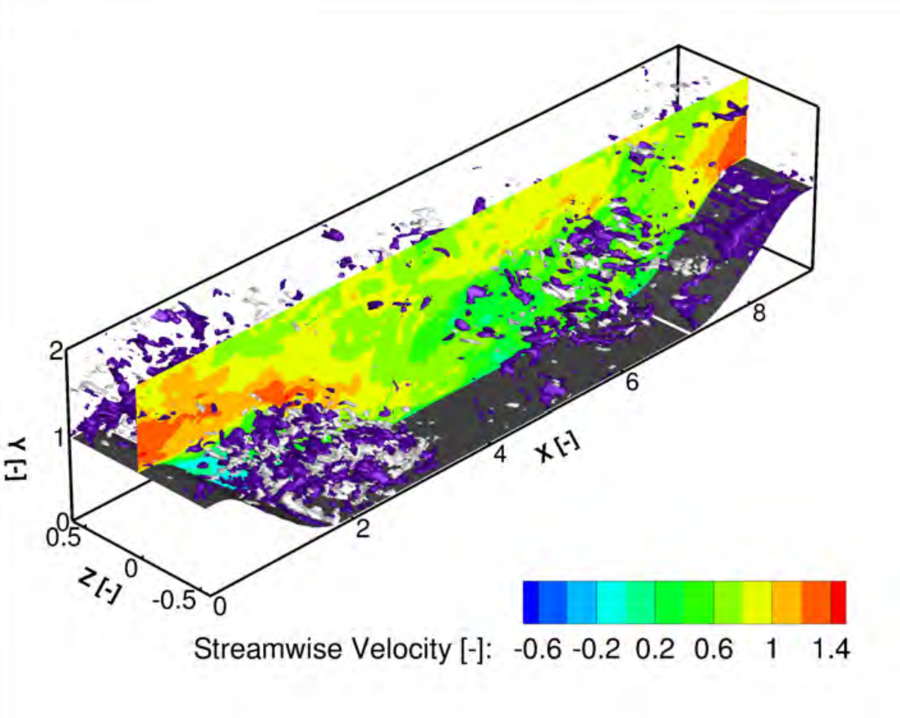

Figure 5.6: Instantaneous non-dimensional streamwise vorticity profiles of ω_x = -10 (purple) and ω_x = 10 (white) with non-dimensional streamwise velocity distribution over Z=0 plane for reference DNS results.

In order to simulate the PTV data structure for the validation dataset, the previously employed pseudo-particle tracking approach for the DNS simulations of the well-developed channel flow case is utilized. Concentration specifications for the downsampling of DNS data is determined in accordance to the experimental measurement campaigns performed for a case of turbulent boundary layer interaction with unsteadily deforming membrane, Chapter 6. The ALE-VIC+ method is initially applied over the central region of the DNS computational domain, Fig.5.6, in absence of any hill structures to enable a comparison with the original VIC+ algorithm. Hence, the vectorial transformations and mathematical formulations of the flow governing equations are verified with a rectangular computational grid structure where the conformal mapping do not necessitate curvilinear mesh formations. Furthermore, the comparisons performed for the velocity magnitude distributions of streamwise, spanwise and normal components with the DNS results also included the statistical data processing approaches of AGW and trilinear interpolation. Then, the computational domains prescribed for the aforementioned data assimilation approaches are modified to include the upstream hill structure so that the ALE-VIC+ method is utilized for dense flow field interpolation in regions where flow interaction with a non-uniform surface occurs.

The spatial resolution for the dense flow field reconstruction procedures are selected to have compatible grid spacing specifications with the DNS simulations for which the AGW failed to provide almost any fluidic information due to the lack of particles to be binned for each grid location. Hence, a clear view of the raw available particle tracking information and the corresponding need for a interpolation approach is provided. The

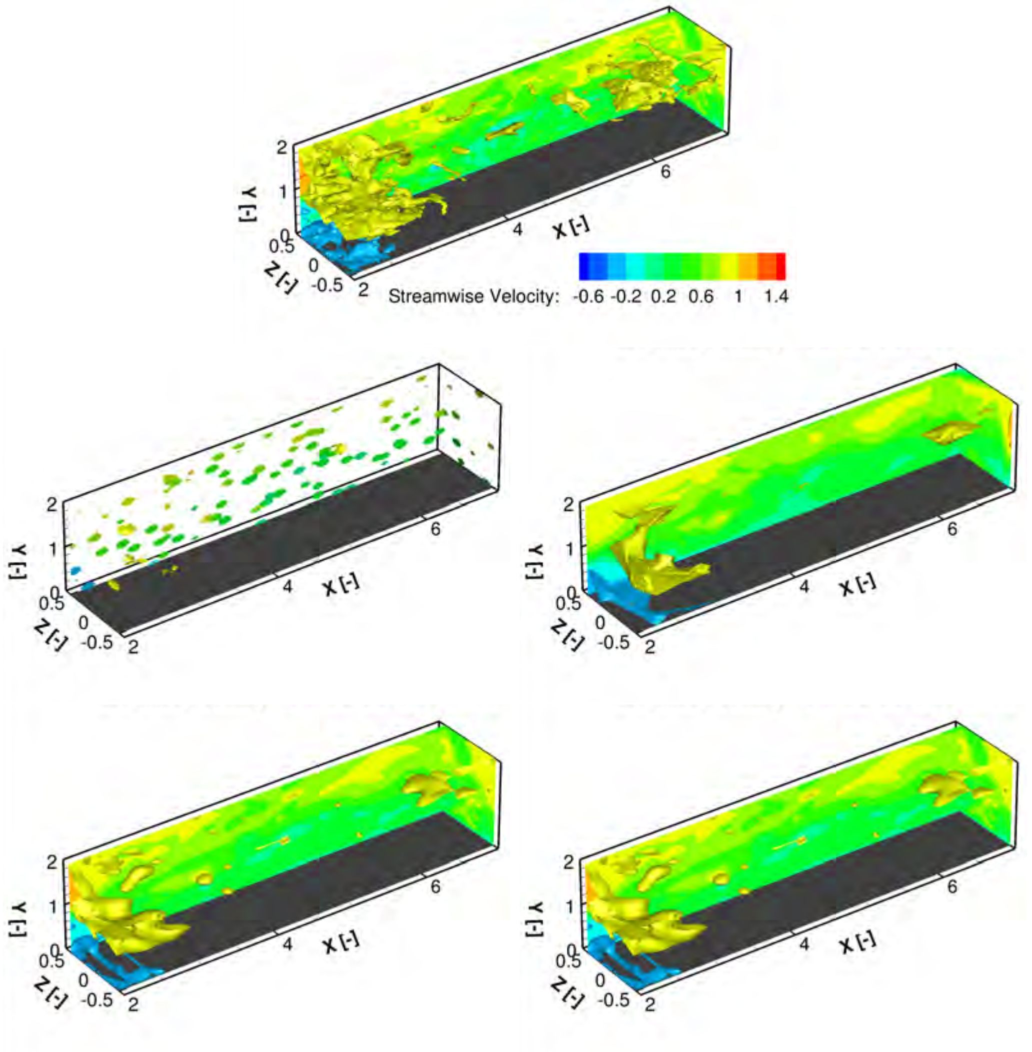

Figure 5.7: Non-dimensional streamwise velocity profiles with planar distributions over the streamwise and spanwise planes of Z=0.5 and X=7 respectively, and isosurfaces of u=1 (yellow) and u=-0.2 (blue) with reference DNS (top), AGW(middle-left), linear interpolation (middle-right), VIC+ (bottom-left) and ALE-VIC+ (bottom-right).

initial comparisons of VIC+ based approaches against the linear interpolation revealed similar profiles of differences for all three velocity components between the two methods, Fig.5.7, Fig.5.8 and Fig.5.9. First of all, both linear interpolation and VIC+ based methods adequately provide coherent information of the instantaneous structures with respect to the reference simulations in an overall sense where the high and low velocity magnitude regions can be identified. Nevertheless, the major improvements obtained with VIC+ based approaches are identified as the detailed flow structures are resolved with greater agreements to the reference solution compared to the linear interpolation.

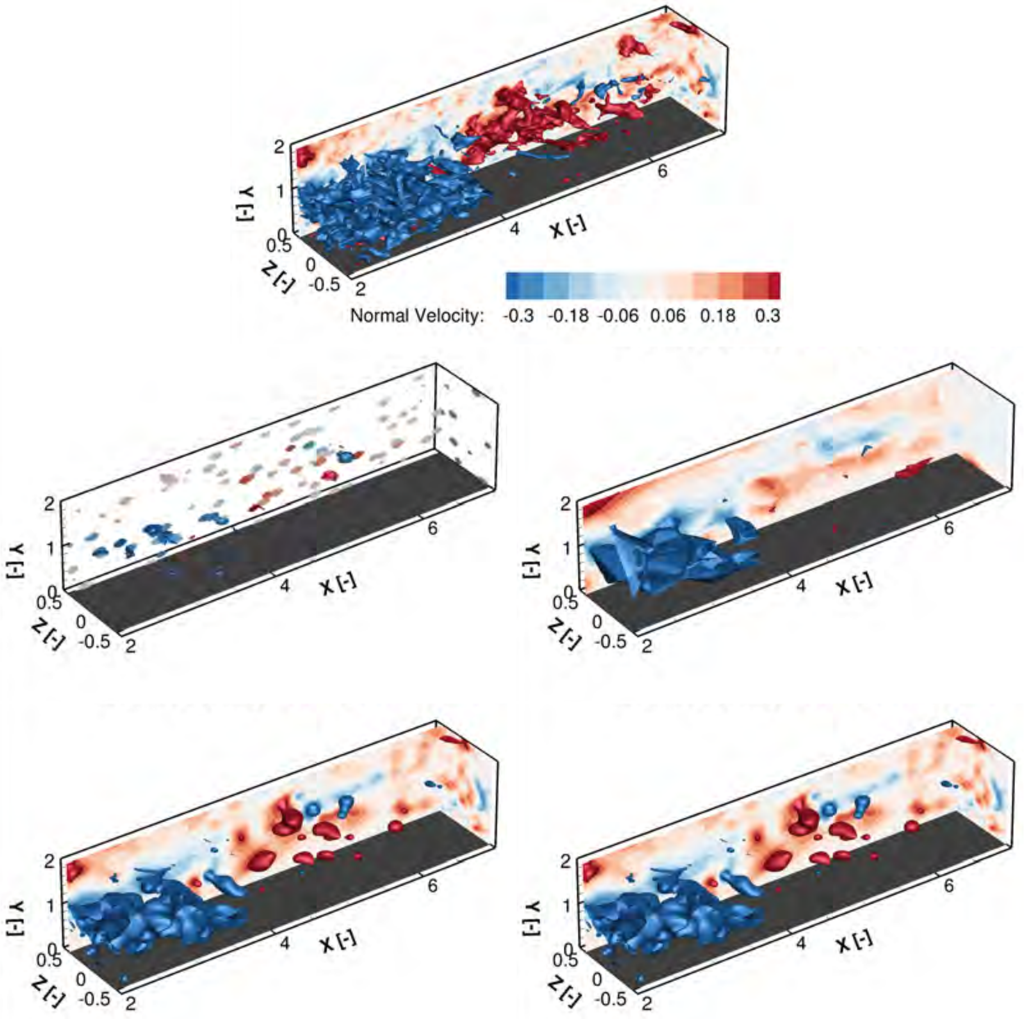

Figure 5.8: Non-dimensional normal velocity profiles with planar distributions over the streamwise and spanwise planes of Z=0.5 and X=7 respectively, and isosurfaces of v=0.3 (red) and v=-0.3 (blue) with reference DNS (top), AGW (middle-left), linear interpolation (middle-right), VIC+ (bottom-left) and ALE-VIC+ (bottom-right).

In that regards, the dominant flow behavior in the streamwise direction characterized by means of an accelerating fluid motion over the hills and a separation region downstream of the first hill structure. In terms of analyzing the streamwise velocity magnitude distribution over the computational domain, a high momentum region closer to the upper boundary due to the accelerations are observed. The recirculating flow features yield a low speed region downstream of the first hill which is recovered to the velocity magnitude levels of $u = 0.7$ for the streamwise component as the flow reattachment takes place at X/h ~4. Owing to these deterministic characteristics of the streamwise flow behavior, identification of instantaneously fluctuating components of the flow is rather challenging where the observed differences between linear interpolation and VIC+ based methods are considerably small, Fig. 5.10.

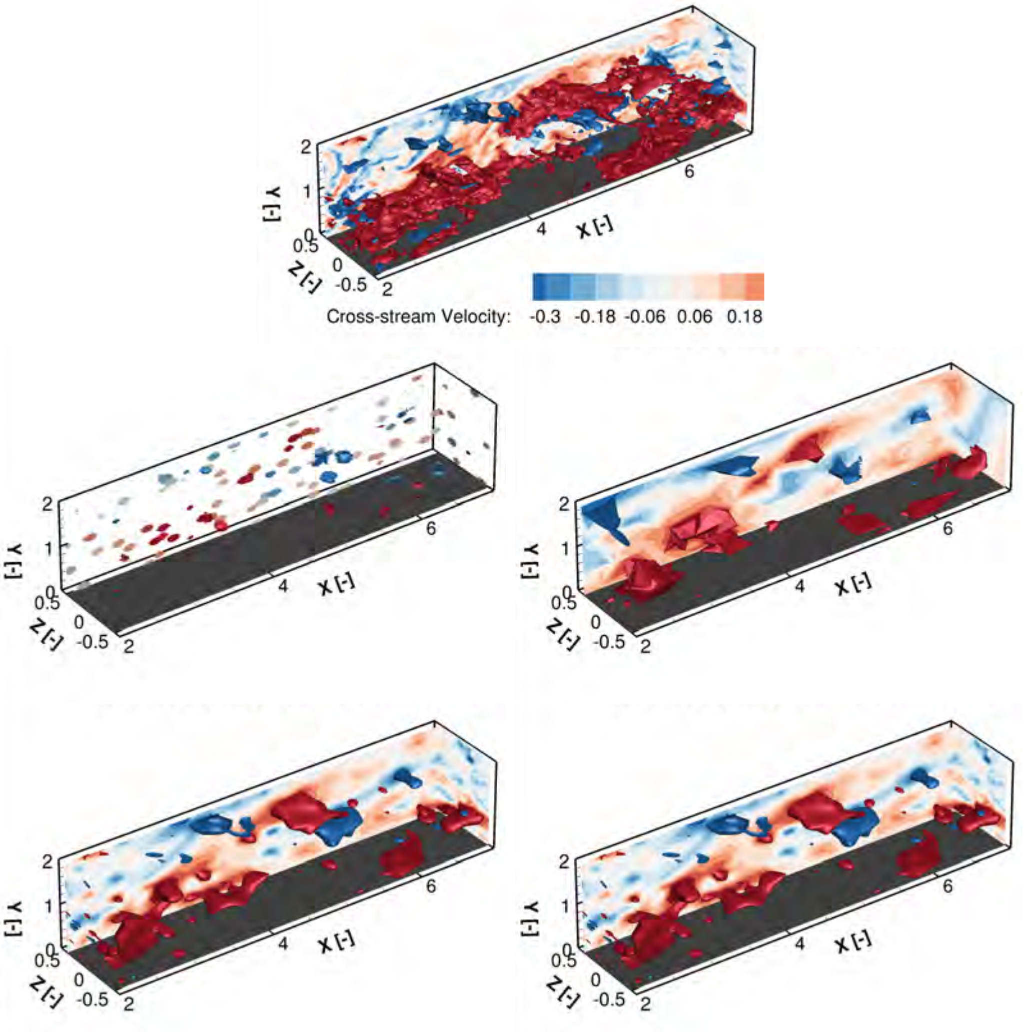

Figure 5.9: Non-dimensional spanwise velocity profiles with planar distributions over the streamwise and spanwise planes of Z=0.5 and X=7 respectively, and isosurfaces of w=0.3 (red) and w=-0.3 (blue) with reference DNS (top), AGW (middle-left), linear interpolation (middle-right), VIC+ (bottom-left) and ALE-VIC+ (bottom-right).

Nevertheless, the overestimation and underestimation errors captured for the planar distribution of streamwise velocity magnitudes over the central streamwise plane ($Z/h=0$) using linear interpolation correspond to larger regions of the local disagreements with reference results compared to VIC+ based approaches, Fig. 5.11. Furthermore, normal and spanwise velocity components providing a clear representation of the instantaneous fluid behavior demonstrate the accuracy improvements achieved by the application of VIC+ based methods where local peaks of low and high velocity magnitudes are resolved with considerably elevated agreement levels to the reference simulations. The global error levels documented in terms of the RMS of absolute velocity magnitude errors refer to the accuracy superiority of VIC+ based approaches against linear interpolation for high resolution flow field reconstruction, Tab.5.2.

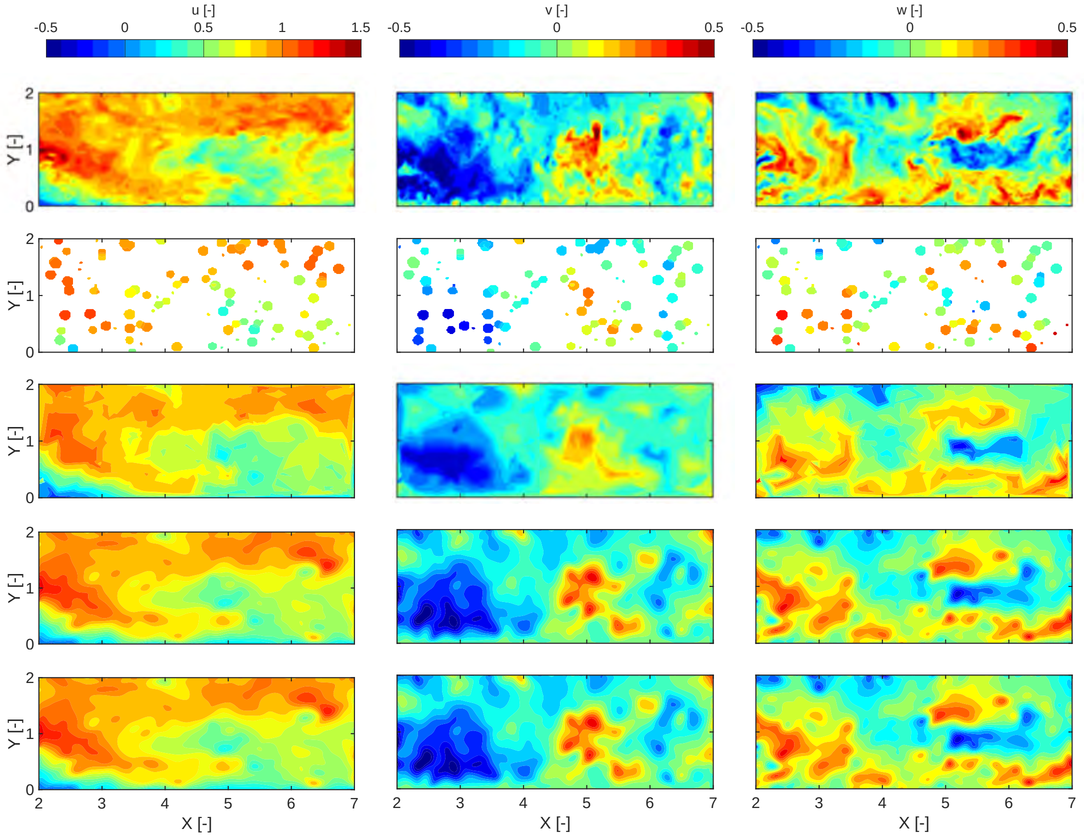

Figure 5.10: Planar distributions of non-dimensional streamwise (left), normal (middle) and spanwise (right) velocity magnitudes at Z=0, with reference DNS (1^{st} row), AGW (2^{nd} row), linear interpolation (3^{rd} row), VIC+ (4^{th} row) and ALE-VIC+ (5^{th} row).

Furthermore, the central region of the computational domain is enclosed with a flat wall boundary which allows the VIC+ to operate with proper boundary condition definitions. Hence, the verification of the mathematical formulations for vectorial transformations of flow variables and mathematical operators for boundary fitted coordinate systems employed for the ALE-VIC+ algorithm can take place to confirm its compatibility with the VIC+ framework. Accordingly, the transformation matrices for the boundary fitted coordinates correspond to identity matrices canceling all the cross derivatives referred for the mapping relation between the computational and physical coordinate systems. In other words, for a case of uniform boundaries the computational and physical coordinate systems become identical so does the algorithms of VIC+ and ALE-VIC+. Thus, the identical results of ALE-VIC+ and VIC+ demonstrated over the velocity magnitude and corresponding error distributions confirm the verification of mathematical formulations employed for the numerical discretizations of governing equations on boundary fitted coordinates., Fig. 5.11.

The ALE-VIC+ variant enables the standard VIC+ method to handle unsteadily deforming non-uniform surfaces by means of generating boundary fitted coordinate systems and, solving the flow governing equations utilizing mapping relations between the computational and physical coordinate systems. Although the periodic hill case employed

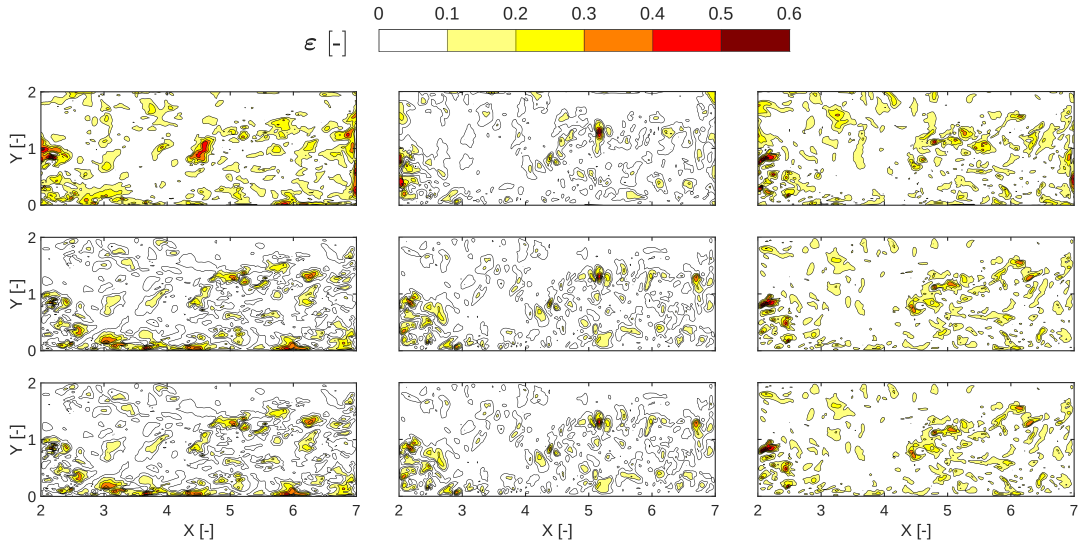

Figure 5.11: Planar distributions for absolute velocity error magnitudes of non-dimensional streamwise (left), normal (middle) and spanwise (right) velocity components at Z=0, with linear interpolation (1^{st} row), VIC+ (2^{nd} row) and ALE-VIC+ (3^{rd} row).

Table 5.2: RMS of absolue velocity magnitude errors with linear interpolation, VIC+ and ALE-VIC+ over the central region of the periodic hill structures.

	ε_u [-]	ε_v [-]	ε_w [-]
Linear Interpolation	0.16	0.12	0.13
VIC+	0.09	0.08	0.09
ALE-VIC+	0.09	0.08	0.09

for the validation studies does not contain any unsteady deformations, it provides a well-suited case study for the boundary fitted application of VIC+ framework. Therefore, the computational domain composed of the two hill form wall structure is cropped to include only the upstream hill to generate a boundary fitted coordinate structure and proceed with the proposed ALE-VIC+ method. In order to increase the resemblance of the grid generation procedure to the post-processing approach followed for the experimental campaign, the boundary fitted grid structure is generated by means of radial basis function interpolations considering a case of surface deformations starting from a rectangular uniform computational domain. Hence, the surface information referring to the coordinates of the hill form are provided to the mesh deformation algorithm and the corresponding curvilinear grid is obtained with the RBF based mesh motion algorithm.

Both linear interpolation and ALE-VIC+ are able to yield physically coherent structures compared to the reference results of the DNS simulation Fig.5.12, Fig.5.13 and Fig.5.14. Previously denoted dominant flow behavior apparent for the streamwise velocity magnitude distributions are accurately depicted as high speed flow elements are concentrated over the hill structure and separated low momentum region is located downstream of the hill. The major differences between the linear interpolation and ALE-VIC+

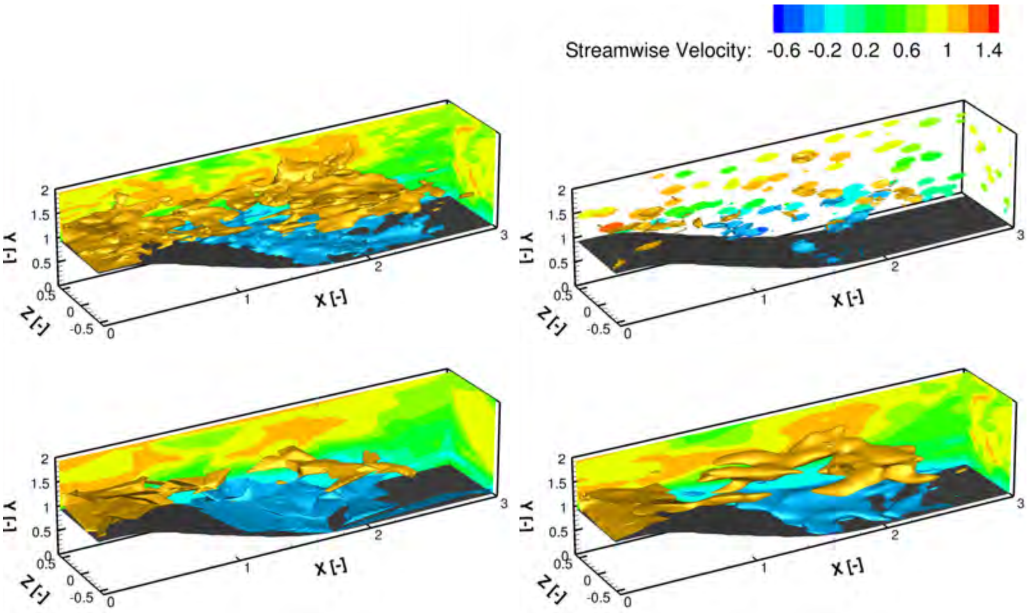

Figure 5.12: Non-dimensional streamwise velocity profiles with planar distributions over the streamwise and spanwise planes of Z=0.5 and X=7 respectively, and isosurfaces of u=1 (yellow) and u=-0.2 (blue) with reference DNS (top-left), AGW (top-right), linear interpolation (bottom-left) and ALE-VIC+ (bottom-right).

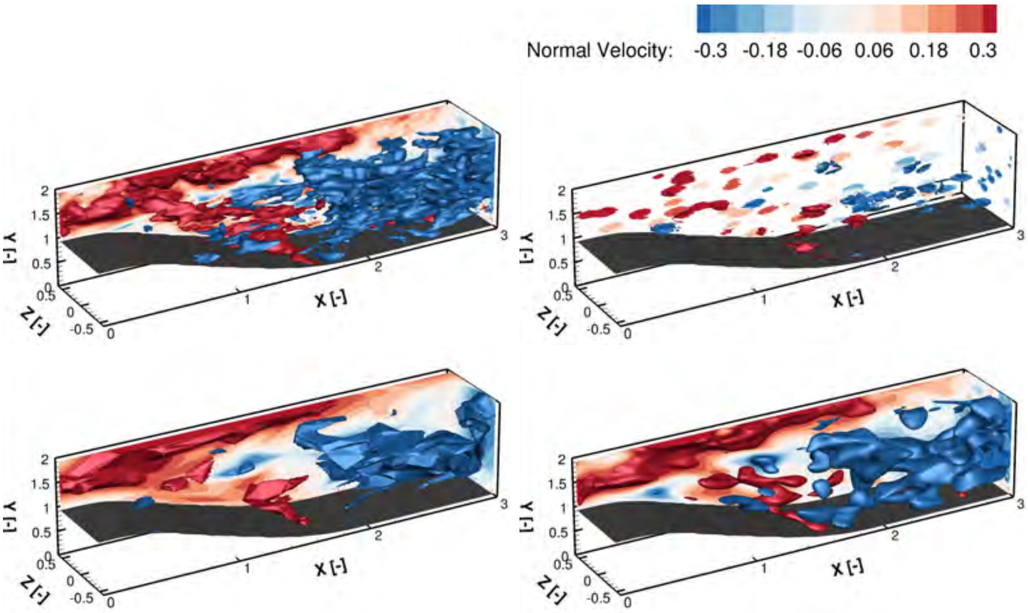

Figure 5.13: Non-dimensional normal velocity profiles with planar distributions over the streamwise and spanwise planes of Z=0.5 and X=7 respectively, and isosurfaces of v=0.3 (red) and v=-0.3 (blue) with reference DNS (top-left), AGW (top-right), linear interpolation (bottom-left) and ALE-VIC+ (bottom-right).

are observed over the local variations of velocity components, Fig.5.15. The lower order of planar variation for the secondary velocity component magnitudes demonstrated the

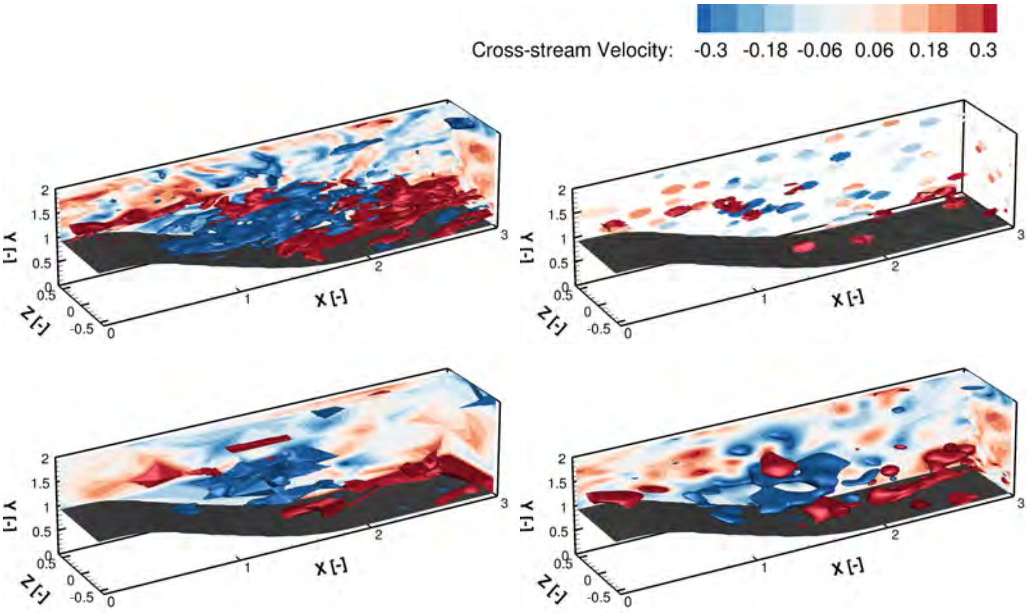

Figure 5.14: Non-dimensional spanwise velocity profiles with planar distributions over the streamwise and spanwise planes of Z=0.5 and X=7 respectively, and isosurfaces of w=0.3 (red) and w=-0.3 (blue) with reference DNS (top-left), AGW (top-right), linear interpolation (bottom-left) and ALE-VIC+ (bottom-right).

accuracy superiority of ALE-VIC+ over the linear interpolation. The peak fluctuation magnitudes are resolved with a greater agreement to the reference simulations by employing ALE-VIC+ whereas the independency of linear interpolation from the relevant flow physics caused overshoots and undershoots throughout the computational domain as observed for the analysis performed in absence of hill forms, Fig.5.21. The global error levels computed for the dense reconstruction of flow variables in terms of the velocity magnitudes further elaborated the improved accuracy levels obtained with the application of ALE-VIC+ compared to linear interpolation, Tab.5.3. Moreover, the planar error distributions of individual velocity components extracted in close proximity of the hill surface also demonstrated the lower orders of error magnitudes for the detailed flow structures resolved by means of the ALE-VIC+ approach, Fig.5.17 where the significance of employing the ALE-VIC+ method is identified by not only its ability to enable the VIC+ framework to be employed for non-uniform surface intrusions but also its capability to increase the physical flow coherence in near wall regions that corresponds the fluid-structure interaction interface.

Table 5.3: RMS of absolue velocity magnitude errors with linear interpolation and ALE-VIC+ over the upwind hill form of the periodic hill structure.

	ε_u [-]	ε_v [-]	ε_w [-]
Linear Interpolation	0.19	0.13	0.14
ALE-VIC+	0.11	0.10	0.11

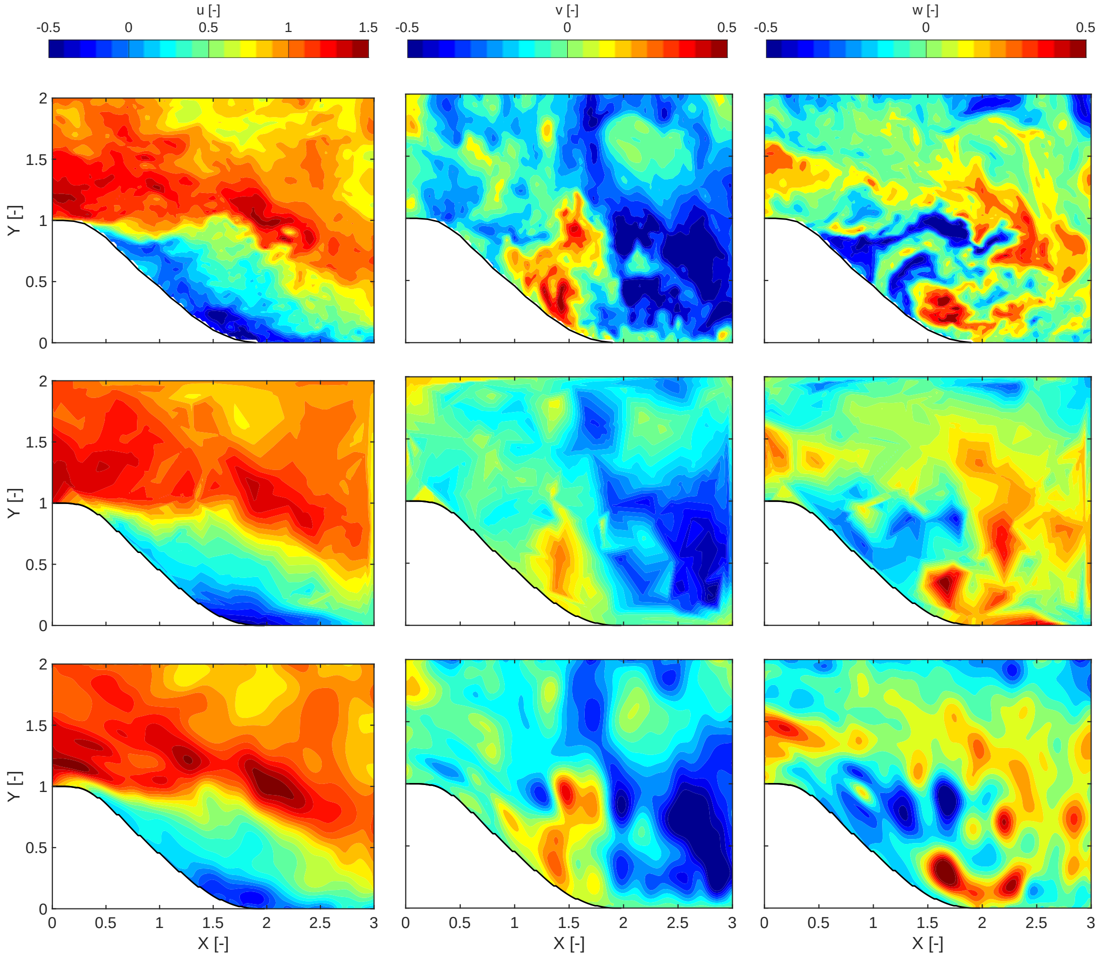

Figure 5.15: Planar distributions of non-dimensional streamwise (left), normal (middle) and spanwise (right) velocity magnitudes at Z=0, with reference DNS (1^{st} row), linear interpolation (2^{nd} row) and ALE-VIC+ (3^{rd} row).

5.3 Immersed Boundary Treatment for VIC+

Validation studies of ImVIC+ method for providing the base algorithm of VIC+ with the capabilities of handling unsteadily deforming non-uniform surfaces without introducing any mesh modifications are performed also over the DNS of flow over periodic hill case. Specifications of the numerical simulations and the corresponding post processing application for experimental data stimulation are provided in Section 5.2 where the particle track concentrations are determined in at the same order chosen for ALE-VIC+ according to the experimental campaign conducted. The comparisons performed with the velocity magnitude distributions of the DNS results including the statistical data processing approaches of AGW and trilinear interpolation as well as the standard VIC+ method quantifying the necessity of ImVIC+ for the case study of interest.

Obviously the initial comparisons of the velocity magnitude distributions reveal similar results in terms of the overall coherence characteristics for both linear interpolation and VIC+ based approaches as denoted previously where both methods identify the re-

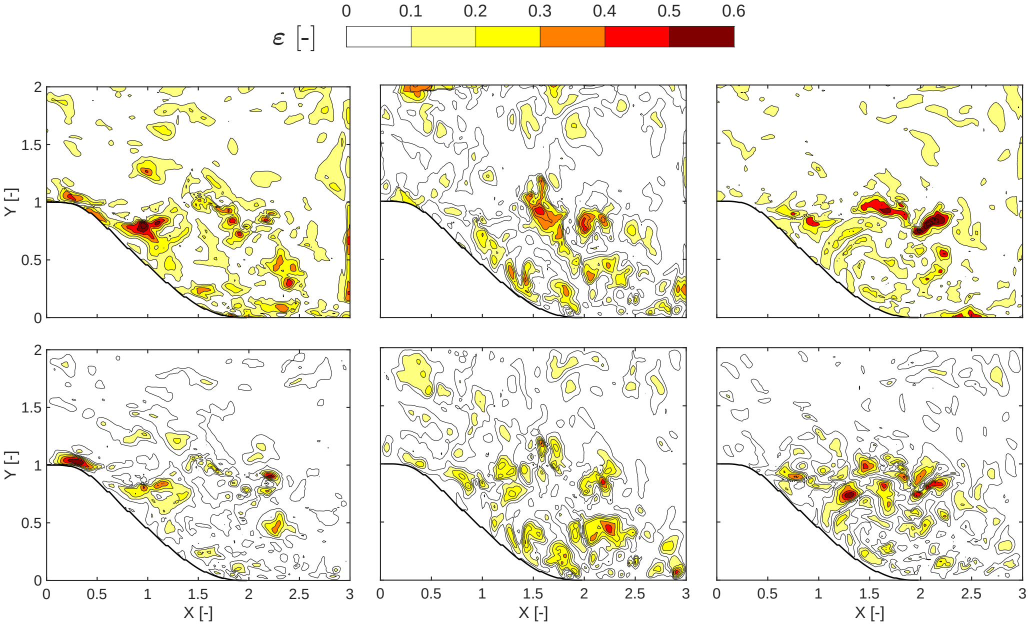

Figure 5.16: Planar distributions for absolute velocity error magnitudes of non-dimensional streamwise (left), normal (middle) and spanwise (right) velocity components at Z=0, with linear interpolation (1^{st} row) and ALE-VIC+ (2^{nd} row).

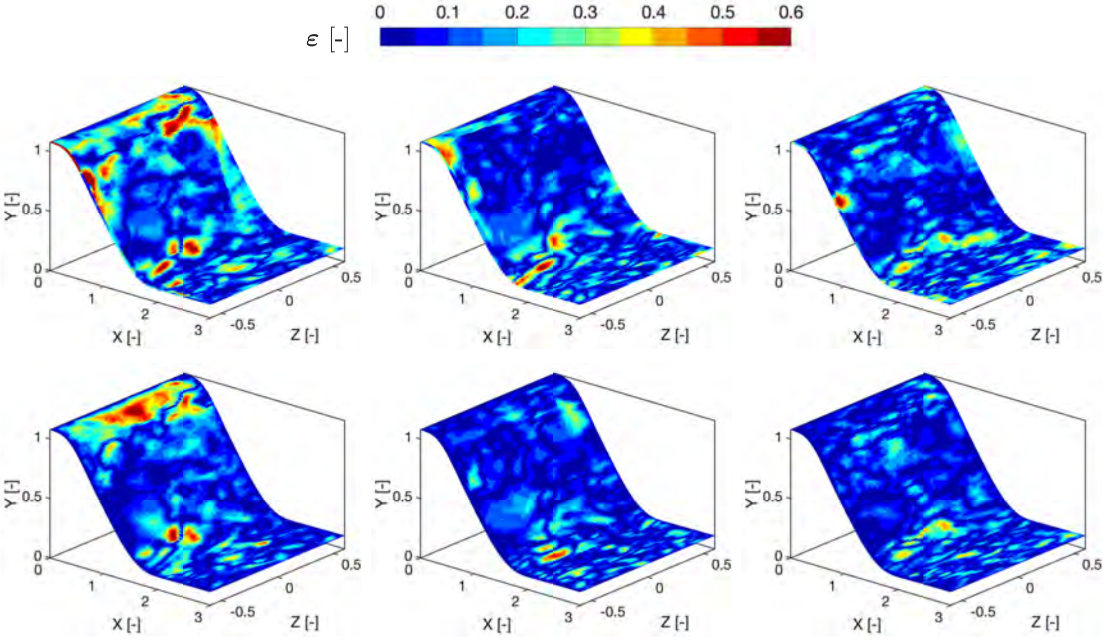

Figure 5.17: Planar distributions for absolute velocity error magnitudes of non-dimensional streamwise (left), normal (middle) and spanwise (right) velocity components at close proximity of the hill surface, with linear interpolation (1^{st} row) and ALE-VIC+ (2^{nd} row).

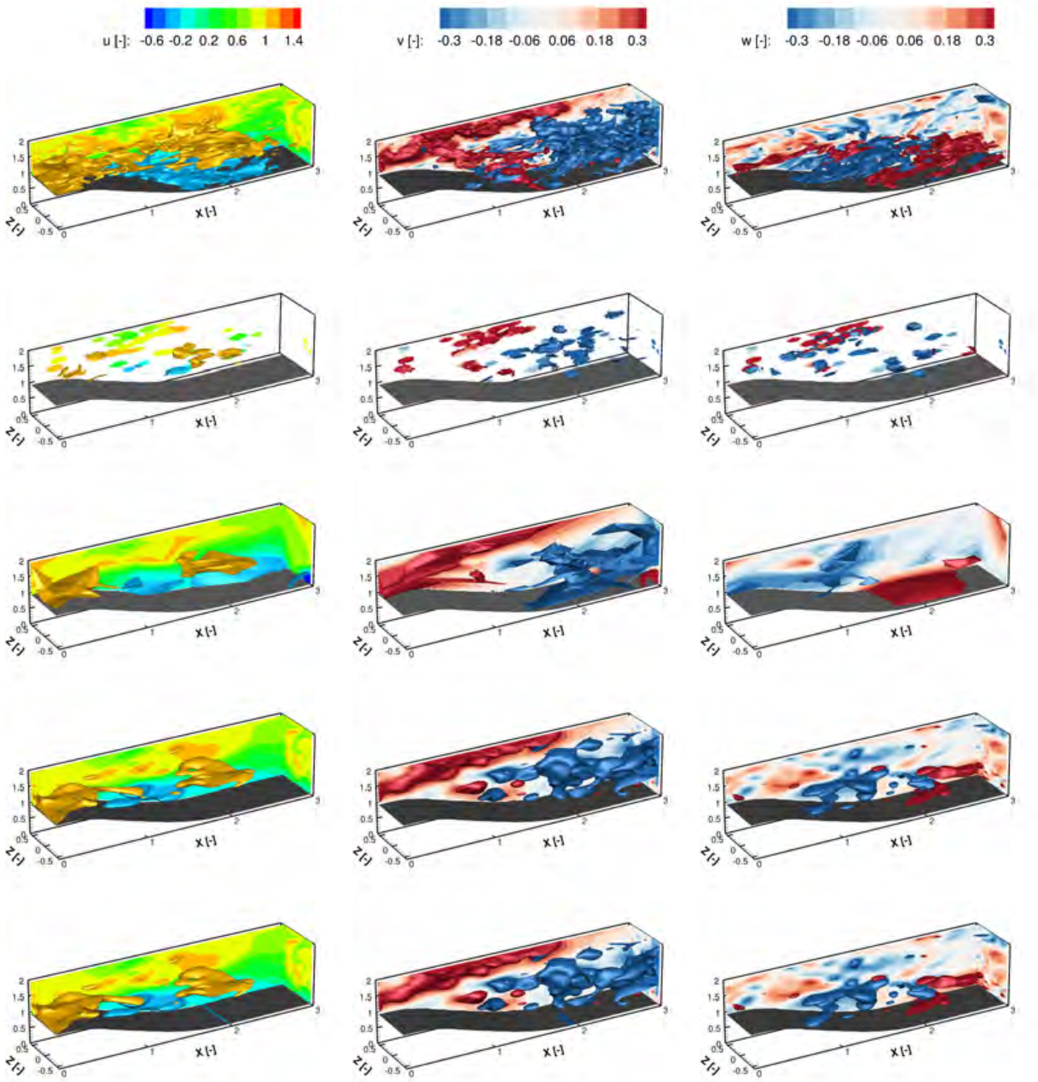

Figure 5.18: Non-dimensional distributions of streamwise (left), normal (middle) and spanwise (right) with reference DNS (1^{st} row), AGW (2^{nd} row), linear interpolation (3^{rd} row), VIC+ (4^{th} row) and ImVIC+ (5^{th} row).

gions of high and low velocity magnitudes in relation to the reference simulations, Fig.5.18. Accordingly, the reconstructed streamwise velocity distributions using both approaches reveal accelerated flow behavior over the hill form and separation regions with recirculatory flow characteristics downstream of the hill. Nevertheless, the detailed flow structures of local high and low velocity magnitude variations are depicted with increased accuracy using the VIC+ based methods as the separation effects are captured with greater agreement to the reference solution due to the governing equation based formulations. Furthermore, the superiority of VIC+ variants becomes even more apparent when the comparisons are performed over the secondary velocity components of normal and spanwise flow elements. In absence of a dominant flow behavior enforced by the immersed boundary forms, reconstructions of secondary flow structures represent the ability of VIC+ based approaches to resolve the fluidic behavior with greater detail as well as preventing overestimation and underestimation errors by means of appropriate boundary condition definition, which is physically accurate for both VIC+ and ImVIC+ beyond X>2, Fig.5.19.

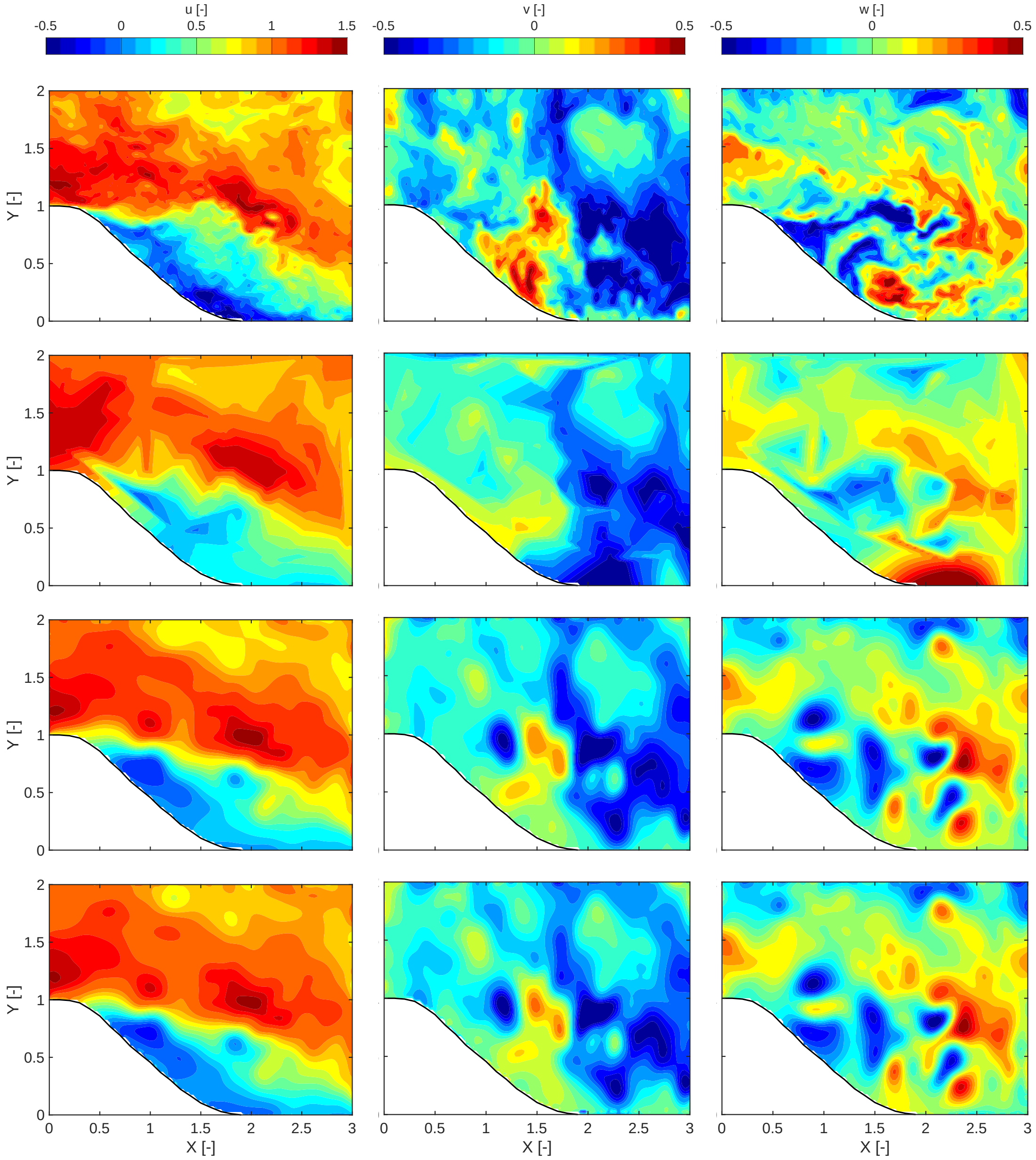

Figure 5.19: Planar distributions of non-dimensional streamwise (left), normal (middle) and spanwise (right) velocity magnitudes at Z=0, with reference DNS (1^{st} row), linear interpolation (2^{nd} row), VIC+ (3^{rd} row) and ImVIC+ (4^{th} row).

Analyzing the influence of the immersed boundary treatment implementation for VIC+ in terms of providing the necessary corrections to the flow properties by imposing no-through boundary condition over the hill surface, it is observed that the corrections provided by the ImVIC+ over the standard VIC+ algorithm are significantly small, Fig.5.19. Considering the orientation of the surface elements for the hill form and the corresponding normal vector directions, there are two velocity components of the flow motion that induce penetration of fluid particles through the hill surface. Although the dominant flow component causing the fluid motion to pass through the boundaries of the hill can be considered as the streamwise velocity vectors, due to their relative magnitudes compared to the normal velocity components, the contribution of normal velocity fluctuations to the total velocity magnitudes penetrating the solid boundaries cannot be overseen. Accordingly, the application of ImVIC+ provides modifications to the flow properties in terms of the magnitudes of both streamwise and normal velocity components that allow the reconstructed flow field properties to approach to the reference simulation results with greater accuracy compared to VIC+, Fig.5.19. In that regards, an increased streamwise flow speed over the top section of the hill and a decreased flow speed at the end of the hill where captured, referring to an elevated level of agreement with the reference DNS data. Moreover, since the spanwise velocity components do not affect the satisfaction of no through boundary condition, the resultant superimposition of potential and rotational flow field characterizations impose any alterations on the spanwise velocity magnitudes which can be depicted when compared to the results of VIC+, Fig.5.19.

Table 5.4: RMS of absolue velocity magnitude errors for linear interpolation, VIC+ and ImVIC+.

	ε_u [-]	ε_v [-]	ε_w [-]
Linear Interpolation	0.25	0.17	0.17
VIC+	0.14	0.12	0.12
ImVIC+	0.13	0.11	0.12

Analyzing through the error distributions of velocity magnitudes, the dominant effect of the immersed boundary treatment is observed for the streamwise velocity components where decreased error levels in close proximity of the periodic hill surface refer to an elevated level of accuracy over the VIC+ application without the immersed boundary treatment, Fig.5.21. Nonetheless, mitigation of error levels observed for the normal velocity components over the error distributions extracted in close proximity of the hill surface denote the necessary moditifications implemented by the ImVIC+ tend to approach the resultant flow field reconstructions to the reference simulations, Fig.5.21. The differences observed over the error distributions tend to decrease significantly in regions away from the hill surface which is consistent with the theoretical formulations of surface singularities where the influence of singularity elements decay with the Euclidean distance, Fig.5.21.

Even though, the modulations achieved on the dense flow field reconstruction with ImVIC+ observed to be relatively mild, this is due to the proximity of the periodic hill structure to the computational domain boundaries as well as the potential component of the flow to be inferior to the turbulent structures represented by means of the rotational component over the Helmholtz decomposition owing to the separation effects downstream of the hill. Accordingly, the corrections induced for the secondary flow structures of normal and spanwise flow components is relatively small, where slight modulations in close proximity of the surface are observed for the surface normal flow elements to satisfy the no-through boundary condition. Similarly, the effect of these modulations dimin-

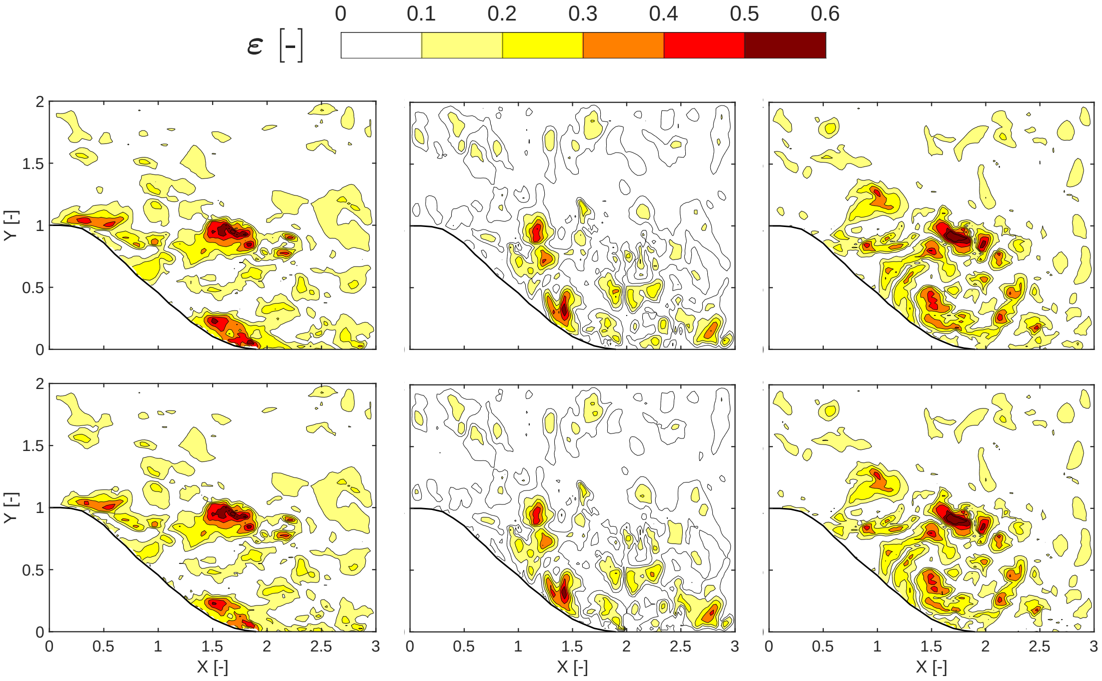

Figure 5.20: Planar distributions for absolute velocity error magnitudes of non-dimensional streamwise (left), normal (middle) and spanwise (right) velocity components at Z=0, with VIC+ (1^{st} row) and ImVIC+ (2^{nd} row).

ish for regions far away from the hill surface. Furthermore, although separation effects correspond to a turbulent flow behavior which cannot be resolved via potential flow definitions solely, the appropriate combination of Vortex-in-Cell approach with the immersed boundary treatment provides the superposition of necessary potential and rotational flow components to reconstruct the flow field properties with increased coherence levels to the physical flow behavior in close proximity of the FSI interface, Tab.5.4.

5.4 Surface Pressure Reconstruction with Boundary Fitted Coordinates

The validation studies for the surface pressure reconstruction procedure using the material acceleration information obtained from particle tracking velocimetry measurements is performed using the exact fully 3D solutions for the unsteady incompressible Navier-Stokes equations defined by Ethier and Steinman (1994). Being inspired from the 2D analytical solution provided for unsteady Navier-Stokes equations yielding the time dependent velocity and pressure fields for Taylor-Green vortices (Taylor and Green, 1937), the proposed analytical solution generates a velocity field information where,

- The influence of viscous dissipation is diminished by the contribution of unsteady terms.
- Mass conservation is satisfied by means of the divergence free condition.

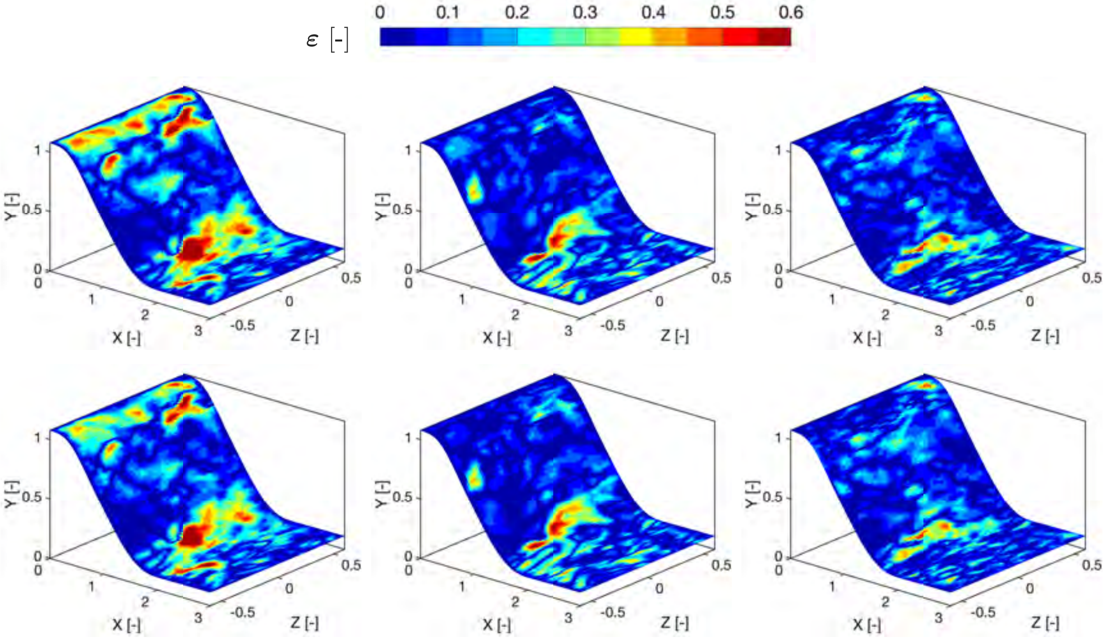

Figure 5.21: Planar distributions for absolute velocity error magnitudes of non-dimensional streamwise (left column), normal (middle column) and spanwise (right column) velocity components at close proximity of the hill surface, with VIC+ (1^{st} row) and ImVIC+ (2^{nd} row).

- The remaining convection terms on the material derivative definition can be represent as the gradient of a scalar function which in turn corresponds to the negative of pressure.

The resultant flow field is referred as a Beltrami flow (Wang, 1990) and corresponds to a family of velocity and pressure fields whose unique determination is satisfied by the choice of constants $a,\ b,\ c,\ d$ which satisfy $a^2 + b^2 = 0$ and $c = id$. In case where a and d is selected to be arbitrary real number the flow field reads as follows,

$$
\begin{aligned}
u &= -a[e^{ax}sin(ax \pm dz) + e^{az}cos(ax \pm dy)]e^{-d^2t} \\
v &= -a[e^{ay}sin(az \pm dx) + e^{ax}cos(ay \pm dz)]e^{-d^2t} \\
w &= -a[e^{az}sin(ax \pm dy) + e^{ay}cos(az \pm dx)]e^{-d^2t} \\
p = -\frac{a^2}{2}&[e^{2ax} + e^{2ay} + e^{2az} + 2sin(ax \pm dy)cos(az \pm dx)ea(y+z) \\
+2sin(ay \pm dz)cos(ax \pm dy)e^{a(z+x)} &+ 2sin(az \pm dx)cos(ay \pm dz)e^{a(x+y)}]e^{-d^2t}
\end{aligned}
\tag{5.1}
$$

For the pressure reconstruction procedure the local and convective components of the acceleration terms are determined by analytically differentiating the velocity terms given above. As the computed material derivative terms are provided to the pressure reconstruction algorithm, the Poisson equation is solved with fully homogeneous boundary conditions and the computed pressure field, which is unique up to a constant, shifted according to an exact pressure value provided by the Eq.(5.1).

5.4.1 Pressure Reconstruction on Rectangular Computational Domain

Initially the numerical integration procedure of the pressure gradients utilizing a fast FFT based Poisson solver is assessed over a computational domain of uniform rectangular shape where the pressure gradients at the grid location are directly computed from the analytical expressions. Accordingly, the computational domain is defined within the limits of (-1,1) m in each three dimensions with a spatial resolution of 0.025 m. The reconstructed pressure information is compared with the exact pressure fields calculated from Eq.(5.1) at Z=0.225 m plane. As the relative error distribution revealed the difference between the numerically calculated and the exact pressure fields, to possess maximum error values below 0.15% where the errors concentrated on regions of high pressure gradients, Fig.5.22.

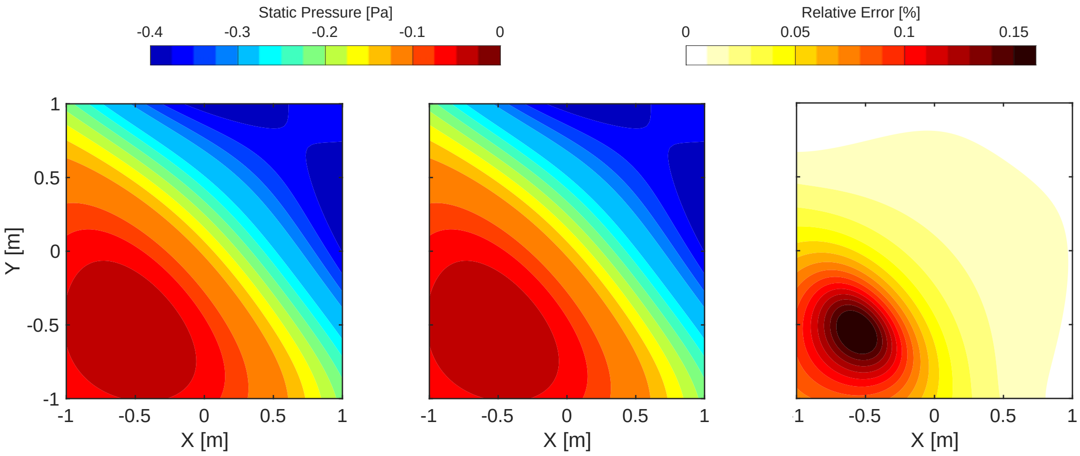

Figure 5.22: Pressure fields with analytical solution (left) and numerical computation (middle) at Z=0.225 m. Relative error distribution of pressure at Z=0.225 m (right).

5.4.2 Pressure Reconstruction on Curvilinear Computational Domain

Furthermore, the surface pressure reconstruction algorithm is tested with boundary fitted coordinate systems providing exact solid boundary conformation over an artificially introduced three dimensional hill form of various heights. The corresponding computational domain is again assigned with the analytical solution of Navier-Stokes equation derived by Ethier and Steinman (1994) which still represents a Beltrami flow (Wang, 1990) where the present hill forms do not possess any influence on the flow characteristics. The objective is set to demonstrate the compatibility of the mesh deformation schemes and accuracy characteristics of the vectorial transformation procedures where the analytical vector field of accelerations are defined and the corresponding pressure gradients are integrated on the generated computational grid.

The 3D hill form is acquired from the wind tunnel experiments of Hunt and Snyder (1980) which is represented by the following formulation,

$$z(r) = \frac{h+c}{1+\left(\frac{r}{L}\right)^4} - c \tag{5.2}$$

where h=0.155 m, L=0.388 m and c=0.01 m. The radius r is defined from the hill center that indicates the region where the upward deflection of the hill is located. The introduced upward deflections are confined within the region of r <0.775 m. In order to demostrate the mesh adaption scheme of radial basis function based grid deformations, the maximum hill height is incrementally increased from a flat surface to 0.12 m, 0.19 m and 0.31 m. Hence, the initially generated uniform structured grid of rectangular form is deformed according to the surface deformations introduced by Eq.(5.2). Horizontal planes of the curvilinear grid formations at different stages of surface deformation are illustrated in Fig.5.23. At each stage of the deformations, the transformation matrices are recalculated according to the deformed grid structure to allow accurate transformations of the pressure gradients over the curvilinear computational grid.

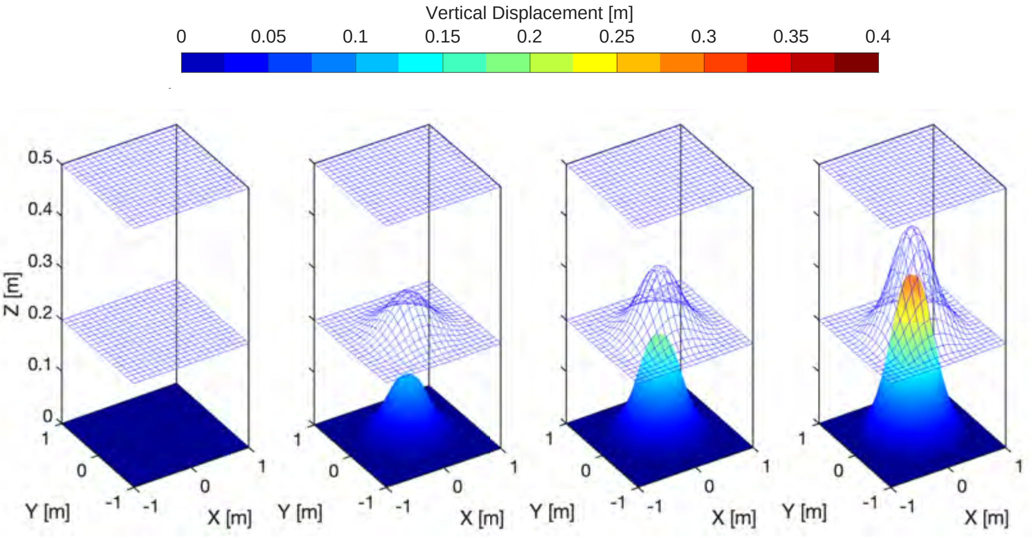

Figure 5.23: Surface deflections at different height scales of three dimensional hill form and samples horizontal planes for the corresponding deformed mesh structures.

Even though the amplitudes of relative error levels calculated for the reconstructed pressure information over the hill surface yielded an increasing trend with the increasing level of hill deflection, the maximum error levels are observed to be limited to of 4% for all four cases, Fig.5.25. Considering the error levels captured for the numerical integration procedure of pressure gradients, the vectorail transformations defined for the mapping relations of computational and physical coordinate structures provide a significant level of coherence for the pressure fields with the analytical flow field description. Nonetheless, it can be seen there exists a distinctive region of error presence over the circumference of the hill region, Fig.5.25. Although considerably small, below 1%, the errors encountered in these regions are associated with the numerical discretizations employed for the determination the transformation matrices. Due to the fact that the hill deformation is defined with a partial function, the corresponding shape reveals a discontinuous form at the boundary of r=0.775 m. Therefore, the employed central differencing approximations for the computation procedure of vector transformations tend to cause underestimations or overestimations in regions where deformation gradients are undefined. Nevertheless, the problem can be easily solved by increasing the spatial resolution of the computational grid definition. However, this option is not pursued in order demonstrate the accurate surface pressure computation capabilities of the BFC approach in case of low spatial resolution in where the nearest neighbor methods utilizing uniform structured grids suffer the most in terms of accuracy (Pan et al., 2016).

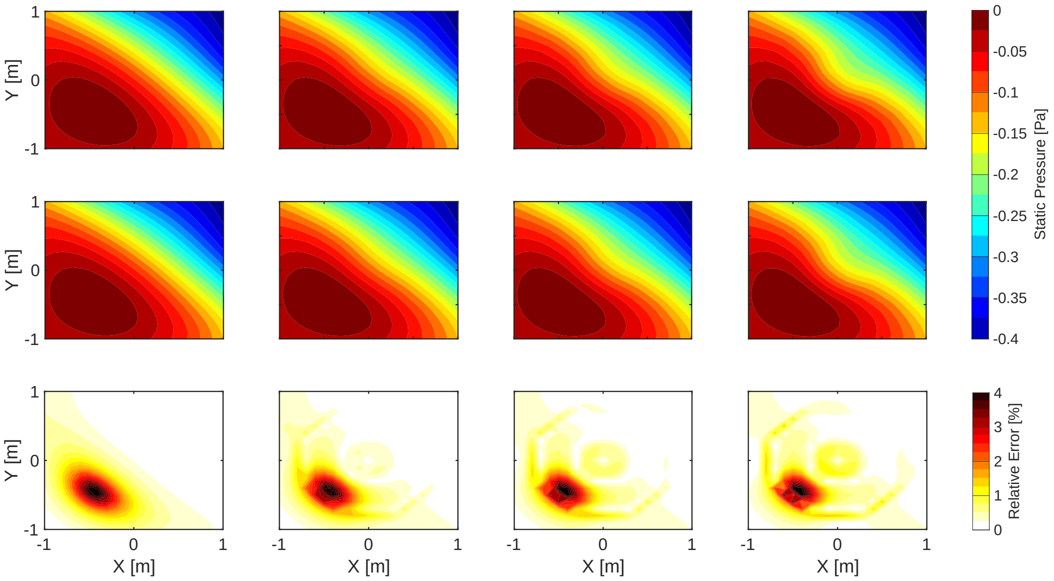

Figure 5.24: Surface pressure fields with analytical solution (1^{st} row), surface pressure reconstruction with boundary fitted coordinate systems over analytical pressure gradients (2^{nd} row) and relative error of pressure (3^{rd} row) for maximum surface deflection levels of h=0 m (1^{st} column), h=0.12 m (2^{nd} column), h=0.19 m (3^{rd} column) and h=0.31 m (4^{th} column).

5.4.3 Pressure Reconstruction on Curvilinear Computational Domain from PTV data

Furthermore, in order to simulate experimental data structure, the theoretical flow field information is employed to assign flow field properties to individual set of particles located throughout the prescribed computational domain. Since the derivation of velocity and pressure field solutions proposed by Ethier and Steinman (1994) utilizes the temporal velocity derivatives to cancel out the viscous contribution, the pressure variation over a specified domain is related to the convective terms that yield a steady state flow behavior. Therefore, to comply with the analytical solution, the velocity vector fields are considered to be steady even though they contain unsteady terms.

Hence, for the particle tracking approach a randomly distributed set of particles are provided to the computational domain where their motion for consecutive steps of the simulated images are calculated using a pseudo-particle tracking approach similarly defined for the pre-processing of DNS simulations employed in Sections 5.2 & 5.3. The velocity fields are considered to be steady referring to the aforementioned discussion on their derivations and their distribution is selected to be equal to their analytical formulation at t=0.5 s. The generated particles are propagated for 7 time steps where the $\Delta t = 10^-3$ corresponding to a acquisition frequency of 1 kHz. The computed 7 particle location over the tracks are regularized with a polynomial fitting of second order from which the velocity and Lagrangian acceleration terms are calculated.

For introducing surface deformations in order to employ curvilinear boundary fitted coordinate systems, artificial 3D fill forms utilized previously are defined with the exact same deformation levels of 4 stages, starting from a flat surface and reaching to 60% of the computational domain height. Accordingly, the computational grid structure is deformed by means of RBF interpolations to provide exact surface corformation. Moreover, the acceleration information scattered over the computational domain is binned at the updated grid locations using AGW with spherical bins of 50% overlap. The assigned acceleration information at the grid locations is transformed to switch the vectorial orientation from Cartesian coordinates of the curvilinear physical grid structure to the rectangular formation of the pressure integration mesh.

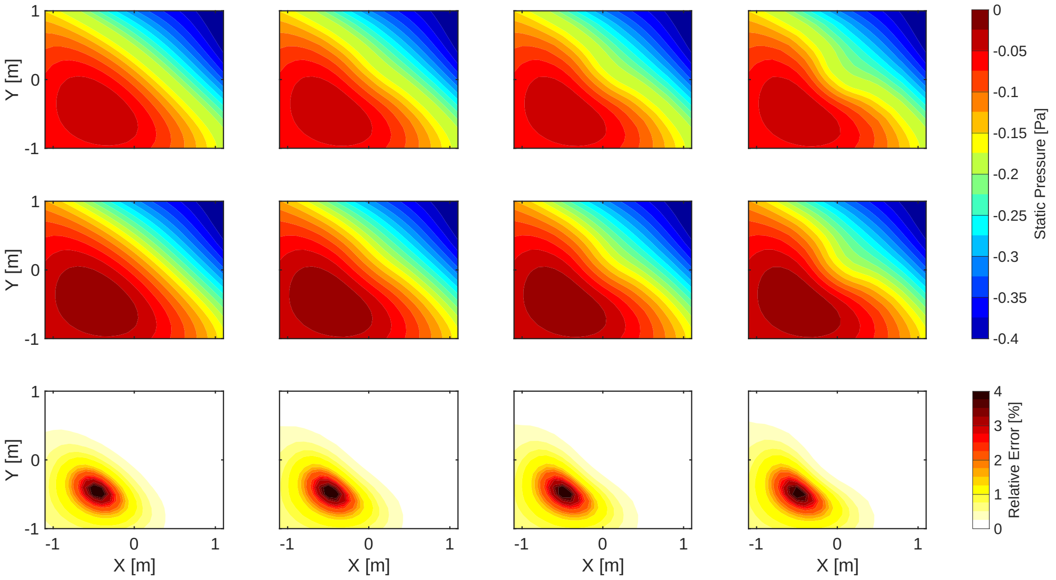

Figure 5.25: Surface pressure fields with analytical solution (1^{st} row), surface pressure reconstruction with boundary fitted coordinate systems over PTV data (2^{nd} row) and relative error of pressure (3^{rd} row) for maximum surface deflection levels of h=0 (1^{st} column), h=0.15 (2^{nd} column), h=0.25 (3^{rd} column) and h=0.4 (4^{th} column).

As the reconstructed pressure fields are compared with the analytical reference, no visual difference in terms of the scalar pressure distribution is captured for all 4 hill forms. Nevertheless, in relation to the vector transformations constructing the link between physical and computational coordinate systems for the integration of pressure gradients, the relative errors are slightly amplified while the maximum error value is bounded at 7%. The differences in the error distribution observed between the various hill shapes are mainly concentrated on the surrounding region of the hill formation which relates to the numerical discretization errors of the central differencing approximations employed for the calculation of transformation variables.

5.4.4 Error Estimation and Uncertainty quantification

In order to access the uncertainty specifications of the boundary fitted surface pressure reconstruction scheme proposed to utilize Lagrangian acceleration information obtained by the particle tracking algorithms, a series of Monte Carlo simulations (Metropolis and Ulam, 1949) are performed with various levels of grid deformations introduced with the artificial hill form.

Accordingly, a synthetic experimental data stimulation procedure is employed for calculating the error propagation through the pressure reconstruction algorithm. The generated particle locations along the reconstructed tracks of the analytical flow field are equipped with 0.2 voxels of Gaussian noise in each 3 dimensions of the Cartesian domain with random variations. Then, the resultant noisy particle locations along the tracks are normalized with polynomial functions of second order to obtain the velocity and material acceleration information. The resultant particle tracking data is processed with the aforementioned procedure of pressure reconstruction with boundary fitted coordinate systems to obtain the pressure field information. The Monte Carlo simulations are performed with 100 samples according to the sampling criteria proposed by Schneiders and Sciacchitano (2017).

For each iteration of the simulations, the resultant pressure fields from the reconstruction algorithm are compared with the analytical pressure field information to extract the error distributions over the computational volume by,

$$\varepsilon_j(\mathbf{x}_i) = P_j^{PTV}(\mathbf{x}_i) - P_j^{Exact}(\mathbf{x}_i) \tag{5.3}$$

where P^{PTV} and P^{Exact} correspond to the pressure fields computed from particle tracking data and the analytical solution respectively while $j = 1, ..., N$ relates to the number of samples for the Monte Carlo simulations. Moreover, the bias and random uncertainty in the pressure reconstruction procedure are obtained by calculating the mean and standard deviations of the error variation ϵ_j. Hence, following the general uncertainty estimation approach of Benedict and Gould (1996), the bias and random uncertainties are computed as,

$$U_b = \frac{\epsilon_{sigma}}{\sqrt{N}} \quad and \quad U_\sigma = \frac{\epsilon_{sigma}}{\sqrt{2(N-1)}} \tag{5.4}$$

where U_b and U_σ correspond to the bias and random uncertainties of the local pressure reconstruction results respectively. The mean and standard deviation of the error terms are calculated via assembling the 100 samples of Monte Carlo simulations.

$$\epsilon_b(\mathbf{x}_i) = \frac{1}{N}\sum_{i=j}^{N}\varepsilon_j(\mathbf{x}_i) \quad and \quad \epsilon_\sigma(\mathbf{x}_i) = \left[\frac{1}{N-1}\sum_{i=j}^{N}(\varepsilon_j(\mathbf{x}_i) - \epsilon_b(\mathbf{x}_i))^2\right]^{\frac{1}{2}} \tag{5.5}$$

The distorted particle tracking information with 0.2 voxels of Gaussian noise introduced over the particle locations elevate maximum pressure reconstruction errors from 0.002 Pa to 0.1 Pa in terms of absolute magnitudes, Fig.5.26. The increase factor of 50 refers directly to the sensitivity of the material acceleration reconstruction performed by the Shake-the-Box algorithm.

Average pressure fields calculated over 100 instances of the Monte Carlo simulations revealed absolute error levels confined to a maximum value of 0.03 Pa which quantify the effect of treating surface deflections with mesh adaptation procedures in terms of the bias uncertainty, Fig.5.27. Evidently, increasing surface deformation is associated with a slight increase of static pressure errors throughout the computational domain as represented over the hill surface, Fig.5.28. The increased uncertainty with the increasing hill height is computed to reach 0.02 Pa for a hill height of 60% compared to the complete vertical length of the computational domain inducing severe deformations over the mesh structure, Fig.5.23. On the other hand, random uncertainty levels are related to the unbiased errors introduced by the artificial noise addition, thus they are independent of the deformation state and the corresponding transformation variables, Fig.5.27. Accordingly, the random uncertainty of the pressure reconstruction method is determined to be 0.08 Pa in average while its distribution over the computational domain is mainly determined by the Dirichlet boundary condition location, Fig.5.28.

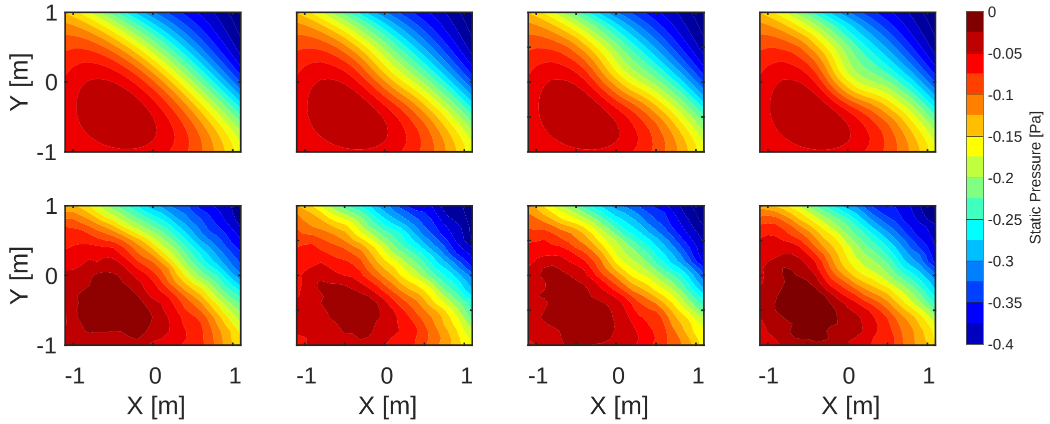

Figure 5.26: Surface pressure fields with analytical solution (1^{st} row) and ensemble averaged surface pressure reconstruction with boundary fitted coordinate systems over PTV data from the 100 samples of Monte Carlo simulations (2^{nd} row) for maximum surface deflection levels of h=0 (1^{st} column), h=0.15 (2^{nd} column), h=0.25 (3^{rd} column) and h=0.4 (4^{th} column).

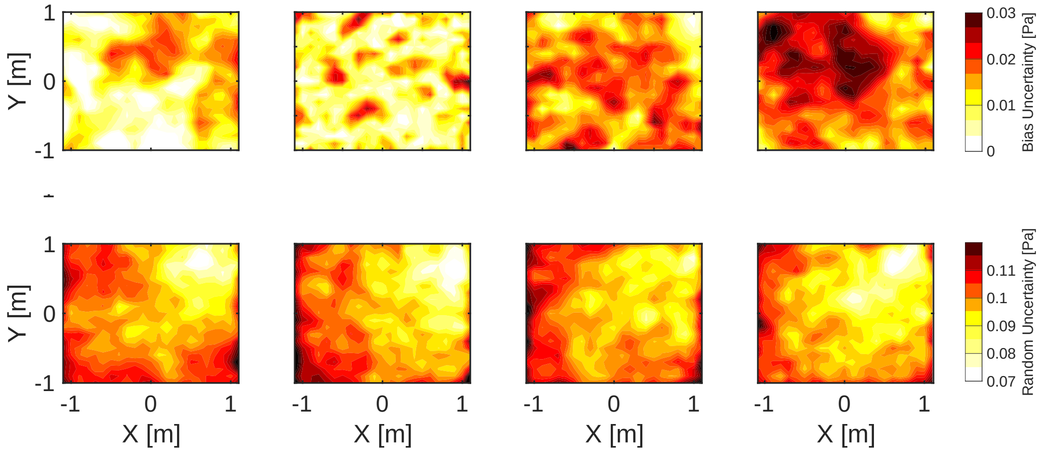

Figure 5.27: Bias (1^{st} row) and random (2^{nd} row)uncertainties for surface pressure reconstruction with 0.2 voxels of Gaussian noise.

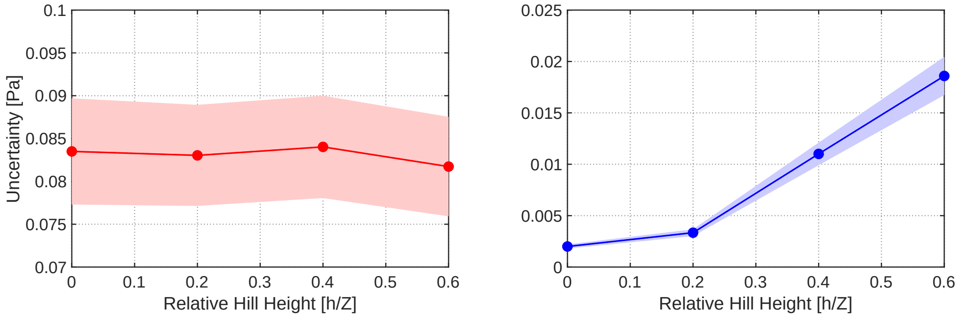

Figure 5.28: Variation of bias (left) and random (right) uncertainties with respect to the relative hill height normalized by the computational domain height.

5.5 Dense Flow Field Reconstruction of PTV Data with a Solenoidal and Irrotational Basis

The validation studies for the proposed dense flow field interpolation algorithms of Sol+ and ISol+ are performed over a theoretical field of wave lattice formation and an experimental case of water submerged transitional circular jet measurements performed by Violato and Scarano (2011).

5.5.1 Theoretical Validation

The theoretical validation study of dense flow field interpolation with basis reconstruction approaches is conducted by an unsteady three dimensional wave lattice formation. The formulation for the synthetic flow field is embarked from the previously conducted validation studies of Schneiders (2017); Gonzalez Saiz et al. (2019) in the following form,

$$\mathbf{u} = \begin{cases} u_i = Asin\left(\frac{2\pi x}{\lambda}\right) sin\left(\frac{2\pi y}{\lambda}\right) \\ u_j = Acos\left(\frac{2\pi x}{\lambda}\right) cos\left(\frac{2\pi y}{\lambda}\right) \\ u_k = A \end{cases} \tag{5.6}$$

The simulated measurement volume is constructed to be composed of 500 voxels in each directions, $500 \times 500 \times 500\text{vox}^3$. The wavelength of the lattice formation is set to be $\lambda = 200$ while the maximum particle displacement is restricted at A=2 voxels. In order to simulate a particle tracking approach with unsteady motion of particles, an iterative approach for particle motion determination is followed.

Starting from an initial velocity field at $t = t_0$, a random particle distribution of concentration $C = 5 \times 10^{-5}\text{par/vox}^3$ is obtained over the computational domain. The generated scattered particles are displaced with the initial velocity field during the pseudo-time variation of $4 \times \Delta t$ to their next assumed locations at $t = t = t_0 + (1, ..., 7)\Delta t$ and the corresponding velocity vectors at each time step are computed employing Eq.(5.6). Utilizing the RK4 numerical integration procedure for discretization of the displacement of particles in each direction, the pseudo particle tracks are generated to represent the velocity and acceleration properties of each particles' propagation in time and space. Furthermore, stimulating the polynomial track reconstruction approach of Shake-the-box for velocity and acceleration computation along the particle tracks, a polynomial fit of second order is applied to the computed particle locations over 7 time instants. The initial assessments are performed with no artificial noise implementation on the synthetic dataset, hence there exist no particle reconstruction errors for the particle tracking information.

Initial assessments performed for the reconstruction of flow field properties with linear interpolation revealed no resemblance of the resultant velocity information to the theoretical flow behavior. Due to the scarcity of particle tracking information over the computational domain, the linear regression cannot reconstruct the necessary gradient of velocity components. Hence, the application of governing equation based approaches enables the velocity gradients to be resolved more accurately to represent the theoretical flow features since the gradients are dictated by means of the vorticity distribution and momentum conservation. However, the flow governing equations utilized for VIC+ approach do not contain a continuity equation that would satisfy the mass conservation. Furthermore, even though momentum conservation provides a certain level of physical coherence for the flow feature to meet the theoretical profiles, the weighting introduced for the cost function determination inferiorizes the contribution of acceleration terms. Therefore, the application of Sol+ where the continuity is inherently imposed by means of vector valued radial basis functions, significantly increases the agreement of the dense interpolation procedure with the analytical flow field by ensuring the conservation of mass over the complete computational domain. Since the grid resolution for the dense interpolation procedure is selected according to the particle track density over the prescribed measurement domain, which yields a stencil of 16 grid locations to be affected by a single PTV data point, Sol+ amplifies the influence of individual particle tracking information scattered throughout the computational domain in terms of introducing an additional constraint on the velocity gradients, Fig.5.29.

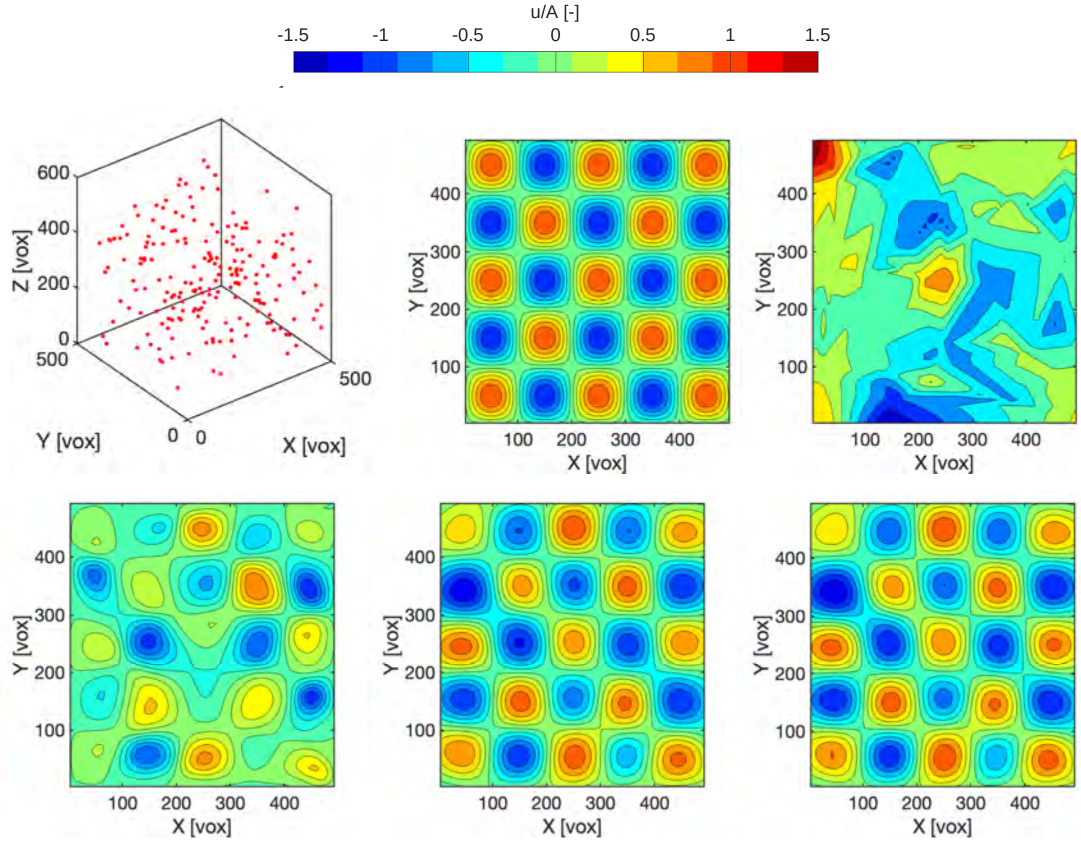

Figure 5.29: Particle track distribution over the computational domain (top-left). Velocity field distributions at Z=0 of analytical solution (top-middle), reconstructed over particle tracking data without artificial noise using linear interpolation (top-right), VIC+ (bottom-left), Sol+ (bottom-middle) and ISol+ (bottom-right).

Moreover, implementation of the irrotational Gaussian progress regression (IGPR) performs a similar task for the material acceleration terms. The mathematical formulations for the employed form of Navier-Stokes equations suggests that the material acceleration terms are required to be irrotational due to their direct relation to the gradient of a scalar variable, static pressure. However, the material acceleration components are calculated based on the velocity and vorticity fields determined throughout the previous stages of the optimization procedure. Contrary to the conventional numerical simulation approaches where the velocity field information for the proceeding time step or iteration is calculated from the momentum conservation equation, there exists no correlation of the acceleration terms to the physical satisfaction of momentum conservation which is rather aimed to achieved within the optimization procedure. Furthermore, as the vorticity transport equation is utilized to eliminate the necessity of defining pressure field information, the scalar term that is to impose an irrotationality condition for the acceleration vectors is absent for the present derivation of momentum conservation. Hence, the ISol+ method combining the matrix based RBF definition to ensure imposition of mass conservation and curl freedom of material accelerations similarly elevates the capabilities of the dense flow field reconstruction algorithm to accurately represent physical flow features by satisfying the necessary physical constraints inherently. Even though, this feature of ISol+ do not provide any significant improvement of accuracy for the dense interpolation procedure of velocity terms owing to the fact that weighting of the respective cost function components restricts the influence of acceleration terms on the velocity field optimization. The major advantage of utilizing ISol+ is further elaborated on the experimental verification procedure as not only the velocity and vorticity distributions but also the static pressure distributions are compared to a reference profile, Fig.5.29.

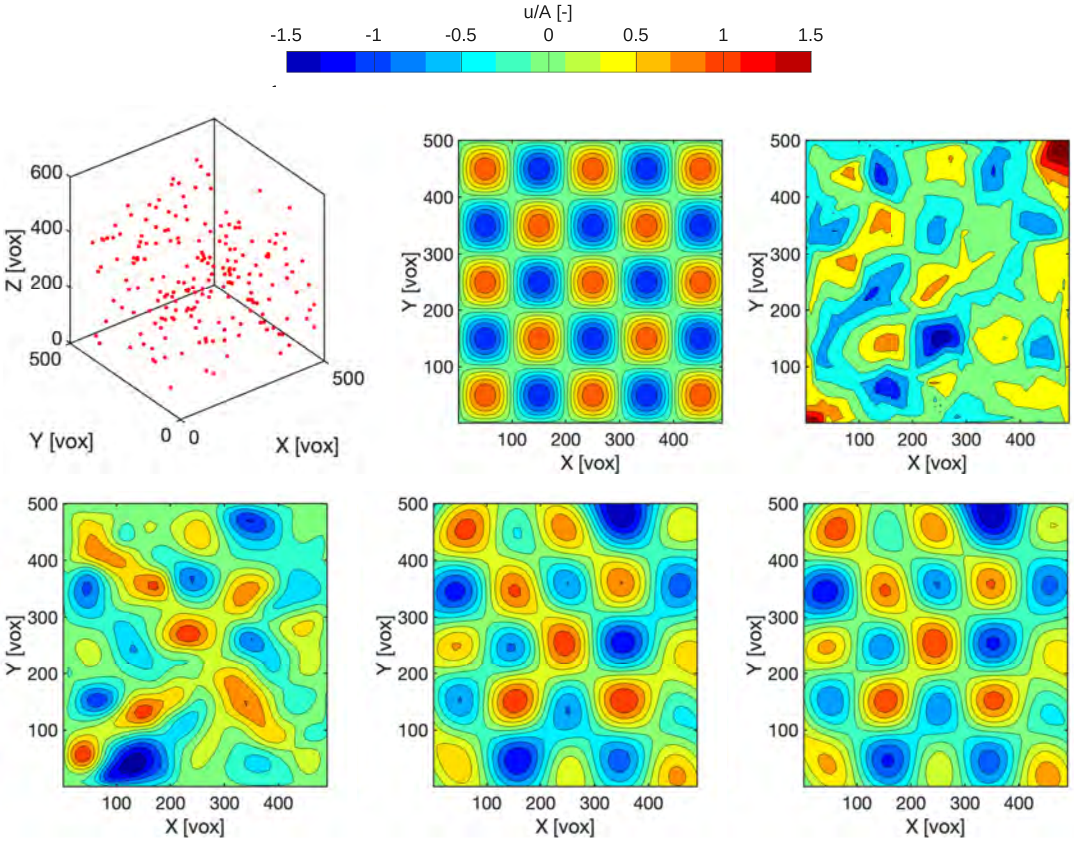

Figure 5.30: Particle track distribution over the computational domain (top-left). Velocity field distributions at Z=0 of analytical solution (top-middle), reconstructed over particle tracking data with artificial noise of 0.2 voxels using linear interpolation (top-right), VIC+ (bottom-left), Sol+ (bottom-middle) and ISol+ (bottom-right).

Furthermore, the proposed reconstruction approaches of Sol+ and ISol+ are also tested in presence of measurement noise at different levels against the performance specifications of linear interpolation and VIC+. The generated synthetic tracks and the corresponding polynomial functions are deviated from the analytical flow field properties via introducing an artificial Gaussian noise of 0.2 voxels to the analytically reconstructed particle locations over the 7 time instants. Corresponding noisy particle locations are fitted with new second order polynomials to compute the velocity and Lagrangian acceleration information for the noisy particle tracks.

Considering the error propagation over the velocity and material acceleration terms, there exists an increased level of violation of the mass conservation when both linear interpolation and VIC+ are applied to reconstruct the volumetric flow features. As these errors are further amplified by the internal numerical errors and mathematical discrepancies of continuity for VIC+, the resultant flow field information significantly divergences from the theoretical reference. Therefore, the Sol+ method by imposing the mass conservation allows the optimization procedure to convergence to a flow state that inherently satisfies the continuity. Owing to the fact that the objective for the optimization procedure is determined to be the exact measurement data which contains the artificially introduced measurement errors, the resultant cost function value for the converged state reveals a larger magnitude compared to the VIC+. This condition refers to the enforcement of mass conservation preventing the dense interpolation to directly meet the erroneous measurement information. Similarly, ISol+ extends the physical interpretation of flow governing equations and the corresponding variables by imposing the irrotationality of the material acceleration terms where the propagated over the accelerations are accommodated by means the irrotational Gaussian progress regression, Fig.5.30..

5.5.2 Experimental Validation

The experimental validation process is performed over the Tomographic PIV data obtained from the transitional circular jet experiments of Violato and Scarano (2011), where a water jet installed at the bottom wall of a water tank with a diameter of D=10 mm. The jet exit velocity is adjusted to 0.45 m/s resulting in a jet diameter based Reynolds number of Re_D=5000, for which the specifications of the data acquisition and tomographic image processing procedures are given in Tab.5.5.

Table 5.5: Setup parameters for the transitional circular jet experiments of Violato and Scarano (2011).

Jet exit velocity	0.45 m/s
Reynolds number	$Re_D = 5,000$
Seeding	Polyamide particles, 56 μm diameter
Illumination	Quantronix Darwin-Duo Nd-YLF laser (2×25 mJ at 1 kHz)
Recording devices	4×Lavision HighSpeedStar 6 CMOS
Imaging	f = 105 mm Nikon objectives
Acqusition frequency	1000 Hz
Measurement field	(cylindrical) 30 mm (d) 50 mm (h)
Interrogation vol.	$40 \times 40 \times 40$ vox ($2 \times 2 \times 2$ mm3)
Vectors per field	$61 \times 102 \times 61$

The instantaneous organization of vorticity features for the reference dataset, visualized using Q-criterion (Hunt et al., 1988), are demonstrated in Fig.5.33. There exist 5 distinguished vortex rings within the measurement volume extending to y/D>4 downstream of the jet nozzle and the first vortex ring follows up on a upstream trace of a vorticity tube (shear layers) occurring due to the significant difference of fluid velocity between the still water and jet stream. The processing of acquired images is performed by Schneiders and Scarano (2016) using the tomographic particle tracking algorithm of Novara and Scarano

(2013) for calculating the Lagrangian acceleration terms to be utilized for pressure field reconstructions. The performed reconstruction resulted in a corresponding particle concentration of approximately 700 particles per D^3. The practical situation experienced in large scale measurements with low densities of particle tracks reconstructed for time resolved flow field information is simulated by means of downsampling the complete set of available scattered information to 19 par/D^3.

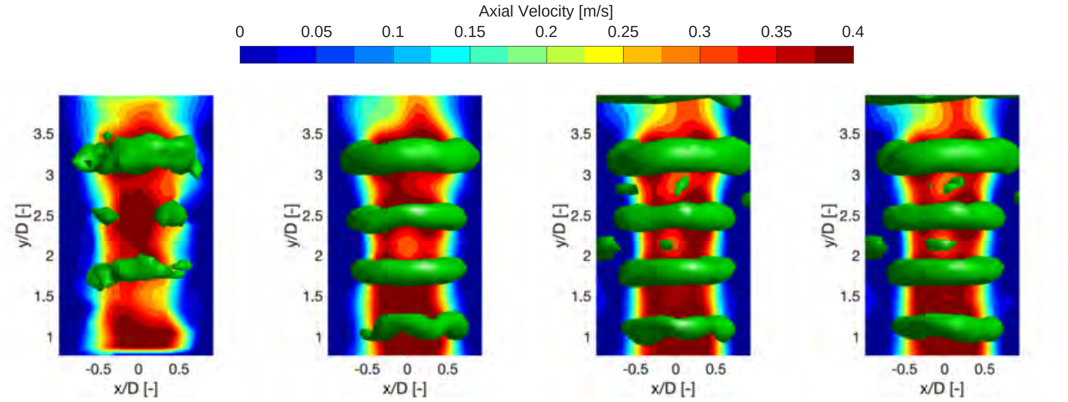

Figure 5.31: Axial velocity distributions over the vertical jet centerline and Q-criterion isosurfaces of Q=1000 $1/s^2$ with linear interpolation (left), VIC+ (middle-left), Sol+ (middle-right) and ISol+ (right).

Considering the theoretical assessments performed over the wave lattice field, linear interpolation yielded similar results for the experimental case of water jet such that the vorticity features are insufficiently resolved. Nonetheless, it should be noted that reconstruction of the axial velocity distributions adequately identify the dominant flow behavior of the jet. However, this due to the fact that axial characteristics of the jet stream are characterized with physical flow features of relatively large correlation lengths.Hence, absence of particles has a less significant effect for determining the velocity gradients over the computational domain for axial velocity profiles which allows their accurate reconstruction with relative ease. In the contrary, the vorticity features closely related to the secondary flow structures of radial velocity profiles are failed to be resolved since the scarcity of particles significantly effects the sharp gradients of velocity distribution especially for the shear layers generated over the entrainment regions. In order to accurately characterize these features the need for governing equation based approach become apparent while analyzing the results of VIC+ procedure. The formulation of the Vortex-in-Cell method allows the accurate characterization of velocity gradients for all three velocity components by combining the Navier-Stokes equations to benefit from the available acceleration information.

Before analyzing the differences between the VIC+ and the proposed methods of Sol+ and ISol+, it should be noted that the experimental campaign performed within a water tank, damps the measurement errors in terms of the diverge freedom since the inertial resistance of water due to its higher density compared to air prevent large gradients of velocity (Asher et al., 2012). Hence, the divergence errors the VIC+ method yields is relatively small. Nevertheless, employing the divergence error description of Zhang et al.

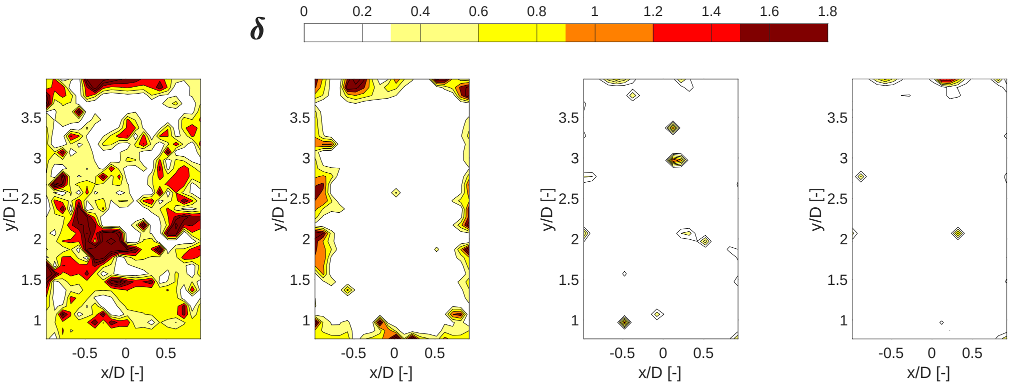

Figure 5.32: Divergence errors determined employing the definition of Zhang et al. (1997) with linear interpolation (left), VIC+ (middle-left), Sol+ (middle-right) and ISol+ (right).

(1997) proposed as,

$$\delta = \frac{\left(\frac{\partial u}{\partial x} + \frac{\partial v}{\partial y} + \frac{\partial w}{\partial z}\right)^2}{\left(\frac{\partial u}{\partial x}\right)^2 + \left(\frac{\partial v}{\partial y}\right)^2 + \left(\frac{\partial w}{\partial z}\right)^2} \tag{5.7}$$

the continuity errors become more apparent within the measurement domain domain, Fig.5.32. Nevertheless, the error distributions over the results of VIC+ and the proposed methods are within a considerably confined regime of computational domain boundaries. Therefore, the resultant differences between different approaches in terms of the velocity and vorticity features are relatively small in comparison to the linear interpolation, Fig.5.31.

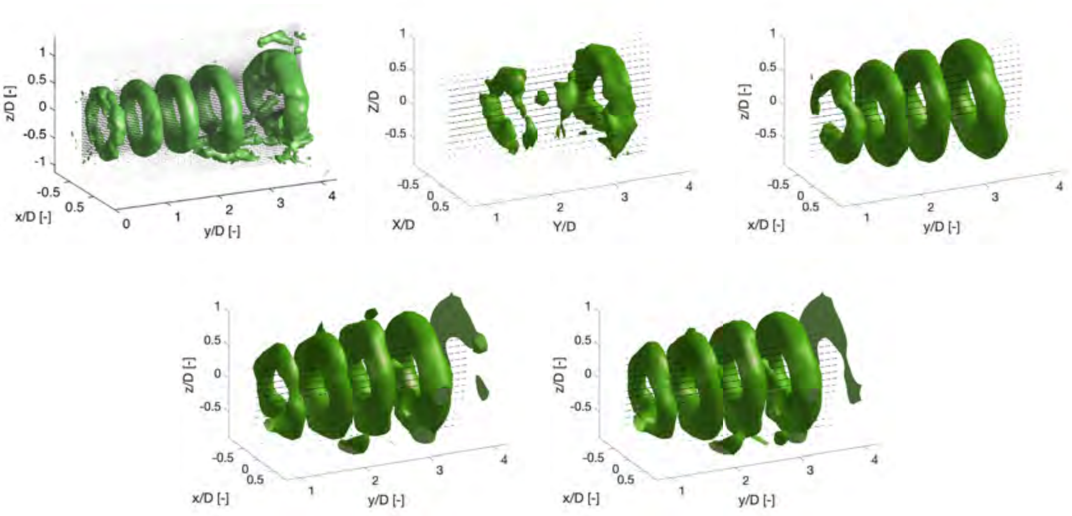

Figure 5.33: Q-criterion isosurfaces of Q=1000 $1/s^2$ with reference Tomo-PIV (top-left), linear interpolation (top-middle), VIC+ (top-right), Sol+ (bottom-left) and ISol+ (bottom-right).

Starting with the vorticity features represented in terms of Q-criterion isosurfaces (Kol, 2007), the improved accuracy with the flow physics based approaches is apparent over the linear interpolation. However, for the VIC+ method there exists three small features that are not resolved while their presence is captured with the application of Sol+ and ISol+. First one is the completeness of the most upstream vortex ring for which VIC+ reveals slightly deconstructed form whereas both Sol+ and ISol+ are able to completely capture vorticity formation. Secondly, the second downstream vortex ring in the reference field possesses small elements of vorticity features underneath which are lost for the VIC+ results while small coherent structures to the aforementioned vorticity features are captured with Sol+ and ISol+. Finally, the most downstream vortex ring is completely absent over the results of VIC+ method whilst both Sol+ and ISol+ are able to reconstruct the initial portion of the vortex ring contained within the prescribed computational domain with an increased agreement to the reference results, Fig.5.33..

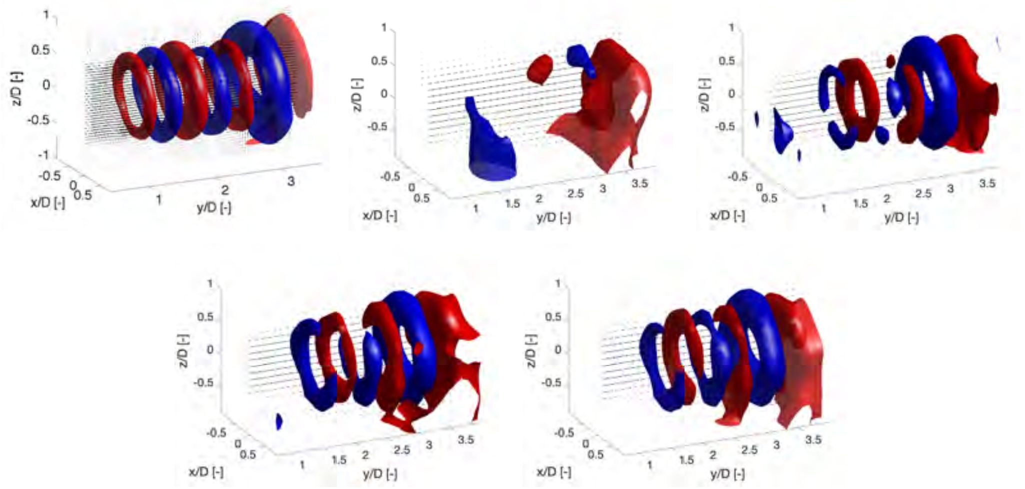

Figure 5.34: Static pressure isosurfaces of $p - p_{ref}$ =14 Pa (red) and $p - p_{ref}$ =-12 Pa (blue) with reference Tomo-PIV (top-left), linear interpolation (top-middle), VIC+ (top-right), Sol+ (bottom-left) and ISol+ (bottom-right).

The pressure reconstruction results clearly demonstrate the significance of utilizing the irrotational Gaussian process regression over Sol+ method to yield ISol+. Due to the low order of influence attributed for the material derivative terms over the optimization procedure based on the weighting of cost function components, all three methods of VIC+, Sol+ and ISol+ mainly utilize the acceleration terms to increase the physical coherence of the resultant velocity fields. Hence, the corresponding material acceleration field is based on the velocity distribution whose mathematical formulation do not induce any form of irrotationality. Therefore, regression of the acceleration fields to represent a curl-free vector field increases physical coherence of the material acceleration terms to meet the flow behavior especially in regions of negligible viscous effects. Consequently, sequentially increased physical validity of the vector fields with Sol+ initiating the satisfaction of mass conservation in terms of divergence freedom of velocity vectors and ISol+ providing irrotationality to the material acceleration fields improves the pressure reconstruction accuracy in comparison to the VIC+ approach, Fig.5.34.

Chapter 6

3D Characterization of Turbulent Boundary Layer Interactions with an Elastic Membrane

As a part of the Holistic Optical Metrology for Aero-Elastic Research (HOMER) project, the experimental setup employed in this thesis work is are designed within the work package 3 to investigate fluid-structure kinematics of turbulent boundary layer-unsteady panel interactions where the experiments are conducted in the low-speed W-wind tunnel of TU Delft High Speed Laboratory.

6.1 Experimental Setup

A schematic representation of the experimental setup is provided in Fig.6.1. The panel to be deformed is a square elastic membrane with sufficiently high moment of inertia to prevent any aeroelastic deformations and have full control over the membrane shape. The membrane is clamped on a aluminum frame of $60 \times 60 \times 30$ cm^3 from all edges to restrict its motion to only elastic deformations. A DC motor is connected to the center of the membrane by means of a gear and rod mechanism, and actuated at three different frequencies of 1 Hz, 3 Hz and 5 Hz with an amplitude of 30 mm from valley to crest. The translation of the central location of membrane is defined as a cycle of vertical motion between maximum and minimum deformation points. The measurements are performed with steady and unsteady membrane deformations are performed where for the steady cases the flow is analyzed with the membrane at neutral position, positive maximum deformation and negative maximum deformation.

A black foil with a regular grid of light-grey dots (0.8 mm diameter, 10 mm distance between adjacent dots, 36x36 dots grid) is applied to the upper face of the model to enable the structural displacement measurements by means of LPT. A 120 cm long rigid plate is installed upstream of the model to ensure well-developed turbulent boundary conditions

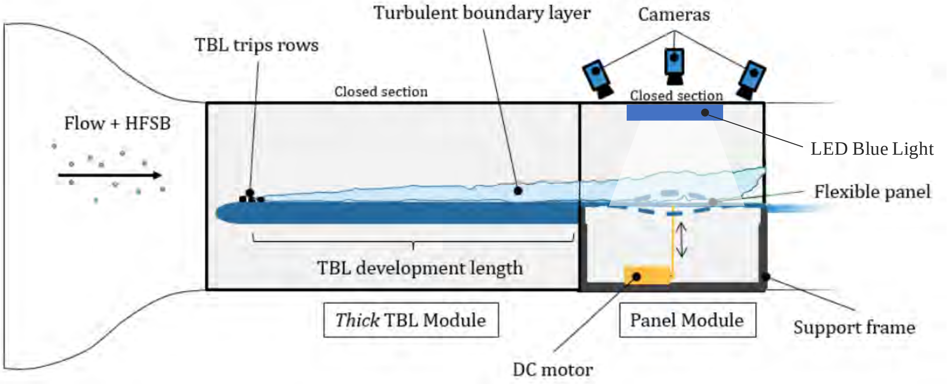

Figure 6.1: Schematic representation of the experimental setup for turbulent boundary layer interactions with unsteadily deforming elastic membrane.

at the test section. At 10 cm from the rigid plate leading edge, Lego blocks of 9.6 mm height are applied to force the transition of the boundary layer from the laminar to the turbulent regime.

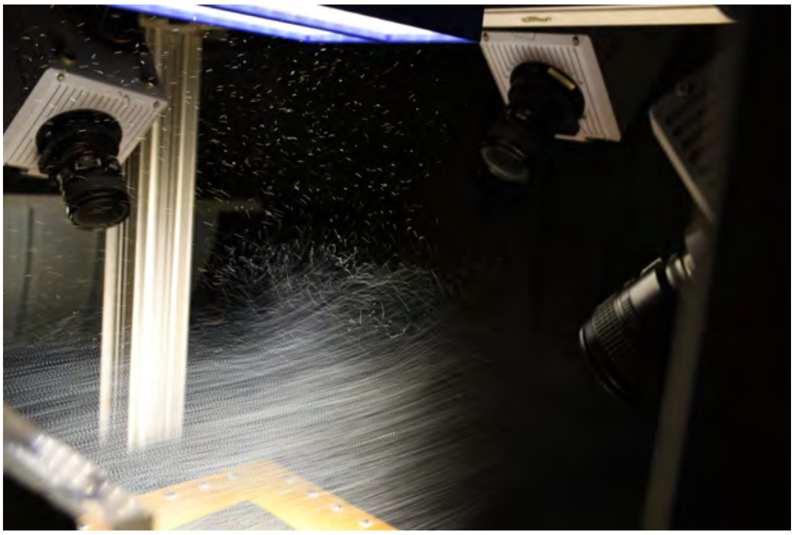

Figure 6.2: Experimental setup in operation with HFSB illuminated by means of the three LED light sources.

The flow is seeded with neutrally-buoyant Hellium Filled Soap Bubble (HFSB) tracers, which are inserted into the flow via an in-house built seeding rake composed of 200 nozzles distributed over 12 wings. The LPT measurements are carried out via three Photron FastCAM SA1.1 CMOS cameras (1024x1024 pixels, 12-bit, 20-m pixel size) mounted 40 cm above the moving panel positioned to form a 60^o angle. Three blue LED light sources are used for volumetric illumination of the flow and elastic membrane. Two of the LED lights are mounted between the cameras projecting the blue light perpendicular to the panel from above and one from the side to enhance illumination power for particles closer to the membrane surface. The experimental setup is equipped with two TruStability® board mount pressure sensors; one located upstream and another located at the central

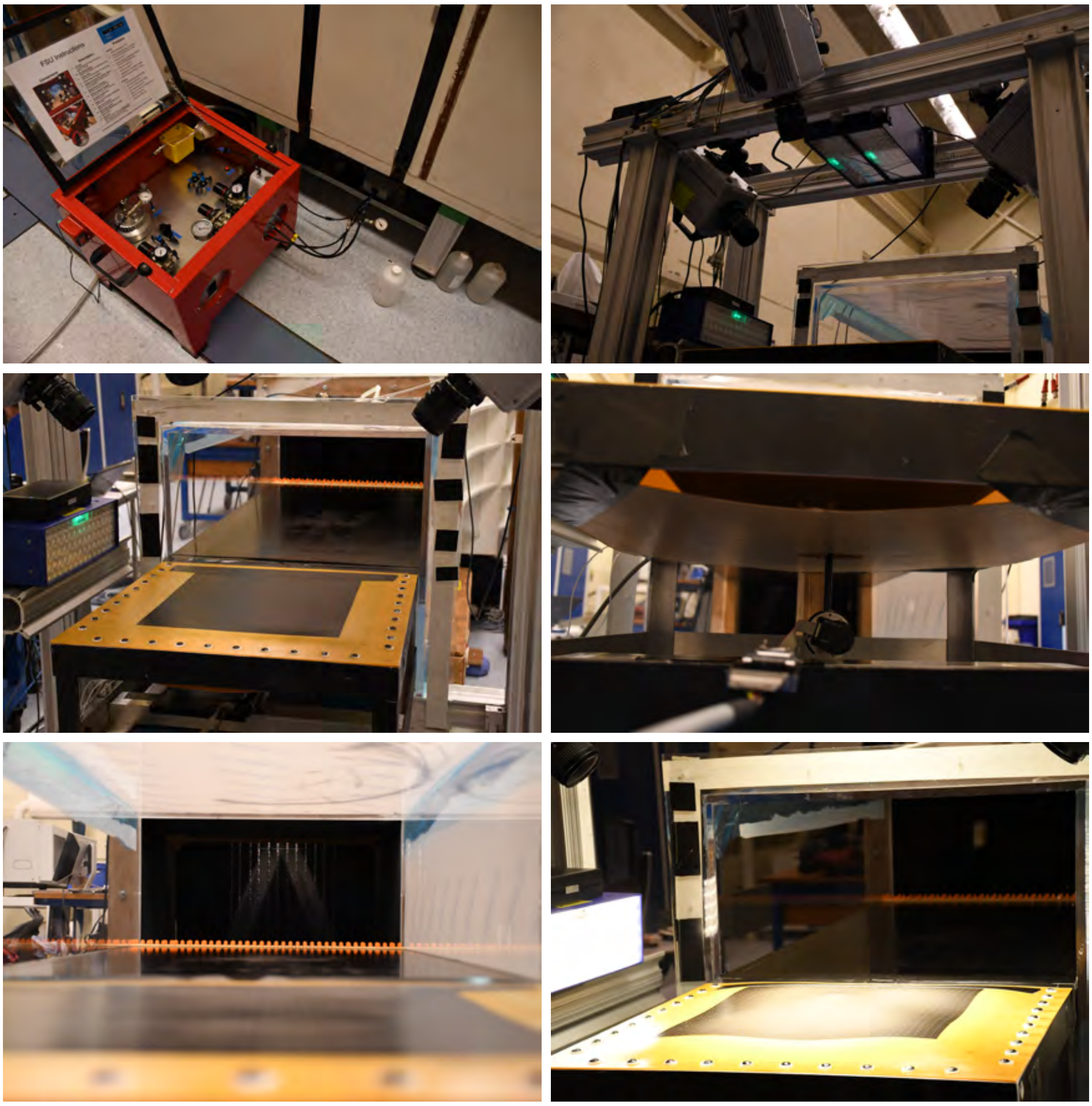

Figure 6.3: HFSB generator (top-left), LED illumination devices and image recording devices (top-right), elastic membrane at neutral position (middle-left), DC motor installment to the elastic membrane (middle-right), turbulent boundary layer tripping elements and HFSB nozzles (bottom-left) and elastic membrane at upward deformed position with LED illumination (bottom-right).

membrane location in order to provide reference static pressure values for comparisons against the results of on-intrusive surface pressure reconstruction algorithms.

6.2 Data Processing

The processing of raw images acquired throughout the experimental campaign for reconstructing location, velocity and acceleration information of fluid and structural tracers, is performed with the commercial software package DaVis version 10.0.5 from LaVision

Table 6.1: Setup parameters for the experimental investigation of turbulent boundary layer interactions with unsteadily deforming elastic membrane.

Freestream velocity	10 m/s
Reynolds number	$Re_l = 500,000$
Seeding	Hellium Filled Soap Bubbles
Illumination	Three LED blue light sources
Recording devices	Three Photron FastCAM SA1.1 CMOS
Acqusition frequency	3000 Hz

GmbH. Moreover, processing of the pressure tab data is conducted using Labview.

6.2.1 Calibration

As the experimental setup is composed of two different measurement systems of Tomo-PIV and surface pressure tabs, each system is required to be calibrated in order to provide the correct correlation of electrical signals and optical images with the physical features of the fluid and structure dynamics.

Calibration of Tomo-PIV System

The calibration for the Tomo-PIV system is performed in two different steps by first creating the orientation definition of the measurement domain referring to the relation between the visual distances throughout the images to the physical coordinates. This procedure is performed by utilizing a specifically developed calibration plate shown in Fig.6.4 over which a grid of black markers with 1cm spatial resolution exists referred as the pinhole model calibration plate. In total, 12 images of the calibration plate at various locations and orientations (8 vertical levels, 2 horizontal rotations, 2 tilted angles) are captured from which the optical transfer function constructed. Then via performing a volume self-calibration over the images of the calibration plate and an initial run of the experimental setup with HFSB, the coordinate system is mapped by means of 3rd order polynomial functions.

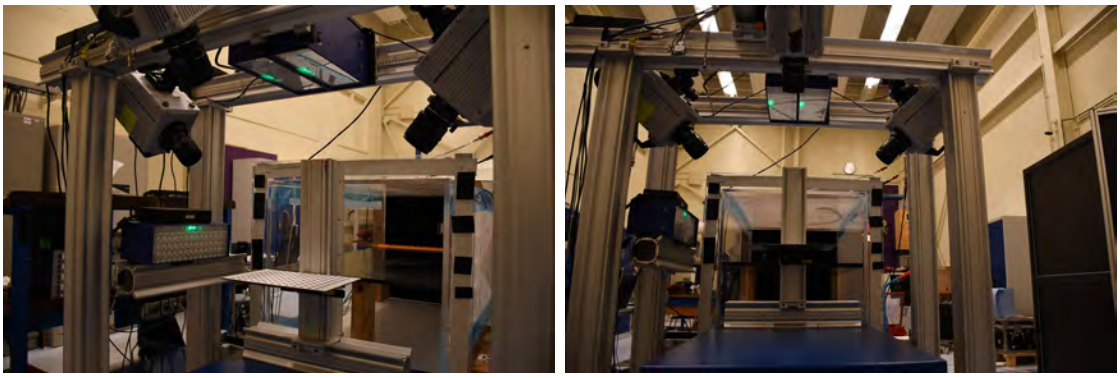

Figure 6.4: Calibration plate and its orientation with respect to the illumination and image acquisition system.

Calibration of Pressure Tabs

The calibration of pressure tabs and the analog to digital data conversion scheme is performed in two steps. First, the average pressure values obtained from the pressure tab measurements in tunnel off conditions are set to be zero so that the dynamic conditions and the corresponding pressure modulations can be quantified directly. Secondly, an artificial noise generation device, a pistonphone, is used to induce pressure waves of 119.2 dB with sinusoidal profiles at 250 Hz which are confirmed with the digital pressure readings in the frequency domain.

Figure 6.5: Pressure tab installment at the central location of the membrane (left) and pressure tab ports (right).

6.2.2 Image Processing

One of the main objectives of the conducted experimental campaign is to obtain simultaneous dynamic information of both fluid and structural domains utilizing the exact same experimental hardware. In that regards, the previously employed Direct Image Correlation (DIC) setup for measuring the structural motions is removed from the experimental setup. Thus, the structural information is reconstructed utilizing the same illumination and image acquisition hardware used for the fluidic region. Hence, in order to attain motion information of these two domains the deterministic step is referred as the image processing procedure.

Flow Domain

For reconstructing fluid motion the acquired images are initially filtered using a Butterworth high-pass filter computed over 15 images for cancellation of background noise in terms of illumination intensity. Then the resultant images are provided to the Shake-the-Box (STB) algorithm for Lagrangian particle traking (Schanz et al., 2016). Throughout the particle tracking procedure the two dimensional particle detection threshold is determined to be 10 particles where the triangulation errors were limited to 1.5 voxels. In the iterative particle reconstruction procedure, particles are shaked within 0.2 voxels while particles within the range of 8 voxels and/or possessing illumination intensities lower than 10% of the average intensity levels are removed. Finally, proceeding to the tracking step, the particle tracks are reconstructed with a minimum length of 7 particles within consecutive images. For the computation of velocity and Lagrangian acceleration information, a minimum number of 5 particles are selected for fitting a 3rd order polynomial for regularizing the particle motions in the temporal domain.

Structural Domain

As the membrane surface is equipped with tracer markers shown in Fig.6.5, surface markers possessed greater light intensities captured by the recording devices compared to the HFSB tracers of the fluid domain. In order to remove the flow tracers from the images, a high-pass time filter is applied to recorded images with a filter length of 3 images. Then, a second non-linear filter is performed for removing the 2D sliding average of particle intensities based on Gaussian distributions of light intensities with a filter length of 12 pixels. The resultant images are processed with the STB algorithm employing the same minimum track length of 7 particles and the resultant particle tracks are reconstructed with polynomial fits of 3rd order over a minimum number of 5 particles.

6.3 Steady Membrane Deformations

The steady flow characteristics are investigated with the membrane stationarily deformed at three different locations; upward, neutral and downward. The steady membrane shape is reconstructed by combining the location information of surface markers obtained from the STB algorithm for 10,000 instantaneous fields. As the imaging range of recording devices allowed accurate reconstruction of particle tracks for the surface markers within a smaller area compared to the full size the black foil, the membrane surface shape is represented with the dimensions of $\sim$150×150 mm^2, Fig.6.6.

It should be noted that due to the fact that as the performed experimental campaign is the second round of experiments performed with the exact same elastic membrane, plastic deformations are observed to be occurred throughout the operational cycles of steady and unsteady measurement configurations. These deformations yielded a certain degree of slag to appear especially when the membrane is set to be resting still at its neutral position. Nevertheless, neither the deformations due to this slag exceeded $\sim$3 mm nor it is an influential factor for the experiments to reach its objective since the exactly controlled motion of the membrane central location is not compromised. Hence, the experimental campaign is proceeded without making any modifications to the setup.

The steady flow field information of particle tracks are also treated in a very similar manner to the structural components as the instantaneous flow field information is combined from two consecutive runs with 10,000 time instants. Then, the scattered particle tracking data is gridded by means of a binning procedure which proceeds with the following steps,

- A structured grid is generated for the membrane at neutral position where mismatches between the exact membrane locations and the grid nodes occurred.

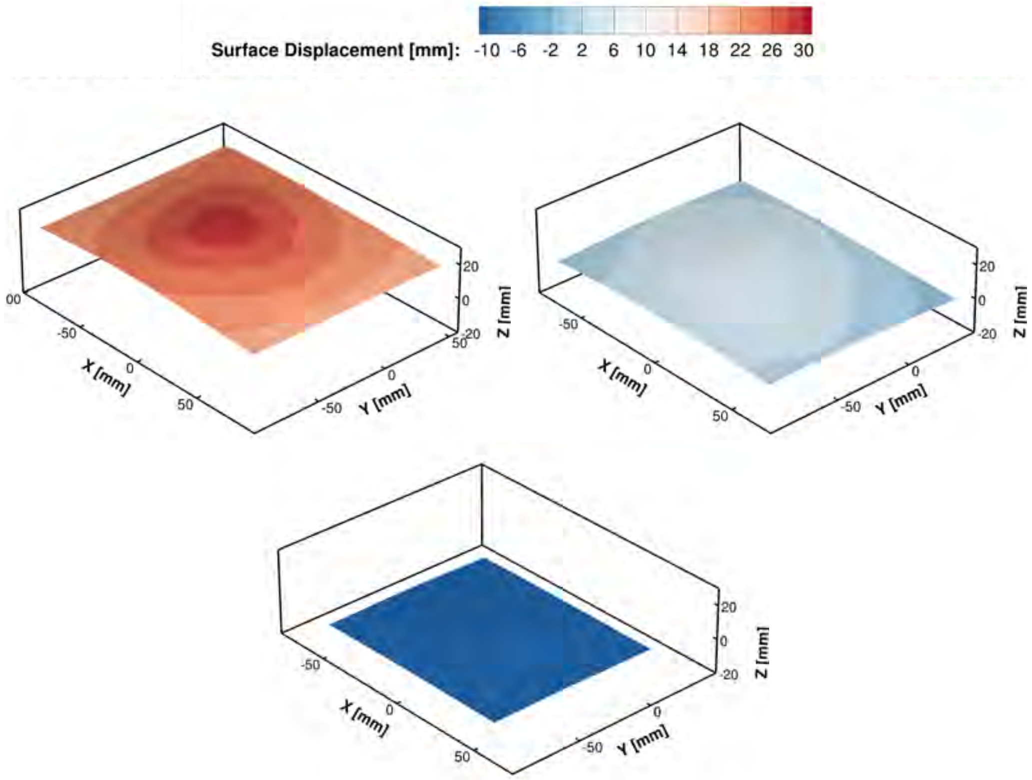

Figure 6.6: Reconstructed membrane shapes with relative surface displacements at upward (left), neutral (middle) and downward (right) deformed positions.

- In order to conform the various configurations of membrane surface shapes exactly, the initially generated structured grid form is deformed by means of radial basis function (RBF) based mesh deformation schemes, following an Arbitrary Lagrangian-Eulerian (ALE) approach where the Eulerian reference frame is created for the fluid side using the Lagrangian information captured for the structure.

- Spherical bins with diameters of double the size of the grid spacing (50% overlap) are employed to capture particle tracks that will be used to reconstruct the fluid information over the measurement domain.

- An Adaptive Gaussian Windowing (AGW) approach is applied within each individual bin for three dimensions of velocity and acceleration vectors to assign to the corresponding flow field information to the grid locations.

Grid spacing for capturing the steady flow field information is defined to be 5 mm which corresponds to the half of the separation distance between the surface markers. Hence, the location information of membrane shape at the grid locations are supersampled by means of trilinear interpolation.

6.3.1 Velocity Field Reconstruction

The velocity field information for three different steady membrane deformation levels of upward, neutral and downward forms reconstructed following the aforementioned procedure of binning. The results are presented with planar profiles of the streamwise velocity distributions accompanied with flow streamlines presenting the main flow direction in order to demonstrate the fluid's response to respective surface deflection levels.

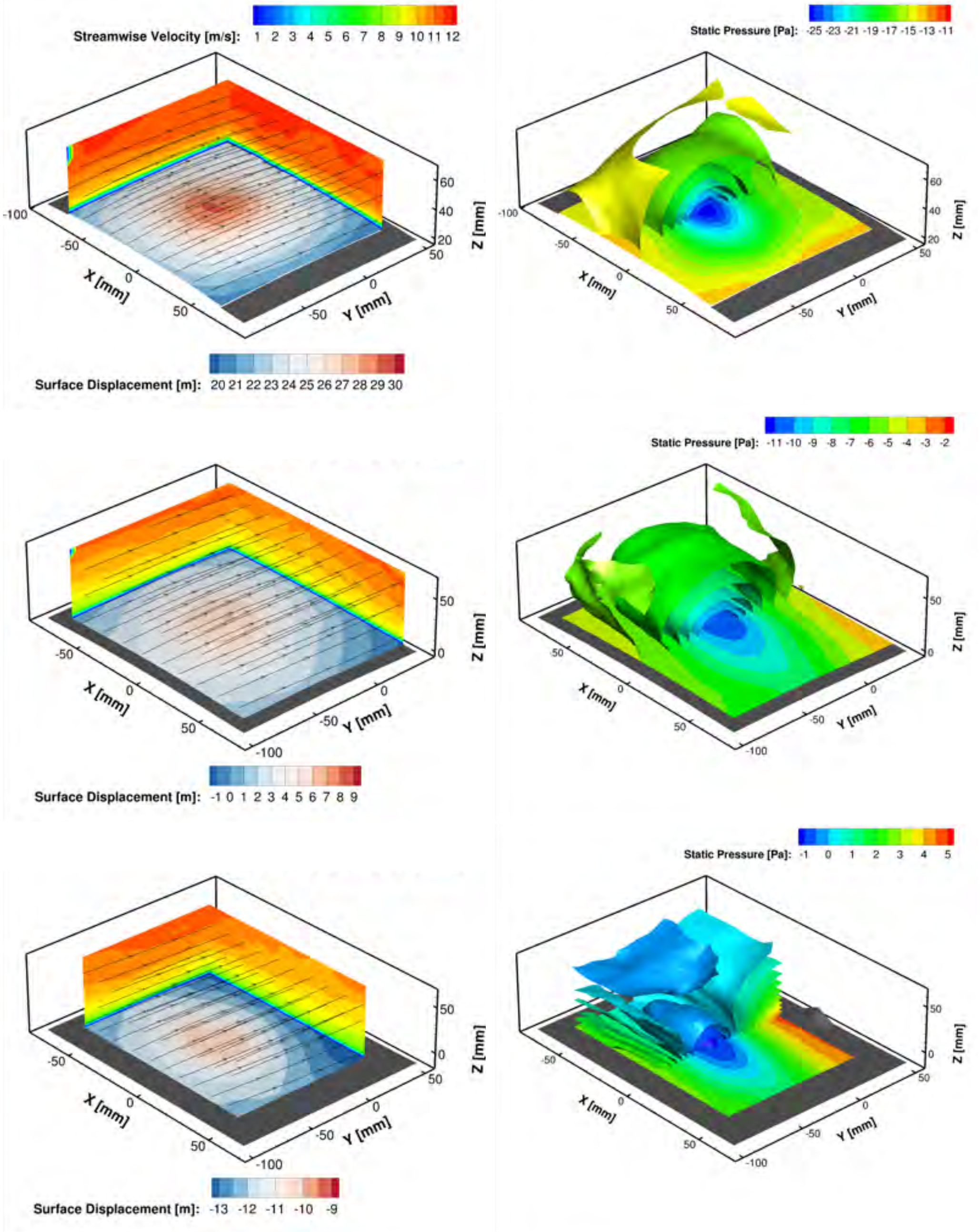

Figure 6.7: Volumetric velocity (left) and pressure (right) field information for steady membrane deformations of upward (top), neutral (middle) and downward (bottom) positions.

Considering the volumetric velocity profiles, two main conclusions are drawn regarding the steady flow behavior. First of all, with increasing deflection level of the surface in the upward direction, the flow remains fully attached to the membrane surface without any case of separation observed. Hence, the corresponding flow behavior of streamlines following the deformed membrane shape yields local contractions of flow cross-sections the regions of high upward deformations that accelerates the flow in consideration of mass conservation complying with the incompressible flow conditions. Furthermore, the scale of the vertical flow motion is in direct correlation with the surface deformation magnitude in the positive upward direction. In a general sense, as the flow approaches to the membrane, it is deflected upward following the membrane surface aligning with the horizontal axis over the central location of the membrane and deflecting downwards, downwind of the deformation center to be aligned with the initial flow direction. The rate of deflection in the wall normal direction and the corresponding velocity component magnitudes increase with in accordance to the deflection levels induced to the membrane.

6.3.2 Pressure Tab Measurements

The steady probe measurements at two different locations of upwind and central membrane are analyzed by combining the measurement data of two consecutive runs as it is performed for the optical measurements to increase the accuracy of time averaged pressure values.

In order to increase the statistical convergence rate on the averaged pressure readings, the time separation of statistically independent samples is determined by means of a time correlation analysis (Hansen and McDonald, 2006). The first zero crossing of the time correlation function is considered to be the integral time scale, T, for the statistically independent samples (Ross, 2017), hence the sampling rate is determined as $1/2T$. The accurate measurement values are considered to be contained within the interval of 3 standard deviations from the time averaged values. Thus, the measured data outside of this region is considered to be outliers which are removed to prevent any overestimation of the fluctuations and to obtain unbaised statistical results (Tim et al., 2007). Finally the measurement uncertainty is determined by,

$$u_p = k\frac{\sigma_p}{\sqrt{N}} \tag{6.1}$$

where u_p, σ_p and N refers to the uncertainty in pressure measurements from the pressure tabs, standard deviation of pressure fluctuations and the number of statistically independent samples. k corresponds to the coverage factor which is selected to be 3 for 99.9% confidence level.

To start with it should be noted that the neutral position for the membrane deformation corresponds to a slightly upward deformed shape in order to obtain a greater level of deformation for the maximum deformation configuration. With the membrane deformed in flow normal direction the cross-sectional area of the control volume of fluid motion is contracted towards the central section of the membrane and expanded dowstream as the membrane converges with the aluminum housing. Hence, with regards to the mass conservation, the flow accelerates as it passes over the central membrane location and

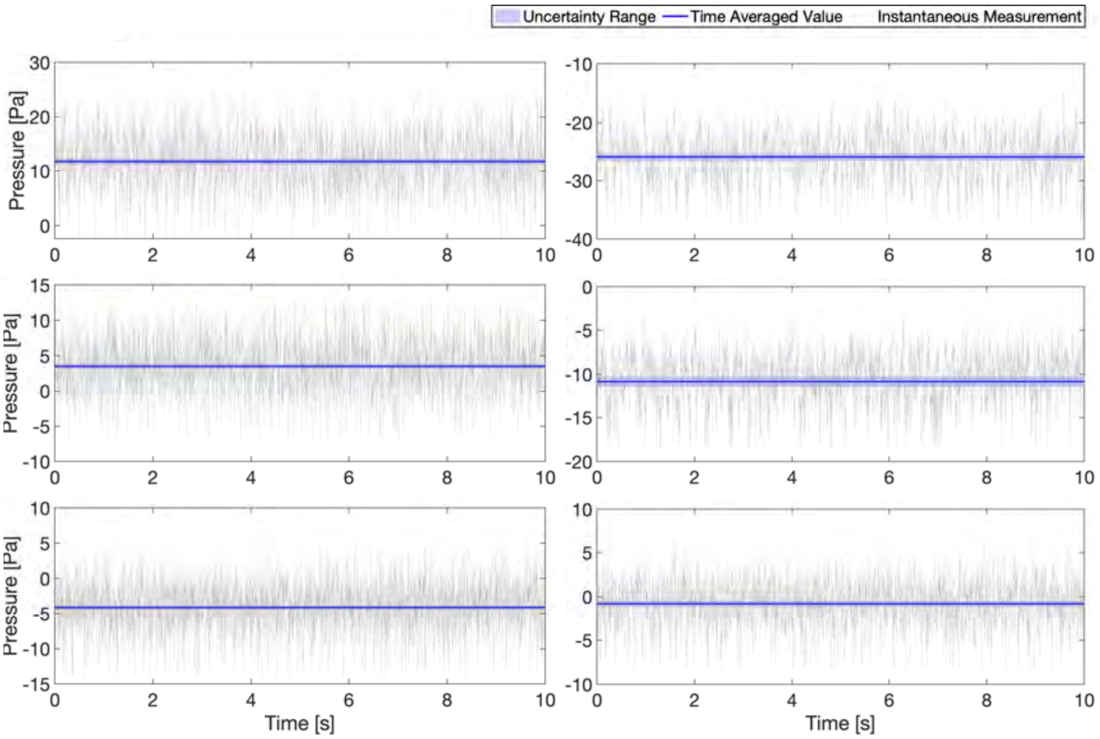

Figure 6.8: Pressure tab measurements of membrane at upward (top), neutral (middle) and downward (bottom) positions for upwind (left) and central (right) pressure tab locations.

decelerates downstream to reach the inflow flow speed. Therefore, in agreement with the Bernoulli principle stating the inverse relation between static pressure and the square of fluid velocity magnitude, pressure decrements is observed over the central membrane location which reduces its amplitude with the decreasing levels of deformation imposed to the membrane shape.

Regarding the pressure measurements obtained from the upwind pressure tab, it should be stated that the membrane experiences a buckling effect in the region where the upwind pressure tab is located due to the possible fatigue effects elastic membrane might have experienced. Thus, especially in case of the upward and neutral positions of the membrane deformations, the buckling creates a smooth cavity where the flow experiences a local deceleration which yields higher static pressure values compared to the ambient conditions. Therefore, in comparison to the expected measurements of similar pressure variation profiles acquired with the central pressure tab at lower amplitudes, it provides the opposite flow behavior. Furthermore, the disagreement of the observed opposite characteristics can be captured by the pressure measurements for the membrane at downward position whose reasoning is referred to the aforementioned sag observed for the membrane form because of the possible plastic deformations, Fig.6.8.

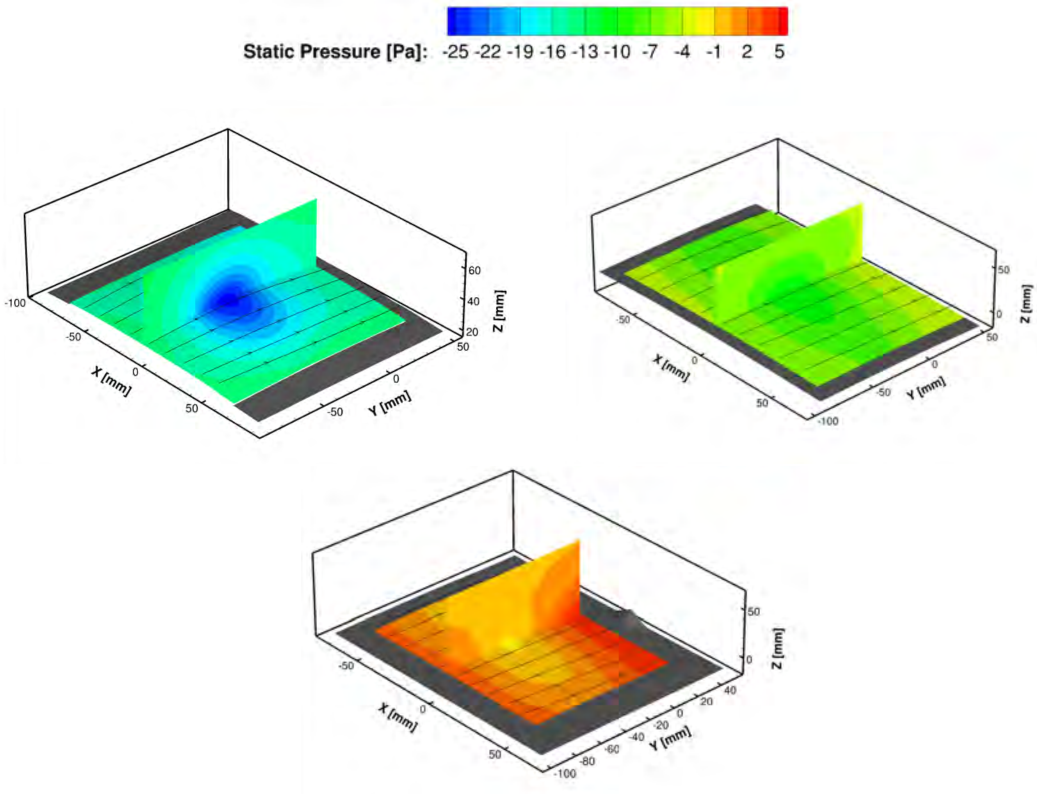

Figure 6.9: Volumetric and surface pressure reconstruction with boundary fitted coordinates from STB data for membrane deformation levels of upward (top-left), middle (top-right) and downward (bottom).

6.3.3 Pressure Field Reconstruction

Considering the decomposed description of material acceleration terms representing the pressure gradients, it can be observed that the velocity gradients in the streamwise and spanwise direction yield positive acceleration values of streamwise velocity components towards the membrane central location where the largest magnitudes of streamwise velocity are observed. Hence, the corresponding effect on the pressure with a minus sign relating the material accelerations to the pressure gradients is a low pressure region over the central location of the membrane. Furthermore, because of the flow deflections in the wall normal direction, streamwise gradients of the wall normal velocity possess positive values with greatest acceleration occur as the flow starts to interact with the deformed membrane shape and immediately switches to negative values over the central location of the membrane in order to follow the membrane shape in absence of any separation. As the flow approaches to the downstream edge of the membrane, the magnitude of acceleration in the negative normal direction diminishes and the flow gets aligned with the horizontal plane, Fig.6.9. During this interaction period the variations in the wall normal velocity component induces negative pressure gradients in the wall normal direction that increase over the central location of the membrane as the streamwise velocity values increase due to the local contraction of the control volume cross sections and amplify the pressure decrease observed over the central membrane location. The scale of this motion in terms of acceleration magnitudes and the corresponding pressure values correlates with the membrane deformation levels. The reconstructed deformed membrane profiles reveal upward directed hill forms at each level of deformation while changing its amplitude in terms of the hill height, Tab.6.2.

Membrane Deformation	Pressure Tab [Pa]	PTV[Pa]
Upward	-25.89	-25.77
Neutral	-10.83	-10.98
Downward	-0.80	-1.18

Table 6.2: Static pressure values at the central membrane location obtained from the pressure tab measurements and pressure reconstruction algorthim.

6.4 Unsteady Membrane Deformations

The unsteady membrane deformations induced by the installed DC motor at three different frequencies of 1 Hz, 3 Hz and 5 Hz are analyzed initially in terms of the instantaneous variation of pressure measurements acquired via the pressure tabs. In order to increase to the reliability of the periodic static pressure evolution obtained over two runs of measurements, static pressure values are analyzed by means of ensemble averaging the static pressure values representing the pressure variation induced due to the sinusoidal membrane motion.

In addition to the unsteady pressure profiles illustrated in Fig.6.8, in order to investigate the unsteady flow features at different steady membrane deformation configurations, frequency spectrums of central pressure tab measurements are decomposed via fast fourier transforming (FFT) the pressure signals which provides the quantification of oscillations frequencies and their respective amplitudes.

Prior to the physical conclusions drawn from the FFT analysis, it should be noted that two very dominant frequencies are observed for all three membrane shapes at similar amplitudes. These frequencies of 120 Hz (Fig.6.12, A) and 240 Hz (Fig.6.12, B) are determined to exist due to the wind tunnel operation specifications. Hence, they are not representatives of the characteristic flow features which are being modified due to the variations on the membrane form. Besides the uncorrelated oscillations within the fluid flow exposed to different membrane shapes, the major variation in the amplitude range of low frequency oscillations reveal a significant increase on the higher amplitude unsteady effects in relation with the upward deformation level of the membrane. Thus, as the intrusion of the membrane form towards the fluid domain is increased with positive upward deformation, the strength of the unsteady fluctuations in terms of low frequency oscillations follow an amplifying trend.

Furthermore, the pressure tab measurements for the unsteady membrane motion is analyzed following an ensemble averaging procedure. The complete data set of 3 measurement runs are partitioned to three periods, $3T$, of pressure readings according to the respective frequencies of membrane motion. Each $3T$ time period of measurements is treated as a sample of membrane motion cycle and the unsteady pressure variations are

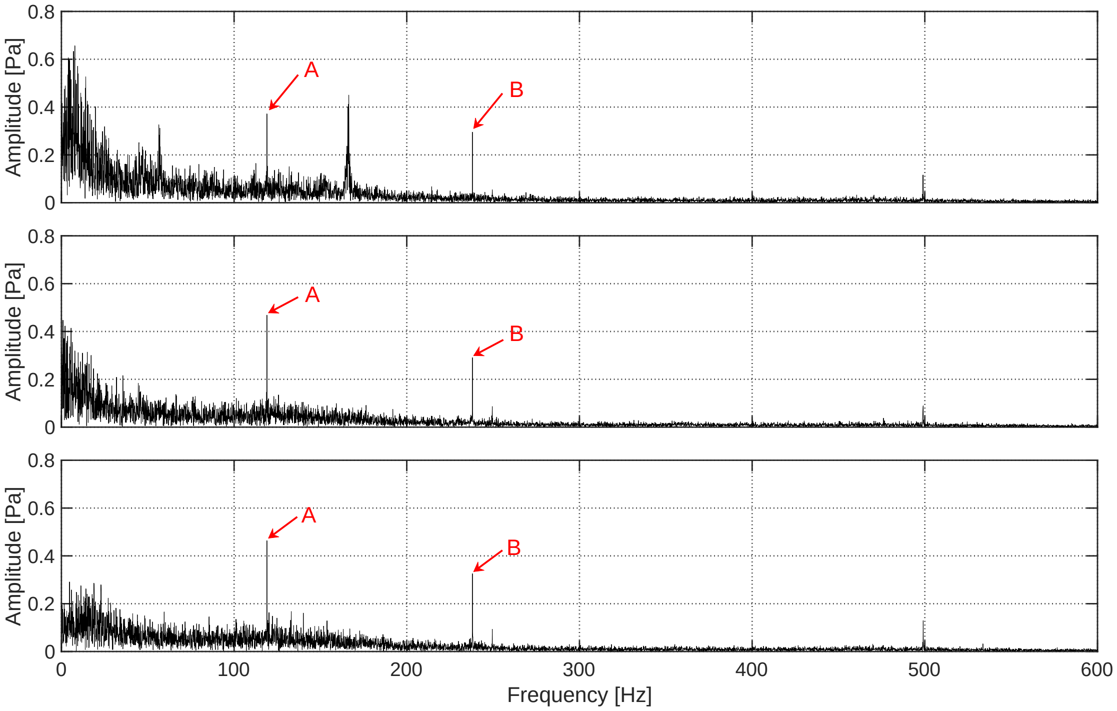

Figure 6.10: Frequency spectrum analysis for instantaneous fluctuations of pressure tab measurements.

computed by ensemble averaging while the uncertainty for the pressure measurements is calculated using Eq.(6.1) over the individual measurement locations of t/T.

With regards to the influence of unsteady membrane motion on the pressure variations observed over the fluid domain which relates an amplification over the pressure variation amplitudes observed over the period of membrane motion, the influence of such an amplification effect cannot be captured due to the low reduced frequencies with respect to the incoming fluid speed except the 5 Hz case. Nevertheless, as the membrane motion frequency is increased, the acceleration of the membrane and its effect on the surface pressure variations, slightly amplify the oscillation amplitude especially at the peak locations of the membrane motion (upward and downward positions). However, the setup operation conditions set to reach the 5 Hz of membrane motion frequency resulted in severe mechanical oscillations on the aliminium housing of the membrane. Therefore, even though theoretically expected results in terms of unsteady variation of pressure values are captured, considering the uncertainty limits shown in Fig.6.11, it shall be denoted that these mechanical oscillations might be influencing the pressure measurements which might be an influential factor for the amplification of oscillation amplitudes.

6.5 Phase-Averaged Flow Characterization

The phase-averaged flow information for the unsteady membrane motion is captured following a similar procedure applied for the steady cases. Each cycle of membrane motion is defined by means of 11 time instants for the respective frequencies and treated

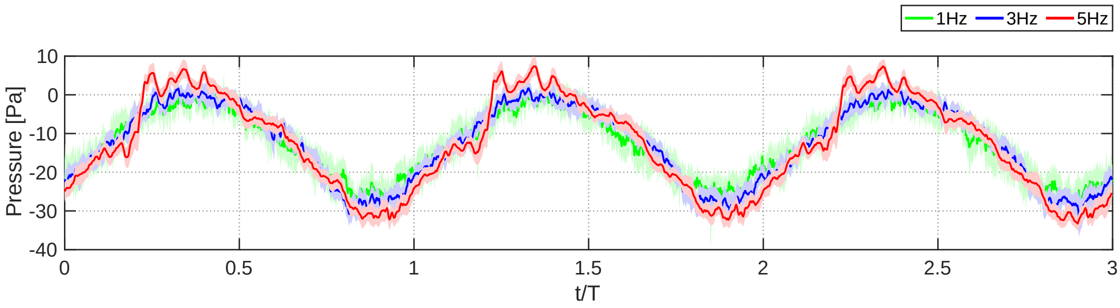

Figure 6.11: Ensemble averaged pressure tab measurements for unsteady membrane motion.

a quasi-steady assumption. Depending on the prescribed time intervals, phases of ΔT time duration are determined for the particle track information to be combined. As the structural measurements provided a greater level certainty and spatial resolution, the fully instantaneous reconstruction of the membrane shape was possible. Hence, the corresponding computational domain is created by starting from a uniformly structured grid and deforming the generated mesh formation using the RBF based mesh deformations based on the location information of membrane surface makers. Finally, the combined particle tracks containing particle velocity and acceleration data are binned over the deformed grid locations.

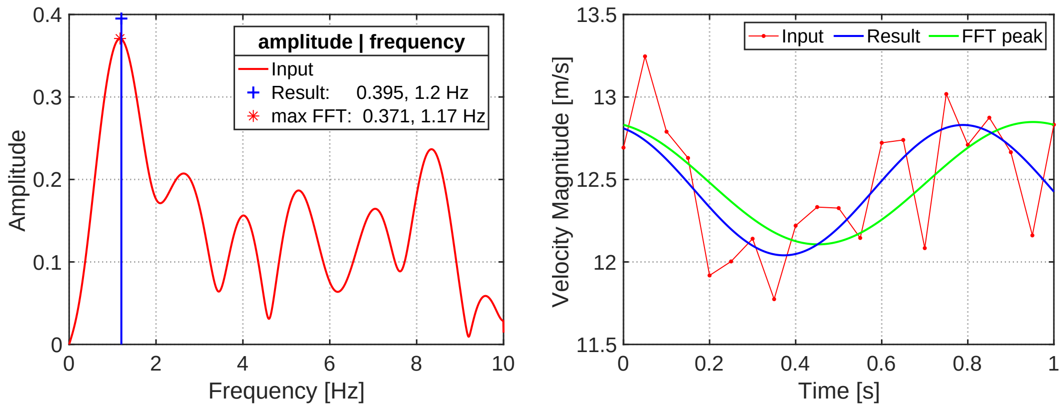

Figure 6.12: Signal reconstruction for the velocity magnitude variation in time performed via employing the FFT analysis on the velocity data acquired proceeding the binning procedure.

The pressure reconstruction algorithm is provided with the material acceleration information captured by the binning procedure and, the corresponding pressure gradient vectors are transformed according to the relation of physical and computational coordinate systems. However, due to the noisy nature of measurement data and the velocity profiles barely reaching the outer edges of the turbulent boundary layers within the reliable measurement domain boundaries, the determination of a reference pressure value in order to obtain a unique solution for the pressure reconstruction problem became non-trivial. Since the expected velocity variations in correspondence to the membrane motion cannot be captured by the binning procedure, the exact values of the reconstructed pressure information deviated from the physical flow behavior when the binned velocity magnitudes are directly employed within the Bernoulli equation.

Therefore the Dirichlet boundary condition for the pressure fields is computed by performing a FFT analysis on the velocity signal captured by the binning procedure at the reference pressure location. As the FFT analysis provided the amplitude of velocity fluctuations at various frequencies, the frequencies of dominant oscillation amplitudes and their respective harmonics are extracted in order to reconstruct the velocity variation cycles at the reference pressure location.

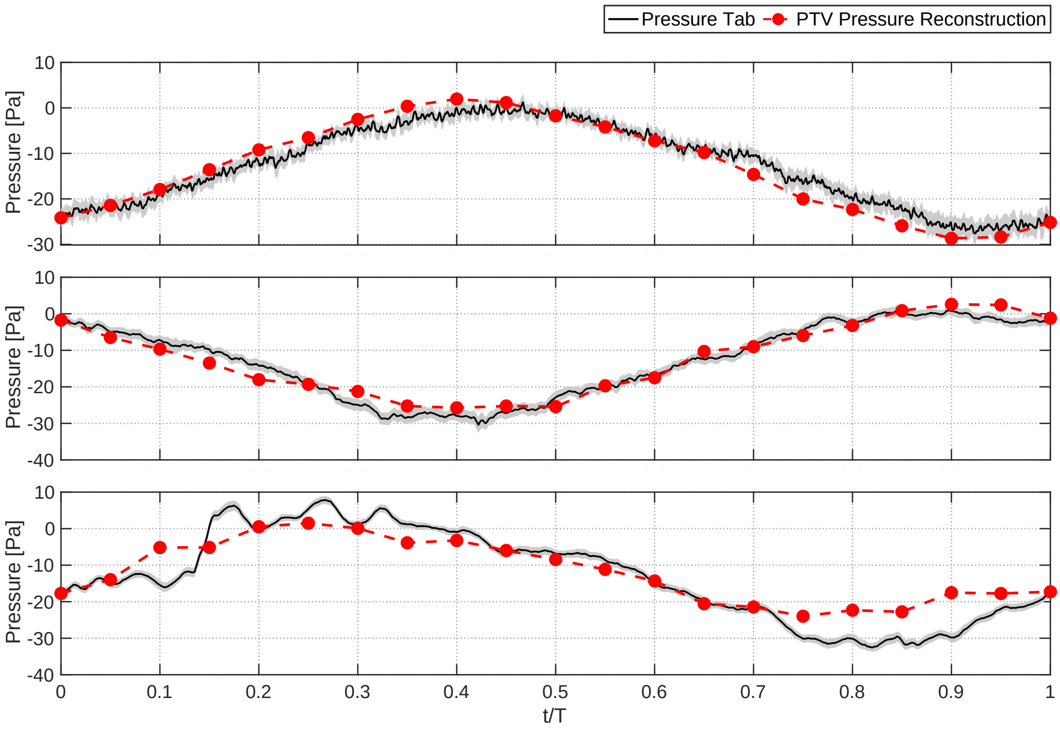

Figure 6.13: Phase averaged pressure reconstruction via ALE method in comparison to the pressure tab measurements for 1Hz (top), 3Hz (middle) and 5Hz (bottom) of unsteady membrane motion.

Utilizing the interpretation ALE method for pressure reconstruction over the experimental PTV data, where at each time instant the Lagrangian information of surface motion is used to deform the computational grid accordingly, the phase averaged flow field information is captured according the quasi-steady state of pressure variations. Referring to the two main aspects of the time evolution of pressure values at the central membrane location, the theoretical assumption of zero normal pressure gradients within the turbulent boundary layer is observed reveal a superior effect for determining the amplitude of pressure variations as the reference pressure value computed using the FFT signal analysis performed over the temporal trace of velocity values provided 70% of the pressure variation amplitudes throughout the motion cycle of the membrane. On the other hand, the integration of phase averaged pressure gradients over the computational domains composed the 30% of the pressure variation amplitudes to reconstruct the total variation cycle of pressure values which yield a significantly good agreement with the pressure tab measurements within the respective uncertainty limits, Fig.6.13.

Even in the case of 5 Hz of membrane motion frequency where certain unreliability concerns arose due to the mechanical oscillations observed on the structural housing of the experimental setup, the reconstructed pressure values are captured in close agreement with the pressure tab measurements. Nevertheless it should be noted that the pressure tab measurements at 5 Hz membrane motion frequency did suffer from larger measurement uncertainties referring to the greater oscillation amplitudes captured especially at the upward deformation point over the motion cycle due to the high impact forces of membrane on the aluminum housing.

6.6 Instantaneous Flow Characterization

Referring to the aforementioned discussion on the complete unsteady nature of FSI problems, the local closure of Collar's triangle of aeroelasticity demands a fully time-resolved characterization of the flow state. As the employed large-scale experimental setup suffers from scarcity of tracer particles which are scattered over the measurement domain, direct usage of the particle tracks reconstructed via STB algorithm becomes inadequate to yield deterministic results with regards to the velocity and acceleration distributions over the region of interest due to the severely downgraded spatial resolution specifications for accurate pressure distribution calculation. An average of ∼150 particles are captured within the measurement domain yielding track concentrations of approximately 50 par/h, where h refers to the maximum deflection height. In the previous chapters where the validation datasets are downsampled to meet the experimental conditions in which the particle concentrations were adjusted according to the present measurement campaign, it is undeniably observed that the standalone processing of particle tracking information for fluid flow characterization neither was able to offer a resemblance with the reference flow fields nor captured any secondary flow effects such as cross flow components.

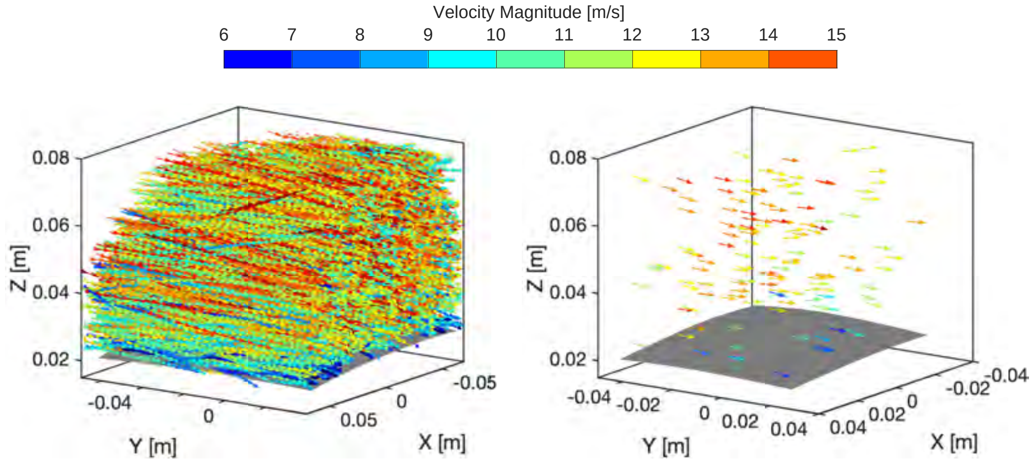

Figure 6.14: Available particle tracking information for phase averaged ensemble of STB output (left) and instantaneous STB output (right).

Similarly, as the unsteadily available particle tracking information is captured at a predefined grid structure by means of the aforementioned binning approach with the membrane unsteadily deforming at three different frequencies, even though bin sizes with significantly increased overlapping characteristics are employed, both velocity and pressure distributions do not provide any characteristic spatial variation while many of the grid locations fall short of local particle densities to allow the binning procedure to assign a flow information. Therefore, trilinear interpolation, VIC+ with Arbitrary Eulerian-Lagrangian (ALE-VIC+) and immersed boundary treatment (ImVIC+) implementations are employed to increase the spatial resolution of flow field information for time-resolved reconstruction of surface pressure distribution over the elastic membrane. Both proposed methods of ALE-VIC+ and ImVIC+ are individually compared against the linear interpolation approach to demonstrate the elevated physical coherence of the densely reconstructed flow field information with the present physical features of the flow via utilizing flow governing equations.

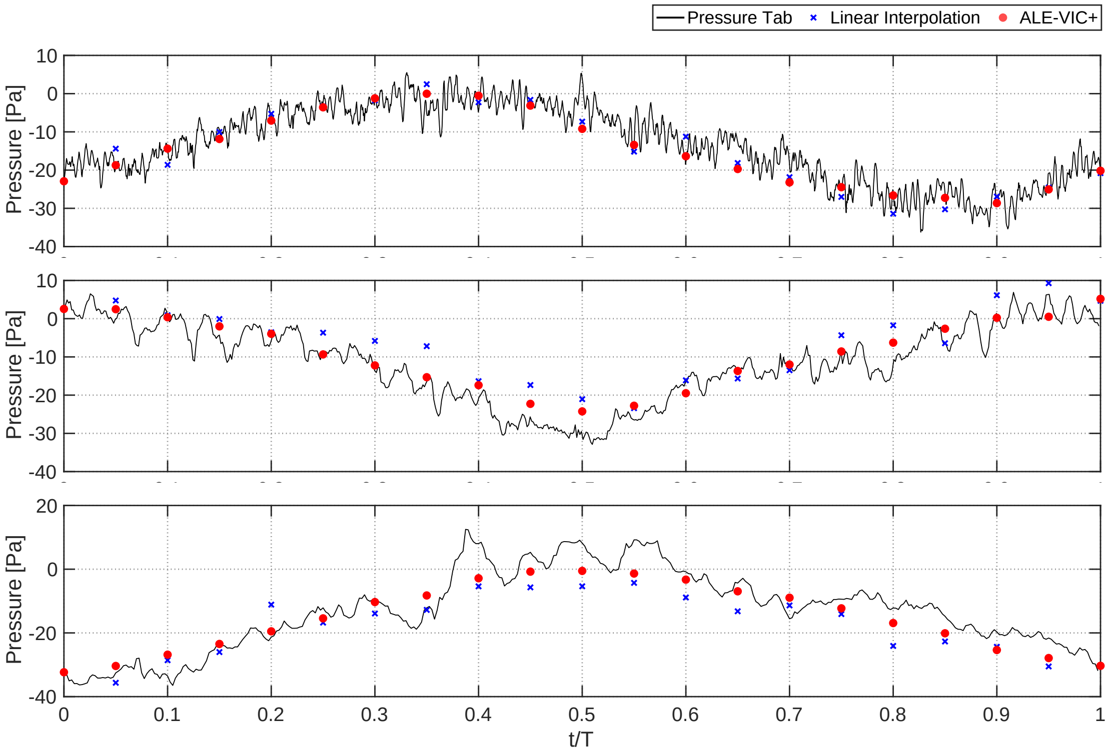

Figure 6.15: Instantaneous pressure reconstruction of linear interpolation and ALE-VIC+ methods in comparison to the pressure tab measurements for 1 Hz (top), 3 Hz (middle) and 5 Hz (bottom) of unsteady membrane motion.

The ALE-VIC+ algorithm proceeds with two main steps where the basis of the method utilizes a boundary fitted coordinate system generated for the membrane which is initiated considering the membrane to be positioned at a neutral position of zero deformations. Then, according to the captured structural information of the membrane motion acquired via surface tracers, the boundary conformation of the grid structure is preserved as the complete computational mesh is deformed using RBF based interpolations over motion cycle of the membrane deformations. Hence, at each time instant the computational grid is updated according to the structural information and the available particle tracking information is augmented with a boundary fitted variant of VIC+ corresponding to the optimization procedure of ALE-VIC+. Contrarily, ImVIC+ method employs a structured uniform grid structure for the dense interpolation of fluid properties whilst providing the appropriate corrections to the velocity field reconstruction procedure to satisfy the necessary physical conditions over the solid surfaces. As the linear interpolation approach is employed to be compared against the ALE-VIC+ and ImVIC+ approaches, results of the trilinear interpolation also employed to determine the boundary conditions for the VIC+ based methods as well as setting an initial estimate to increase the convergence speed. Therefore, with regards to the available particle track distributions concentrated over the central membrane region the generated computational domains are localized over the near proximity of the membrane central position in order to provide reliable boundary condition definitions for the aforementioned post processing procedures.

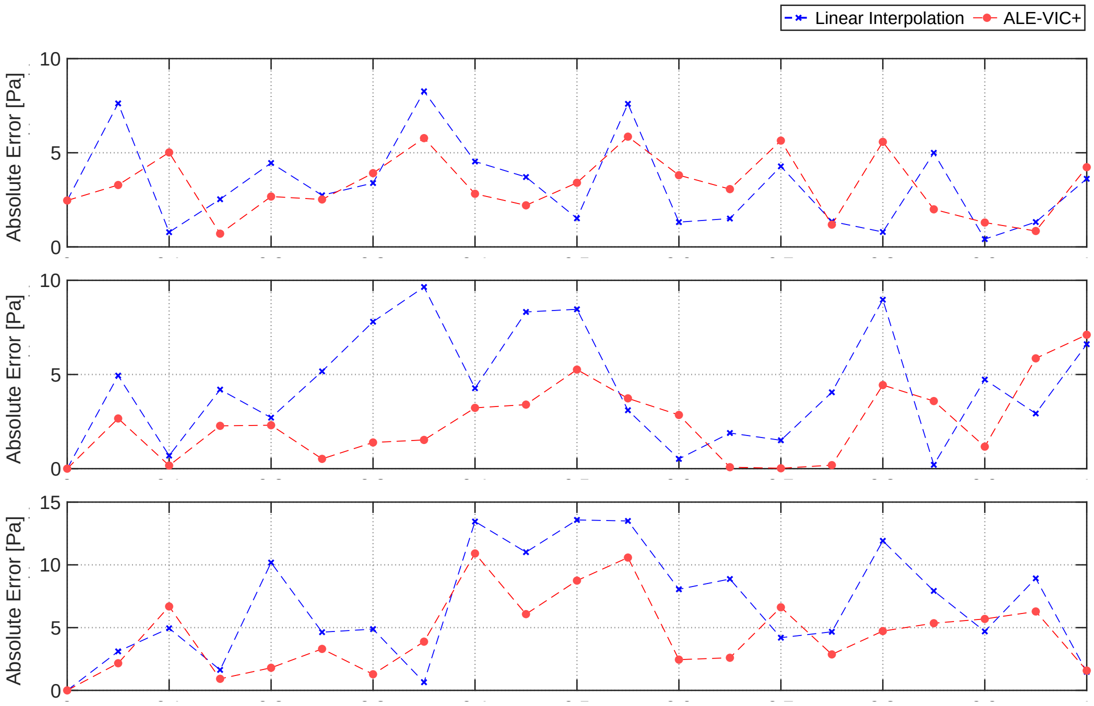

Figure 6.16: Instantaneous pressure reconstruction errors of linear interpolation and ALE-VIC+ methods for 1 Hz (top), 3 Hz (middle) and 5 Hz (bottom) of unsteady membrane motion.

The boundary fitted surface pressure reconstruction algorithm is also employed for the pressure computations over the measurement domain from the densely interpolated particle tracking information as the VIC+ based algorithms allow the reconstruction of material derivatives. Whereas, the pressure reconstruction employing the results of ImVIC+ method is performed over the uniform Cartesian grid with masking the internal region of the solid intrusion. Hence, the static pressure values over the exact surface locations are computed with an omni-directional integration procedure similar to the approach proposed by Jux et al. (2020) where the linear system of equations for the solution of Poisson equation for integrating the pressure gradients is constructed by means of Taylor series approximations for unstructured mesh formations (Feng et al., 2018). The Dirichlet boundary conditions for the unique pressure determination is performed by means of a sinusoidal fitting to the velocity readings at the pressure reference location employing the FFT reconstruction algorithm explained previously. The resultant velocity values are used to the compute the reference pressure value by means of the Bernoulli's principle.

Considering the physical behavior of a flow passing over a locally contracting control volume cross-section, the aforementioned characteristics of local acceleration and deceleration features hold in a general sense which can be obtained when multiple time instants are combined and temporal fluctuations are inherently lost. As the fully time-resolved characteristics are analyzed, these fluctuations become dominant factors determining the velocity and pressure distributions over the measurement domain. In regards to the present experimental conditions in which the turbulent boundary layer profiles are captured to be larger then the previously conducted planar PIV measurements, the reconstructed computational domains are barely able to reach to the boundary layer thicknesses as the measurement domains are cropped to ensure reliable boundary condition deformations.

Table 6.3: Instantaneous pressure reconstruction errors [Pa] of linear interpolation and ALE-VIC+ methods for 1 Hz, 3 Hz and 5 Hz of unsteady membrane motion.

	1 Hz	3 Hz	5 Hz
Linear Interpolation	3.78	3.84	10.10
ALE-VIC+	2.80	2.14	5.07

Nevertheless, even though time-resolved fields represent the instantaneous turbulent boundary layer conditions over the computational domains, the influence of membrane deformations are clearly observed when the time evolution of surface pressure at the central membrane location is reconstructed over 21 time instants for each frequency of motion representing the complete motion cycles of the membrane deformations. As the corresponding reduced frequencies obtained with the membrane motion of 1 Hz and 3 Hz are $k \leq 0.05$, the instantaneous impact the unsteady membrane motion imposes on the flow conditions is rather insignificant since the flow profile proceeds over a quasi-steady state, Figs.6.15 & 6.17 (1^{st} and 2^{nd} rows). Nevertheless, the reduced frequency generated with 5 Hz membrane motion frequency corresponding to $k \approx 0.1$ with the half chord length of 0.25 m, falls in the regime of unsteady aerodynamic features (Leishman, 2016). Thus, in comparison to the pressure tab measurements the time-resolved surface pressure, reconstructed pressure profiles yields almost identical pressure variations which are in great agreement for 1 Hz and 3 Hz cases while the 5 Hz case exhibits underestimated static pressure values for the time period where the membrane approaches its lower most position, Figs.6.15 & 6.17 (3^{rd} row). Even though with both time resolved reconstruction methods of ALE-VIC+ and ImVIC+, the underestimation errors observed over the high amplitude fluctuations of pressure tab measurements are observed to be lower compared to the phase averaged pressure reconstruction approach performed by binning the STB data directly.

Furthermore, comparing the reconstructed surface pressure information from trilinear interpolation to ALE-VIC+ and ImVIC+, a clear difference between the trilinear interpolation and VIC+ based methods is captured where the latter two methods approach the pressure tab measurements significantly in both three frequencies. Although the overall

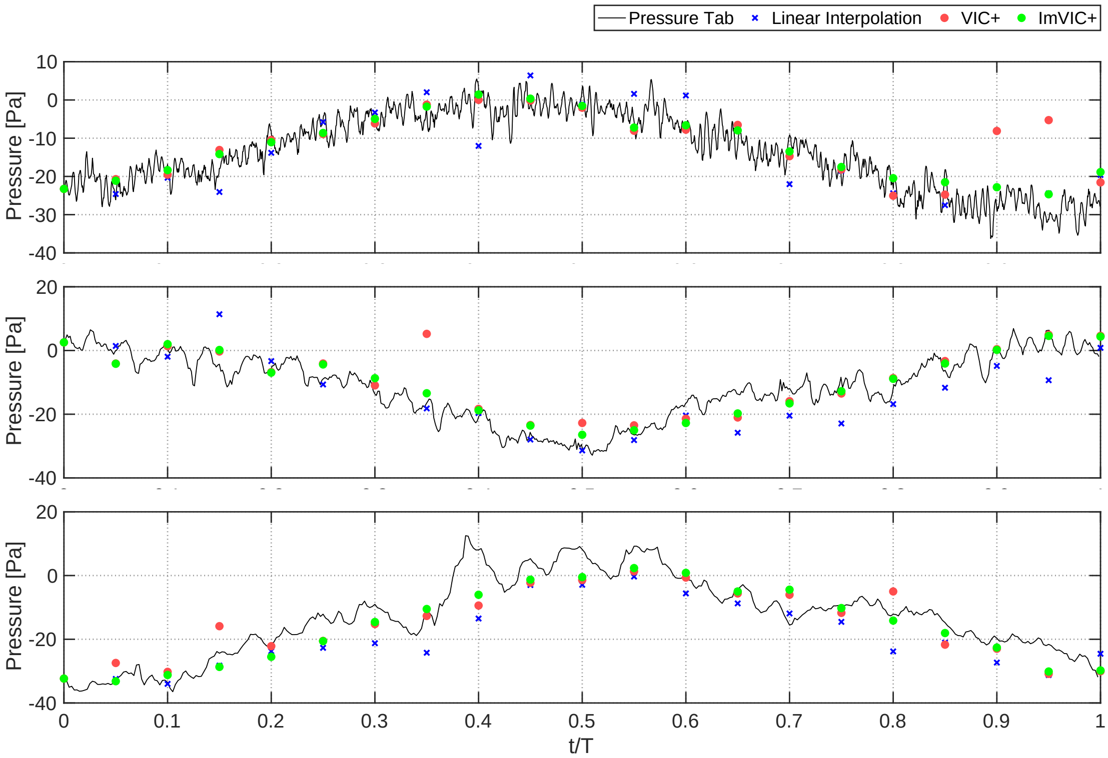

Figure 6.17: Instantaneous pressure reconstruction of linear interpolation, VIC+ and ImVIC+ methods in comparison to the pressure tab measurements for 1 Hz (top), 3 Hz (middle) and 5 Hz (bottom) of unsteady membrane motion.

pressure profiles of all three methods, including standard VIC+ without an immersed boundary treatment, the variations between the different approaches are observed to be relatively confined, both ALE-VIC+ and ImVIC+ enabled a greater agreement with the pressure tab measurements by minor improvements. There exists three main reasons for these minor variations between the different methods which can be deducted in accordance to the validation studies.

First of all, the present flow conditions and the objective of reconstructing surface pressure under these conditions include a relatively straightforward flow formation in absence of major secondary flow structures, such as strong vortices. Hence, the spatial variations of both velocity and pressure distributions are composed of mild gradients of flow properties over the measurement domain where the overall flow profiles do not contain any separation features as well as dominant vortices. Therefore, as the linear interpolation is performed, these smooth gradients can be reconstructed without severe loss of accuracy over the computational domain.

Secondly, as the flow behavior is determined by these smooth variations over the measurement domain, the flow properties outside the turbulent boundary layer are independent of the fluctuations present within the turbulent boundary layers which yields a dominant pressure variation determined by the Bernoulli principle. Considering the fact that assumption of zero pressure gradients in the surface normal direction within the turbulent boundary layers is violated in physical cases, pressure variation levels of

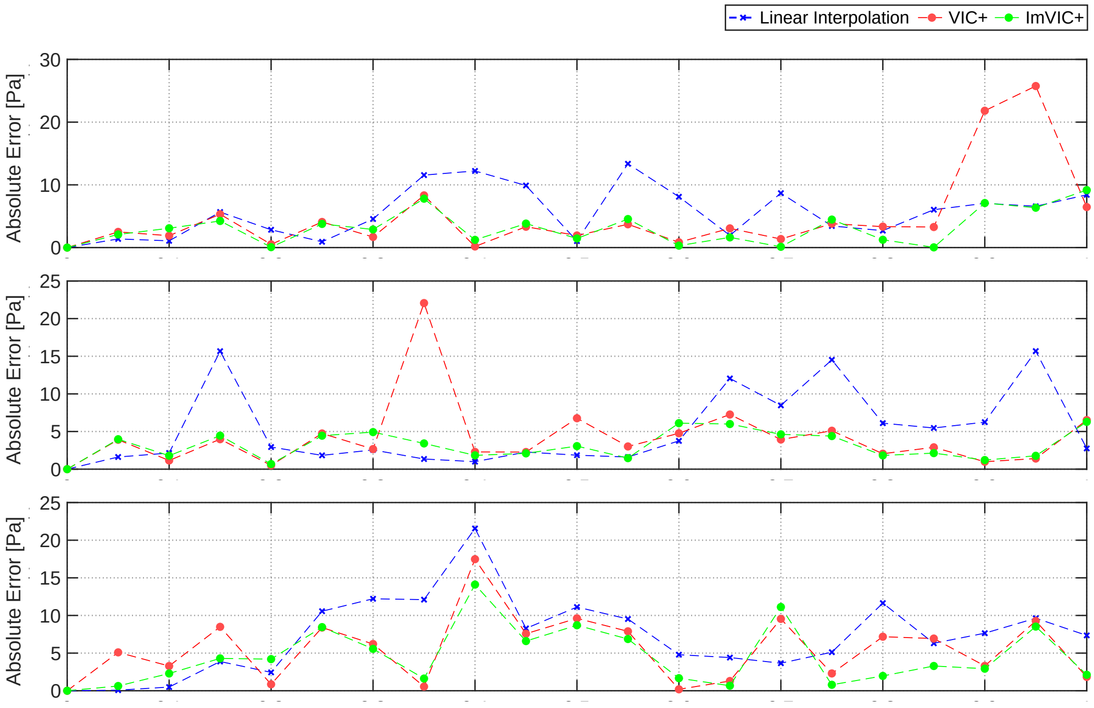

Figure 6.18: Instantaneous pressure reconstruction errors of linear interpolation, VIC+ and ImVIC+ methods for 1Hz(top), 3Hz(middle) and 5Hz(bottom) of unsteady membrane motion.

approximately 6∼8 Pa are captured between the surface locations and the outer edges of the turbulent boundary layers. Nonetheless, when these pressure variations are normalized with the absolute pressure difference captured at highest and lowest points of the membrane motion which is ∼30 Pa, the pressure modulations aimed to be reconstructed with a superior accuracy by ALE-VIC+ and ImVIC+ correspond to ∼25%, Figs.6.16 & 6.18.

Finally, the boundary conditions for ALE-VIC+ and ImVIC+ methods are determined via linearly interpolating the STB data over the corresponding boundaries. Hence, as the reference pressure location for the Dirichlet boundary condition is located considerably close to the boundaries of the computational domain, the variation of velocity values between the trilinear interpolation and VIC+ based approaches is significantly small. Therefore, as the sinusoidal fitting is performed over these velocity values, the difference between the three different algorithms is almost completely smoothened out. Thus, with the dominance of Bernoulli principle over the temporal variation of pressure distributions, the attainable improvements with the applications of ALE-VIC+ and ImVIC+ over the trilinear interpolation is further reduced, Tab.6.3 & 6.4..

Finally, concentrating on the modifications observed with the implementation on an immersed boundary treatment for VIC+ specifically, the resultant pressure profiles are captured which is in direct correlation with the validation studies performed on the flow over the periodic hills case. As the membrane surface and the corresponding the computational domain is enclosed by the boundaries of the grid structure the improvements obtained in terms of the agreement with the pressure tab measurements are relatively small

Table 6.4: Instantaneous pressure reconstruction errors [Pa] of linear interpolation, VIC+ and ImVIC+ methods for 1 Hz, 3 Hz and 5 Hz of unsteady membrane motion.

	1 Hz	3 Hz	5 Hz
Linear Interpolation	5.44	5.24	7.32
VIC+	6.27	4.96	5.22
ImVIC+	1.71	2.08	3.64

compared to the complete modulation levels over the membrane motion cycle. Nevertheless, there are two important factors that yield the application of ImVIC+ promising. First of all, the flow behavior is absent of any separation effects which correlates the rotational component of the flow structure to the turbulent boundary layer characteristics. Hence, the overall flow structure is characterized by the smooth fluid flow following the membrane shape that relates the potential component to be the deterministic element. Additionally, as the influence of surface singularities mitigate away from the surface, the time evolution of velocity magnitudes at the pressure reference location is almost identical with VIC+ without the immersed boundary treatment. Hence, due to the fact that the dominant factor for pressure variation in the temporal domain is the reference pressure values obtained utilizing the Bernoulli principle, the results of VIC+ and ImVIC+ reveal a significant similarity compared with the pressure tab measurements. Nonetheless, there exists certain time instants where major differences between VIC+ and ImVIC+ are observed. This is due to the local presence of high velocity magnitudes of captured particle tracks closer to the surface elements owing to the turbulent boundary layer structure, that influence the surrounding flow behavior during the optimization procedure. Thus, the corresponding influence of immersed boundary treatment provides the necessary local corrections to the flow properties to satisfy the zero normal velocity condition and modify the acceleration values accordingly. Consequently, the RMS of absolute error values in terms of static pressure properties result in consistently lower values for implementation of immersed boundary treatment over VIC+, ImVIC+.

Chapter 7

Conclusions and Recommendations

Characterization of fluid-structure interactions (FSI) involves time-resolved determination of fluidic behavior in relation to the structural deformations. In use of experimental simulations where the physical features of the fluid and solid domains are captured by means of large scale tomographic PIV/PTV measurement techniques, instantaneous characterization requires further processing of the raw measurement data in terms of assimilation and reconstruction of various fluid properties. Although there exists available methods for this purpose, these methods do not provide specific capabilities of resolving wall adjacent flow field properties, handling of non-uniform surface deformations and correction of erroneous experimental data acquisitions. In that regards, Section 7.1 summarizes the conclusions of the work content of the thesis project and, 7.2 provides recommendations for possible future improvements of the proposed methods and introducing alternatives.

7.1 Conclusions

Available spatial resolution characteristics for time-resolved flow field measurements with large scale tomographic PIV/PTV techniques are significantly restricted due to the tracer particle specifications of Hellium Filled Soap Bubbles (HFSB). This restriction requires additional post-processing algorithms to be applied over the raw experimentally acquired data in order to mitigate the effect of experimental trade-off between the temporal and spatial resolution specifications allowing instantaneous flow field characterization. In accordance to the literature review, governing equation based techniques such as FlowFit (Gesemann et al., 2016) and VIC+ (Schneiders and Scarano, 2016) stand out in terms of providing high resolution flow features by assimilating the available scattered particle tracking information for global time-resolved flow field reconstruction. Nevertheless, as accurate characterization of FSI problems requires proper determination of flow structures in close proximity of the interaction interface, which significantly affects the reconstruction accuracy of the complete fluidic domain, three main drawbacks of these algorithms arise.

First of all, the near wall flow features for turbulent boundary layers are determined in viscous force dominance for a thin layer of fluid particles where the VIC+ algorithm does not contain the necessary governing equation details to cohere with the appropriate flow physics. In combination with the scarcity of particle tracking information captured within the sublayers of a turbulent boundary layer, the velocity profiles reconstructed by means of VIC+ deviate from the physical flow behavior. In order to account for the effect of viscous interactions in close proximity of wall surfaces for determination of appropriate boundary conditions, a wall function approach for the VIC+ algorithm is implemented, utilizing the universal logarithmic laws of turbulent boundary layers. The introduced wall function approach for VIC+ is tested with numerical simulations of a well-developed channel flow. The wall function application enabled accurate characterization of average streamwise velocity profiles while owing to the fact that the *Law of the wall* only refers to an empirical representation of average streamwise velocity characteristics, the fluctuating components, as well as the spanwise and normal velocity profiles, revealed underestimations within the regions of experimental data absence. Nevertheless, slight improvements of streamwise velocity fluctuations are achieved due to the local applications of the wall functions compared to the standard formulation of VIC+ with no-slip boundary condition.

Secondly, FSI problems include unsteadily deforming non-uniform domains where accurate determination of fluid and structure behaviors requires proper definitions of interface conditions. Since, the VIC+ method is developed to be based on characterizing the fluid properties for regions of uniform rectangular computational domains with sole fluid presence, there exists no prior attempt to characterize kinematic interaction relations of solid boundaries intruding the fluid domain. Therefore, in order to enable the handling of non-uniform solid boundary intrusions of unsteadily deforming surfaces for the VIC+ approach, the well established computational FSI frameworks of the Arbitrary Lagrangian-Eulerian (ALE) and the immersed boundary treatment methods are introduced over the standard VIC+ algorithm, providing the capability of determining close proximity flow behavior of the FSI interface.

The ALE approach is introduced to leverage from the individual advantages of Eulerian and Lagrangian descriptions for optimizing the computational cost requirements with high accuracy physical descriptions. Accordingly, an implementation of the ALE method is proposed to formulate the standard VIC+ algorithm to operate with boundary fitted coordinate systems for exact conformation of the FSI interface. The resultant ALE-VIC+ method is designed to be equipped with a radial basis function (RBF) based mesh deformation scheme to ensure the adaptability of the grid formations to the unsteady deformations of the FSI interface. The proposed ALE-VIC+ method is tested with a numerical simulation case of flow over periodic hills where the results are compared against the Adaptive Gaussian Windowing and trilinear interpolation approaches. The initial verification tests of the mathematical formulations of ALE-VIC+ are performed over a rectangular uniform domain which confirmed the exact matching of the reconstructed flow field characteristics with VIC+ in absence of curvilinear coordinates. Then, the flow properties over the hill forms are utilized to evaluate the capabilities of ALE-VIC+ over trilinear interpolation of fluid variables. Even though, both linear interpolation and ALE-VIC+ approaches resulted in coherent flow behaviors with the hill form, the local variations of velocity components revealed major differences between the two, favoring the

ALE-VIC+ in terms of accuracy where the amplitudes of velocity components are resolved with greater agreements to the reference flow field information using ALE-VIC+.

Furthermore, the hybrid mesh-particle approaches such as the VIC framework, allows fast FFT based Poisson solvers to increase computational efficiency using uniform predefined computational grids. Hence, immersed boundary treatments proposed for numerical investigation of FSI problems, introduce additional velocity or forcing terms to characterize the influence of physical intrusions, while preserving the grid structure. In case of vortex simulations, kinematic boundary conditions over the interaction interfaces are satisfied by means of additional potential flow components. Accordingly, an implementation of the immersed boundary treatment is proposed for the VIC+ algorithm where the no-through boundary condition over the non-uniform solid surfaces is satisfied by means of representing the structural surfaces with singularity components, or commonly referred as the panel method. The resultant approach of ImVIC+ computes the velocity field information according to the Helmholtz decomposition where the vortex strengths are used as optimization variables to capture the rotational flow properties while the surface singularities introduce a potential flow component to satisfy the boundary conditions over intruding surfaces. The ImVIC+ method is also tested with the numerical simulations of a flow over periodic hills similar to ALE-VIC+. The ImVIC+ method enabled improvements of reconstruction accuracy over the standard VIC+ algorithm for the flow properties in close proximity of the hill surfaces in terms of streamwise and normal velocity components composing the surface flow penetrations. The modifications achieved on the flow field properties by means of the ImVIC+ approach are confined to the close proximity of the FSI interface and do not affect the regions far away from solid boundaries where the experimental particle tracking information accurately constructs an objective function for the optimization procedure.

Moreover, the local closure of Collar's triangle demands surface loading over the structural elements to be determined according to the the fluid behavior. In that regards, optical measurement techniques of PIV/PTV enables non-intrusive characterization of surface pressure information over solid boundaries while tracking the corresponding structural deformations. Accordingly, the ALE method is interpreted to proposed an alternative surface pressure reconstruction scheme based on PIV data over unsteadily deforming non-uniform boundaries with boundary fitted coordinate systems generated by means of RBF based mesh deformations. Hence, the pressure gradients characterized using the material acceleration values reconstructed via the Shake the box algorithm are integrated on prescribed computational grids which are formed using the Lagrangian descriptions of surface tracer motions. Therefore, the exact conformation of the deformed surface shapes obliterated the necessity of any extrapolation methods for surface pressure distribution determination. The resultant pressure field computations yielded relative error levels below 4% compared to analytical flow field properties where the majority of the errors are related to the numerical method of choice for the integration of pressure gradients rather than the discretizations of mesh deformations and vectorial transformations.

Finally, experimental data acquisition procedures of PIV/PTV contain measurement errors of different forms. As the reconstructed flow field information from the experimentally acquired images used for the data assimilation procedures, these errors propagate to yield physically devaint flow field properties. Throughout the state-of-the-art noise canceling approaches, these errors are characterized with non-zero divergence of velocity vectors that correspond to continuity errors for incompressible flows. Nevertheless, VIC+ method neither contains a cancellation algorithm for possible mass conservation violations nor impose the continuity throughout its formulations. Therefore, an alternative dense flow field interpolation method of Sol+ is proposed to mitigate the propagations of measurement and numerical discretization errors for time-resolved flow field characterization using solenoidal RBFs. Similarly, the inviscid formulation of vorticity transport equation yields a mathematical discretization of the acceleration fields which needs to be rotational free. Hence, in order to ensure the resultant acceleration fields are irrotational, the SGPR algorithm of Azijli and Dwight (2015) is modified with irrotational RBFs to yield the irrotational Gaussian process regression (IGPR) where the ISol+ approach is introduced to utilize the IGPR method for filtering out the rotational components of the reconstructed material acceleration fields.

The proposed methods of Sol+ and ISol+ are tested with theoretical and experimental cases where the theoretical assessment is performed with an artificial Gaussian noise addition to simulate measurement errors contained within the input data of particle tracking information. The mass conservative formulation of Sol+ inherently prevented measurement errors to drive the optimization procedure away from the physical flow features which increased the agreement of the resultant velocity fields with the analytical flow field properties, especially in presence of artificial measurement noise. While the ISol+ did not provide any noticeable accuracy improvement for the velocity and vorticity field characterization due to the scaling specifications of cost function parameters, the major advantage of enforcing irrotationality of material accelerations is observed in terms of the pressure field reconstructions where the accuracy of the static pressure field information obtained using the results of ISol+ revealed greater agreement with the reference experimental data, compared to the standard VIC+ algorithm.

Consequently, the developed methods of wall function implementation, ALE-VIC+ and ImVIC+ are employed for the experimental investigations of turbulent boundary layer interactions with unsteadily deforming elastic membrane. Initial assessments of the volumetric flow field properties are performed over steady membrane deformations and phase averaged unsteady characterizations of velocity and pressure field information in accordance to a quasi-steady assumption of the flow features. The proposed methods of ALE-VIC+ and ImVIC+ are utilized for fully time-resolved surface pressure reconstructions where the instantaneously available low density particle tracking information is assimilated towards dense interpolation of material accelerations to capture temporal evolution of static pressure values at the central membrane location. The superior accuracy specifications of ALE-VIC+ and ImVIC+ methods against trilinear interpolation, achieved by enabling the kinematic discretization of the unsteadily deforming membrane motion, provided greater agreement of the non-intrusive instantaneous pressure field computations with the pressure tab measurements.

7.2 Future Recommendations

Throughout the thesis report, certain short comings of the proposed methods are documented as the algorithms are tested against various reference datasets. Hence the recommendations of future improvements are derived accordingly to compensate these shortcoming and further evolve the introduced approaches.

First of all, the wall function implementation only handles the streamwise velocity components due to the descriptions of universal logarithmic laws. Therefore, actual near wall flow properties are to be captured within the data assimilation algorithms by proper means of viscous considerations over the governing equations. Hence, accurate discretization of the viscous effects shall enable the implementation of physically exact no-slip boundary conditions so that the flow field properties in close proximity of the FSI interfaces can be reconstructed with increased accuracy. Furthermore, with the appropriate formulation of governing equations including the consideration of viscous effects, the immersed boundary treatment can also be modified with surface parallel vortex sheets to satisfy the no-slip boundary condition as well as the no-through boundary condition over solid physical intrusion surfaces.

Secondly, the alternative approach of dense flow field interpolations with matrix valued RBFs revealed promising results towards employment of the proposed method in experimental simulations. In that regards, the use of solenoidal RBF obliterated the need for describing velocity boundary conditions. Nevertheless, boundary conditions for the material acceleration computation procedure are still required to be provided in terms of the temporal velocity derivatives $(\partial\mathbf{u}/\partial t)$. Due to the fact that computation of accurate values for $\partial\mathbf{u}/\partial t$ is extremely challenging owing to the scattered flow field information for large scale tomographic experiments, the use of optimization variables in terms of the material accelerations by utilizing irrotational RBFs can remove this necessity and improve the accuracy of the acceleration field reconstructions which also transfers to the pressure field information. Alternatively, the $\partial\mathbf{u}/\partial t$ values can be introduced as optimization variables. Since for incompressible flows mass conservation corresponds to divergence free velocity fields, the divergence of $\partial\mathbf{u}/\partial t$ are also required to be equal to zero. Therefore, reconstructing $\partial\mathbf{u}/\partial t$ by means of solenoidal RBFs can also remove the obligation of providing boundary conditions for the acceleration computation. Moreover, as $\partial\mathbf{u}/\partial t$ are computed using the vorticity transport equation and a corresponding Poisson relation between the temporal derivatives of velocity and vorticity fields, using $\partial\mathbf{u}/\partial t$ as optimization variables shall reduce the number of numerical calculations which would yield a reduction in the accumulation of numerical discretization and truncation errors.

Furthermore, taking into account the recent developments on Vortex-in-Cell based data assimilation algorithms towards utilizing a sequence of time instants for increasing the accuracy of instantaneous flow field reconstruction such as VIC++ and TSA, the use of solenoidal RBFs with additional optimization variables defined for $\partial\mathbf{u}/\partial t$ can be further elaborated with elevated accuracy possibilities of material acceleration determinations.

References

Adrian, R. J. (2005). Twenty years of particle image velocimetry. *Experiments in Fluids*, 39(2):159–169.

Afzal, N. (2001). Power law and log law velocity profiles in turbulent boundary-layer flow: equivalent relations at large reynolds numbers. *Acta Mechanica*, 151:195216.

Agui, J. C. and Jimenez, J. (1987). On the performance of particle tracking. *Journal of Fluid Mechanics*, 185:447468.

Aguirre-Pablo, A. A., Aljedaani, A. B., Xiong, J., Idoughi, R., Heidrich, W., and Thoroddsen, S. T. (2019). Single-camera 3d ptv using particle intensities and structured light. *Experiments in Fluids*, 60(2):25.

Ahmad, R. (2007). *Improving A Gradient Based Algorithm Using The Momentum Term*, pages 81–92.

Amodei, L. and Benbourhim, M. (1991). A vector spline approximation. *Journal of Approximation Theory*, 67(1):51 – 79.

Anderson, D., Tannehill, J., and Pletcher, R. (2016). *Computational fluid mechanics and heat transfer, Third edition.*

Anderson, J. (2010). *Fundamentals of Aerodynamics.* McGraw-Hill Education.

Asher, W. E., Liang, H., Zappa, C. J., Loewen, M. R., Mukto, M. A., Litchendorf, T. M., and Jessup, A. T. (2012). Statistics of surface divergence and their relation to air-water gas transfer velocity. *Journal of Geophysical Research: Oceans*, 117(C5).

Assato, M., Sena, J., Fico, N., and Girardi, R. (2005). Air intake influence on the test-section flow quality of an open-circuit wind tunnel.

Atkinson, C. and Soria, J. (2007). Algebraic reconstruction techniques for tomographic particle image velocimetry. *Proceedings of the 16th Australasian Fluid Mechanics Conference, 16AFMC.*

Attenborough, M. (2003). Systems of linear equations, matrices, and determinants. In Attenborough, M., editor, *Mathematics for Electrical Engineering and Computing*, pages 295 – 345. Newnes, Oxford.

Augier, B., Yan, J., Korobenko, A., Czarnowski, J., Ketterman, G., and Bazilevs, Y. (2015). Experimental and numerical fsi study of compliant hydrofoils. *Comput. Mech.*, 55(6):1079–1090.

Aurenhammer, F. (1991). Voronoi diagrams—a survey of a fundamental geometric data structure. *ACM Comput. Surv.*, 23(3):345–405.

Auteri, F., Carini, M., Zagaglia, D., Montagnani, D., Gibertini, G., Merz, C., and Zanotti, A. (2015). A novel approach for reconstructing pressure from piv velocity measurements. *Experiments in Fluids*, 56.

Azijli, I. and Dwight, R. (2015). Solenoidal filtering of volumetric velocity measurements using gaussian process regression. *Exp Fluids*, 56:198.

Balaras, E. (2004). Modeling complex boundaries using an external force field on fixed cartesian grids in large-eddy simulations. *Computers & Fluids*, 33(3):375 – 404.

Battle, G. and Federbush, P. (1993). Divergence-free vector wavelets. *The Michigan Mathematical Journal*, 40.

Baur, T. and Kongeter, J. (1999). *PIV with high temporal resolution for the determination of local pressure reductions from coherent turbulence phenomena.*

Bazilevs, Y., Calo, V., Hughes, T., and Zhang, Y. (2008). Isogeometric fluid-structure interaction: Theory, algorithms, and computations. *Computational Mechanics*, 43:3–37.

Beale, J. T. and Greengard, C. (1994). Convergence of euler-stokes splitting of the navier-stokes equations. *Communications on Pure and Applied Mathematics*, 47(8):1083–1115.

Beckert, A. and Wendland, H. (2001). Multivariate interpolation for fluid-structure-interaction problems using radial basis functions. *Aerospace Science and Technology*, 5(2):125 – 134.

Belytschko, T. and Kennedy, J. (1978). Computer models for subassembly simulation. *Nuclear Engineering and Design*, 49(1):17 – 38.

Benedict, L. H. and Gould, R. D. (1996). Towards better uncertainty estimates for turbulence statistics. *Experiments in Fluids*, 22(2):129–136.

Bernard, P. S. (1999). *Toward a Vortex Method Simulation of Non-Equilibrium Turbulent Flows*, pages 161–181. Springer Netherlands, Dordrecht.

Bernardini, M. and Pirozzoli, S. (2011). Wall pressure fluctuations beneath supersonic turbulent boundary layers. *Physics of Fluids*, 23(8):085102.

Beyer, R. P. (1992). A computational model of the cochlea using the immersed boundary method. *Journal of Computational Physics*, 98(1):145 – 162.

Beyer, R. P. and LeVeque, R. J. (1992). Analysis of a one-dimensional model for the immersed boundary method. *SIAM Journal on Numerical Analysis*, 29(2):332–364.

Blazek, J. (2005). Chapter 11 - principles of grid generation. In Blazek, J., editor, *Computational Fluid Dynamics: Principles and Applications (Second Edition)*, pages 373 – 413. Elsevier Science, Oxford, second edition edition.

Bos, F. M., van Oudheusden, B. W., and Bijl, H. (2013). Radial basis function based mesh deformation applied to simulation of flow around flapping wings. *Computers & Fluids*, 79:167 – 177.

Buhmann, M. D. (2003). *Radial Basis Functions: Theory and Implementations.* Cambridge Monographs on Applied and Computational Mathematics. Cambridge University Press.

Busch, J., Giese, D., Wissmann, L., and Kozerke, S. (2013). Reconstruction of divergence-free velocity fields from cine 3d phase-contrast flow measurements. *Magnetic resonance in medicine*, 69(1):200210.

Caridi, G. (2018). *Development and application of helium-filled soap bubbles.* PhD thesis, TU Delft Aerodynamics.

Casa, L. D. C. and Krueger, P. S. (2013). Radial basis function interpolation of unstructured, three-dimensional, volumetric particle tracking velocimetry data. *Measurement Science and Technology*, 24(6):065304.

Casey, T. A., Sakakibara, J., and Thoroddsen, S. T. (2013). Scanning tomographic particle image velocimetry applied to a turbulent jet. *Physics of Fluids*, 25(2):025102.

Cebeci, T. (2013). Chapter 4 - general behavior of turbulent boundary layers. In Cebeci, T., editor, *Analysis of Turbulent Flows with Computer Programs (Third Edition)*, pages 89 – 153. Butterworth-Heinemann, Oxford, third edition edition.

Cecrdle, J. (2015). Introduction to aircraft aeroelasticity and whirl flutter. In Cecrdle, J., editor, *Whirl Flutter of Turboprop Aircraft Structures*, pages 1 – 12. Woodhead Publishing, Oxford.

Chang, K.-A. and Liu, P. L.-F. (1998). Velocity, acceleration and vorticity under a breaking wave. *Physics of Fluids*, 10(1):327–329.

Charonko, J. J., King, C. V., Smith, B. L., and Vlachos, P. P. (2010). Assessment of pressure field calculations from particle image velocimetry measurements. *Measurement Science and Technology*, 21(10):105401.

Chawner, J. (1990). *Development of an Algebraic Grid Generation Method with Orthogonality and Clustering Control.* University of Texas at Arlington.

Chen, Z. L., Hickel, S., Devesa, A., Berland, J., and Adams, N. A. (2014). Wall modeling for implicit large-eddy simulation and immersed-interface methods. *Theor. Comput. Fluid Dyn.*, 28:1–21.

Chicone, C. (2017). Chapter 11 - equations of fluid motion. In Chicone, C., editor, *An Invitation to Applied Mathematics*, pages 293 – 319. Academic Press.

Christensen, K. and Adrian, R. (2002). Measurement of instantaneous eulerian acceleration fields by particle image accelerometry: method and accuracy. *Experiments in Fluids*, 33(6):759–769.

Christiansen, I. (1973). Numerical simulation of hydrodynamics by the method of point vortices. *Journal of Computational Physics*, 13(3):363 – 379.

Clauser, F. H. (1956). The turbulent boundary layer**the research presented in this article was supported by the office of scientific research, a.r.d.c.; u. s. air force, under contract af 18(600)671. the author was assisted by his colleagues drs. s. corrsin, g. corcos, and d. johnson. volume 4 of *Advances in Applied Mechanics*, pages 1 – 51. Elsevier.

Cohen Tenoudji, F. (2016). *Optimal Filtering: Wiener and Kalman Filters*, pages 543–562. Springer International Publishing, Cham.

Collar, A. R. (1978). The first fifty years of aeroelasticity.

Cottet, G.-H. and Koumoutsakos, P. (2000). Vortex methods - theory and practice.

Cottet, G.-H. and Poncet, P. (2004). Advances in direct numerical simulations of 3d wall-bounded flows by vortex-in-cell methods. *Journal of Computational Physics*, 193(1):136 – 158.

Craft, T., Gant, S., Gerasimov, A., Iacovides, H., and Launder, B. (2002). Wall-function strategies for use in turbulent flow cfd.

Dabiri, J. O., Bose, S., Gemmell, B. J., Colin, S. P., and Costello, J. H. (2014). An algorithm to estimate unsteady and quasi-steady pressure fields from velocity field measurements. *Journal of Experimental Biology*, 217(3):331–336.

de Boer, A., der Schoot, V., and Bijl, H. (2006). New method for mesh moving based on radial basis function interpolation.

de Boer, A., van der Schoot, M., and Bijl, H. (2007). Mesh deformation based on radial basis function interpolation. *Computers & Structures*, 85(11):784 – 795. Fourth MIT Conference on Computational Fluid and Solid Mechanics.

de Kat, R. and van Oudheusden, B. W. (2012). Instantaneous planar pressure determination from piv in turbulent flow. *Experiments in Fluids*, 52(5):1089–1106.

de Silva, C., Philip, J., and Marusic, I. (2013). Minimization of divergence error in volumetric velocity measurements and implications for turbulence statistics. *Experiments in Fluids*, 54.

Deck, S. (2012). Recent improvements in the zonal detached eddy simulation (zdes) formulation. *Theoretical and Computational Fluid Dynamics*, 26(6):523–550.

Degand, C. and Farhat, C. (2002). A three-dimensional torsional spring analogy method for unstructured dynamic meshes. *Computers & Structures*, 80(3):305 – 316.

Dixit, S.A., R. O. (2009). Determination of skin friction in strong pressure-gradient equilibrium and near-equilibrium turbulent boundary layers. *Exp Fluids*, 47:1045.

Dixit, S. A. and Ramesh, O. N. (2008). Pressure-gradient-dependent logarithmic laws in sink flow turbulent boundary layers. *Journal of Fluid Mechanics*, 615:445475.

Dodu, F. and Rabut, C. (2002). Vectorial interpolation using radial-basis-like functions. *Computers & Mathematics with Applications*, 43(3):393 – 411.

Dodu, F. and Rabut, C. (2004). Irrotational or divergence-free interpolation. *Numerische Mathematik*, 98:477–498.

Dong, H. and Egbert, G. D. (2018). Divergence-free solutions to electromagnetic forward and adjoint problems: a regularization approach. *Geophysical Journal International*, 216(2):906–918.

Draghicescu, C. I. and Draghicescu, M. (1995). A fast algorithm for vortex blob interactions. *Journal of Computational Physics*, 116(1):69 – 78.

Eitel-Amor, G., Flores, O., and Schlatter, P. (2014). Hairpin vortices in turbulent boundary layers. *Journal of Physics: Conference Series*, 506:012008.

Elsinga, G., Scarano, F., Wieneke, B., and Oudheusden, B. (2006). Tomographic particle image velocimetry. *Experiments in Fluids*, 41:933–947.

Elsinga, G. E., Wieneke, B., Scarano, F., and Schröder, A. (2008). *Tomographic 3D-PIV and Applications*, pages 103–125. Springer Berlin Heidelberg, Berlin, Heidelberg.

Espinosa, H. D., Lee, S., and Moldovan, N. (2006). A novel fluid structure interaction experiment to investigate deformation of structural elements subjected to impulsive loading. *Experimental Mechanics*, 46(6):805–824.

Ethier, C. R. and Steinman, D. A. (1994). Exact fully 3d navierstokes solutions for benchmarking. *International Journal for Numerical Methods in Fluids*, 19(5):369–375.

Facci, A., Falcucci, G., Agresta, A., Biscarini, C., Jannelli, E., and Ubertini, S. (2019). Fluid structure interaction of buoyant bodies with free surface flows: Computational modelling and experimental validation. *Water*, 11:1048.

Fadlun, E., Verzicco, R., Orlandi, P., and Mohd-Yusof, J. (2000). Combined immersed-boundary finite-difference methods for three-dimensional complex flow simulations. *Journal of Computational Physics*, 161(1):35 – 60.

Fanchi, J. R. (2002). Chapter 7 - measures of rock-fluid interactions. In Fanchi, J. R., editor, *Shared Earth Modeling*, pages 108 – 132. Butterworth-Heinemann, Woburn.

Farhat, C., Degand, C., Koobus, B., and Lesoinne, M. (1998). Torsional springs for two-dimensional dynamic unstructured fluid meshes. *Computer Methods in Applied Mechanics and Engineering*, 163(1):231 – 245.

Feng, L., Liu, F., Turner, I., Yang, Q., and Zhuang, P. (2018). Unstructured mesh finite difference/finite element method for the 2d time-space riesz fractional diffusion equation on irregular convex domains. *Applied Mathematical Modelling*, 59:441 – 463.

Fernholz, H. and Finleyt, P. (1996). The incompressible zero-pressure-gradient turbulent boundary layer: An assessment of the data. *Progress in Aerospace Sciences*, 32(4):245 – 311.

Fornefett, M., Rohr, K., and Stiehl, H. (2001). Radial basis functions with compact support for elastic registration of medical images. *Image and Vision Computing*, 19(1):87 – 96.

Fosas de Pando, M. (2012). *Tonal noise generation in flows around aerofoils: a global stability analysis*. PhD thesis.

Frankel, T. (2004). *The Geometry of Physics: An Introduction*. Cambridge University Press.

Fujisawa, N., Tanahashi, S., and Srinivas, K. (2005). Evaluation of pressure field and fluid forces on a circular cylinder with and without rotational oscillation using velocity data from PIV measurement. *Measurement Science and Technology*, 16(4):989–996.

Fukuchi, Y. (2012). *Influence of number of cameras and preprocessing for thick volume Tomographic PIV*. Lisbon, Portugal.

Fuselier, E. J. and Wright, G. B. (2015). A radial basis function method for computing helmholtz-hodge decompositions.

Gesemann, S., Huhn, F., Schanz, D., and Schröder, A. (2016). *From Noisy Particle Tracks to Velocity, Acceleration and Pressure Fields using B-splines and Penalties*. Lisbon, Portugal.

Ghaemi, S., Ragni, D., and Scarano, F. (2012). Piv-based pressure fluctuations in the turbulent boundary layer. *Experiments in Fluids*, 53(6):1823–1840.

Ghaemi, S. and Scarano, F. (2011). Counter-hairpin vortices in the turbulent wake of a sharp trailing edge. *Journal of Fluid Mechanics*, 689:317356.

Ghia, U., Ghia, K. N., and Studerus, C. J. (1976). Use of surface-oriented coordinates in the numerical simulation of flow in a turbine cascade. In van de Vooren, A. I. and Zandbergen, P. J., editors, *Proceedings of the Fifth International Conference on Numerical Methods in Fluid Dynamics June 28 – July 2, 1976 Twente University, Enschede*, pages 197–204, Berlin, Heidelberg. Springer Berlin Heidelberg.

Ghias, R., Mittal, R., and Lund, T. (2004). *A Non-Body Conformal Grid Method for Simulation of Compressible Flows with Complex Immersed Boundaries*.

Gillebaart, T., Blom, D., van Zuijlen, A., and Bijl, H. (2016). Adaptive radial basis function mesh deformation using data reduction. *J. Comput. Phys.*, 321(C):997–1025.

Gomes, J. P. and Lienhart, H. (2006). Experimental study on a fluid-structure interaction reference test case. In Bungartz, H.-J. and Schäfer, M., editors, *Fluid-Structure Interaction*, pages 356–370, Berlin, Heidelberg. Springer Berlin Heidelberg.

Gonzalez Saiz, G., Sciacchitano, A., and Scarano, F. (2019). Dense volumetric velocity field reconstruction with time-segment assimilation. In Kähler, C., Hain, R., Scharnowski, S., and Fuchs, T., editors, *Proceedings of the 13th International Symposium on Particle Image Velocimetry*, pages 102–112. Universitat der Bundeswehr Munchen. 13th International Symposium on Particle Image Velocimetry , ISPIV 2019 ; Conference date: 22-07-2019 Through 24-07-2019.

Gresho, P. M. and Sani, R. L. (1987). On pressure boundary conditions for the incompressible navier-stokes equations. *International Journal for Numerical Methods in Fluids*, 7(10):1111–1145.

Gubin, L., Polyak, B., and Raik, E. (1967). The method of projections for finding the common point of convex sets. *USSR Computational Mathematics and Mathematical Physics*, 7(6):1 – 24.

Gunaydinoglu, E. and Kurtulus, D. (2020). Pressurevelocity coupling algorithm-based pressure reconstruction from piv for laminar flows. *Experiments in Fluids*, 61.

Gurka, R., Liberzon, A., D, H., and Rubinstein, D. (1999). Computation of pressure distribution using piv velocity data.

Handscomb, D. (1991). Interpolation and differentiation of multivariate functions and interpolation of divergence-free vector fields using surface splines.

Handscomb, D. (1993). Local recovery of a solenoidal vector field by an extension of the thin-plate spline technique. *Numerical Algorithms*, 5:121–129.

Hansen, J.-P. and McDonald, I. R. (2006). Chapter 9 - theories of time-correlation functions. In Hansen, J.-P. and McDonald, I. R., editors, *Theory of Simple Liquids (Third Edition)*, pages 255 – 290. Academic Press, Burlington, third edition edition.

Haritonidis, J. H. (1989). *The Measurement of Wall Shear Stress*, pages 229–261. Springer Berlin Heidelberg, Berlin, Heidelberg.

Haussling, H. (1979). Boundary-fitted coordinates for accurate numerical solution of multibody flow problems. *Journal of Computational Physics*, 30(1):107 – 124.

Helenbrook, B. T. (2003). Mesh deformation using the biharmonic operator. *International Journal for Numerical Methods in Engineering*, 56(7):1007–1021.

Hess, J. and Smith, A. (1967). Calculation of potential flow about arbitrary bodies. *Progress in Aerospace Sciences*, 8:1 – 138.

Hill, M. J. M. (1894). On a spherical vortex. *Philosophical Transactions of the Royal Society of London. A*, 185:213–245.

Hirata, T. (2005). 3-d voronoi tessellation algorithms. *Japan Journal of Industrial and Applied Mathematics*, 22(2):223.

Hirt, C., Amsden, A., and Cook, J. (1974). An arbitrary lagrangian-eulerian computing method for all flow speeds. *Journal of Computational Physics*, 14(3):227 – 253.

Houghton, E., Carpenter, P., Collicott, S. H., and Valentine, D. T. (2017). Chapter 6 - thin airfoil theory. In Houghton, E., Carpenter, P., Collicott, S. H., and Valentine, D. T., editors, *Aerodynamics for Engineering Students (Seventh Edition)*, pages 391 – 447. Butterworth-Heinemann, seventh edition edition.

Hughes, T. J., Liu, W. K., and Zimmermann, T. K. (1981). Lagrangian-eulerian finite element formulation for incompressible viscous flows. *Computer Methods in Applied Mechanics and Engineering*, 29(3):329 – 349.

Huhn, F., Schanz, D., Gesemann, S., and Schröder, A. (2016). Fft integration of instantaneous 3d pressure gradient fields measured by lagrangian particle tracking in turbulent flows. *Experiments in Fluids*, 57(9):151.

Hunt, J., Wray, A., and Moin, P. (1988). Eddies, streams, and convergence zones in turbulent flows. *Studying Turbulence Using Numerical Simulation Databases*, -1:193–208.

Hunt, J. C. R. and Snyder, W. H. (1980). Experiments on stably and neutrally stratified flow over a model three-dimensional hill. *Journal of Fluid Mechanics*, 96(4):671704.

Hwang, T., Doh, D., Jo, H., Tsubokura, M., Piao, B., Kuroda, S., Kobayashi, T., Tanaka, K., and Takei, M. (2007). Analysis of fluidelastic-structure interactions in an impinging jet with a dynamic 3d-ptv and non-contact 6d-motion tracking system. *Chemical Engineering Journal*, 130(2):153 – 164. Special Issue for the 4th World Congress on Industrial Process Tomography.

Imaichi, K. and Ohmi, K. (1983). Numerical processing of flow-visualization pictures measurement of two-dimensional vortex flow. *Journal of Fluid Mechanics*, 129:283311.

Jakobsen, M. L., Dewhirst, T. P., and Greated, C. A. (1997). Particle image velocimetry for predictions of acceleration fields and force within fluid flows. *Measurement Science and Technology*, 8(12):1502–1516.

Jaw, S., Chen, J.-H., and Wu, P.-C. (2009). Measurement of pressure distribution from piv experiments. *Journal of Visualization*, 12:27–35.

Jenkins, J. A. (2002). Chapter 13 - the method of the extremal metric. In Khnau, R., editor, *Geometric Function Theory*, volume 1 of *Handbook of Complex Analysis*, pages 393 – 456. North-Holland.

Jensen, A., Sveen, J. K., Grue, J., Richon, J.-B., and Gray, C. (2001). Accelerations in water waves by extended particle image velocimetry. *Experiments in Fluids*, 30(5):500–510.

Jeon, Y., Gomit, G., Earl, T., Chatellier, L., and David, L. (2018). Sequential least-square reconstruction of instantaneous pressure field around a body from tr-piv. *Experiments in Fluids*, 59.

Jeon, Y. J. and Sung, H. J. (2011). Piv measurement of flow around an arbitrarily moving body. *Experiments in Fluids*, 50(4):787–798.

Jodai, Y. and Elsinga, G. E. (2016). Experimental observation of hairpin auto-generation events in a turbulent boundary layer. *Journal of Fluid Mechanics*, 795:611633.

Johnson, B. and Thompson, J. (1978). *A Discussion of Boundary-Fitted Coordinate Systems and Their Applicability to the Numerical Modeling of Hydraulic Problems.* U.S. Army Misc Paper H-78-9, Viksburg,MS.,USA.

Jones, W. and Samareh-Abolhassani, J. (2012). *A grid generation system for multi-disciplinary design optimization.*

Joseph, D. (2006). Helmholtz decomposition coupling rotational to irrotational flow of a viscous fluid. *Proceedings of the National Academy of Sciences*, 103:14272 – 14277.

Joseph, D., Funada, T., and Wang, J. (2007). *Helmholtz decomposition coupling rotational to irrotational flow*, page 1634. Cambridge Aerospace Series. Cambridge University Press.

Jux, C.; Sciacchitano, A. S. F. (2018). Surface pressure visualization by 3d ptv. *Proceedings 18th International Symposium on Flow Visualization.*

Jux, C., Sciacchitano, A., and Scarano, F. (2020). Flow pressure evaluation on generic surfaces by robotic volumetric ptv. *Measurement Science and Technology.*

Jux, C., S. F. . S. A. (2019). Aerodynamic pressure reconstruction on generic surfaces from robotic piv measurements. In C. J. Khler, R. Hain, S. S. . T. F., editor, *Proceedings of the 13th International Symposium on Particle Image Velocimetry: 22-27 July*, pages 1478–87, Munich, Germany.

Katz, J. and Plotkin, A. (2001). *Low-Speed Aerodynamics.* Cambridge Aerospace Series. Cambridge University Press, 2 edition.

Kawata, T. and Obi, S. (2014). Velocitypressure correlation measurement based on planar piv and miniature static pressure probes. *Experiments in Fluids*, 55.

Kedward, L., Allen, C., and Rendall, T. (2017). Efficient and exact mesh deformation using multiscale rbf interpolation. *J. Comput. Phys.*, 345(C):732–751.

Kim, K.-S., Lee, S.-J., and Suh, J.-C. (2005). A combined vortex and panel method for numerical simulations of viscous flows: a comparative study of a vortex particle method and a finite volume method. *International Journal for Numerical Methods in Fluids*, 49(10):1087–1110.

Kim, Y.-C., Suh, J.-C., and Lee, K.-J. (2012). Vortex-in-cell method combined with a boundary element method for incompressible viscous flow analysis. *International Journal for Numerical Methods in Fluids*, 69(10):1567–1583.

Kol, V. (2007). Vortex identification: New requirements and limitations. *International Journal of Heat and Fluid Flow*, 28(4):638 – 652. Including Special Issue of Conference on Modelling Fluid Flow (CMFF06), Budapest.

Kompenhans, J., Raffel, M., Dieterle, L., Dewhirst, T., Vollmers, H., Ehrenfried, K., Willert, C., Pengel, K., Khler, C., Schröder, A., and Ronneberger, O. (1999). Particle image velocimetry in aerodynamics: Technology and applications in wind tunnels.

Koumoutsakos, P. (2005). Multi scale flow siimulations using particles. *Annual Review of Fluid Mechanics*, 37(1):457–487.

Kudela, H. and Kozlowski, T. (2009). Vortex in cell method for exterior problems.

Kudela, H. and Regucki, P. (2002). The vortex-in-cell method for the study of three-dimensional vortex structures. In Bajer, K. and Moffatt, H. K., editors, *Tubes, Sheets and Singularities in Fluid Dynamics*, pages 49–54, Dordrecht. Springer Netherlands.

Kunze, S. and Brücker, C. (2011). Flow control over an undulating membrane. *Experiments in Fluids*, 50(3):747–759.

Leishman, J. (2016). *Principles of Helicopter Aerodynamics*. Cambridge Aerospace Series. Cambridge University Press.

Leveque, R. J. and Calhoun, D. (2001). Cartesian grid methods for fluid flow in complex geometries. In Fauci, L. J. and Gueron, S., editors, *Computational Modeling in Biological Fluid Dynamics*, pages 117–143, New York, NY. Springer New York.

Lewis, R. I. (1991). *The basis of surface singularity modelling*, page 343. Cambridge Engine Technology Series. Cambridge University Press.

Li, H., Wang, D., and Xu, H. (2020). Improved law-of-the-wall model for turbulent boundary layer in engineering. *AIAA Journal*, 58(8):3308–3319.

Li, Y., Perlman, E., Wan, M., Yang, Y., Meneveau, C., Burns, R., Chen, S., Szalay, A., and Eyink, G. (2008). A public turbulence database cluster and applications to study lagrangian evolution of velocity increments in turbulence. *Journal of Turbulence*, 9:N31.

Liburdy, J. A. and Young, E. F. (1992). Processing of three-dimensional particle tracking velocimetry data. *Optics and Lasers in Engineering*, 17(3):209 – 227. Special Issue on Optical Methods for Thermal & Fluid Flow Diagnostics.

Liu, D. C. and Nocedal, J. (1989). On the limited memory bfgs method for large scale optimization. *Mathematical Programming*, 45(1):503–528.

Liu, X. and Katz, J. (2006). Instantaneous pressure and material acceleration measurements using a four-exposure piv system. *Experiments in Fluids*, 41(2):227.

Liu, X., Moreto, J. R., and Siddle-Mitchell, S. (2016). *Instantaneous Pressure Reconstruction from Measured Pressure Gradient using Rotating Parallel Ray Method.*

Löhner, R. and Yang, C. (1996). Improved ale mesh velocities for moving bodies. *Communications in Numerical Methods in Engineering*, 12(10):599–608.

Lorenzoni, V., Tuinstra, M., Moore, P., and Scarano, F. (2009). *Aeroacoustic Analysis of a Rod-Airfoil Flow by Means of Time-Resolved PIV.*

Lowitzsch, S. (2005). A density theorem for matrix-valued radial basis functions. *Numerical Algorithms*, 39:253–256.

Luke, E., Collins, E., and Blades, E. (2012). A fast mesh deformation method using explicit interpolation. *Journal of Computational Physics*, 231(2):586 – 601.

Maas, H. G., Gruen, A., and Papantoniou, D. (1993). Particle tracking velocimetry in three-dimensional flows. *Experiments in Fluids*, 15(2):133–146.

Malik, N. A. and Dracos, T. (1995). Interpolation schemes for three-dimensional velocity fields from scattered data using taylor expansions. *Journal of Computational Physics*, 119(2):231 – 243.

Malik, N. A., Dracos, T., and Papantoniou, D. A. (1993). Particle tracking velocimetry in three-dimensional flows. *Experiments in Fluids*, 15(4):279–294.

Maljaars, P., Bronswijk, L., Windt, J., Grasso, N., and Kaminski (2018). Experimental validation of fluidstructure interaction computations of flexible composite propellers in open water conditions using bem-fem and rans-fem methods. *J. Mar. Sci. Eng.*

Malon, J. R. (1977). A fifty channel electrically scanned pressure module. In *Proceedings of the 23rd International Instrumentation Symposium.*

Mandal, B. and Mazumdar, H. (2015). The importance of the law of the wall. *International Journal of Applied Mechanics and Engineering*, 20.

Marchi, S. D. (2009). Geometric greedy and greedy points for rbf interpolation. In *roceedings of the International Conference on Computational and Mathematical Methods in Science and Engineering, CMMSE 2009.*

Marchioro, C. and Pulvirenti, M. (1994). *General Considerations on the Euler Equation*, pages 1–58. Springer New York, New York, NY.

Marinus, B. (2011). *Multidisciplinary Optimization of Aircraft Propeller Blades*. PhD thesis.

Mcclure, J. and Yarusevych, S. (2019). Planar momentum balance in three-dimensional flows: applications to load estimation. *Experiments in Fluids*, 60.

Mella, D., Brevis, W., Higham, J., Racic, V., and Susmel, L. (2019). Image-based tracking technique assessment and application to a fluidstructure interaction experiment. *Proceedings of the Institution of Mechanical Engineers, Part C: Journal of Mechanical Engineering Science*, 233(16):5724–5734.

Melling, A. (1997). Tracer particles and seeding for particle image velocimetry. *Measurement Science and Technology*, 8(12):1406–1416.

Mellor, G. L. and Gibson, D. M. (1966). Equilibrium turbulent boundary layers. *Journal of Fluid Mechanics*, 24(2):225253.

Mengaldo, G., Liska, S., Yu, K., Colonius, T., and Jardin, T. (2017). *Immersed Boundary Lattice Green Function methods for External Aerodynamics.*

Metropolis, N. and Ulam, S. (1949). The monte carlo method. *Journal of the American Statistical Association*, 44(247):335–341.

Michler, A. K. (2011). Aircraft control surface deflection using rbf-based mesh deformation. *International Journal for Numerical Methods in Engineering*, 88(10):986–1007.

Millikan, C. (1938). *A Critical Discussion of Turbulent Flows in Channels and Circular Tubes*. GALCIT/P-114. Guggenheim Aeronautical Laboratory.

Mittal, R. and Iaccarino, G. (2005). Immersed boundary methods. *Annual Review of Fluid Mechanics*, 37(1):239–261.

Mittal, R., Utturkar, Y., and Udaykumar, H. (2002). *Computational modeling and analysis of biomimetic flight mechanisms*.

Morgenthal, G. and Walther, J. (2007). An immersed interface method for the vortex-in-cell algorithm. *Computers & Structures*, 85:712726.

Morris, A. S. and Langari, R. (2016). Pressure measurement. In Morris, A. S. and Langari, R., editors, *Measurement and Instrumentation (Second Edition)*, pages 463 – 491. Academic Press, Boston, second edition edition.

Murai, Y., Nakada, T., Suzuki, T., and Yamamoto, F. (2007). Particle tracking velocimetry applied to estimate the pressure field around a savonius turbine. *Measurement Science and Technology*, 18(8):2491–2503.

Murray, N., Ukeiley, L., and Raspet, R. (2007). *Calculating Surface Pressure Fluctuations from PIV Data Using Poisson's Equation*.

Narcowich, F. J. and Ward, J. D. (1994). Generalized hermite interpolation via matrix-valued conditionally positive definite functions. *Mathematics of Computation*, 63(208):661–687.

Neeteson, N. J. and Rival, D. E. (2015). Pressure-field extraction on unstructured flow data using a voronoi tessellation-based networking algorithm: a proof-of-principle study. *Experiments in Fluids*, 56(2):44.

Nieuwstadt, F. T., Westerweel, J., and Boersma, B. J. (2016). *Turbulence: Introduction to Theory and Applications of Turbulent Flows*. Springer International Publishing.

Niu, J., Lei, J., and He, J. (2017). Radial basis function mesh deformation based on dynamic control points. *Aerospace Science and Technology*, 64:122 – 132.

Noh, W. F. (1963). Cel: A time-dependent, two-space-dimensional, coupled eulerian-lagrange code.

Novara, M. and Scarano, F. (2012). Lagrangian acceleration evaluation for tomographic piv: a particle-tracking based approach. In *16th Int Symp on Applications of Laser Techniques to Fluid Mechanics*, Lisbon, Portugal.

Novara, M. and Scarano, F. (2013). A particle-tracking approach for accurate material derivative measurements with tomographic piv. *Experiments in Fluids*, 54.

Oudheusden, B., Scarano, F., Roosenboom, E., Casimiri, E., and Souverein, L. (2007). Evaluation of integral forces and pressure fields from planar velocimetry data for incompressible and compressible flows. volume 43, pages 1–12.

Ould-Salihi, M. L., Cottet, G. H., and El Hamraoui, M. (2001). Blending finite-difference and vortex methods for incompressible flow computations. *SIAM Journal on Scientific Computing*, 22(5):1655–1674.

Pan, Z., Whitehead, J., Thomson, S., and Truscott, T. (2016). Error propagation dynamics of PIV-based pressure field calculations: How well does the pressure poisson solver perform inherently? *Measurement Science and Technology*, 27(8):084012.

Panciroli, R. and Porfiri, M. (2013). Evaluation of the pressure field on a rigid body entering a quiescent fluid through particle image velocimetry. *Experiments in Fluids*, 54(12):1630.

Panton, R. L. (2020). Kelvin's circulation theorem.

Pardo, S. R., Natti, P. L., Romeiro, N. M. L., and Cirilo, E. R. (2012). A transport modeling of the carbon-nitrogen cycle at igap i lake - londrina, paran state, brazil. *Acta Scientiarum. Technology*, 34(2).

Patel, D. and Upadhyay, S. (2013). Optical flow measurement using lucas kanade method. *International Journal of Computer Applications*, 61:6–10.

Patil, M., Hodges, D., and Cesnik, C. (2001). Limit-cycle oscillations in high-aspect-ratio wings. *Journal of Fluids and Structures*, 15(1):107 – 132.

Patterson, J. and for Aeronautics, U. S. N. A. C. (1952). *A Miniature Electrical Pressure Gage Utilizing a Stretched Flat Diaphragm.* Technical note. National Advisory Committee for Aeronautics.

Peskin, C. (1982). The fluid dynamics of heart valves: Experimental, theoretical, and computational methods. *Annual Review of Fluid Mechanics*, 14:235–259.

Peskin, C. S. (1972). Flow patterns around heart valves: A numerical method. *Journal of Computational Physics*, 10(2):252 – 271.

Peskin, C. S. (2002). The immersed boundary method. *Acta Numerica*, 11:479517.

Peterson, K., Regaard, B., Heinemann, S., and Sick, V. (2012). Single-camera, three-dimensional particle tracking velocimetry. *Optics express*, 20:9031–7.

Pirnia, A., McClure, J., Peterson, S., Helenbrook, B., and Erath, B. (2020). Estimating pressure fields from planar velocity data around immersed bodies; a finite element approach. *Experiments in Fluids*, 61.

Plessix, R.-E. (2006). A review of the adjoint-state method for computing the gradient of a functional with geophysical applications. *Geophysical Journal International*, 167(2):495–503.

Ploumhans, P. and Winckelmans, G. (2000). Vortex methods for high-resolution simulations of viscous flow past bluff bodies of general geometry. *Journal of Computational Physics*, 165(2):354 – 406.

Ploumhans, P., Winckelmans, G., Salmon, J., Leonard, A., and Warren, M. (2002). Vortex methods for direct numerical simulation of three-dimensional bluff body flows: Application to the sphere at re=300, 500, and 1000. *Journal of Computational Physics*, 178:427–463.

Ponchaut, N. F., Mouton, C., Hornung, H. G., and Dabiri, D. (2005). Particle tracking velocimetry method : Advances and error analysis.

Porcu, E., D. D. B. M. (2013). Radial basis functions with compact support for multivariate geostatistics. *Stoch Environ Res Risk Assess*, 27,:909922.

Prabhakara, S., D. M. (2004). The no-slip boundary condition in fluid mechanics. *Reson*, 9:6171.

Pröbsting, S., Scarano, F., Bernardini, M., and Pirozzoli, S. (2013). On the estimation of wall pressure coherence using time-resolved tomographic piv. *Experiments in Fluids*, 54(7):1567.

Raffel, M., Willert, C., and Kompenhans, J. (1998). *Particle Image Velocimetry: A Practical Guide.*

Ragni, D., Ashok, A., van Oudheusden, B. W., and Scarano, F. (2009). Surface pressure and aerodynamic loads determination of a transonic airfoil based on particle image velocimetry. *Measurement Science and Technology*, 20(7):074005.

Rajat Mittal, V. S. and Udaykumar, H. S. (2004). Flutter, tumble and vortex induced autorotation. *Theoret Comput Fluid Dynamics*, 17:165170.

Rapp, B. E. (2017). Chapter 9 - fluids. In Rapp, B. E., editor, *Microfluidics: Modelling, Mechanics and Mathematics*, Micro and Nano Technologies, pages 243 – 263. Elsevier, Oxford.

Rendall, T. and Allen, C. (2009). Efficient mesh motion using radial basis functions with data reduction algorithms. *Journal of Computational Physics*, 228(17):6231 – 6249.

Rendall, T. C. S. and Allen, C. B. (2010). Parallel efficient mesh motion using radial basis functions with application to multi-bladed rotors. *International Journal for Numerical Methods in Engineering*, 81(1):89–105.

Ribeiro, P. C., [de Campos Velho], H. F., and Lopes, H. (2016). Helmholtzhodge decomposition and the analysis of 2d vector field ensembles. *Computers & Graphics*, 55:80 – 96.

Robey, R. (2001). Chapter 4.4 - blast tubes. In BEN-DOR, G., IGRA, O., and ELPERIN, T., editors, *Handbook of Shock Waves*, pages 623 – 650. Academic Press, Burlington.

Romeiro, N., Mangili, F., Costanzi, R., Cirilo, E., and Natti, P. L. (2018). Numerical simulation of bod5 dynamics in igapó i lake, londrina, paraná, brazil: Experimental measurement and mathematical modeling. *Semina: Cincias Exatas e Tecnolgicas*, 38.

Ross, S. M. (2017). Chapter 11 - analysis of variance. In Ross, S. M., editor, *Introductory Statistics (Fourth Edition)*, pages 489 – 518. Academic Press, Oxford, fourth edition edition.

Rufolo, G., Marini, M., Roncioni, P., and Borrelli, S. (2007). In flight aerodynamic experiment for the unmanned space vehicle ftb-1.

Saarenrinne, P., Piirto, M., and Eloranta, H. (2001). Experiences of turbulence measurement with piv. *Measurement Science and Technology*, 12(11):1904–1910.

Sadati, M., Luap, C., Krger, M., and ttinger, H. C. (2011). Hard vs soft constraints in the full field reconstruction of incompressible flow kinematics from noisy scattered velocimetry data. *Journal of Rheology*, 55(6):1187–1203.

Sagredo, B. and Tercero, J. C. O. (2003). Z-splines: moment conserving cardinal spline interpolation of compact support for arbitrarily spaced data.

Sakr, E. M., Zayed, H. A., El-Mawla, S. A., Kenawy, M. A., and Nagy, M. R. (1995). Study of stress-strain characteristics of sbr and blended nr/sbr rubber. *Czechoslovak Journal of Physics*, 45(3):275–282.

Sarpkaya, T. and Ihrig, C. J. (1986). Impulsively Started Steady Flow About Rectangular Prisms: Experiments and Discrete Vortex Analysis. *Journal of Fluids Engineering*, 108(1):47–54.

Scarano, F. and Ghaemi, S. (2012). Sensing wall-pressure fluctuations by particle image velocimetry. In d'Acoustique, S. F., editor, *Acoustics 2012*, Nantes, France.

Schanz, D., Gesemann, S., and Schröder, A. (2016). Shake-the-box: Lagrangian particle tracking at high particle image densities. *Experiments in Fluids*, 57:1–27.

Schiavazzi, D., Coletti, F., Iaccarino, G., and Eaton, J. K. (2014). A matching pursuit approach to solenoidal filtering of three-dimensional velocity measurements. *Journal of Computational Physics*, 263:206 – 221.

Schneiders, J. (2017). *Bridging PIV spatial and temporal resolution using governing equations and development of the coaxial volumetric velocimeter*. PhD thesis, TU Delft.

Schneiders, J., Azijli, I., Scarano, F., and Dwight, R. (2015). Pouring time into space. In *11th International Symposium on Particle Image Velocimetry*, Santa Barbara.

Schneiders, J. and Scarano, F. (2018). On the use of full particle trajectories and vorticity transport for dense velocity field reconstruction. In *LXLASER2018: 19th International Symposium on the Application of Laser and Imaging Techniques to Fluid Mechanics*, Lisbon, Portugal.

Schneiders, J., Singh, P., and Scarano, F. (2016a). Instantaneous flow reconstruction from particle trajectories with vortex-in-cell. In *18th International Symposium on Applications of Laser Techniques to Fluid*, Lisbon, Portugal.

Schneiders, J. F. G., Caridi, G. C. A., Sciacchitano, A., and Scarano, F. (2016b). Large-scale volumetric pressure from tomographic ptv with hfsb tracers. *Experiments in Fluids*, 57(11):164.

Schneiders, J. F. G. and Scarano, F. (2016). Dense velocity reconstruction from tomographic ptv with material derivatives. *Experiments in Fluids*, 57(9):139.

Schneiders, J. F. G., Scarano, F., and Elsinga, G. E. (2017). Resolving vorticity and dissipation in a turbulent boundary layer by tomographic ptv and vic+. *Experiments in Fluids*, 58(4):27.

Schneiders, J. F. G., Scarano, F., Jux, C., and Sciacchitano, A. (2018). Coaxial volumetric velocimetry. *Measurement Science and Technology*, 29(6):065201.

Schneiders, J. F. G. and Sciacchitano, A. (2017). Track benchmarking method for uncertainty quantification of particle tracking velocimetry interpolations. *Measurement Science and Technology*, 28(6):065302.

Schräder, D. and Wendland, H. (2011). Analytically divergence-free discretization methods for darcy's problem. *Math. Comput.*, 80:263–277.

Schröder A, Geisler R, S. A. W. B. H. A. S. F. E. G. P. C. (2009). *Lagrangian aspects of coherent structures in a turbulent boundary layer flow using TR-Tomo PIV and FTV.* Melbourne, Victoria, Australia.

Sethian, J. and Ghoniem, A. F. (1988). Validation study of vortex methods. *Journal of Computational Physics*, 74(2):283 – 317.

Settles, G. S. (1986). Modern developments in flow visualization. *AIAA Journal*, 24(8):1313–1323.

Sezan, M. I. and Stark, H. (1982). Image restoration by the method of convex projections: Part 2-applications and numerical results. *IEEE Transactions on Medical Imaging*, 1(2):95–101.

Shams, A., Jalalisendi, M., and Porfiri, M. (2015). Experiments on the water entry of asymmetric wedges using particle image velocimetry. *Physics of Fluids*, 27(2):027103.

Sheng, C. and Allen, C. B. (2013). Efficient mesh deformation using radial basis functions on unstructured meshes. *AIAA Journal*, 51(3):707–720.

Slaouti, A. and Stansby, P. (1992). Flow around two circular cylinders by the random-vortex method. *Journal of Fluids and Structures*, 6(6):641 – 670.

Smith, M. J., Cesnik, C. E. S., and Hodges, D. H. (2000). Evaluation of some data transfer algorithms for noncontiguous meshes. *Journal of Aerospace Engineering*, 13(2):52–58.

Soifer, V. (2013). 1 - main equations of diffraction theory. In *Computer Design of Diffractive Optics*, Woodhead Publishing Series in Electronic and Optical Materials, pages 1 – 24. Woodhead Publishing.

Song, S. M., N. S. G. G. H. . P. N. J. (1993). Noise reduction in three-dimensional phase-contrast mr velocity measurements. *Journal of magnetic resonance imaging : JMRI*, 3(4):587596.

Sonnemans, P. J. M. (1992). *Application of body fitted-coordinates in heat conduction problems.* PhD thesis, Technische Univ., Eindhoven (Netherlands).

Stack, J., Mangalam, S., and Berry, S. (1987). *A unique measurement technique to study laminar-separation bubble characteristics on an airfoil.*

Stein, L. R., Gentry, R. A., and Hirt, C. W. (1977). Computational simulation of transient blast loading on three-dimensional structures. *Computer Methods in Applied Mechanics and Engineering*, 11(1):57 – 74.

Sukumar, N. and Bolander, J. E. (2003). Numerical computation of discrete differential operators on non-uniform grids.

Suzuki, T., J. H. . Y. (2009). Unsteady ptv velocity field past an airfoil solved with dns: Part 1. algorithm of hybrid simulation and hybrid velocity field at re 103. *Exp Fluids*, 47:957.

Takizawa, K., Henicke, B., Puntel, A., Spielman, T., and Tezduyar, T. E. (2011). Space-time computational techniques for the aerodynamics of flapping wings. *Journal of Applied Mechanics*, 79(1). 010903.

Tang, D. and Dowell, E. (2004). Effects of geometric structural nonlinearity on flutter and limit cycle oscillations of high-aspect-ratio wings. *Journal of Fluids and Structures*, 19(3):291 – 306.

Tang, D. and Dowell, E. H. (2001). Experimental and theoretical study on aeroelastic response of high-aspect-ratio wings. *AIAA Journal*, 39(8):1430–1441.

Tarafder, S., Saha, G., and Sayeed, T. (2010). Analysis of potential flow around 3-dimensional hydrofoils by combined source and dipole based panel method. *Journal of Marine Science and Technology*, 18.

Taylor, G. I. and Green, A. E. (1937). Mechanism of the production of small eddies from large ones. *Proceedings of the Royal Society of London. Series A - Mathematical and Physical Sciences*, 158(895):499–521.

Terra, W., Sciacchitano, A., and Scarano, F. (2017). Aerodynamic drag of a transiting sphere by large-scale tomographic-piv. *Experiments in Fluids*, 58(7):83.

Tezduyar, T. (2001). Finite element methods for flow problems with moving boundaries and interfaces. *Arch Computat Methods Eng*, 8:83.

Thames, F. C., Thompson, J. F., Mastin], C. W., and Walker, R. L. (1977). Numerical solutions for viscous and potential flow about arbitrary two-dimensional bodies using body-fitted coordinate systems. *Journal of Computational Physics*, 24(3):245 – 273.

Thompson, J. F., Mastin, C. W., Thames, F. C., and Shanks, S. P. (1975). Use of numerically generated body-fitted coordinate systems for solution of the Navier-Stokes equations. In *2nd Computational Fluid Dynamics Conference*, pages 68–80.

Thompson, J. F., Thames, F. C., Hodge, J. K., Shanks, S. P., Reddy, R. N., and Mastin, C. W. (1976). Solutions of the navier-stokes equations in various flow regimes on fields containing any number of arbitrary bodies using boundary-fitted coordinate systems. In van de Vooren, A. I. and Zandbergen, P. J., editors, *Proceedings of the Fifth International Conference on Numerical Methods in Fluid Dynamics June 28 – July 2, 1976 Twente University, Enschede*, pages 421–427, Berlin, Heidelberg. Springer Berlin Heidelberg.

Thompson, J. F., Thames, F. C., and Mastin, C. (1974). Automatic numerical generation of body-fitted curvilinear coordinate system for field containing any number of arbitrary two-dimensional bodies. *Journal of Computational Physics*, 15(3):299 – 319.

Thompson, J. F., Warsi, Z. U., and Mastin, C. W. (1985). *Numerical Grid Generation: Foundations and Applications*. Elsevier North-Holland, Inc., USA.

Tim, W., Matthias, Z., Mark, P., Markus, G., Martin, W., and Leif, K. (2007). 5 - digital processing. In GROSS, M. and PFISTER, H., editors, *Point-Based Graphics*, The Morgan Kaufmann Series in Computer Graphics, pages 186 – 244. Morgan Kaufmann, Burlington.

Tokarev, M. P., Alekseenko, M. V., Bilsky, A. V., Dulin, V. M., and Markovich, D. M. (2013). Tomographic piv measurements in a swirling jet flow.

Trumper, M. T., Behrouzi, P., and McGuirk, J. J. (2018). Influence of nozzle exit conditions on the near-field development of high subsonic and underexpanded axisymmetric jets. *Aerospace*, 5(2).

Tsai, H. M., Wong, A. S. F., Cai, J., Zhu, Y., and Liu, F. (2001). Unsteady flow calculations with a parallel multiblock moving mesh algorithm. *AIAA Journal*, 39(6):1021–1029.

Tu, J., Yeoh, G.-H., and Liu, C. (2013). Chapter 8 - some advanced topics in cfd. In Tu, J., Yeoh, G.-H., and Liu, C., editors, *Computational Fluid Dynamics (Second Edition)*, pages 349 – 394. Butterworth-Heinemann, second edition edition.

Udaykumar, H., Mittal, R., and Shyy, W. (1999). Computation of solid-liquid phase fronts in the sharp interface limit on fixed grids. *J. Comput. Phys.*, 153(2):535574.

Unverdi, S. O. and Tryggvason, G. (1992). A front-tracking method for viscous, incompressible, multi-fluid flows. *Journal of Computational Physics*, 100(1):25 – 37.

Utturkar, Y., Mittal, R., Rampunggoon, P., and Cattafesta, L. (2002). *Sensitivity of synthetic jets to the design of the jet cavity*, chapter 2002-0124.

van de Meerendonk, R., Percin, M., and van Oudheusden, B. W. (2018). Three-dimensional flow and load characteristics of flexible revolving wings. *Experiments in Fluids*, 59(10):161.

Van Gent, P. (2018). *From Particles to Pressure PIV-based pressure reconstruction for base flows*. PhD thesis.

van Gent, P. L., Michaelis, D., van Oudheusden, B. W., Weiss, P. É., de Kat, R., Laskari, A., Jeon, Y. J., David, L., Schanz, D., Huhn, F., Gesemann, S., Novara, M., McPhaden, C., Neeteson, N. J., Rival, D. E., Schneiders, J. F. G., and Schrijer, F. F. J. (2017). Comparative assessment of pressure field reconstructions from particle image velocimetry measurements and lagrangian particle tracking. *Experiments in Fluids*, 58(4):33.

Vedula, P. and Adrian, R. (2005). Optimal solenoidal interpolation of turbulent vector fields: Application to ptv and super-resolution piv. *Experiments in Fluids*, 39:213–221.

Vennell, R. and Beatson, R. (2009). A divergence-free spatial interpolator for large sparse velocity data sets. *Journal of Geophysical Research: Oceans*, 114(C10).

Violato, D., Moore, P., and Scarano, F. (2011). Lagrangian and eulerian pressure field evaluation of rod-airfoil flow from time-resolved tomographic piv. *Experiments in Fluids*, 50(4):1057–1070.

Violato, D. and Scarano, F. (2011). Three-dimensional evolution of flow structures in transitional circular and chevron jets. *Physics of Fluids*, 23(12):124104.

von Kármán, T. (1930). *Mechanische Ähnlichkeit und Turbulenz*. Sonderdrucke aus den Nachrichten von der Gesellschaft der Wissenschaften zu Göttingen : Mathematisch-physische Klasse. Weidmannsche Buchh.

Voth, G. A., Satyanarayan, K., and Bodenschatz, E. (1998). Lagrangian acceleration measurements at large reynolds numbers. *Physics of Fluids*, 10(9):2268–2280.

Wagner, H. (1932). über stoßund gleitvorgänge an der oberfläche von flüssigkeiten. *ZAMM - Journal of Applied Mathematics and Mechanics / Zeitschrift fr Angewandte Mathematik und Mechanik*, 12(4):193–215.

Walther, J. H. and Morgenthal, G. (2002). An immersed interface method for the vortex-in-cell algorithm. *Journal of Turbulence*, 3:N39.

Wang, C. (1990). Exact solutions of the navier-stokes equations-the generalized beltrami flows, review and extension. *Acta Mechanica*, 81:6974.

Wang, G., Chen, X., and Liu, Z. (2018). Mesh deformation on 3d complex configurations using multistep radial basis functions interpolation. *Chinese Journal of Aeronautics*, 31(4):660 – 671.

Wang, Y., Qin, N., and Zhao, N. (2014). Fast mesh deformation based on delaunay graph and radial basis function. In *Eighth International Conference on Computational Fluid Dynamics (ICCFD8)*, Chengdu, China.

Wang, Z. and Przekwas, A. (2012). *Unsteady flow computation using moving grid with mesh enrichment.*

Wei, T., S. R. . M. P. (2005). Comment on the clauser chart method for determining the friction velocity. *Exp Fluids*, 38:695699.

Weiler, M., Botchen, R., Stegmaier, S., Ertl, T., Huang, J., Jang, Y., Ebert, D. S., and Gaither, K. P. (2005). Hardware-assisted feature analysis and visualization of procedurally encoded multifield volumetric data. *IEEE Computer Graphics and Applications*, 25(5):72–81.

Wendland, H. (1998). Error estimates for interpolation by compactly supported radial basis functions of minimal degree. *Journal of Approximation Theory*, 93(2):258 – 272.

Wendland, H. (1999). On the smoothness of positive definite and radial functions. *Journal of Computational and Applied Mathematics*, 101(1):177 – 188.

Wendland, H. (2009). Divergence-free kernel methods for approximating the stokes problem. *SIAM J. Numerical Analysis*, 47:3158–3179.

Weyburne, D. (2011). On the origin of the log law region: Instantaneous velocity profile models.

White, F. (2006). *Viscous Fluid Flow*, chapter Solutions of the Newtonian viscous-flow equations. Boston, MA: McGraw-Hill.

Wick, A. (2001). Generation of dynamic grids using structural analogy. In *Proceedings of the 17th GAMM-Seminar*, pages 147–157, Leipzig.

Wieneke, B. (2005). Stereo-piv using self-calibration on particle images. *Experiments in Fluids*, 39(2):267–280.

Wieneke, B. (2012). Iterative reconstruction of volumetric particle distribution. *Measurement Science and Technology*, 24(2):024008.

William Sellers, I. and Kjelgaard, S. (1997). *The Basic Aerodynamics Research Tunnel - A facility dedicated to code validation.*

Wu, J. and JaJa, J. (2013). High performance fft based poisson solver on a cpu-gpu heterogeneous platform. pages 115–125.

Yang, G. Z., Kilner, P. J., Firmin, D. N., Underwood, S. R., Burger, P., and Longmore, D. B. (1993). 3d cine velocity reconstruction using the method of convex projections. In *Proceedings of Computers in Cardiology Conference*, pages 361–364.

Yu, F., Gupta, N., and Hoy, J. (2005). Non-intrusive pressure measurement based on ultrasonic waves. *Insight*, 47:285–288.

Zanoun, E.-S., Durst, F., and Nagib, H. (2003). Evaluating the law of the wall in two-dimensional fully developed turbulent channel flows. *Physics of Fluids*, 15(10):3079–3089.

Zanoun, E. S., Jehring, L., and Egbers, C. (2014). Three measuring techniques for assessing the mean wall skin friction in wall-bounded flows. *Thermophysics and Aeromechanics*, 21:179–190.

Zarruk, G. A., Brandner, P. A., Pearce, B. W., and Phillips, A. W. (2014). Experimental study of the steady fluidstructure interaction of flexible hydrofoils. *Journal of Fluids and Structures*, 51:326 – 343.

Zhang, J., C. S. L. A. (2000). Flexible filaments in a flowing soap film as a model for one-dimensional flags in a two-dimensional wind. *Nature*, 408:835839.

Zhang, J., Tao, B., and Katz, J. (1997). Turbulent flow measurement in a square duct with hybrid holographic piv. *Experiments in Fluids*, 23(5):373–381.

Zheng, L. and Zhang, X. (2017). Chapter 8 - numerical methods. In Zheng, L. and Zhang, X., editors, *Modeling and Analysis of Modern Fluid Problems*, Mathematics in Science and Engineering, pages 361 – 455. Academic Press.

Zhu, L. and Peskin, C. S. (2003). Interaction of two flapping filaments in a flowing soap film. *Physics of Fluids*, 15(7):1954–1960.

Zienkiewicz, O., Taylor, R., and Nithiarasu, P. (2014). Fluidstructure interaction. In Zienkiewicz, O., Taylor, R., and Nithiarasu, P., editors, *The Finite Element Method for Fluid Dynamics (Seventh Edition)*, pages 423 – 449. Butterworth-Heinemann, Oxford, seventh edition edition.